

ARTIFICIAL AERATION ON STEPPED SPILLWAYS WITH PIERS AND FLARES TO MITIGATE CAVITATION DAMAGE

by

Jaco Koen

*Thesis presented in fulfilment of the requirements for the degree of Master
of Science in Engineering in the Faculty of Civil Engineering at
Stellenbosch University*



Supervisor: Prof G.R. Basson
Co-supervisor: Mr. D.E. Bosman

Department of Civil Engineering
Division of Water and Environmental Engineering

December 2017

Declaration

By submitting this thesis electronically, I declare that the entirety of the work contained therein is my own, original work, that I am the sole author thereof (save to the extent explicitly otherwise stated), that reproduction and publication thereof by Stellenbosch University will not infringe any third-party rights and that I have not previously in its entirety or in part submitted it for obtaining any qualification.

Signature: _____
J Koen

Date: December 2017

Abstract

Stepped spillways have been used for approximately 3500 years and, with the recent technical advances in Roller Compacted Concrete construction, these spillways have received a renewed interest over the past few decades. However, because of the possibility of cavitation damage to the spillway chute at higher discharges, the maximum discharge that these spillways can safely handle has been limited. A pre-emptive measure to combat cavitation damage is to introduce flow aeration at the pseudo-bottom. In order to aerate the flow, various crest pier aeration structures were investigated to ultimately increase the maximum safe unit discharge capacity of stepped spillways.

Different aeration structures were investigated, on two types of spillways (Type A and Type B), with the aid of two physical hydraulic models. The Type A spillway was a 1:15 scale, USBR stepped spillway with transitional crest steps and a constant step height of 1.5 m. The spillway performance of each aeration structure was determined by measuring the air concentration at the pseudo-bottom and the minimum pressure at the step riser. Experiments on the Type A spillway were carried out at a prototype unit discharge of 30 m²/s for the investigation of different pier configurations near the spillway crest. The crest pier configurations comprised two pier nose shapes, two pier lengths and the addition of a flare to the pier. The pier configuration results were compared with the performance of an unaerated stepped spillway. The maximum safe unit discharge capacity of an unaerated stepped spillway had previously been determined by Calitz (2015) to be 25 m²/s. The implementation of the bullnose, short pier, increased the maximum safe unit discharge capacity to 30 m²/s, by eliminating the risk of cavitation damage in the vicinity of the natural aeration inception point.

The Type B spillway was a WES stepped spillway, with a smooth ogee crest and constant step height of 1 m, which was used to evaluate the Chinese developed Flaring Gate Pier (FGP) design. The model scale for this spillway was 1:50. The design of the model was based on the Dachaoshan Dam (China), which has a design unit discharge of 165 m²/s. The FGP designs consisted of an X-Shape and a Y-Shape FGP, together with a slit-type flip bucket. The performance of these aerators was compared to an unaerated stepped spillway for prototype unit discharges of 50 m²/s to 200 m²/s. The most notable improvement was the increase in the maximum safe unit discharge capacity to 50 m²/s in the case of the X-Shape FGP.

In summary, the addition of a short, bullnose crest pier on low head/velocity stepped spillways increased the maximum safe unit discharge capacity to 30 m²/s. In the case of a high head/velocity stepped spillway, while the X-Shape FGP improved the maximum safe discharge capacity to 50 m²/s.

Opsomming

Getrapte oorlope is vir meer as 3500 jaar al in gebruik, en met die onlangse tegniese vooruitgang in roller-gekompakteerde beton konstruksie het hierdie oorlope die afgelope paar dekades 'n hernude belangstelling aangewakker. As gevolg van die moontlike kavitasie-skade aan die oorloop oppervlakte met hoë deurstromings, is die maksimum deurstroming wat hierdie oorlope veilig kan hanteer, beperk. 'n Voorkomingsmaatreël om kavitasie-skade te verhoed, is om die vloei naby die pseudo-bodem kunsmatig te belug. Ten einde die vloei kunsmatig te belug, is verskeie kruin belugting strukture in hierdie tesis ondersoek met die doel om die maksimum veilige eenheidsdeurstroming van getrapte oorlope te verhoog.

Verskillende belugtingstrukture is op twee tipes getrapte oorlope (Tipe-A en Tipe-B) met behulp van twee fisiese, hidrouliese modelle ondersoek. Tipe-A oorloop was 'n 1:15 skaal, USBR-getrapte oorloop met oorgangs trappe op die kruin en 'n konstante trap hoogte van 1.5 m. Die gedrag van elke belugtingstruktuur is bepaal deur die lug konsentrasie by die pseudo-bodem en die minimum drukke by die vertikale trap te meet. Eksperimente is uitgevoer op die Tipe-A oorloop met 'n prototipe eenheidsdeurstroming van 30 m²/s vir die ondersoek van verskillende pyler konfigurasies naby die oorloop kruin. Hierdie pyler konfigurasies bestaan uit twee pyler neus vorms, twee pyler lengtes en die byvoeging van 'n vlerkie aan die pyler. Die resultate van die verskillende pyler konfigurasies was vergelyk met 'n onbelugte getrapte oorloop. Calitz (2015) het voorheen die maksimum veilige eenheidsdeurstroming van 'n onbelugte getrapte oorloop bepaal as 25 m²/s. Die implementering van 'n kort, bul neus pyler, het die maksimum veilige eenheidsdeurstroming vermeerder tot 30 m²/s deur die risiko van kavitasie-skade in die omgewing van die natuurlike aanvangs belugtingspunt uit te skakel.

Tipe-B oorloop was 'n WES getrapte oorloop bestaande uit 'n gladde ogee kruin en 'n konstante trap hoogte van 1 m. Die model was gebruik om die Chinees-ontwikkelde "Flaring Gate Pier" (FGP) ontwerp te evalueer. 'n Skaal van 1:50 was vir die oorloop gebruik. Die ontwerp van die oorloop is gebaseer op die Dachaoshan Dam wat geleë is in China, met 'n ontwerp eenheidsdeurstroming van 165 m²/s. Die verskillende FGP ontwerpe bestaan uit 'n X-Vorm en 'n Y-Vorm FGP tesame met 'n spleetvormige "flip bucket". Die gedrag van hierdie belugters is vergelyk met 'n onbelugte getrapte oorloop vir prototipe eenheidsdeurstromings van 50 m²/s tot en met 200 m²/s. Die mees noemenswaardigste verbetering was die toename van die maksimum veilige eenheidsdeurstromings kapasiteit tot 50 m²/s vir die X-Vorm FGP.

In opsomming, die toevoeging van 'n kort, bul neus kruin pyler het op lae hoogte/snelheid getrapte oorlope die maksimum veilige eenheidsdeurstromings kapasiteit vermeerder tot 30 m²/s. Vir die geval van 'n hoë hoogte/snelheid getrapte oorloop, het die X-Vorm FGP die veilige eenheidsdeurstromings kapasiteit verbeter tot 50 m²/s.

Acknowledgements

I would like to acknowledge and extend my deepest gratitude towards the following people and financial institutions for their advice, guidance and support.

- Prof Gerrit Basson, my supervisor, for his mentorship, support and guidance throughout my study. Thank you for inspiring me to specialise as a hydraulic engineer;
- Mr. Eddie Bosman, my co-supervisor, for the endless amount of guidance and assistance during the latter part of my study period. I admire the broad spectrum of your intellect and expertise;
- Stellenbosch University, together with the Wilhelm Frank Trust, for funding the construction of the physical models and for the financial support which made this study possible;
- Mr. Christiaan Visser and Mr. Ning Ma, hydraulic laboratory managers, for their assistance and guidance regarding the construction of the physical models;
- Mr. Johan Nieuwoudt, Mr. Iliyaaz Williams and Mr. Marvin Lindoor, for their assistance and hard work in the physical preparation of the hydraulic experiments;
- My parents, Kobus and Marianne Koen, for their endless love, motivation and belief during this tasking time;
- To my friends and loved ones, thank you for your encouragement and belief during these two years;

Most importantly, I would like to thank God for the mental and physical ability which He has entrusted to me. This daunting task would not have been possible without Him.

Table of Contents

Declaration.....	i
Abstract.....	ii
Opsomming	iii
Acknowledgements.....	iv
Table of Contents.....	v
List of Figures	x
List of Tables	xvi
List of Appendices.....	xviii
Nomenclature	xix
Abbreviations and Acronyms.....	xxii
1 Introduction	1
1.1 Background.....	1
1.2 Objective of the Study.....	5
1.3 Overview of the Thesis	6
2 Literature.....	7
2.1 Background to the Development of Stepped Spillways	7
2.1.1 Stepped Spillway History	7
2.1.2 Modern Construction Methods.....	9
2.2 Stepped Spillway Flow Regimes.....	12
2.2.1 Nappe Flow Regime	12
2.2.2 Skimming Flow Regime	13
2.2.3 Transitional Flow Regime.....	14
2.2.4 Onset of Skimming Flow	14
2.3 Air Entrainment.....	18
2.3.1 Regions of Air Entrainment	19
2.3.2 Boundary Layer Growth.....	22
2.3.3 Surface Inception Point.....	23
2.3.4 Pseudo-bottom Inception Point.....	25

Table of Contents

2.3.5	Summary	26
2.4	Air Concentration	28
2.4.1	Mean Air Concentration along a Stepped Spillway.....	28
2.4.2	Pseudo-Bottom Air Concentration.....	30
2.4.3	Air Concentration over the Flow Depth.....	32
2.4.4	De-aeration in Impact Regions.....	33
2.4.5	Forced Aeration	34
2.5	Pressure	36
2.5.1	Pressures along the Stepped Spillway	36
2.5.2	Pressure Profiles on the Steps.....	38
2.5.3	Summary	40
2.6	Cavitation.....	41
2.6.1	Cavitation Damage	42
2.6.2	Cavitation Limitation Predictions	42
2.7	Spillway Crest Pier.....	48
2.7.1	Flow Characteristics.....	48
2.7.2	Flaring Gate Pier (FGP)	50
2.8	Scale Effects.....	53
2.8.1	Hydraulic Similarity	53
2.8.2	Similarity Laws.....	54
2.8.3	Scale Model Criteria.....	57
2.8.4	Self-Similarity.....	58
2.8.5	Avoidance of Scale Effects	59
3	Hydraulic Model Methodology	61
4	General Laboratory Facilities and Instrumentation.....	63
4.1	Laboratory Flow System	63
4.2	Instrumentation	64
4.2.1	Discharge	64
4.2.2	Pressure	65

Table of Contents

4.2.3	Air Concentration	66
4.3	Statistical Analysis	68
4.3.1	Air Concentration	68
4.3.2	Pressure	68
4.4	Sensitivity Analysis of Recording Length.....	71
4.4.1	Air Concentration	72
4.4.2	Pressure	73
4.5	Model Coordinate System.....	74
4.6	Presentation of Recorded Data.....	75
4.6.1	Air Concentration	75
4.6.2	Pressure	75
4.6.3	Position on the Stepped Spillway	75
5	Type A Stepped Spillway: Evaluation of Crest Piers and X-Shape FGP	76
5.1	Type A Stepped Spillway Design	76
5.1.1	Crest Design.....	78
5.1.2	The Rear Slope.....	81
5.1.3	The Toe	81
5.2	Spillway Crest Pier Design.....	82
5.2.1	Pier Nose Design.....	82
5.2.2	Pier Lengths	83
5.2.3	Flaring Gate Pier (FGP) Design	85
5.3	Experimental Setup for the Evaluation of Crest Piers.....	86
5.3.1	Model Layouts	86
5.3.2	Model Setup	87
5.3.3	Measuring Locations.....	88
5.3.4	Model Test Conditions on the Type A Stepped Spillway	89
5.4	Repeatability of Crest Pier Experiments.....	90
5.4.1	Air Concentration	90
5.4.2	Pressure	91

Table of Contents

5.5	Experimental Setup for the Evaluation of the X-Shape FGP	93
5.5.1	Model Layouts	93
5.5.2	Model Setup	94
5.5.3	Air Concentration Measurement.....	95
5.5.4	Measuring Locations.....	96
5.6	Repeatability of X-Shape FGP Experiments.....	97
5.6.1	Air Concentration	97
5.6.2	Pressure	98
5.7	Results.....	100
5.7.1	Visual Observations	100
5.7.2	Air Concentration Results	103
5.7.3	Pressure Results	106
5.8	Analysis of the Test Results on the Type A Stepped Spillway.....	109
5.8.1	Cavitation Limits	109
5.8.2	Crest Pier Evaluation	110
5.8.3	X-Shape FGP Evaluation.....	113
5.9	Summary of the Type A Stepped Spillway Experiments.....	114
6	Type B Stepped Spillway: Evaluation of X- and Y- Shape FGPs	115
6.1	Type B Stepped Spillway Design	115
6.1.1	Crest Design.....	117
6.1.2	The Rear Slope.....	119
6.1.3	The Toe	119
6.2	Crest Pier and Flaring Gate Pier Designs	120
6.2.1	Crest Pier Design.....	120
6.2.2	Flaring Gate Pier Design.....	121
6.3	Experimental Setup.....	124
6.3.1	Model Layouts	124
6.3.2	Model Setup	125
6.3.3	Measuring Procedures.....	126

Table of Contents

6.3.4	Measuring Locations.....	127
6.3.5	Model Test Conditions on the Type B Stepped Spillway	129
6.4	Repeatability of Experiments	130
6.4.1	Air Concentration	130
6.4.2	Pressure	131
6.5	Results.....	133
6.5.1	Visual Observations	133
6.5.2	Stage-Discharge Relationship.....	136
6.5.3	Air Concentration Results	137
6.5.4	Pressure Results	139
6.5.5	Ski-jump Trajectory Results	141
6.6	Analysis of the Test Results on the Type B Stepped Spillway.....	142
6.6.1	Cavitation Evaluation	142
6.6.2	Y-Shape FGP and Slit-type Flip Bucket Evaluation	149
6.7	Summary of the Type B Stepped Spillway Experiments.....	151
7	Conclusions.....	152
7.1	Literature Conclusions	152
7.2	Hydraulic Model Conclusions.....	153
7.2.1	Type A Stepped Spillway Investigation	153
7.2.2	Type B Stepped Spillway Investigation	153
8	Recommendations	155
	References	156
	Appendices	162
	Appendix A.....	163
	Appendix B.....	166
	Appendix C	169
	Appendix D	173
	Appendix E.....	180
	Appendix F.....	184

List of Figures

Figure 1.1: Oroville spillway damage, 27 February 2017, USA (Kolke, 2017).....	1
Figure 1.2: Self-aeration definition sketch (Pfister and Hager, 2011).....	2
Figure 1.3: Model dimensions for the 1:15 scale stepped spillway which implements a standard USBR (1987) ogee profile, transitional crest steps and two pier designs (Calitz, 2015).....	3
Figure 1.4: (i) Typical cross section through the Dachaoshan Dam (CHINCOLD, 2004) and (ii) photograph indicating the effect of the FGP on the spillway overflow (Hongta Group, 2017).	4
Figure 2.1: (i) Old stepped weir in Akarnania, Greece with the (ii) Step details (Chanson, 2000).	7
Figure 2.2: Timber crib dam built in Russia, estimated 1700 A.D. (Chanson, 2004).....	8
Figure 2.3: Maximum unit discharge capacities of stepped spillways (Chanson, 2004).....	9
Figure 2.4: (i) Formed conventional cast-in-place concrete and (ii) Pre-cast concrete facing elements (Chanson, 1994b).	10
Figure 2.5: (i) Guariraba weir, Brazil, with a gabion stepped spillway and a (ii) Typical stepped gabion weir (Chanson, 1994b).....	11
Figure 2.6: Nappe flow, (i) with fully developed hydraulic jump, (ii) with a partially developed hydraulic jump and (iii) without a hydraulic jump (Chanson, 1994b).....	12
Figure 2.7: Skimming flow regime with a (i) wake-step interface sub-regime, (ii) wake-wake interface sub-regime and (iii) recirculating cavity flow sub-regime (Chanson, 1994b).....	13
Figure 2.8: Transitional flow regime (Baylar, et al., 2006).....	14
Figure 2.9: Comparison of the different skimming flow onset prediction equations.....	17
Figure 2.10: Concept of entrained and entrapped air (Khatsuria, 2004).	18
Figure 2.11: Graphical representation of the different skimming flow regions.....	19
Figure 2.12: Graphical presentation of: (A) - Surface inception point, (B) - Pseudo-bottom inception point, (C) - Boundary layer, (D) - Pseudo-bottom (Pfister and Hager, 2011).	20
Figure 2.13: Schematic sketch of the development of a boundary layer bounded on one side (Çengel, et al., 2006).	22
Figure 2.14: Evaluation of the surface- and pseudo-bottom inception point location.	26
Figure 2.15: Mean air concentration along a stepped spillway (recreated from Matos, 2000).	29

List of Figures

Figure 2.16: Mean air concentration along a stepped spillway (recreated from Matos, 2000).	30
Figure 2.17: Schematic indicating the air inception process at the pseudo-bottom.....	30
Figure 2.18: Air concentration variation over the flow depth for a 50° spillway (Pfister and Hager, 2011).	32
Figure 2.19: Deflector aerator flow regions illustrating the de-aeration of air (Chanson, 1994a).	33
Figure 2.20: Definition sketch of a stepped spillway with a deflector aerator and bottom air concentration curve (Pfister, et al., 2006).	34
Figure 2.21: (i) Schematic sketch of the two different pier designs. (ii) Mean air concentration of a Type 1 pier. (iii) Mean air concentration of a Type 2 pier (Calitz, 2015)....	35
Figure 2.22: Pressure evolution along the centre of the horizontal steps of a stepped spillway (Sánchez-Juny, et al., 2000).....	36
Figure 2.23: Minimum pressure development for a prototype unit discharge of 30 m ² /s (Calitz, 2015).....	37
Figure 2.24: CFD simulation indicating the streamline and pressure data (Frizell and Renna, 2009).	38
Figure 2.25: Pressure profiles on the horizontal face indicating (i) Mean pressure, (ii) Maximum pressure and (iii) Minimum pressure (Sánchez-Juny, et al., 2000).....	39
Figure 2.26: Pressure profiles on the vertical face indicating (i) Mean pressure, (ii) Maximum pressure and (iii) Minimum pressure (Sánchez-Juny, et al., 2000).....	40
Figure 2.27: Collapse of an individual bubble near a surface boundary (Falvey, 1990).	42
Figure 2.28: High speed video frames taken at critical cavitation indices showing the formation of cavitation voids (Frizell, et al., 2012).....	45
Figure 2.29: Incipient cavitation number for various unit discharges corresponding to a stepped spillway with inclination angle of 51.3° and a step height of 1.5 m.	47
Figure 2.30: Flow separation around a cylindrical pier (Chadwick et al., 2013).....	48
Figure 2.31: Vortex shedding from alternative sides (Siqueira, 2005).....	49
Figure 2.32: Dachaoshan Dam, China (Hongta Group, 2017).	50
Figure 2.33: (i) Schematic illustration of the Y-Shape FGP (Ting, et al., 2011). (ii) Y-Shape FGP at Dachaoshan Dam, China (Cheng, 2005).	51
Figure 2.34: (i) Schematic illustration of an X-shape FGP (Ting, et al., 2011) and (ii) the typical flow pattern of X-shaped FGP (Wei, 2013).	52
Figure 2.35: Examples of self-similarity include, (i) ferns (Smith, 2015) and (ii) river networks (Grambeau, 2017).	58
Figure 2.36: Void fractions and turbulence intensity (Felder and Chanson, 2017).....	59

List of Figures

Figure 2.37: Evaluating a 1:15 model to eliminate scale effects based on minimum Weber and Reynolds numbers.....	60
Figure 4.1: Laboratory flow cycle.....	63
Figure 4.2: (i) SAFMAG electromagnetic flow meter and (ii) Needle gauge.....	64
Figure 4.3: Typical setup for WIKA S-10 pressure transducers.	65
Figure 4.4: (i) Schematic illustration of the conductive probe tip (Eckhard, 2016) and (ii) laboratory conductive needle probe tip (0.1 mm).	66
Figure 4.5: Schematic illustration of the conductivity acquisition in a bubble column (Eckhard, 2016).....	67
Figure 4.6: Normal distribution indicating the confidence intervals between the standard deviations (Perekupka, 2015).	69
Figure 4.7: Histogram and normal distribution bell curve for step 25.	70
Figure 4.8: Histogram and normal distribution bell curve for step 31.	70
Figure 4.9: Average air concentration, standard deviation and bubble counts for various acquisition periods.....	72
Figure 4.10: Minimum pressures for various acquisition periods and locations.....	73
Figure 4.11: Standard deviation for various acquisition periods and locations.....	74
Figure 4.12: Model coordinate system (Calitz, 2015).....	74
Figure 5.1: Schematic illustration of the Type A stepped spillway model (Not according to scale).....	77
Figure 5.2: Definition sketch of an ogee crest (recreated from USBR, 1987).....	79
Figure 5.3: Crest and transitional step zone as proposed by CEDEX.....	80
Figure 5.4: (i) Pier nose design per ASCE guidelines (1995). Prototype design of the (ii) bullnose pier shape and (iii) parabolic pier shape (dimensions in m prototype).	82
Figure 5.5: Schematic illustration of the two different pier lengths (dimensions in m prototype).	83
Figure 5.6: Bullnose pier located at step 1 for a prototype discharge of 40 m ² /s.....	84
Figure 5.7: Bullnose pier located at step 4 for a prototype discharge of 40 m ² /s.....	84
Figure 5.8: (i) Prototype design of X-shaped FGP and (ii) Isometric illustration of FGP with parabolic pier nose (dimensions in m prototype).....	85
Figure 5.9: (i) Illustration of the pier setup and experimental area. (ii) Schematic drawing of pressure and air concentration measuring locations (dimensions in mm model).	87
Figure 5.10: Air concentration comparisons of repeated test results at 35 m ² /s.....	91
Figure 5.11: Pressure comparisons of repeated test results at 35 m ² /s.	92

List of Figures

Figure 5.12: Comparison of the (i) prototype flow pattern at the Suofengying Dam, China (Anonymous, 2012) and the (ii) model flow pattern.....	93
Figure 5.13: Model setup and experimental area.	94
Figure 5.14: Photographs indicating (i) the air void behind the probe tip and the (ii) air mixture on the step once the probe enters the recirculating zone caused by the step profile.	95
Figure 5.15: (i) Schematic presentation of an outboard motor's anti-ventilation plate (Anonymous, 2013) and (ii) the addition thereof to the conductivity needle probe.	95
Figure 5.16: Air concentration comparisons of repeated test results at 30 m ² /s.....	98
Figure 5.17: Pressure comparison of repeated test results at 30 m ² /s.	99
Figure 5.18: Photographs indicating (i) the redirection of flow and (ii) a significant amount of entrained air downstream of the bullnose pier.	100
Figure 5.19: Photographs indicating (i) the adherent flow behaviour, (ii) the jet flow and air pockets and the (iii) flow separation behind the parabolic short pier.	101
Figure 5.20: Photographs indicating the adherent flow to the pier sides for the (i) bullnose long pier and the (ii) parabolic long pier.....	101
Figure 5.21: Photographs illustrating the (i) flow redirection, (ii) impact zone and (ii) aeration performance for the X-Shape FGP.	102
Figure 5.22: Air concentration and pressure results for the no pier model.	110
Figure 5.23: Air concentration and pressure results for the bullnose and parabolic short piers.	111
Figure 5.24: Air concentration and pressure results for the bullnose, short and long pier.	112
Figure 5.25: Air concentration and pressure results for the bullnose, X-Shape FGP.	113
Figure 5.26: Air concentration and pressure results for the parabolic, X-Shape FGP.	114
Figure 6.1: Schematic design of the Dachaoshan dam indicating a (i) typical cross-section and (ii) back view (Nan and Rummyantsev, 2014).....	115
Figure 6.2: Schematic illustration of the 1:50 model setup (Not according to scale).	116
Figure 6.3: Standard WES spillway crest (US Army Waterways Experimental Station, 1959).	118
Figure 6.4: (i) Pier design guidelines of the US Army WES (1959) and (ii) model pier design.	120
Figure 6.5: Illustration of the (i) prototype Y-Shape FGP design (Hongta Group, 2017) and the (ii) model Y-Shape FGP design.	121
Figure 6.6: Illustration of the (i) prototype X-Shape FGP design (Large Dam Safety Supervision Centre, 2015) and the (ii) model X-Shape FGP design.	122

List of Figures

Figure 6.7: (i) Schematic illustration of the Y-shape FGP together with the slit-type flip bucket and corresponding (ii) laboratory model.....	123
Figure 6.8: (i) Illustration of the pier setup and experimental area. (ii) Position of the pressure measuring locations.....	125
Figure 6.9: Conductivity needle probe setup for air concentration measurement.....	126
Figure 6.10: Laboratory setup for the measurement of the ski-jump length.	127
Figure 6.11: Air concentration comparison of repeated test results at 100 m ² /s.....	131
Figure 6.12: Pressure comparison of repeated test results at 100 m ² /s.	132
Figure 6.13: Photographs indicating the (i) unutilised spillway area, (ii) the large deflection that form the ski-jump regime and (iii) smooth flow transition which occur at the crest piers.	133
Figure 6.14: Photographs indicating the (i) wider bottom outlet of the X-Shape FGP, (ii) performance at a unit discharge of 30 m ² /s and (iii) the formation of the ski-jump flow regime.	134
Figure 6.15: Photographs indicating the performance of the Y-Shape FGP and slit-type flip bucket for unit discharges of (i) 50 m ² /s and (ii) 150 m ² /s.....	135
Figure 6.16: Stage-discharge relationship for the Type B stepped spillway design.....	136
Figure 6.17: Cavitation analysis based on the air concentration and pressure measurements for the control experiment.	144
Figure 6.18: Cavitation analysis based on the air concentration and pressure measurements for the Y-Shape FGP experiment.....	146
Figure 6.19: Cavitation analysis based on the air concentration and pressure measurements for the X-Shape FGP experiment.....	148
Figure 6.20: Photographs comparing the projected trajectory for the unit discharges of (i) 50 m ² /s and (ii) 100 m ² /s.....	149
Figure 6.21: Graphical comparison of the lower trajectory for the Y-Shape FGP and flip bucket.	150
Figure 6.22: Graphical comparison of the upper trajectory for the Y-Shape FGP and flip bucket.	150
Figure 8.1: Possible implementation of the Y-Shape FGP and slit-type flip bucket.....	155
Figure E.1: Pressure contour plots for the no pier control experiments.	181
Figure E.2: Pressure contour plots for the Y-Shape FGP experiments.....	182
Figure E.3: Pressure contour plots for the X-Shape FGP experiments.....	183
Figure F.1: Cavitation analysis for the control experiment at a unit discharge of 50 m ² /s...	185
Figure F.2: Cavitation analysis for the control experiment at a unit discharge of 100 m ² /s.	185
Figure F.3: Cavitation analysis for the control experiment at a unit discharge of 150 m ² /s.	186

List of Figures

Figure F.4: Cavitation analysis for the control experiment at a unit discharge of 200 m ² /s.	186
Figure F.5: Cavitation analysis for the Y-Shape FGP at a unit discharge of 50 m ² /s.....	187
Figure F.6: Cavitation analysis for the Y-Shape FGP at a unit discharge of 100 m ² /s.....	187
Figure F.7: Cavitation analysis for the Y-Shape FGP at a unit discharge of 150 m ² /s.....	188
Figure F.8: Cavitation analysis for the Y-Shape FGP at a unit discharge of 200 m ² /s.....	188
Figure F.9: Cavitation analysis for the X-Shape FGP at a unit discharge of 50 m ² /s.....	189
Figure F.10: Cavitation analysis for the X-Shape FGP at a unit discharge of 100 m ² /s.....	189
Figure F.11: Cavitation analysis for the X-Shape FGP at a unit discharge of 150 m ² /s.....	190
Figure F.12: Cavitation analysis for the X-Shape FGP at a unit discharge of 200 m ² /s.....	190

List of Tables

Table 2.1: Prediction of cavitation damage with respect to spillway velocities.	46
Table 2.2: Prototype implementations of the FGP design (Guo, 2012, Matos & Meireles, 2014).	50
Table 3.1: Test schedule.....	62
Table 4.1: Statistical summary of the pressure data (Type A configuration).	69
Table 4.2: Various acquisition periods for the pressure and air concentration tests.....	71
Table 5.1: Design summary of ogee crest (Calitz, 2015).	78
Table 5.2: Design of ogee profile (Calitz, 2015).....	80
Table 5.3: Additional prototype head (m) caused by various pier positions.	83
Table 5.4: Experimental model layouts.	86
Table 5.5: Summary of the measuring locations.....	87
Table 5.6: Air concentration and pressure measuring locations.	88
Table 5.7: Model test conditions on the Type A stepped spillway.....	89
Table 5.8: Statistical air concentration data (%) for measuring locations at Step 29B and Step 29D.	90
Table 5.9: Statistical pressure data ($p/\gamma h$) for measuring locations at Step 29B and Step 29D.	92
Table 5.10: Experimental model layouts for the evaluation of the X-Shape FGP.....	93
Table 5.11: Summary of the measuring locations.....	94
Table 5.12: Air concentration and pressure measuring locations.	96
Table 5.13: Statistical air concentration data (%) for Step 9A and Step 29A.	97
Table 5.14: Statistical pressure data ($p/\gamma h$) for measuring locations at Step 9A and Step 29A.	99
Table 5.15: Air concentration results for the crest pier models at a unit discharge of 30 m ² /s.	104
Table 5.16: Air concentration results for the X-Shape FGP models at a unit discharge of 30 m ² /s.....	105
Table 5.17: Minimum pressure results for the pier model setups at a unit discharge of 30 m ² /s.	107
Table 5.18: Minimum pressure results for the X-Shape FGP models at a unit discharge of 30 m ² /s.....	108
Table 6.1: Design summary of the WES (1959) profile.....	117
Table 6.2: Design of WES (1959) crest profile.....	119
Table 6.3: Different model layouts.....	124

List of Tables

Table 6.4: Summary of measuring locations.	125
Table 6.5: Pressure measuring locations.	128
Table 6.6: Air concentration measuring locations.	128
Table 6.7: Model test conditions on the Type B stepped spillway.	129
Table 6.8: Statistical air concentration data (%) for a unit discharge of 100 m ² /s.	130
Table 6.9: Statistical pressure data (p/γ/h) for a unit discharge of 100 m ² /s.	132
Table 6.10: Centreline air concentration results for the Type B spillway investigation.	138
Table 6.11: Centreline pressure results for the Type B spillway investigation.	139
Table 6.12: Trajectory results (m) for the Y-Shape FGP and slit-type flip bucket.	141
Table 6.13: Safe spillway length for the different model setups (dimensions in m prototype).	151
Table D.1: Pressure results for the no pier control experiments.	174
Table D.2: Pressure results for the Y-Shape FGP experiments.	176
Table D.3: Pressure results for the X-Shape FGP experiments.	178

List of Appendices

Appendix A: As built drawings of the 1:15 scale Type A stepped spillway model.....	163
Appendix B: As built drawings of the 1:50 scale Type B stepped spillway model.....	166
Appendix C: Detailed as-built model drawings of the 1:50 scale, Type B stepped spillway aeration structures	169
Appendix D: Pressure results for the 1:50 scale Type B stepped spillway	173
Appendix E: Pressure contour plots for the 1:50 scale Type B stepped spillway	180
Appendix F: Cavitation analysis of the 1:50 Type B stepped spillway	184

Nomenclature

Symbol	Description	Units
a	Acceleration	m/s^2
b	Flaring Gate Pier discharge bay width after contraction	m
B	Flaring Gate Pier discharge bay width before contraction	m
C	Local air concentration	%
C_d	Ogee spillway crest design discharge coefficient	<i>Dimensionless</i>
C_e	Ogee spillway crest discharge coefficient	<i>Dimensionless</i>
C_{mean}	Mean air concentration	%
E	Euler number	<i>Dimensionless</i>
f	Darcy-Weisbach friction factor	<i>Dimensionless</i>
f_{bi}	Bottom friction factor as defined by Boes and Hager (2003b)	<i>Dimensionless</i>
f_i	Mean bottom friction factor as defined by Tozzi (1994, cited in Khatsuria, 2004)	<i>Dimensionless</i>
F	Force	N
F_*	Froude number defined in terms of roughness height,	<i>Dimensionless</i>
	$F_* = \frac{q}{\sqrt{g \sin \theta k_s^3}}$	
F_b	Roughness Froude number as defined by Boes and Minor (2000), $F_b = \frac{q}{\sqrt{g \sin(\theta) \cdot h^3}}$	<i>Dimensionless</i>
F_i	Froude number at the inception point, $F_i = \frac{q}{\sqrt{g \cdot (\frac{h}{l}) \cdot k_s^3}}$	<i>Dimensionless</i>
F_r	Froude number, $F_r = \frac{v}{\sqrt{g y}}$	<i>Dimensionless</i>
g	Gravitational acceleration	m/s^2
h	Step height	m
h_{atm}	Atmospheric pressure head	m
h_g	Gauge pressure head	m
h_{pi}	Piezometric head	m
h_v	Vapour pressure head	m
H	Gauge pressure head	m
H_d	Ogee spillway design head	m
H_e	Ogee spillway head	m

Nomenclature

Symbol	Description	Units
k_s	Surface roughness	m
l	Step length	m
L	Effective crest length	m
L_{cr}	Critical distance downstream of the inception point where 8% air concentration is present	m
L_i	Streamwise distance from the spillway crest to the surface inception point	m
L_m	Model distance from the spillway crest to a specific point under consideration	m
L_p	Prototype distance from the spillway crest to a specific point under consideration	m
L_{pb}	Streamwise distance from the spillway crest to the pseudo-bottom inception point	m
L_s	Safe spillway length, originating at the crest apex to a position upstream of cavitation pressures	m
p	Gauge pressure reading	V
p_{cal}	Calibration pressure reading corresponding to a zero discharge	V
P	Pressure	N/m^2
P_d	Upstream vertical height to spillway crest	m
q	Unit discharge	m^2/s
q_{Design}	Design unit discharge with a probability of 0.2%	m^2/s
q_{Check}	Check unit discharge with a probability of 0.02%	m^2/s
Re	Reynolds number	<i>Dimensionless</i>
s_i	Dimensionless location parameter	<i>Dimensionless</i>
s'	Dimensionless distance along the spillway, $s' = \frac{L-L_i}{y_i}$	<i>Dimensionless</i>
V	Velocity	m/s
V_{bi}	Velocity at pseudo-bottom inception point	m/s
W	Weber number	<i>Dimensionless</i>
x	Streamwise coordinate originating at the spillway crest	m
$X_{i,crit}$	Dimensionless critical distance downstream of the inception point	<i>Dimensionless</i>
y_1	Flow depth before hydraulic jump (Nappe flow)	m
y_2	Flow depth after hydraulic jump (Nappe flow)	m
y_{90}	Mixture flow depth between pseudo-bottom and the location where 90% air concentration is present	m

Nomenclature

Symbol	Description	Units
y_c	Critical depth for a rectangular channel, $y_c = \left(\frac{q^2}{g}\right)^{\frac{1}{3}}$	m
$(y_c)_{onset}$	Critical depth at which the skimming flow regime occurs	m
y_i	Flow depth at inception point, $y_i = 0.4hF_b^{0.6}$	m
y_p	Pool depth on step (Nappe flow)	m
z	Coordinate of the vertical step face originating at the outer step edge	m
β	Flaring Gate Pier contraction ratio ($\beta = \frac{b}{B}$)	<i>Dimensionless</i>
γ	Specific weight of water	N/m^3
\varnothing	Spillway inclination angle	$^\circ$
φ_b	Initial angle of streamlines to the horizontal	$^\circ$
δ	Boundary layer thickness	m
ΔP	Change in pressure	N/m^2
ν	Kinematic viscosity	m^2/s
σ	Cavitation index	<i>Dimensionless</i>
σ_{bi}	Pseudo-bottom cavitation index	<i>Dimensionless</i>
σ_c	Critical cavitation index	<i>Dimensionless</i>
σ_T	Surface tension of water	N/m

Abbreviations and Acronyms

ASCE	American Society of Civil Engineers
CEDEX	Centro de Estudios y Experimentación de Obras Públicas (Civil engineering research agency in Spain)
CFD	Computational Fluid Dynamics
CHINCOLD	Chinese National Committee on Large Dams
FGP	Flaring Gate Pier
HZDR	Helmholtz-Zentrum Dresden-Rossendorf
ICOLD	International Congress on Large Dams
GE-RCC	Grout Enriched Roller Compacted Concrete
RCC	Roller Compacted Concrete
RSA	Republic of South Africa
USA	United States of America
USBR	United States Bureau of Reclamation
WES	Waterways Experiment Station

1 Introduction

1.1 Background

A spillway is defined as a hydraulic structure provided at storage and retention dams to release surplus or flood water which cannot be safely stored. Due to the natural, variable inflow into impounding reservoirs and dams, there will be times when the demand is surpassed and the storage capacity is exceeded. The excess water discharges over the spillway crest and accelerates down the spillway face, which induces high velocities. These high velocities generate low pressure regions in which cavitation may be imminent and which can cause major damage to the spillway or even endanger the dam's structural integrity.

A study by Nortjé (2002) attributed the main cause of dam failures to insufficient spillway capacity, which is responsible for 39% of the total dam failures in South Africa. The erosion of bywash spillways for embankment dams amounted to 20%. A recent example of a dam failure caused by an insufficient spillway design is the Oroville dam, located in California, USA. After heavy rain in Northern California, the dam's storage capacity was quickly exceeded and the surplus water was discharged over both the main- and emergency spillways. Tremendous discharges resulted in high velocities, which caused cavitation damage on the main spillway (**Figure 1.1**) and erosion on the emergency spillway, which threatened to undercut the entire dam. The possible dam collapse threatened the safety of the nearby town and nearly 200 000 people were evacuated. Fortunately, a dam collapse was avoided, but the main spillway suffered significant damage and the bare slope of the emergency spillway was considerably eroded, resulting in an estimated repair cost of \$500 million (Evans, 2017).



Figure 1.1: Oroville spillway damage, 27 February 2017, USA (Kolke, 2017).

The purpose of this investigation was thus to increase the safe discharge capacity of spillways, more specifically focussing on stepped spillways. Instead of using a traditional smooth ogee profile, a stepped profile is an inexpensive solution, which comprises a series of drops in the step invert from the crest to the toe. As a result of the recent technical advances in Roller Compacted Concrete (RCC) construction, these steps can easily be incorporated by use of the construction technique which places the concrete in successive horizontal layers. The incorporation of the steps in the RCC construction technique reduces the cost and time of construction (Chatila and Jurdi, 2004).

In combination with the less expensive RCC technique, the stepped spillway will generate substantial energy losses, thus reducing the need for a more costly stilling basin. The energy losses are generated in the form of a reduction in acceleration and development of excessive turbulence on the steps. The turbulence aids the development of the boundary layer, ensuring earlier entrainment of air into the flow. The decreased acceleration, the air entrainment and the use of resistant materials all reduce the risk of possible cavitation damage as suggested by Hay (1988).

Flow aeration, or air entrainment, is defined as the entrapment of air bubbles and pockets that are transported within the flow. Air entrainment arises as a result of the growth of a turbulent boundary layer. As the turbulent boundary layer grows, a point is reached where the boundary layer reaches the free surface. This is denoted as the surface inception point. If the turbulence overcomes the surface tension, air is entrained into the flow (Pfister and Hager, 2011). The self-aeration process is illustrated in **Figure 1.2**.

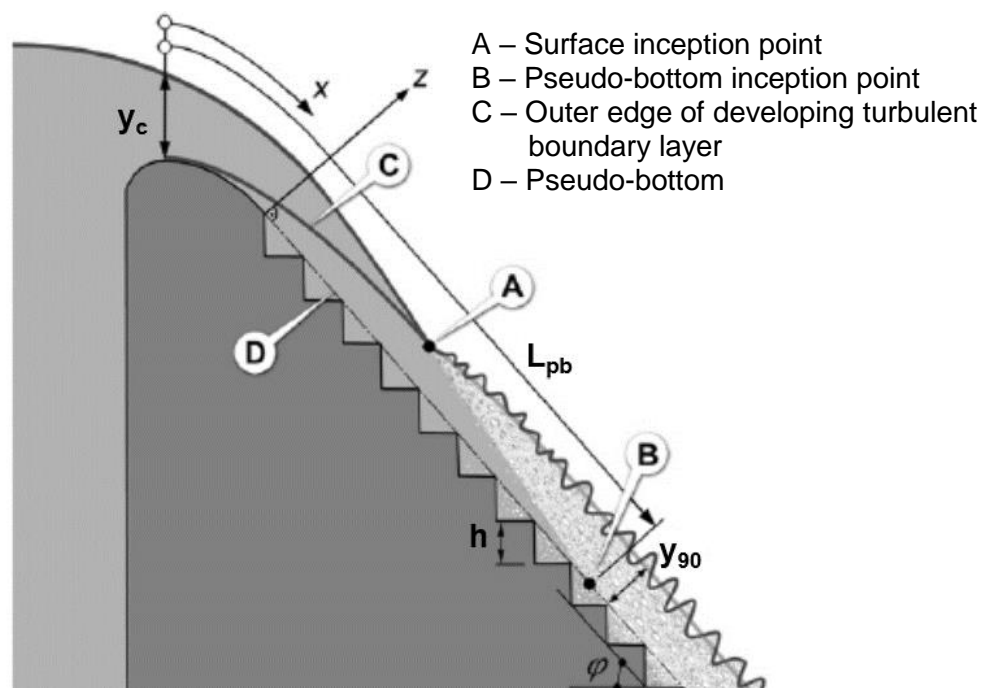


Figure 1.2: Self-aeration definition sketch (Pfister and Hager, 2011).

This thesis expanded on the initial research of Calitz (2015) by evaluating various crest pier designs with the addition of the Chinese developed Flaring Gate Pier (FGP). Calitz (2015) concluded that the introduction of crest piers alleviated the risk of cavitation damage, which in turn increased the safe unit discharge capacity of stepped spillways.

This study investigated the artificial aeration of piers and flares on two types of stepped spillways (referred to as Types A and B):

- A. A standard USBR (1987) spillway with a design discharge head of 4.2 m, step height of 1.5 m, chute slope of 51.3° and transitional crest steps (see to **Figure 1.3**):

This part of the thesis expands on the research by Calitz (2015), who investigated the efficiency of artificial aeration on a stepped spillway with different pier configurations near the spillway crest. Based on the outcome of his study, Calitz (2015) recommended further tests to establish the optimum position of the pier along the ogee profile. This thesis therefore includes the investigation of this aspect, i.e. different pier lengths at different locations, varying from near the crest to further down the chute. Other modifications of the pier included the variation of the upstream pier nose shape and the addition of a flare on the longer pier length.

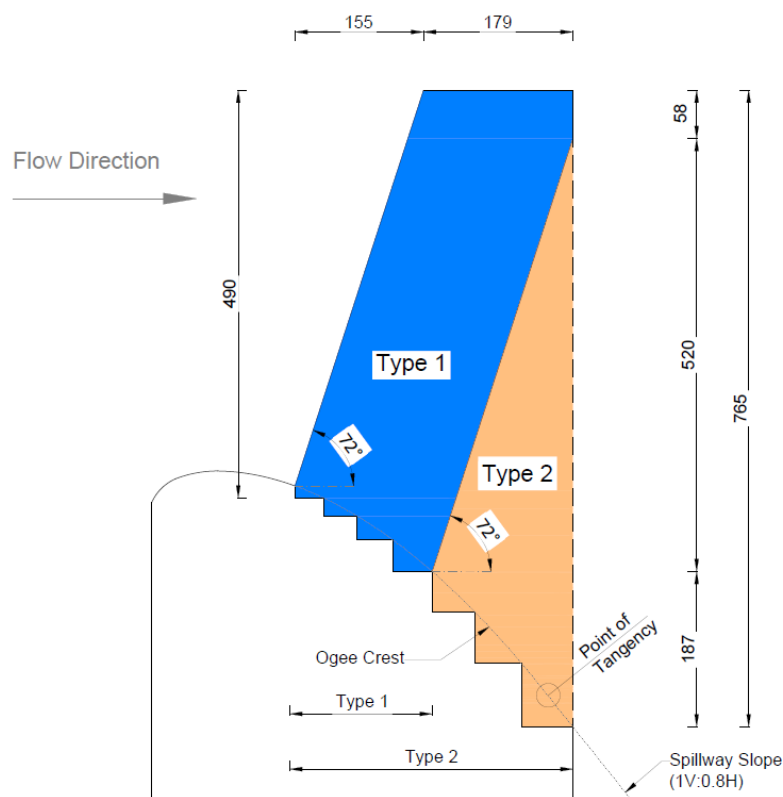


Figure 1.3: Model dimensions for the 1:15 scale stepped spillway which implements a standard USBR (1987) ogee profile, transitional crest steps and two pier designs (Calitz, 2015).

B. A standard WES (1959) spillway with a design discharge head of 17.9 m, step height of 1.0 m, chute slope of 55° and smooth ogee profile (see **Figure 1.4**)

Based on limited information from the literature regarding the combined implementation of Flaring Gate Piers (FGP) and stepped spillways, several existing Chinese dams have been designed with very large design unit discharges. It was thus decided to evaluate the performance of these spillways by investigating their aeration and the corresponding pressures. The Dachaoshan Dam is an example of the use of the aforementioned spillway design which implements FGPs, thereby enabling it to pass significantly large unit discharges (in the case of the Dachaoshan Dam, the design unit discharge is $165 \text{ m}^2/\text{s}$). The top part of the spillway is smooth, with steps commencing at the downstream ends of the FGPs. The piers protrude upstream of the dam wall and relatively far down the spillway, where they terminate at the end of the flares.

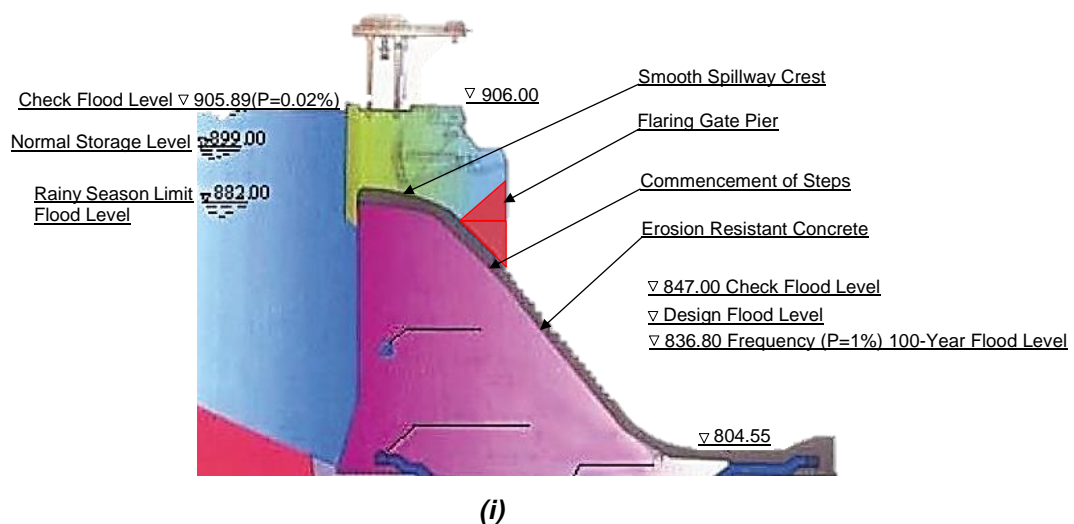


Figure 1.4: (i) Typical cross section through the Dachaoshan Dam (CHINCOLD, 2004) and (ii) photograph indicating the effect of the FGP on the spillway overflow (Hongta Group, 2017).

1.2 Objective of the Study

The main objective of this study was to investigate the safe discharge capacities of two types of stepped spillways (Types A and B as described in **Section 1.1**), each using different artificial aeration structures. To determine the safe discharge capacities, physical model studies were performed, comprising air concentration and pressure measurements on the spillway chutes as well as visual observations. Since sufficient air concentration in zones of possible cavitation can prevent cavitation damage, the limits of safe unit discharges could be determined.

Because the step configurations, chute slopes and design heads of Type A and Type B stepped spillways differ significantly, two models of different scale had to be used in the study to conform to the available flow capacity of the hydraulics laboratory at Stellenbosch University. The Type A stepped spillway with the lower design unit discharge was modelled on a scale of 1:15 and Type B, with a higher design unit discharge was modelled on a scale of 1:50.

It should be noted that all parameters and experimental results herein-after mentioned have been transformed to reflect the values and dimensions as it would have been observed in prototype, unless otherwise stated.

1.3 Overview of the Thesis

The thesis is structured as follows:

- The background and objectives are presented in **Chapter 1**.
- A literature review is discussed in **Chapter 2**, which presents a summary of the relevant phenomena and research by others associated with stepped spillways.
- The approach to the physical model studies, configurations tested and parameters recorded is described in **Chapter 3**.
- The available laboratory facilities, instrumentation and methods of measurements are presented in **Chapter 4**. Contained within this chapter are mutually applicable aspects comprising the statistical analysis, sensitivity analysis of the recording length, and presentation of the recorded data.
- Tests on the 1:15 scale model with the *Type A stepped spillway* and aeration structures (crest piers with different upstream nose configurations, pier lengths and flares) are presented in **Chapter 5** under the following headings:
 - Dimensions of model and aerator structures;
 - Measuring procedure and measuring locations;
 - Results, including visual observations, air concentrations and pressures on the spillway chute;
 - Analysis and interpretation of results with respect to the limits of safe unit discharge capacities that will prevent cavitation damage;
 - Summary containing the important findings.
- Tests on the 1:50 scale model with the *Type B stepped spillway*, together with the X- and Y-Shape Flaring Gate Pier (FGP) aeration structures, are presented in **Chapter 6** under the following headings:
 - Dimensions of model and aerator structures;
 - Measuring procedure and measuring locations;
 - Results, including visual observations, air concentrations and pressures on the spillway chute;
 - Analysis and interpretation of results with respect to the limits of safe unit discharge capacities that will prevent cavitation damage;
 - Summary containing the important findings.
- **Chapter 7** summarises the final conclusions which are presented in Chapters 5 and 6.
- Recommendations for possible further studies are addressed in **Chapter 8**.

2 Literature

This chapter reviews relevant information from literature regarding stepped spillways. A summary of the background and flow regimes of stepped spillways are presented followed by in depth research on the subject matter, namely air entrainment, air concentration, pressure, cavitation, crest piers and scale effects. A summary at the end of each section emphasises the important findings and the application thereof in the model study.

2.1 Background to the Development of Stepped Spillways

2.1.1 Stepped Spillway History

The stepped spillway has been used for approximately 3500 years. It dates back to the era of antiquity (preceding 500 B.C). Stepped chutes have been used ever since, for three applications: stepped spillways, stepped waterways and town water supply systems. The stepped geometry was originally selected because of the simplicity of its shape and the fact that it added structural stability to the dam wall. These stepped chutes were at first primarily constructed by using cut-stone masonry and timber, with a wider range of materials emerging during the 19th century (Chanson, 2004).

The oldest known stepped chutes were those built in Greece. The knowledge, skills and expertise involved in building stepped spillways were transferred by the Romans, Arabs and Spaniards successively in the Mediterranean area. The oldest stepped spillway is thought to be the overflow stepped weir in Akarnania, Greece (**Figure 2.1**) which was built in approximately 1300 B.C. The weir was constructed as an earthfill embankment with a 25 m long crest. The downstream steps were constructed by using masonry rubble set in mortar (Chanson, 2004).

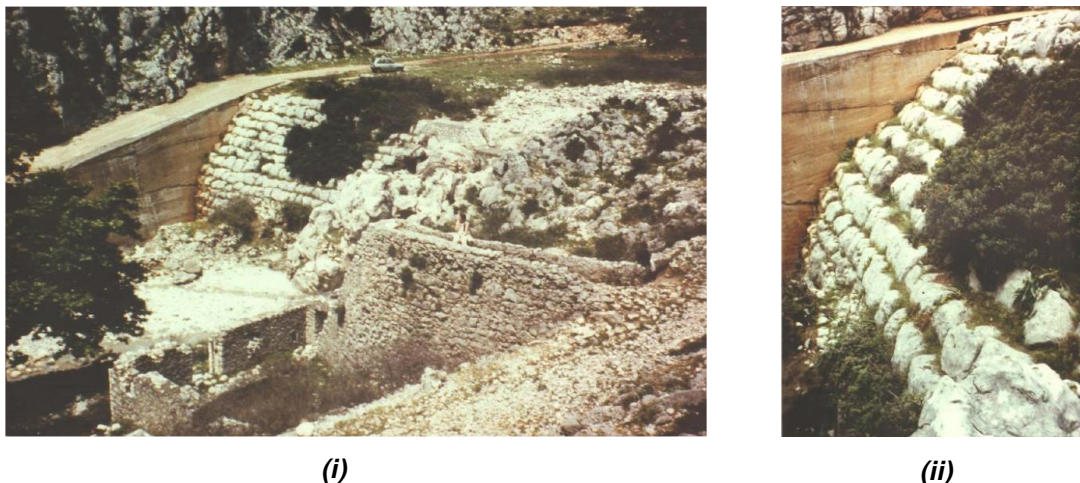


Figure 2.1: (i) Old stepped weir in Akarnania, Greece with the (ii) Step details (Chanson, 2000).

In the 17th century developments were made when timber crib dams were constructed with stepped overflows. During the 19th and start of the 20th century these timber crib dams were popular in America, Australia and New Zealand. Many timber dams were less than 10 m high, although some were successfully constructed with heights of up to 30 m. These dams could sustain considerable flood discharges with minimal damage. Illustrated in **Figure 2.2** is an example of a stepped timber crib dam wall built in Russia (Chanson, 1994b).

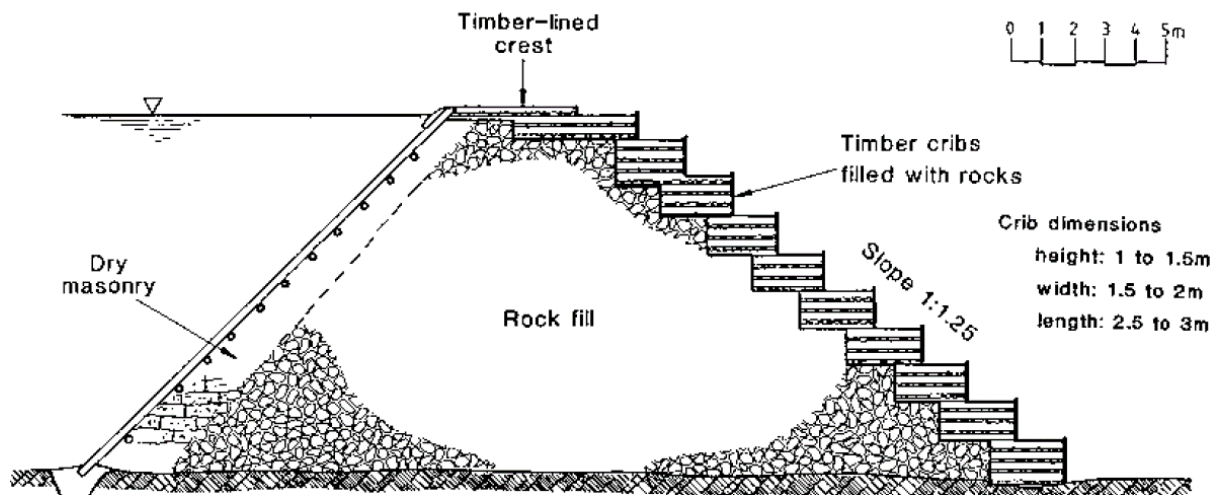


Figure 2.2: Timber crib dam built in Russia, estimated 1700 A.D. (Chanson, 2004).

The recent development of new construction materials such as RCC and reinforced gabions has increased the popularity of stepped spillways. Since the 1970s, several dams have been constructed worldwide as overflow stepped spillways. The recent construction also introduced new design techniques such as implementing embankment overtopping protection by using pre-cast concrete blocks and cast-in-situ concrete (Chanson, 2004).

Numerous stepped spillways have been used for more than a century, such as those of the Pas-du-Riot Dam (France, 1873) and the Gold Creek Dam (Australia, 1890). This emphasises the long-lasting operation of stepped spillways and the reliability of the design, together with the expertise of the designers (Chanson, 2004).

An important concern associated with the recent construction of stepped spillways is the apparent oblivion of the designers to past designs and expertise. As a result of designers' lack of knowledge and of the expertise associated with ancient stepped spillways, modern stepped spillways are still based on ancient maximum discharge per unit width capabilities. Refer to **Figure 2.3** for the maximum unit discharge capacities of stepped spillways constructed within the 19th and 20th centuries. As illustrated, the maximum unit discharge rarely exceeds 30 m²/s, which is due to the loss of the hydraulic expertise.

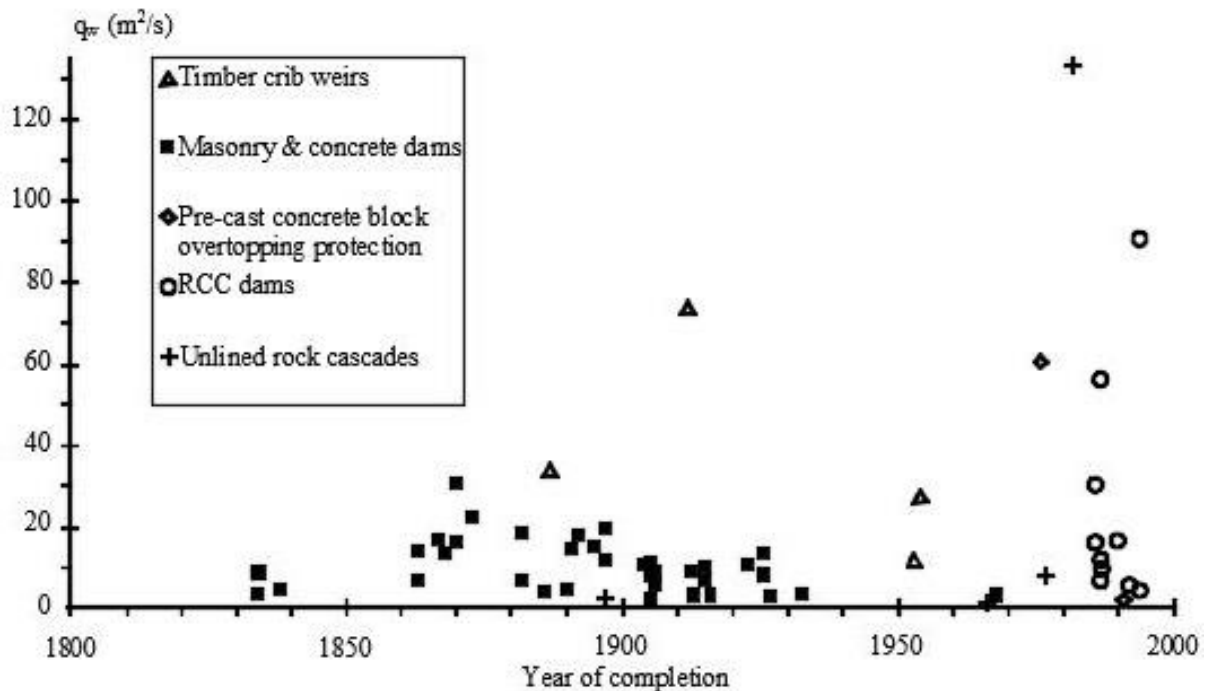


Figure 2.3: Maximum unit discharge capacities of stepped spillways (Chanson, 2004).

2.1.2 Modern Construction Methods

This section presents the modern construction methods which contributed to the viable use of stepped spillway gravity dams in preference to earth- and rockfill dams. Two of these modern construction techniques are Roller Compacted Concrete (RCC) and gabions. Since this thesis focuses on large dam stepped spillways, RCC is the preferred construction method. However, gabions are also discussed, for use in smaller stepped weirs and gabion dams (eg. Rietspruit outfall, RSA).

2.1.2.1 Roller Compacted Concrete (RCC)

RCC is a zero-slump concrete, which is transported, spread and compacted in horizontal lifts by using traditional earth moving equipment. In its unhardened state, RCC has sufficient strength to support a vibratory roller while being compacted.

Since the late 1970s, RCC has become a popular material for the construction of gravity dams. The primary advantages of RCC gravity dams are cost effectiveness, reduced foundation surface compared to earth- or rockfill structures, and a shorter construction time (Bass, 1993). The low cost of RCC gravity dams is due to small material volumes, lower cost per unit volume compared to conventional concrete, a construction technique with reduced amount of formwork, and the reduced cost of auxiliary structures (stilling basin and intake structures) (Chanson, 1994b).

The applications of RCC include the construction of new dams and the rehabilitation of existing dams. During the period 1980-2000, in the United States more than 50 dam rehabilitations took place while 30 new dams higher than 15 m were constructed by using RCC (Ditchey and Campbell, 2000). As reported by the International Congress on Large Dams (ICOLD) more than 220 dams higher than 15 m had been constructed by the end of 2001 by using RCC.

RCC is typically placed in horizontal layers by large trucks or conveyor belts. After the placement, the concrete is spread by large bulldozers and scrapers, followed by compaction, performed by heavy vibratory rollers. Subsequent layers are placed, until the desired step height has been reached (Ljubomir, 2005). The spillway step height is usually between one and four times the thickness of the compacted lift, which is typically 0.3 m. Thus, the step heights range between 0.3 and 1.2 m (Boes and Minor, 2000).

The disadvantage of using RCC compared to conventional concrete is that it has a lower resistance to erosion and cavitation of the exposed layer. These limitations can be attributed to the use of substandard materials, foundation materials, unfavourable weather conditions and ambient temperatures, spillway discharge characteristics and construction duration (Ditchey and Campbell, 2000). The following alternative techniques exist for the construction of the downstream spillway with two of which are demonstrated in **Figure 2.4**:

- Unformed exposed RCC;
- Formed exposed RCC;
- Formed grout enriched RCC (GE-RCC);
- Formed conventional cast-in-place concrete (**Figure 2.4 (i)**);
- Pre-cast concrete facing elements (**Figure 2.4 (ii)**).

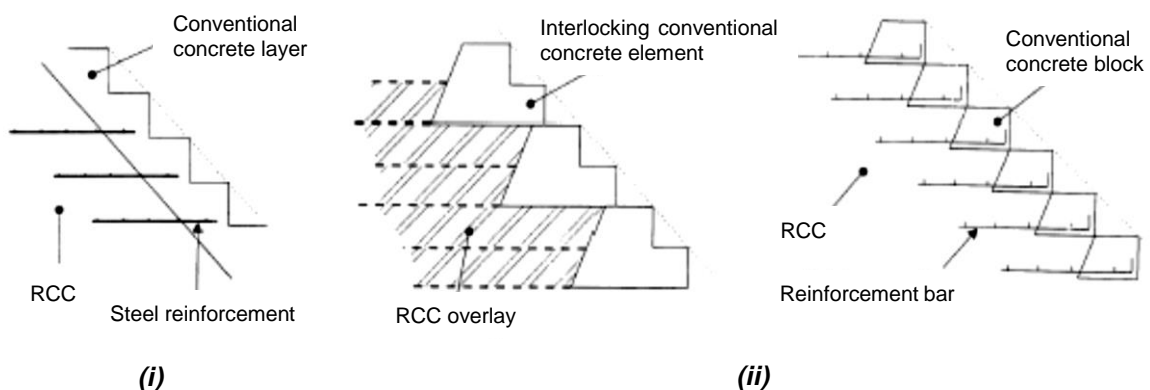
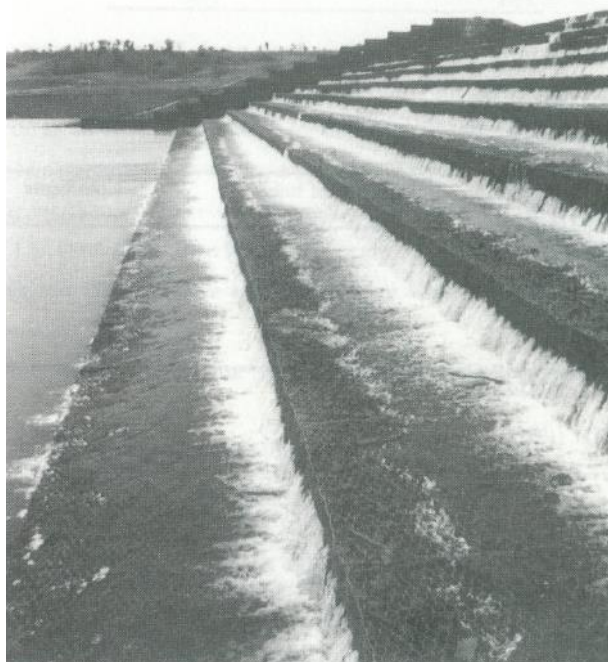


Figure 2.4: (i) Formed conventional cast-in-place concrete and (ii) Pre-cast concrete facing elements (Chanson, 1994b).

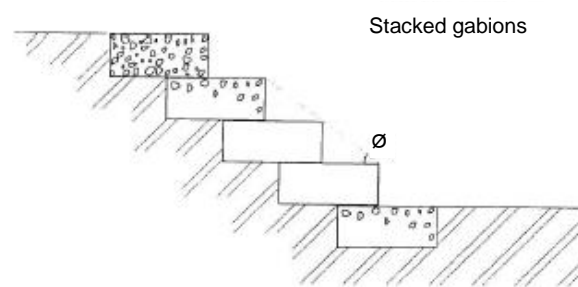
2.1.2.2 Gabions

Gabions are widely used for earth retaining structures, weirs, channel linings and even spillways. The advantages of using gabions compared to other materials are their stability, low cost, flexibility and porosity. An important factor of gabions is the porosity which prevents the large uplift pressures.

Gabions consist of rectangular cages and filling material. Typical gabions dimensions are heights of 0.5 to 1 m, a width identical to the height and a length-to-height ratio of between 1.5 and 4. The rectangular cage is normally constructed by using a soft steel wire with a zinc coating. The durability of the gabions is determined by the quality of the wire and coating. The durability is affected by debris impact, gabion flexing and corrosion. The filling material consists of loose or compacted rocks. The stone size of these rocks should be at least 1 to 1.5 times the mesh size but less than $\frac{2}{3}$ of the minimum dimension of the gabion cage (Chanson, 1994b). An existing stepped spillway is presented in **Figure 2.5 (i)** while a typical stepped gabion weir is presented in **Figure 2.5 (ii)**.



(i)



(ii)

Figure 2.5: (i) Guariraba weir, Brazil, with a gabion stepped spillway and a (ii) Typical stepped gabion weir (Chanson, 1994b).

2.2 Stepped Spillway Flow Regimes

The stepped flow conditions are classified, according to their characteristics into two distinct flow regions, namely nappe and skimming flow regimes. The nappe flow regime occurs in conditions where there are low discharges and large steps, while the skimming flow regime occurs where there are high discharges and small steps. A third, less significant, flow regime also exists, namely the transitional flow regime which is observed to occur between the nappe and skimming flow regimes. These regimes are discussed in the following subsections.

2.2.1 Nappe Flow Regime

The nappe flow regime is defined as a succession of free-falling nappes of water down a series of steps. The steps act as an overfall with the water plunging from one step to another, and an air pocket is observed below the nappe. Nappe flow is typically found in the case of small discharges and large steps (Boes and Minor, 2000). The nappe flow regime is divided into three different sub-regimes as illustrated in **Figure 2.6**:

- Nappe flow with a fully-developed hydraulic jump (**Figure 2.6 (i)**);
- Nappe flow with a partially-developed hydraulic jump (**Figure 2.6 (ii)**);
- Nappe flow without a hydraulic jump (**Figure 2.6 (iii)**).

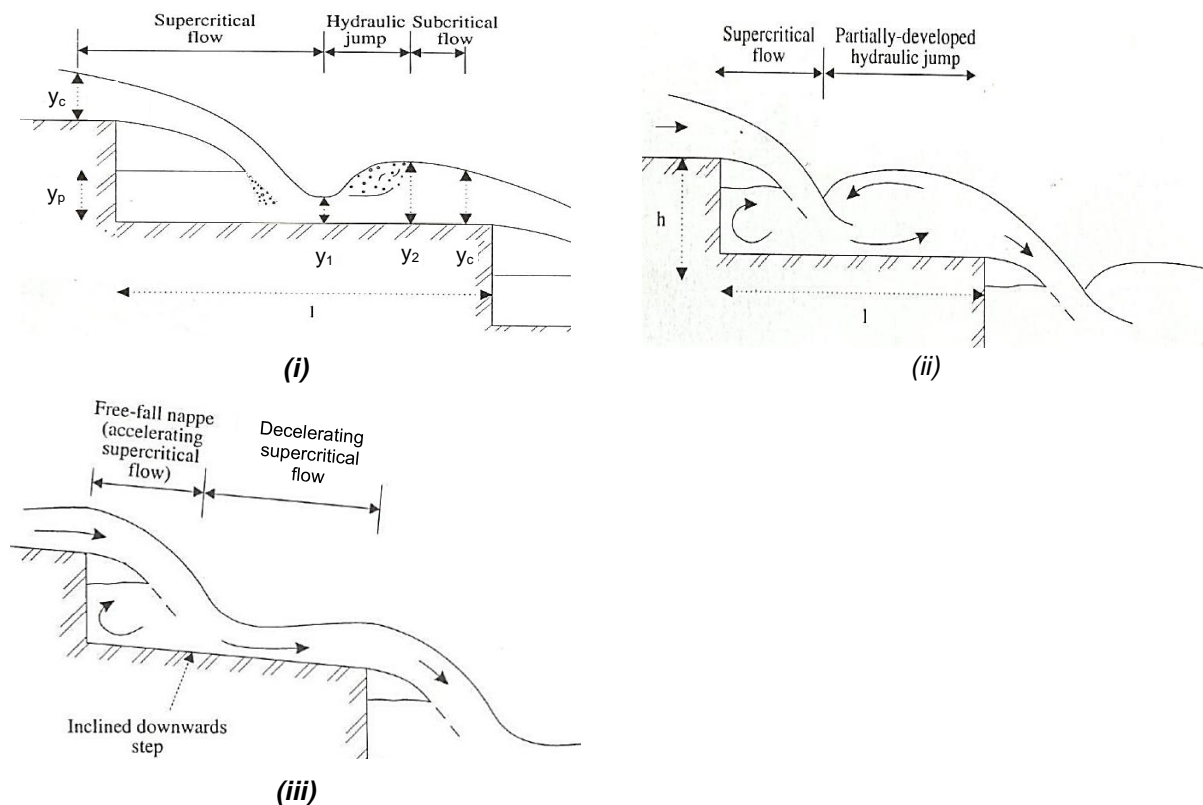


Figure 2.6: Nappe flow, (i) with fully developed hydraulic jump, (ii) with a partially developed hydraulic jump and (iii) without a hydraulic jump (Chanson, 1994b).

2.2.2 Skimming Flow Regime

The skimming flow regime is defined as a coherent stream of water cushioned by the recirculating vortices as it skims over the steps. The pseudo-bottom is formed by the external edges of the steps over which the flow passes. In the triangular cavities between the steps, recirculating vortices develop and are maintained by the transmission of shear stress from the water flowing past the step edges. The skimming flow regime generally occurs with large discharges or small steps (Boes and Minor, 2000). The skimming flow regime is divided into three sub-regimes per spillway slope (θ) (Chanson, 1994b). These sub-regimes are listed below and indicated in **Figure 2.7**.

- Wake-step interference sub-regime, $\theta < 27^\circ$ (**Figure 2.7 (i)**);
- Wake-wake interference sub-regime, $\theta = 27^\circ$ (**Figure 2.7 (ii)**);
- Recirculating cavity flow regime, $\theta > 27^\circ$ (**Figure 2.7 (iii)**).

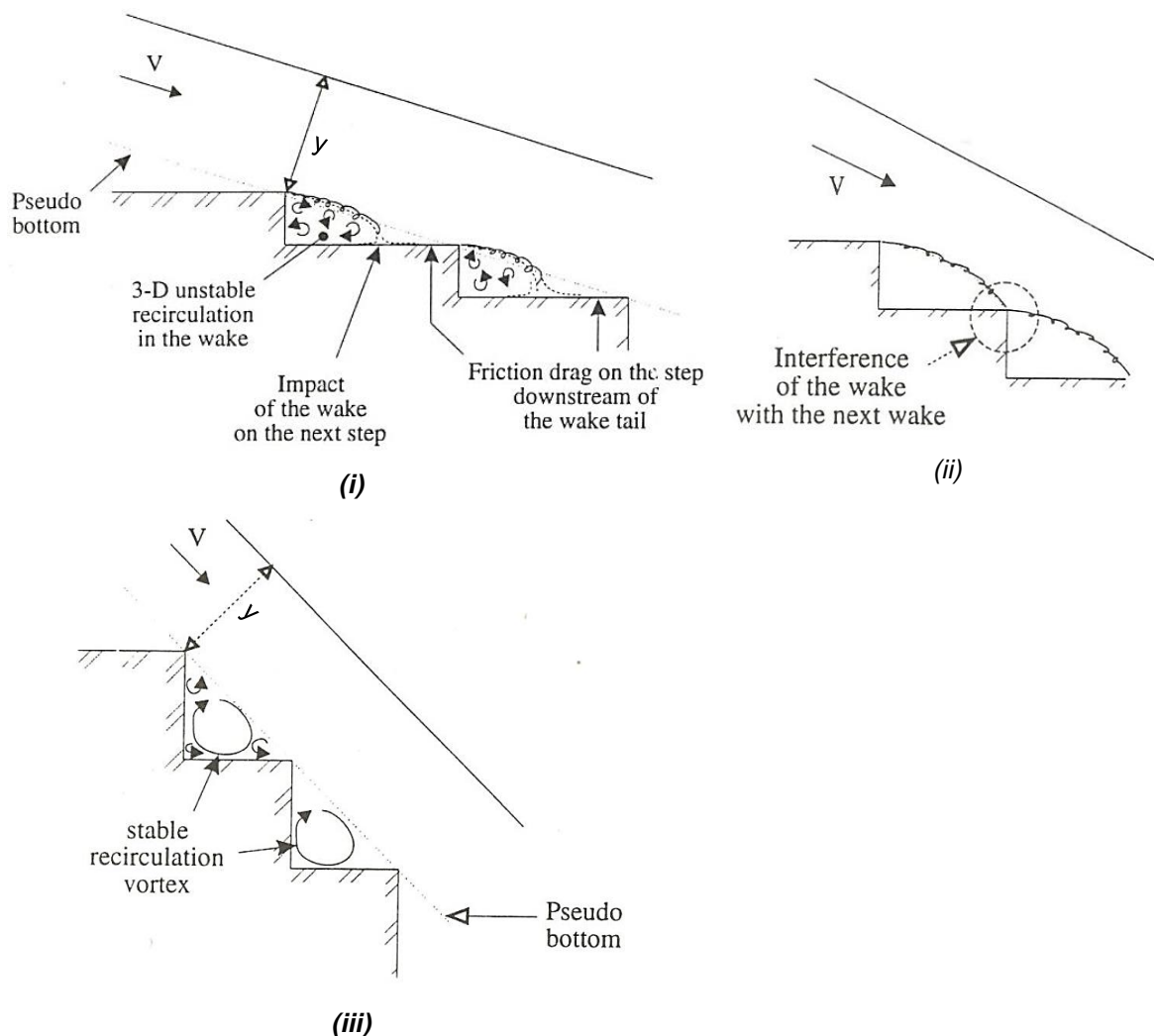


Figure 2.7: Skimming flow regime with a (i) wake-step interface sub-regime, (ii) wake-wake interface sub-regime and (iii) recirculating cavity flow sub-regime (Chanson, 1994b).

2.2.3 Transitional Flow Regime

The transitional flow regime is an intermediate flow regime between the nappe and skimming flow regimes. The transitional flow regime (**Figure 2.8**) is defined as the flow condition where both the nappe and skimming flow regimes occur simultaneously on different sections of the stepped spillway (Ohtsu and Yasuda, 1997). The occurrence of a transitional flow regime should be avoided if possible, due to the undesirable wave phenomena that occur on stepped spillways. The wave phenomenon is caused by hydrodynamic instabilities and vibrations that result from a change from aerated to unaerated nappes in the transition regime (Chanson, 1994b).

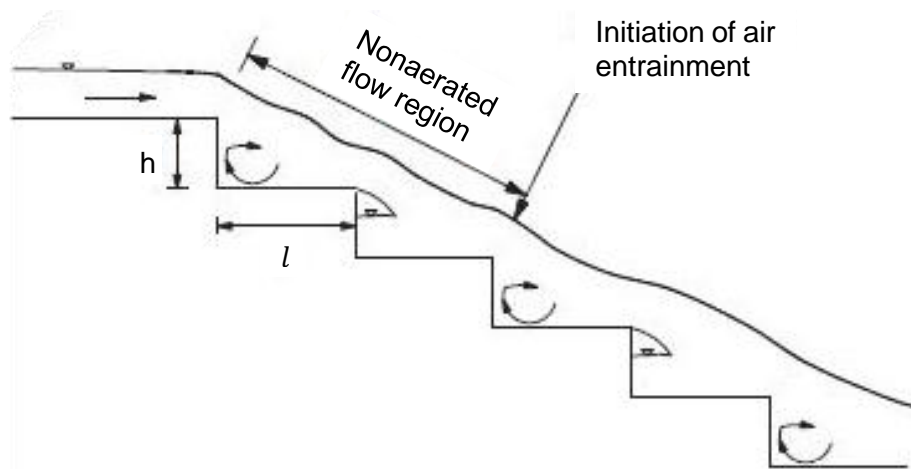


Figure 2.8: Transitional flow regime (Baylar, et al., 2006).

2.2.4 Onset of Skimming Flow

As previously mentioned, the nappe flow regime occurs when there are small discharges and flat slopes, whereas an increase in either might induce the skimming flow regime. A fundamental difference between the nappe and skimming flow regimes is the pressure distribution. In the nappe flow regime, the nappes are weightless and the pressure gradient across the nappe is nearly zero. In the skimming flow regime, the pressure is quasi-hydrostatic. The transition between nappe and skimming flow regime is characterised by a very strong pressure redistribution. This pressure redistribution is associated with a change in streamline directions. In the nappe flow, the streamlines follow a curved path as set out by the stepped geometry whereas with a skimming flow the streamlines are parallel to the pseudo-bottom (Chanson, 1996). The following subsections depict various equations that may be used to predict the onset of the skimming flow regime.

2.2.4.1 Chanson (1994b)

The onset of skimming flow is defined by Chanson (1994b) as the disappearance of the cavity beneath the free-falling nappe and the water flowing as a quasi-homogeneous stream. The onset of skimming flow is a function of discharge, step height and step length. Chanson developed an empirical equation (**Equation 2-1**) to predict the onset of skimming flow. It must be emphasised that the equation was developed for h/l ratios between 0.2 and 1.25. Refer to **Figure 2.8** for the definition of h and l .

$$\frac{(y_c)_{onset}}{h} = 1.057 - 0.465 \cdot \left(\frac{h}{l}\right) \quad 2-1$$

where:

$(y_c)_{onset}$ = Critical depth at which skimming flow regime occurs

2.2.4.2 Chanson (1996)

Chanson (1996) later developed an analytical (**Equation 2-2**) by considering nappe flow down a single-step, together with his definition of the onset of skimming flow. The analytical solution agrees reasonably well with concrete stepped models, but overestimates the onset for gabion stepped models.

$$\frac{(y_c)_{onset}}{h} = \frac{Fr^{\frac{2}{3}} \sqrt{1 + \frac{1}{Fr^2}}}{\sqrt{1 + 2 \cdot Fr^2 \left(1 + \frac{1}{Fr^2}\right)^{\frac{3}{2}} \left(1 - \frac{\cos \varphi_b}{\sqrt{1 + \frac{1}{Fr^2}}}\right)}} \quad 2-2$$

where:

Fr = Froude number at the step edge $\left(Fr = \frac{v}{\sqrt{gy}}\right)$

φ_b = Initial angle of the streamlines with the horizontal

2.2.4.3 Chamani and Rajaratnam (1999)

Chamani and Rajaratnam (1999) used a different definition for the onset of skimming flow than Chanson (1994b) had. In their experiments, the onset of skimming flow was visually observed and it was noted that the air pockets under the nappe did not disappear at the commencement of the skimming regime. Thus, Chamani and Rajaratnam (1999) assumed that the skimming flow starts when the nappe leaving a step has a slope equal to that of the spillway when impacting on the next step. They suggested that the following equations should be used to estimate the upper nappe boundary (**Equation 2-3**) and lower skimming boundary (**Equation 2-4**):

Upper nappe boundary

$$\frac{h}{l} = 0.405 \cdot \left(\frac{y_c}{h}\right)^{-0.62} \quad 2-3$$

Lower skimming boundary

$$\frac{h}{l} = \sqrt{0.89 \cdot \left[\left(\frac{y_c}{h}\right)^{-1} - \left(\frac{y_c}{h}\right)^{-0.34} + 1.5\right]} - 1 \quad 2-4$$

2.2.4.4 James, Comminos and Palmer (1999)

A study conducted by James *et al.* (1999) used the same definition for the onset of skimming flow as Chamani and Rajaratnam (1999). The following empirical equation (**Equation 2-5**) was proposed by them to estimate the onset of skimming flow:

$$\frac{y_c}{h} = 0.541 \cdot \left(\frac{h}{l}\right)^{-1.07} \quad 2-5$$

2.2.4.5 Boes and Hager (2003b)

These authors defined the onset of skimming flow as a coherent stream of water flowing over the pseudo-bottom with the absence of air pockets under the nappes. Boes and Hager (2003b) performed various experiments and found that the onset of skimming flow can be formulated as:

$$\frac{y_c}{h} = 0.91 - 0.14 \cdot \tan(\theta) \quad 2-6$$

2.2.4.6 Summary

As the aim of this thesis is to increase the unit discharge by optimising the crest pier design, large discharges are required, which introduces the skimming flow regime. The onset of the skimming flow regime must be determined to ensure that the measurements and observations are within the required flow region. The different equations for skimming flow onset prediction were graphically compared, as indicated in **Figure 2.9**, for various prototype unit discharges on a standard stepped spillway. The standard stepped spillway is characterised by a 1.5 m step height, 1 m step tread and inclination angle of 51.3°. To ensure that the skimming flow regime had been reached, the onset was determined by using the most conservative prediction equation. As illustrated in **Figure 2.9**, Boes and Hager's (2003b) prediction equation is the most conservative and resulted in a minimum prototype unit discharge of 3 m²/s.

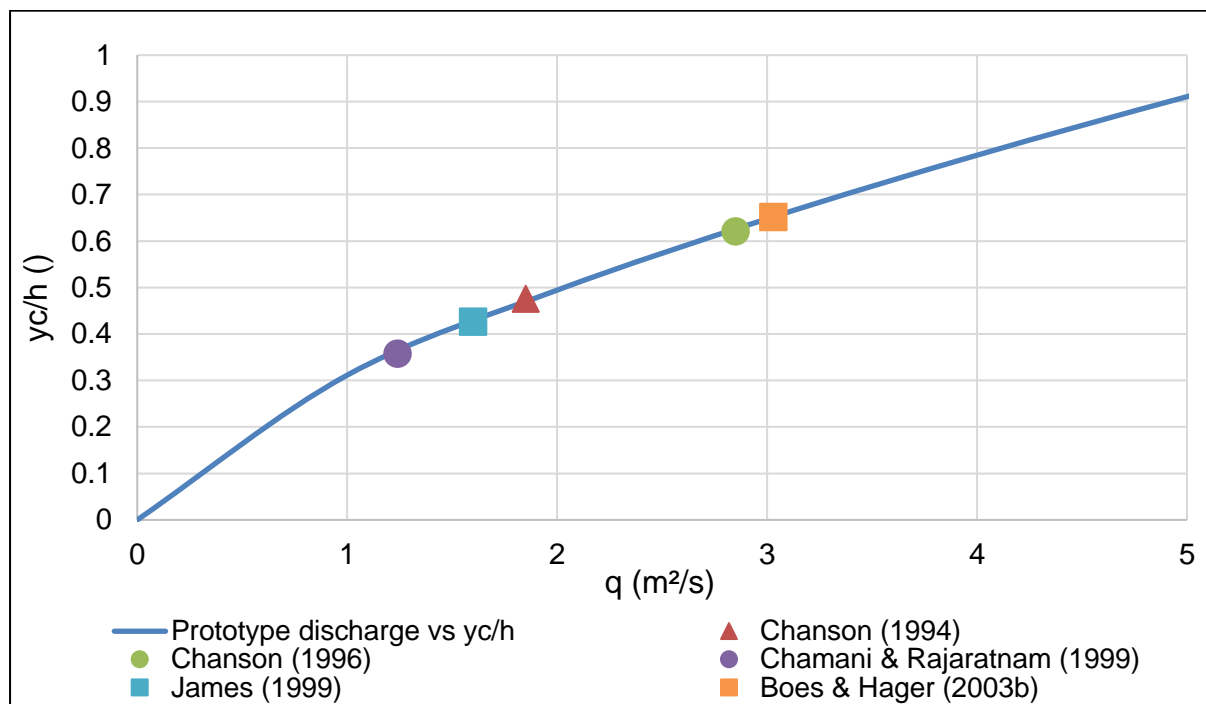


Figure 2.9: Comparison of the different skimming flow onset prediction equations.

2.3 Air Entrainment

Air entrainment on stepped spillways can be seen as either a problem or a solution. High velocity free-surface flows engulf air downstream of the non-aerated region. The surface appearance changes from clear and glossy to irregular, white and bubbly following the entrainment of air. Knowledge of aeration and the regions in which it exists (**Subsection 2.3.1**) is important to designers considering flow bulking relative to the non-aerated flow depth. In regions with considerable air entrainment, adequate side walls should be provided. Aeration also mitigates the risk of cavitation damage if the entrained air is close to the surface boundary (Khatsuria, 2004).

Self-aeration occurs on stepped spillways with the development of a turbulent boundary layer. As the boundary layer intersects the water surface, enough kinetic energy is present to overcome the surface tension and gravitational forces, and subsequently self-aeration commences (Chanson, 1994b). The total amount of conveyed air consists of entrained and entrapped air as illustrated in **Figure 2.10**. According to Khatsuria (2004), entrained air can be defined as ‘air that is being transported along with the flow in the form of air bubbles, which, at some point, have been pulled into the flowing water through the process of air entrainment’ while entrapped air is defined as ‘air that is being transported along with the flow because it is trapped in the surface roughness’.

Although the total amount of air conveyed is important when considering the bulking of flow, the focus of this thesis will be on the amount of entrained air only, in the context of cavitation prevention.

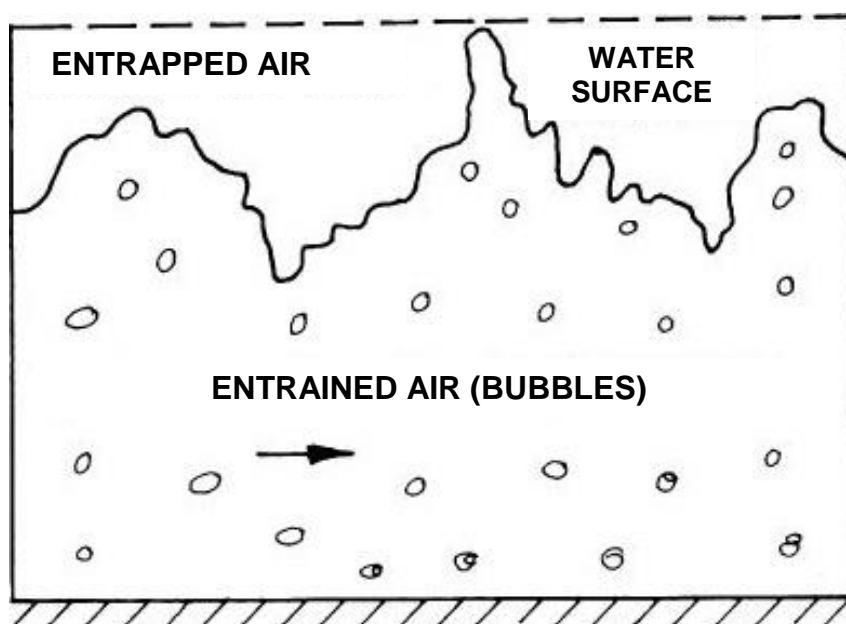


Figure 2.10: Concept of entrained and entrapped air (Khatsuria, 2004).

2.3.1 Regions of Air Entrainment

Stepped spillways are typically designed for discharges within the skimming flow regime. The skimming flow regime consists of three different flow standards:

- Main flow (Flow direction is imposed by the slope);
- Secondary flow (Large eddies which form in between the steps);
- Biphasic flow (Flow due to the mixture of air and water).

The details of the aforementioned standards are affected by the step size, geometric entrance conditions, length of the stepped region, and flow rates (Simões, *et al.*, 2012). The flow standards divide the spillway into four distinct flow regions as listed (Amador, *et al.*, 2004b):

1. Non-aerated flow (black water);
2. Rapidly varied flow;
3. Gradually varied flow (white water);
4. Uniform flow (white water).

Figure 2.11 graphically illustrates the different skimming flow regions corresponding to the numerical order listed.

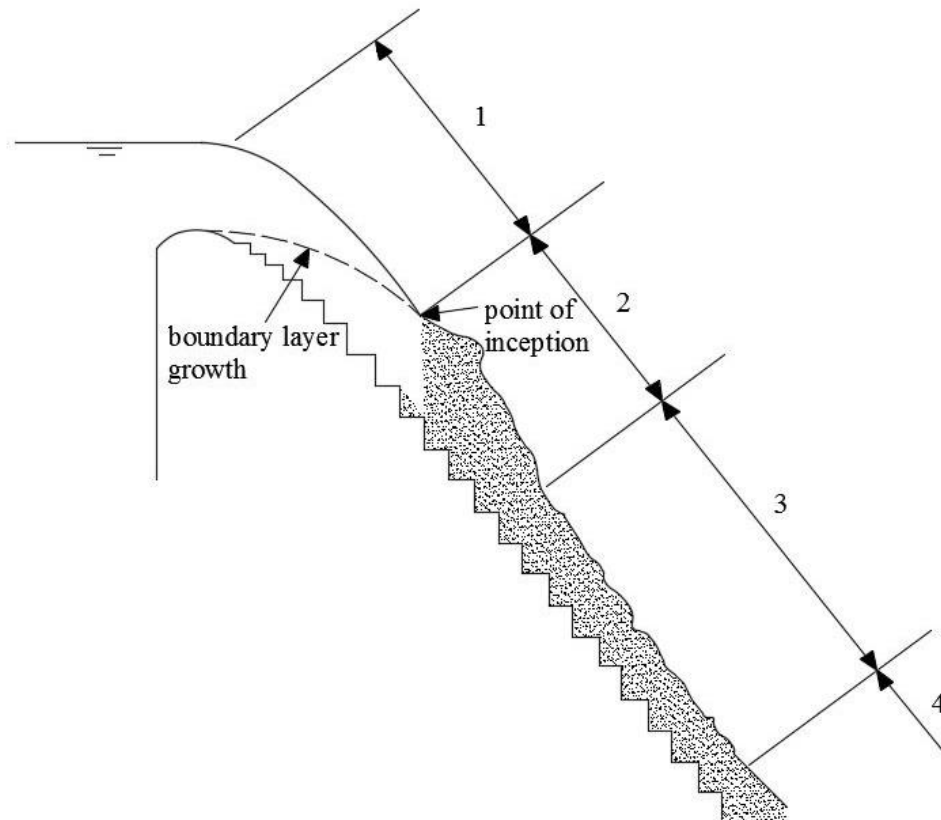


Figure 2.11: Graphical representation of the different skimming flow regions (recreated from Amador, *et al.*, 2004b).

2.3.1.1 Non-aerated Flow (Region 1)

As the flow passes over the spillway crest, it is accelerated down the spillway chute. The initial region immediately downstream of the crest consists of only water with a free surface seemingly smooth and glassy. As the flow passes over the steps, the flow resistance increases, which initiates the growth of a turbulent boundary layer, as illustrated in **Figure 2.11**. The growth of the boundary layer is affected by the step height and flow direction. The flow in the non-aerated region is generally defined as monophasic (Simões, *et al.*, 2012).

Once the outer edge of the boundary layer reaches the free surface, natural surface aeration is initiated. The position of air entrainment is defined as the 'surface inception point' and marks the boundary of the non-aerated flow region.

2.3.1.2 Rapidly Varied Flow (Region 2)

This specific flow region is generally defined as the region which is bordered by the surface inception point and pseudo-bottom inception point. Refer to **Figure 2.12** for a graphic representation of the two separate inception points. In the rapidly varied region, both the monophasic and two-phase flows are present as illustrated in **Figure 2.12**.

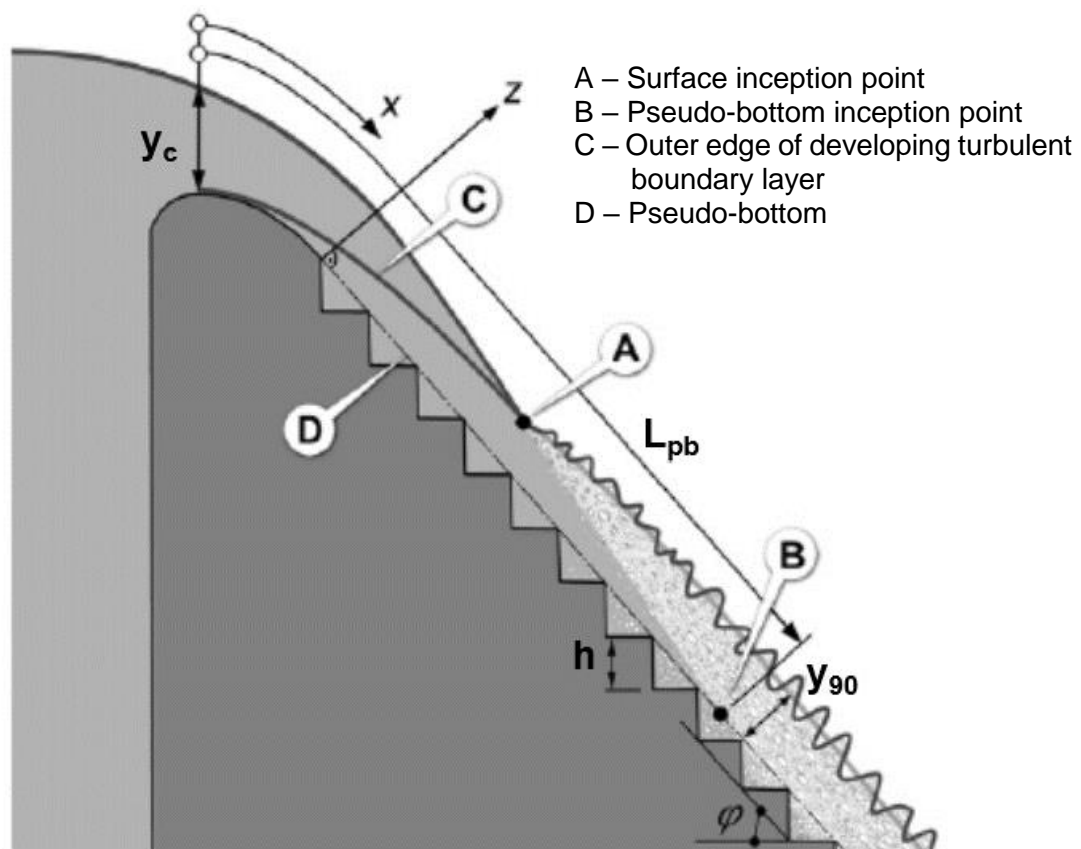


Figure 2.12: Graphical presentation of: (A) - Surface inception point, (B) - Pseudo-bottom inception point, (C) - Boundary layer, (D) - Pseudo-bottom (Pfister and Hager, 2011).

Directly downstream of the surface inception point, convex streamline curvatures are present, resulting in a sudden aeration, followed by a concave flow which favours the buoyancy of bubbles and causes a decrease in air concentration, as illustrated in **Figure 2.11** (Amador, *et al.*, 2004a).

Boes and Hager (2003a) mathematically defined the pseudo-bottom inception point as the location where the air concentration at the pseudo-bottom is equal to 1%. Downstream of the pseudo-bottom inception point, air is fully entrained over the flow depth.

2.3.1.3 Gradually Varied- and Uniform Flow Regions (Region 3 & 4)

The rapidly varied flow region is succeeded by the gradually varied flow region. In this region, the flow gradually changes form and flow characteristics, until a point of equilibrium is reached. This point will define the onset of the uniform flow region, where the flow depth, velocity and air concentration values will remain constant along the spillway. Fully developed two-phase flow conditions are present for both the gradually varied and the uniform flow regions (Amador, *et al.*, 2004a).

2.3.2 Boundary Layer Growth

A boundary layer is defined as a retarded fluid layer near a bounded surface where a shearing action is present due to viscosity. The largest portion of a stepped spillway is bounded only on the spillway surface, with small sections bounded by the surface and side walls. To describe the boundary layer growth, consider a flow bounded on one side passing over a horizontal stationary plate, as indicated in **Figure 2.13**.

The incipient flow has a uniform velocity profile (U_0) and as it comes into contact with the stationary plate, the layer of fluid in the immediate vicinity decelerates and adheres to the surface. The second layer is also decelerated, creating a shearing action with the third layer, with the trend continuing. The decelerated region is known as the boundary layer, with the fluid outside of the boundary layer remaining free of shear forces (Chadwick, *et al.*, 2013).

Two different boundary layers exist, the laminar and the turbulent boundary layers. Initially the flow is smooth, with the development of a laminar boundary layer. At the transition point (x_{cr}), the laminar flow becomes unstable and eddies start to develop. After a short transition region, the turbulent boundary layer is created, with a steeply sheared velocity profile near the plate surface and a more uniform profile further away (Chadwick, *et al.*, 2013). **Figure 2.13** illustrates that the turbulent boundary layer region is divided into four sub regions (Bakker, 2006):

- Viscous sublayer – Strong viscous shear forces;
- Buffer layer – Strong viscous shear forces;
- Overlap layer – Mixture of shear forces and eddies;
- Turbulent layer – Large scale turbulent eddies.

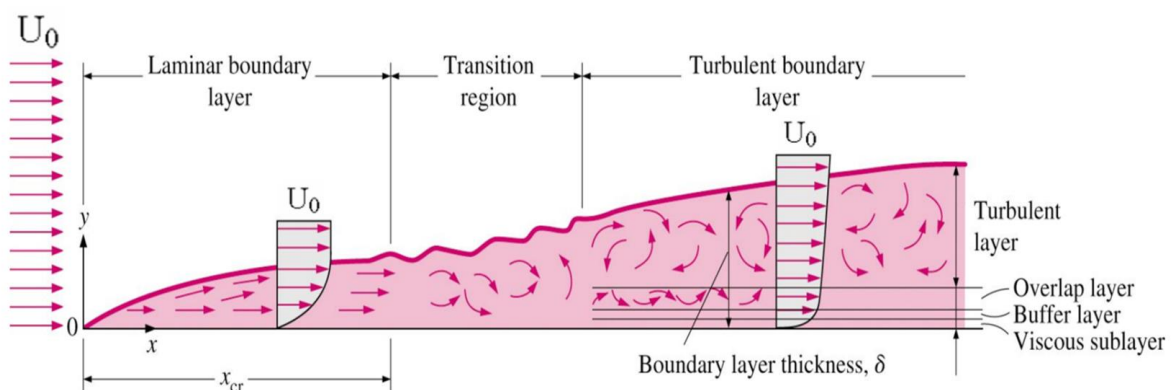


Figure 2.13: Schematic sketch of the development of a boundary layer bounded on one side (Çengel, *et al.*, 2006).

Air entrainment occurs when the boundary layer thickness (δ) reaches the fluid surface. The boundary layer thickness is defined as the perpendicular distance from the pseudo-bottom to the location where the velocity reaches 99% of the free-stream velocity. Chanson (1994b) developed a boundary layer growth equation (**Equation 2-7**) to estimate the boundary layer thickness at a certain point.

$$\frac{\delta}{x} = 0.06106 \cdot \sin(\theta)^{0.133} \left(\frac{x}{k_s}\right)^{-0.17} \quad \mathbf{2-7}$$

where:

- δ = Boundary layer thickness (m)
- x = Streamwise distance from the spillway crest (m)
- k_s = Surface roughness (m)

2.3.3 Surface Inception Point

2.3.3.1 Wood, Ackers and Loveless (1983)

These authors developed an equation (**Equation 2-8**) to predict the location of the inception point on a smooth spillway. Due to the stepped spillway having a higher surface roughness than that of a smooth spillway, this initial equation will overpredict the location of the inception point. Chanson (1994b) proved that the boundary layer growth rate is approximately 2.8 times larger on stepped spillways than on smooth spillways. The equation was developed by using a regression analysis of theoretical results covering a range of slopes, roughnesses and discharges (Wood, *et al.*, 1983).

$$\frac{L_i}{k_s} = 13.6 \cdot (\sin \theta)^{0.0796} F_*^{0.713} \quad \mathbf{2-8}$$

where:

- L_i = Distance from the start of the growth of the boundary layer to the surface inception point (m)
- k_s = Surface roughness, step depth normal to the free surface
($k_s = h \cdot \cos \theta$).
- F_* = Froude number defined in terms of roughness height on a stepped

$$\text{spillway} \left(F_* = \frac{q}{\sqrt{g \sin(\theta) k_s^3}} \right).$$

2.3.3.2 Chanson (1994b)

Chanson reiterated the complexity of the position of the inception point which is affected by the flow discharge, bottom roughness, crest design, step geometry and spillway geometry. Several stepped spillways include transitional steps near the crest which contribute to the multiplicity of influences that affect the position of the inception point. Chanson continued the work of Wood, *et al.* (1983) by re-analysing the flow properties at the inception point of model experiments. Chanson redefined the surface roughness as the depth of a step normal to the free surface ($k_s = h \cos \theta$). The application of this definition, together with a statistical analysis, resulted in the development of a prediction equation. It must be emphasised that the equation was developed for various spillway slopes of between 27° and 53°.

$$\frac{L_i}{k_s} = 9.719 \cdot (\sin \theta)^{0.0796} (F_*)^{0.713} \quad 2-9$$

2.3.3.3 Chamani (2000)

Chamani conducted various experiments for two different slopes of 51° and 59°, to investigate the air inception characteristics on stepped spillways. It was confirmed as part of this study that Chanson's (1994b) equation agreed well with the experimental results. A linear relationship between $\frac{L_i}{k_s}$ and the Froude number at the inception point was identified by Chamani. Chanson's equation was modified to include this finding and developed the following empirical equation:

$$\frac{L_i}{k_s} = 8.29 \cdot F_i^{0.85} \quad 2-10$$

where:

$$F_i = \text{Froude number at the inception point} \left(F_i = \frac{q}{\sqrt{g \left(\frac{h}{l} \right) k_s^3}} \right)$$

2.3.3.4 Matos (2000)

Through experimental investigations of air concentration and velocity data, Matos (2000) revealed that the point of inception is located upstream of the location predicted by visual observation. Matos provided an equation to determine the point of inception on stepped spillways with slopes approximating 53.1°.

$$\frac{L_i}{k_s} = 6.289 \cdot F_*^{0.734} \quad 2-11$$

2.3.3.5 Boes and Minor (2000)

Boes and Minor (2000) realised that the location of the inception point was important to give designers an idea of the unaerated region on a stepped spillway. These authors conducted hydraulic model experiments on a stepped spillway having slopes of 30° and 50°. From the experimental results, it was concluded that the unaerated spillway length can be approximated by using the following equation:

$$\frac{L_i}{k_s} = 9.72 \cdot F_b^{0.86} \quad \mathbf{2-12}$$

where:

$$F_b = \text{Roughness Froude number as defined by Boes and Minor (2000)}$$

$$\left(F_b = \frac{q}{\sqrt{g \sin(\theta) h^3}} \right)$$

Boes and Minor's (2000) equation highlights the small influence of the step height, whereas the locations of the inception point is determined predominantly by the unit discharge.

2.3.4 Pseudo-bottom Inception Point

2.3.4.1 Boes and Hager (2003a)

Boes and Hager defined the point of inception as the location where the pseudo-bottom air concentration is equal to 1%. Hydraulic model experiments were conducted on stepped spillway slopes of 30°, 40° and 50° within the skimming flow regime. From the results, Boes and Hager developed an equation to predict the location of the pseudo-bottom inception point. Their equation was rearranged to include the dimensionless parameter $\frac{L_{pb}}{k_s}$ which is presented in **Equation 2-13**.

$$\frac{L_{pb}}{k_s} = \frac{11.8 \cdot F_b^{0.80}}{\sin(2\theta)} \quad \mathbf{2-13}$$

where:

$$L_{pb} = \text{Streamwise distance between the spillway crest and the pseudo-bottom inception point.}$$

2.3.5 Summary

The location of the surface inception point defines the boundary of the unaerated region as indicated in **Figure 2.11**. Since the air concentrations and pressures are to be measured within the unaerated region, the location of the surface inception point is of the utmost importance. The predictive equations for the location of the surface and pseudo-bottom inception points, as mentioned in **Sections 2.3.3** and **2.3.4**, were evaluated for various prototype unit discharges. The stepped spillway characteristics comprised a 1.5 m step height, 1 m step tread, and an inclination angle of 51.3° , as previously mentioned in **Subsection 2.2.4.6**.

See **Figure 2.14** for a comparison of the predictive equations for the non-dimensional ratio of the inception length (L_i/k_s) versus the Froude number (F^*).

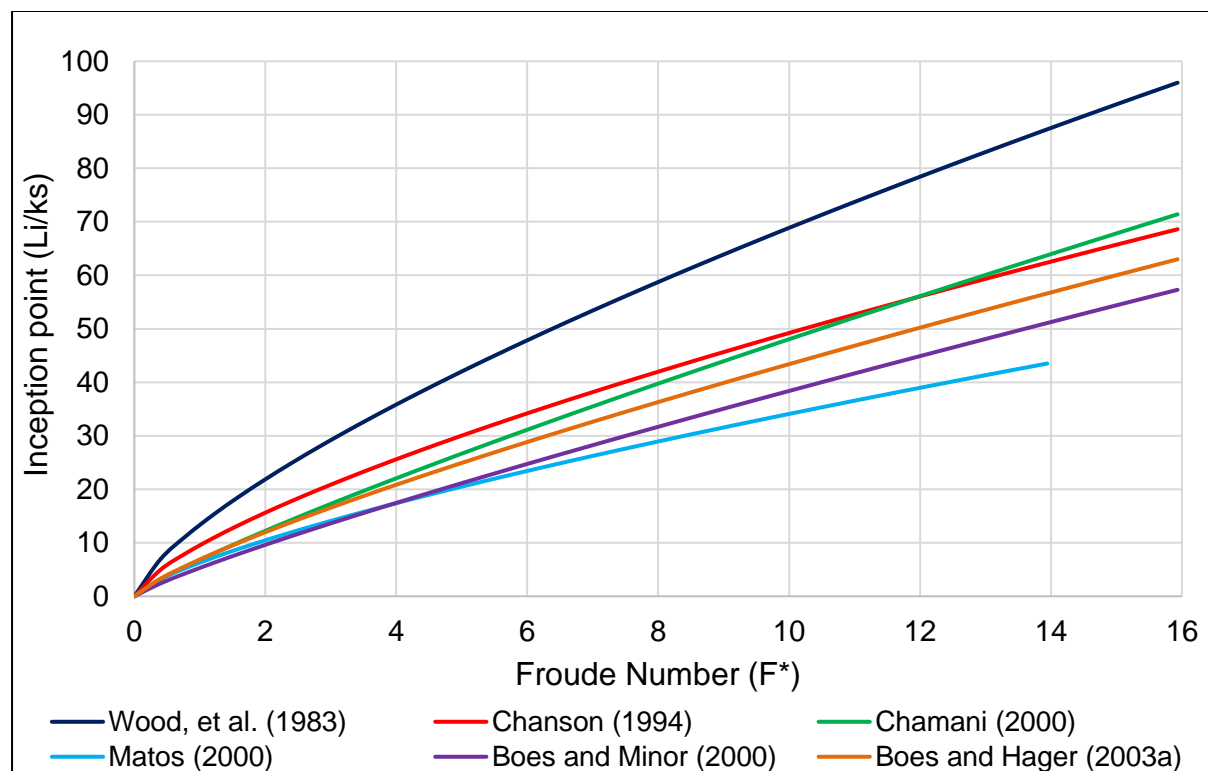


Figure 2.14: Evaluation of the surface- and pseudo-bottom inception point location.

It is evident from **Figure 2.14** that the location of the inception point varies for different Froude numbers. The Froude number is dependent on the unit discharge, which is expected since it is anticipated that the inception point will move downstream for increasing discharges.

The Froude criteria for each of the prediction models are summarised below:

- The prediction model presented by Wood, *et al.* (1983), was developed for smooth concrete spillways, and thus is not applicable to the current study. The entrainment length calculated for stepped spillways by this method is longer, compared to those calculated by other prediction models, due to the increased surface roughness of the stepped spillway in comparison with smooth spillways.
- A maximum estimated Froude number of 25 was obtained by Chamani (2000, as cited in Boes and Hager, 2003a).
- Matos (2000, as cited in Boes and Hager, 2003a) obtained a maximum Froude number of approximately 14 during experimental tests.
- Boes and Minor (2000, as cited in Boes and Hager, 2003a), Chanson (1994b, as cited in Boes and Hager, 2003a) and Boes and Hager (2003a) obtained Froude numbers exceeding 80 in their respective studies.

2.3.5.1 Applicable Equation to Predict the Inception Point

Various formulas for estimating the point of inception have been presented. These formulas were developed by means of visual observations, numerical derivations based on first principles, and depth-average air concentration data. The prediction formula presented by Boes and Hager (2003a) was developed by statistical analysis of semi-experimental air concentration data measured at the pseudo-bottom. Similar to that of Boes and Hager (2003a), the current study investigated the possibility of reducing the risk of cavitation damage by means of aeration. Since cavitation damage occurs on the concrete surface, air concentration was measured close to the surface, at the pseudo-bottom, which emphasised the importance of determining the length of the spillway to the inception point. The equation of Boes and Hager (2003a) was adopted for the estimation of the inception point location for the following reasons:

- Boes and Hager (2003a) defined the point of inception as the location where a 1% air concentration is present at the pseudo-bottom.
- The proposed equation is applicable to large Froude numbers exceeding 80.
- Comparing the results in **Figure 2.14**, the Boes and Hager's (2003a) equation represents an approximation of the average length to inception of all the equations presented.

2.4 Air Concentration

The local air concentration is defined as the volume of air per unit volume of air and water averaged over a specified time period (Matos, 2000). The air concentration varies along the spillway until an equilibrium concentration is reached in the uniform flow region. The air concentration distribution on a stepped spillway within the skimming flow regime is like that of a self-aerated flow on a smooth, unstepped spillway. Small differences were observed by Chanson and Toombes (2002), where they found that the upper layers on stepped spillways were more aerated than those on smooth spillways and less air was observed in the lower layers. This suggests that the stepped spillway has a stronger droplet ejection mechanism in skimming flows.

2.4.1 Mean Air Concentration along a Stepped Spillway

The mean air concentration is defined as a depth-average concentration measured at a specific location on a stepped spillway. The mean air concentration at any point can be expressed as:

$$C_{mean} = \frac{1}{y_{90}} \int_0^{y_{90}} C(y) dy \quad 2-14$$

where:

C_{mean}	=	Mean air concentration
y_{90}	=	Depth at which the local air concentration is equal to 90% (m)
C	=	Local air concentration

Refer to **Figure 2.15** for the development of the mean air concentration in the skimming flow regime. At the point of inception (step number 13) the mean air concentration is approximately 0.2 (Matos, 2000). Boes (1999) came to a similar conclusion when he estimated the mean air concentration at the inception point as 0.27. The dissimilarity of 0.07 can be attributed to different definitions of the inception point. Downstream of the inception point three distinct regions can be noted:

- i. The first region is characterised by a sudden increase in the mean air concentration, which attains a maximum value (step number 17) within a very short distance. The rapid increase in air concentration can be attributed to air being entrained into the flow at the surface inception point.
- ii. A subsequent downstream region exists (steps number 17 to 21) where the mean air concentration decreases until a minimum local concentration is reached. The detrainment of air is believed to be due to the flow curvature, which tends to promote

the release of air bubbles. This region coincides between the vertical where the surface wave reaches its peak, and that where it appears to end, as illustrated in **Figure 2.15** (Matos, 2000).

- iii. A third region is identified where a trend of increasing mean air concentration is observed along the spillway. Within this region, the waviness of the flow is reduced. Near the downstream section of the spillway, the mean air concentration approaches the equilibrium concentration for self-aerated flows of identical slope. According to Hager (1991), this is estimated as 0.63 for the specific model illustrated.

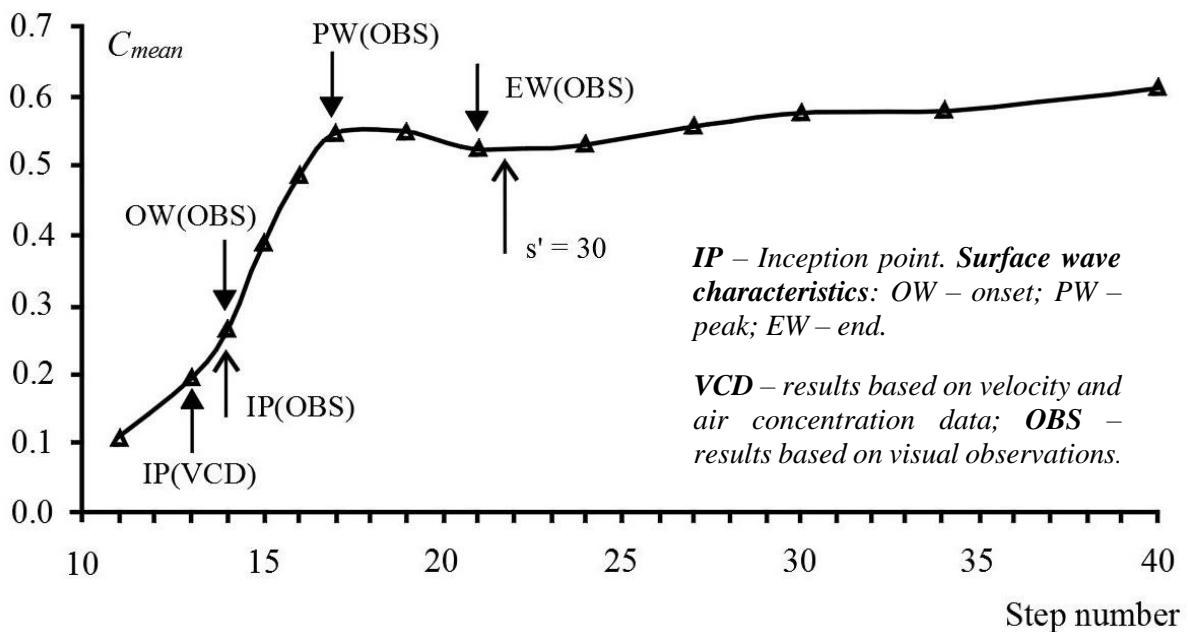


Figure 2.15: Mean air concentration along a stepped spillway (recreated from Matos, 2000).

The mean air concentration is plotted in **Figure 2.16** as a function of the dimensionless parameter $s' = \frac{L-L_i}{y_i}$, where L is the distance from the crest to the point under consideration. As shown in **Figure 2.16**, the discharge has a small influence on the mean air concentration. Matos (2000) developed the following regression formulae to estimate the mean air concentration along the spillway:

$$C_{mean} = 0.210 + 0.297e^{\{-0.497 \cdot [\ln(s') - 2.972]^2\}} \quad \text{for } 0 < s' < 30 \quad \text{2-15}$$

$$C_{mean} = \left(0.888 - \frac{1.065}{\sqrt{s'}}\right)^2 \quad \text{for } s' \geq 30 \quad \text{2-16}$$

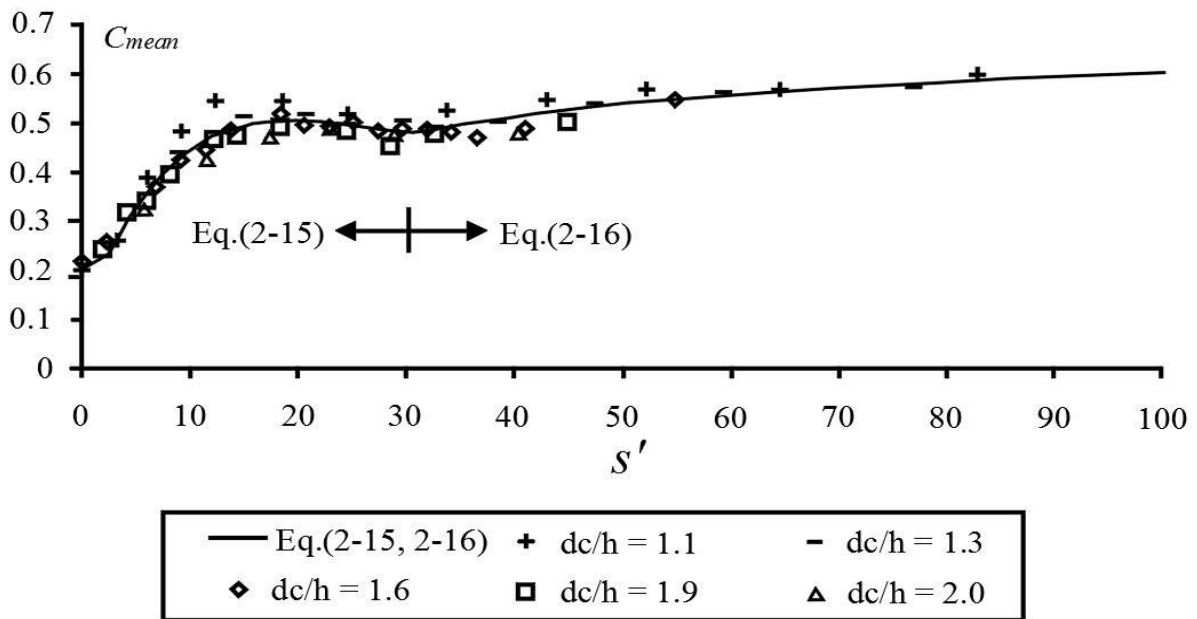


Figure 2.16: Mean air concentration along a stepped spillway (recreated from Matos, 2000).

2.4.2 Pseudo-Bottom Air Concentration

The pseudo-bottom air concentration was studied by Pfister and Hager (2011) near the pseudo-bottom inception point. The pseudo-bottom inception point was defined by Boes and Hager (2003a) as the location where the time-averaged air concentration was equal to 1%. **Figure 2.17** illustrates the air entrainment mechanism in the vicinity of the pseudo-bottom inception point as explained by Pfister and Hager (2011).

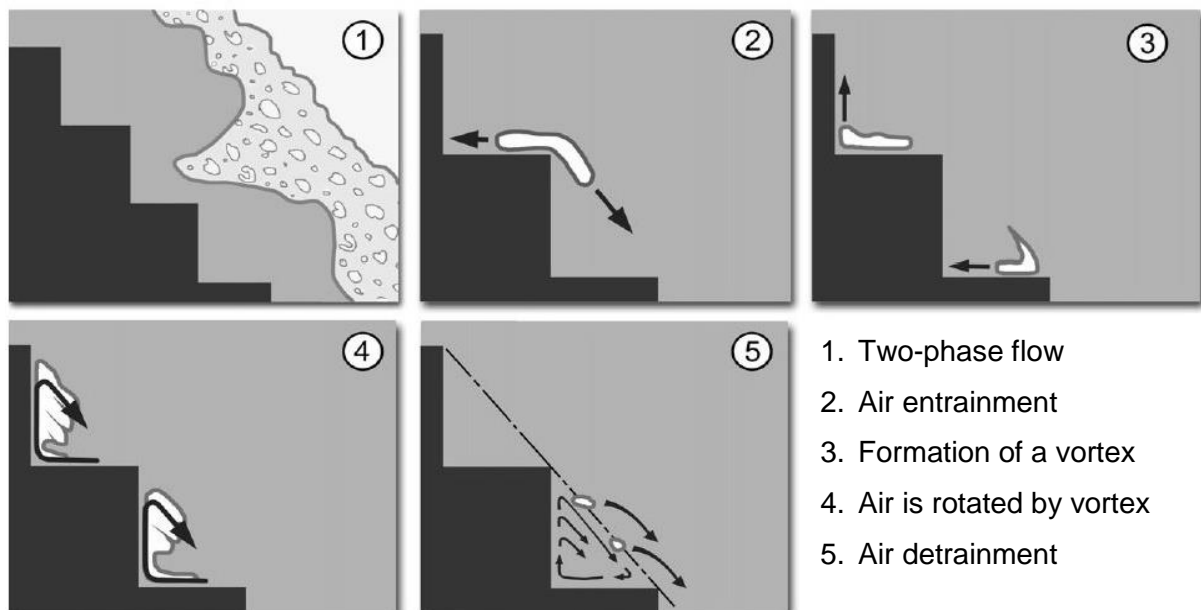


Figure 2.17: Schematic indicating the air inception process at the pseudo-bottom (Pfister and Hager, 2011).

The pseudo-bottom aeration process, as illustrated in **Figure 2.17**, is explained by the following steps (Pfister and Hager, 2011):

1. The flow at this point is classified as two-phase flow. The upper layer is highly turbulent and comprises surface waves, air troughs and entrained air. The bottom layer consists only of water and is classified as the black water region. Air troughs occasionally expand in the flow direction as a result of the local turbulence. These air troughs extend to the pseudo-bottom and impinge on a step edge.
2. The lower portion of the air trough slows down and is detached from the aerated flow to form a longitudinal trough shape. Due to the sub pressures that exist on the step edge, air is entrained on the horizontal step surfaces of the adjacent steps.
3. A local streamwise vortex is generated over a step edge, with the entrained air concentrated at the vortex centre.
4. The air is rotated by means of the vortex, which is aided by the shearing action between the main flow and the step edges, and by the fact that air bubbles rise.
5. At the end of the entrainment cycle, the air is detrained from the step niches into the black water region, as a result of instantaneous ejections of air into the main flow.

The pseudo-bottom aeration process is repeated each time an air trough extends to the step edge. Due to the constant repetition of the process, the instantaneous location of the pseudo-bottom inception point varies over a few steps.

2.4.3 Air Concentration over the Flow Depth

Pfister and Hager (2011) conducted experimental studies to examine the variation in air concentration over the flow depth. **Figure 2.18** illustrates their findings for various $\frac{x}{L_i}$ positions and two discharges. Similar findings were presented by Chanson and Toombes (2002), Carosi and Chanson (2008) and Matos *et al.* (2000). The symbol definitions are as follows:

- x is defined as the streamwise coordinate originating at the spillway crest.
- y is defined as the flow depth measured perpendicular to the pseudo-bottom.
- y_{90} is defined as the flow depth at which the air concentration is equal to 90%.

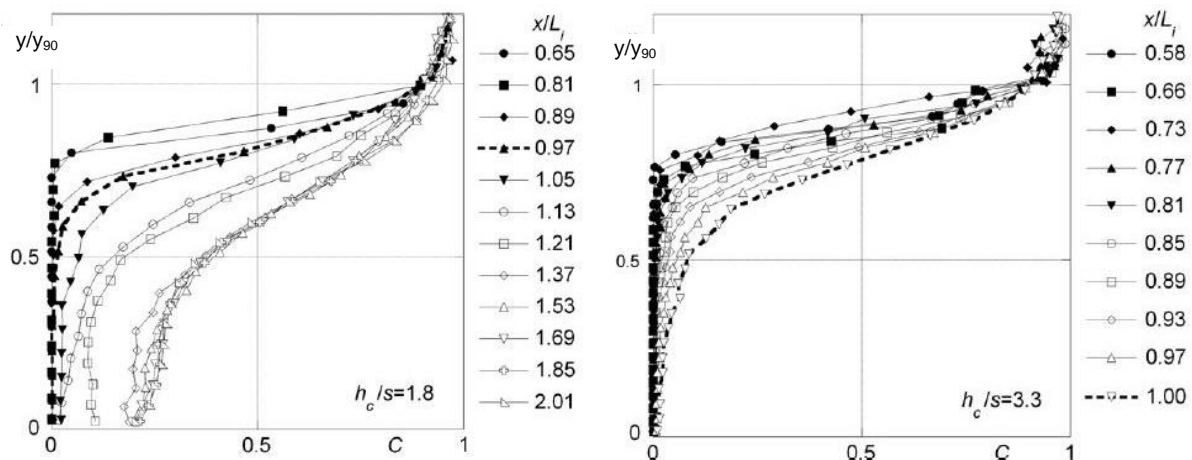


Figure 2.18: Air concentration variation over the flow depth for a 50° spillway (Pfister and Hager, 2011).

Pfister and Hager (2011) identified three flow zones namely:

- $\frac{x}{L_i} < 0.8$ where upstream of the inception point, black water was observed for $\frac{y}{y_{90}} < 0.7$.
- $\frac{x}{L_i} \approx 1$ at the inception point the flow is primarily aerated close to the free surface. A small amount of air bubbles is transported below $\frac{y}{y_{90}} < 0.5$.
- $\frac{x}{L_i} > 1.5$ towards the equilibrium flow, the pseudo-bottom flow velocity is slower than the surface flow velocity, which indicates a slower rate of air transport.

2.4.4 De-aeration in Impact Regions

Chanson (1994a) conducted a physical model investigation in which the processes of aeration and de-aeration were identified for a bottom aeration device, also known as a deflector aerator. Five distinct flow regions were introduced, as illustrated in **Figure 2.19**, with the addition of the bottom aerator, and these are:

1. The approach flow region upstream of the aerator;
2. The transition region which coincides with the length of the aerator;
3. The aeration region downstream of the aerator;
4. The impact region;
5. The downstream flow region.

Air is entrained at both the upper and lower air-water interfaces, as well as by plunging jet entrainment at the intersection of the jet with the recirculating pool, formed at the end of the cavity within the aeration region. Downstream of the aeration region, within the impact region, air is detrained/de-aerated. This detrainment is subject to a rapid, pulsating, change in pressure from a negative to a positive pressure at the impact point. Chanson (1994a) found that up to 80% of the entrained air along the jet was detrained within the impact region. The quantity of de-aeration is based on the jet velocity at impact; jet thickness at impact; gravity; angle of the jet with the spillway at impact; spillway inclination angle and the quantity of air entrained. A similar study by Pfister, *et al.* (2006) mentioned a sudden air detrainment downstream of a deflector aerator, which is discussed in **Section 2.4.5.1**.

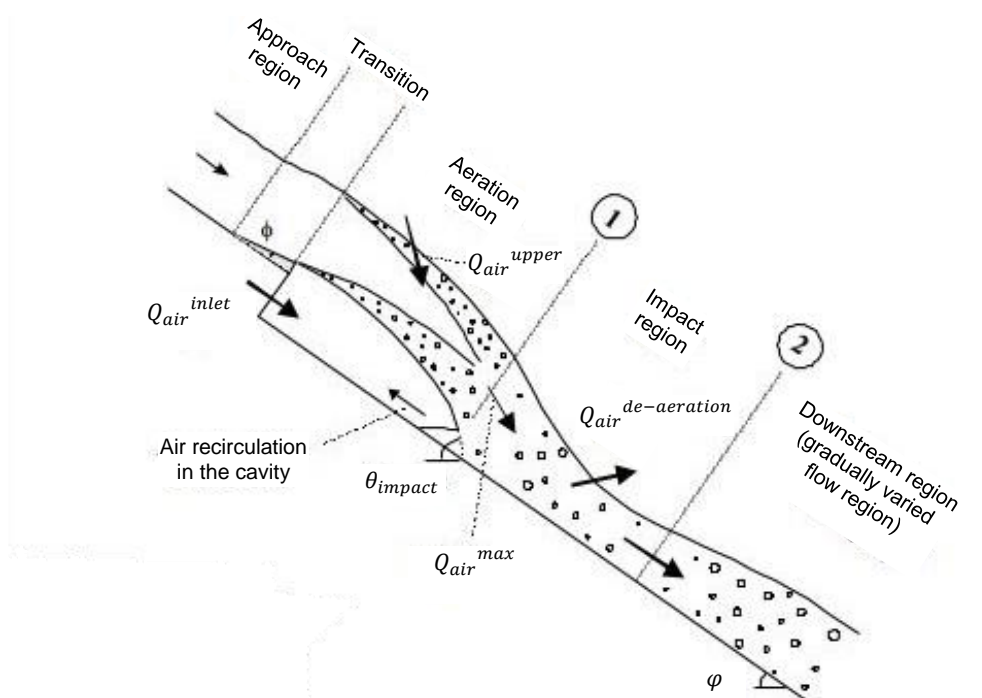


Figure 2.19: Deflector aerator flow regions illustrating the de-aeration of air (Chanson, 1994a).

2.4.5 Forced Aeration

The critical section of a stepped spillway is the unaerated region located near the spillway crest. Due to negative pressures that occur on the step edges and the absence of air within this region, the potential for cavitation damage increases. A simple and effective way to prevent cavitation damage is to introduce air near the spillway surface by artificial aeration.

Artificial aeration is achieved by means of installing an aerator. Khatsuria (2004) defined an aerator as 'a device that deliberately causes a large cavity or void to be formed on the underside of a high velocity jet.' The cavity is created within a pressure region that is negative relative to atmospheric pressure and air is drawn to the cavity via a vent or directly from the atmosphere. Different types of aerators exist, such as deflectors or ramps, offsets, steps, grooves and crest piers (Khatsuria, 2004). Two of these aerators are discussed in the following subsections.

2.4.5.1 Deflector Aerator

Model studies were conducted (Pfister, *et al.*, 2006) to investigate the effect of a deflector aerator, located at the first vertical step (**Figure 2.20**), on the amount of entrained air near the pseudo-bottom. The results indicated that a significant amount of air was entrained directly downstream of the aerator, but was quickly detrained within less than two step heights. Pfister *et al.* (2006) associated the significant air detrainment with the jet's impact on the horizontal step face and the generation of turbulent vortices which lose air as the vortex rolls up on the step face. Downstream of the sudden air detrainment, a gradual decrease in air concentration is observed before the pseudo-bottom inception point is reached. Beyond the inception point, the air concentration is dictated by the self-aeration of the spillway and is unaffected by the aerator.

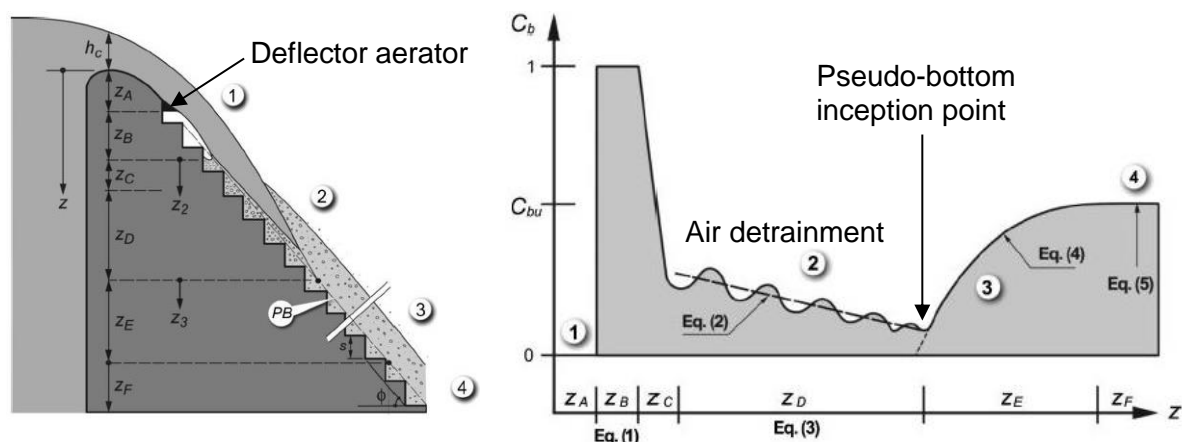


Figure 2.20: Definition sketch of a stepped spillway with a deflector aerator and bottom air concentration curve (Pfister, *et al.*, 2006).

2.4.5.2 Crest Pier

Calitz (2015) conducted a physical hydraulic model study to investigate whether the introduction of a crest pier could initiate an earlier onset of air entrainment. Two different piers were used in this study, both designed as bullnose piers, but consisted of different lengths, as indicated in **Figure 2.21 (i)**. The results indicated that directly downstream of the Type 1 pier, shown in **Figure 2.21 (ii)**, air was entrained but reduced downstream as the air spread across the width of the spillway. Further downstream, the air concentration decreased until a location was reached just upstream of the pseudo-bottom inception point. From this point the air concentration gradually increased across the width of the spillway until the critical point was reached. Calitz (2015) found that for the Type 2 pier, shown in **Figure 2.21 (iii)**, a local increase in air concentration was observed directly downstream of the pier which did not spread across the width of the spillway as effectively had been the case for the Type 1 pier.

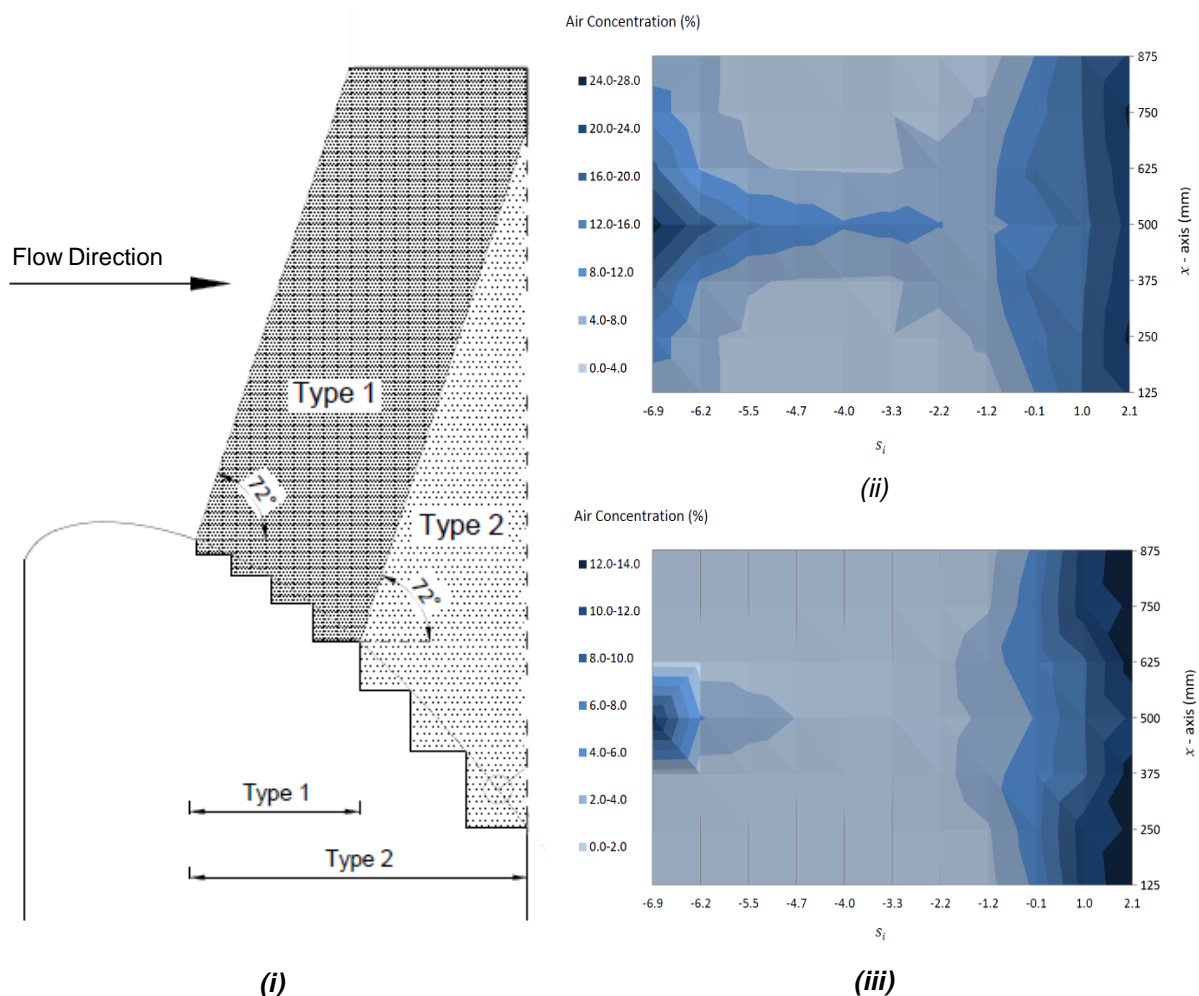


Figure 2.21: (i) Schematic sketch of the two different pier designs. (ii) Mean air concentration of a Type 1 pier. (iii) Mean air concentration of a Type 2 pier (Calitz, 2015).

2.5 Pressure

The hydrodynamic pressure field is important when considering the safety of steep sloping stepped spillways. In the skimming flow regime, a triangular area exists, between the step profile and pseudo-bottom, which contains maximum turbulence. The pressure fields within these triangular areas are expected to exhibit intense pressure fluctuations, which could cause intermittent cavitation inception. This is particularly important for the unaerated region between the crest and the pseudo-bottom inception point (Khatsuria, 2004). Downstream of the pseudo-bottom inception point, air will have reached the structure surface, which is thus well protected against cavitation, as was found by Peterka (1953).

2.5.1 Pressures along the Stepped Spillway

Sánchez-Juny *et al.* (2000) conducted experimental tests to investigate the development of pressure along the centre of the horizontal faces of a stepped spillway. The results were presented in dimensionless units and included the mean, minimum and maximum pressures as illustrated in **Figure 2.22**.

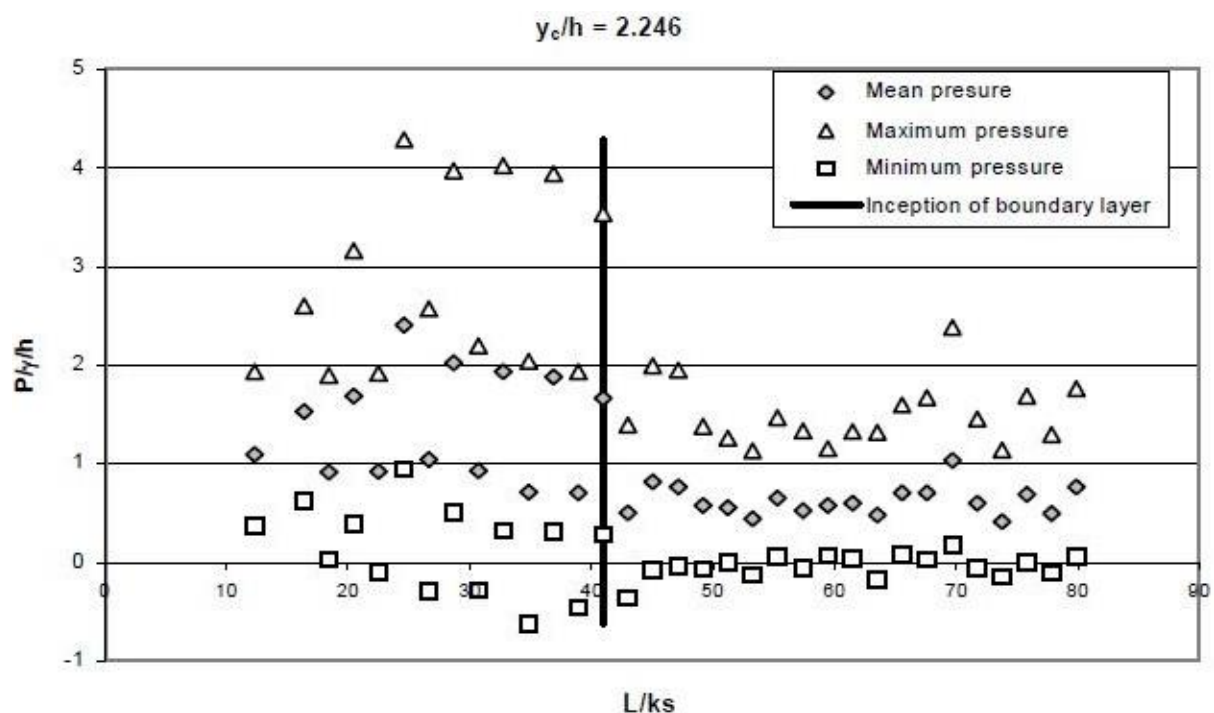


Figure 2.22: Pressure evolution along the centre of the horizontal steps of a stepped spillway (Sánchez-Juny, *et al.*, 2000).

Sánchez-Juny *et al.* (2000) made the following observations concerning the pressure development:

- The fluctuating pressure profile as illustrated in **Figure 2.22**, is separated into two distinct regions with the point of inception acting as the border. Within the upstream region, the pressures undergo a greater variability than downstream, where the flow is fully developed.
- Mean pressures are positive all along the spillway. Negative pressures are observed when considering the minimum values that were recorded.
- Maximum and minimum pressures occur in the upstream region.
- The measured pressures exhibit a wavy pattern down the spillway. Similar behaviour was observed by Ohtsu and Yasuda (1997) and Sánchez-Juny *et al.* (2008). Downstream of the inception point, the introduction of air near the spillway surface prevents cavitation damage and reduces the pressure fluctuations. This is termed the cushioning effect.

A study by Calitz (2015) illustrated a similar pressure development along the length of the spillway, as indicated in **Figure 2.23**. This supported the previous findings of Sánchez-Juny *et al.* (2000), which had stated that the most severe minimum pressures occurred near the inception point. The exact position of the minimum pressure location is debateable since it occurred downstream of the inception point as indicated in **Figure 2.23**, which contradicts the findings of Sánchez-Juny *et al.* (2000).

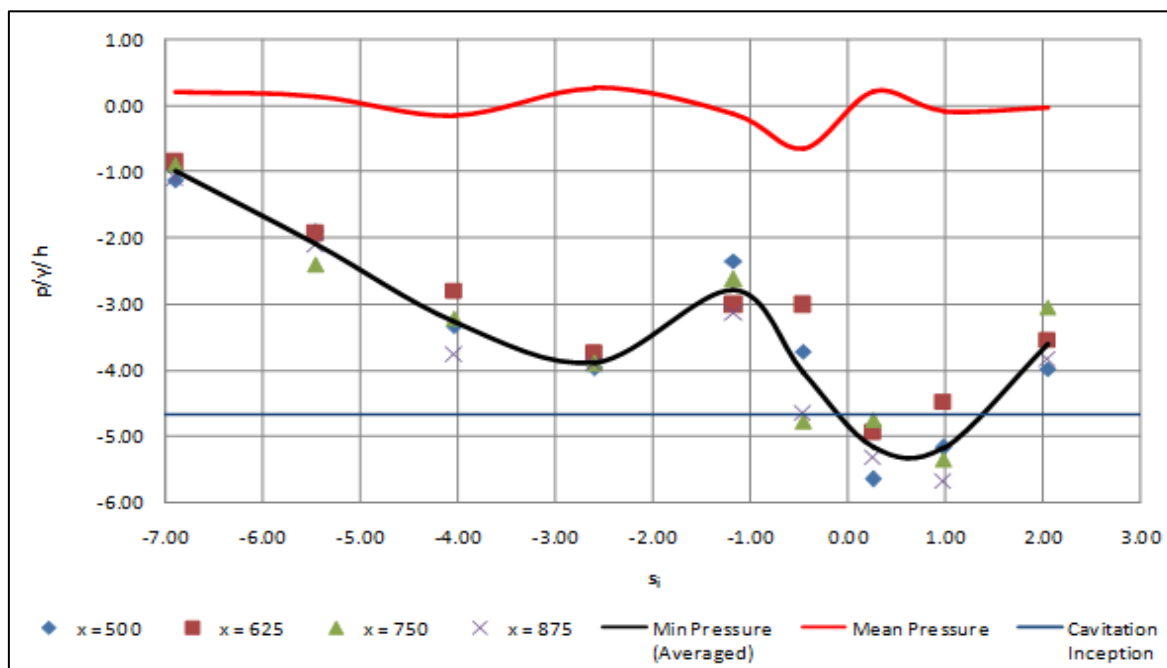


Figure 2.23: Minimum pressure development for a prototype unit discharge of 30 m²/s (Calitz, 2015).

2.5.2 Pressure Profiles on the Steps

In order to investigate the pressure distribution on the horizontal and vertical step faces, a general understanding of the flow behaviour is required. **Figure 2.24** indicates the pressure and streamline results which were obtained from a Computational Fluid Dynamic (CFD) simulation for a single step. It is important to note the area of impact on the horizontal step (Step 2) and the vortex located at the inner region of the step.

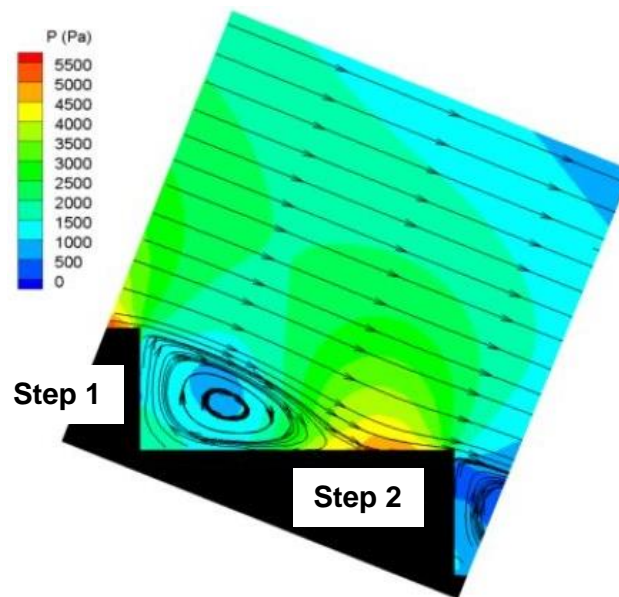


Figure 2.24: CFD simulation indicating the streamline and pressure data (Frizell and Renna, 2009).

2.5.2.1 Pressure Profile on the Horizontal Face of the Step

Sánchez-Juny *et al.* (2000) and Amador *et al.* (2005) emphasised several points regarding the horizontal face pressure profiles (See **Figure 2.25**):

- The flow impacts on the downstream half of the horizontal face. Above the impact zone the pressure increases until a maximum pressure is reached at the outer edges.
- The upstream section of the horizontal face is characterised by a boundary separation due to the vortex as illustrated in **Figure 2.24**. An increase in discharge results in a decrease in pressure and even negative pressures can be measured as illustrated in **Figure 2.25 (iii)**.
- The lowest minimum pressures, in **Figure 2.25 (iii)**, occur in the area $0.6 \leq \frac{y}{L} \leq 0.7$. As the discharge increases, the occurrence area moves slightly downstream.

Chapter 2

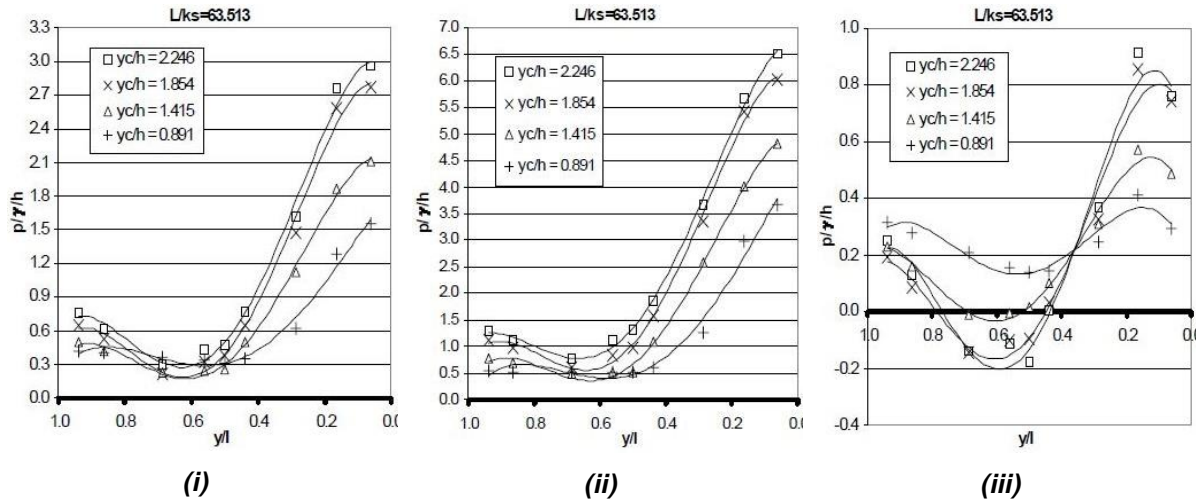


Figure 2.25: Pressure profiles on the horizontal face indicating (i) Mean pressure, (ii) Maximum pressure and (iii) Minimum pressure (Sánchez-Juny, et al., 2000).

2.5.2.2 Pressure Profile on the Vertical Face of the Step

Similar to the horizontal pressure profiles, certain aspects of the vertical profile were pointed out by Sánchez-Juny *et al.* (2000) and Amador *et al.* (2005) as illustrated in **Figure 2.26**:

- The region near the outer edge of the step is characterised by a boundary separation layer which is caused by the step vortex (**Figure 2.24**). Minimum pressures (**Figure 2.26 (iii)**) proved negative in this region and the possibility of cavitation damage exists. Mean pressures (**Figure 2.26 (i)**) indicate that negative pressures are experienced for $\frac{z}{h} \leq 0.6$, reaching a minimum value at the outer step edge.
- The area near the horizontal face of the adjacent step receives the impact of the vortex system. Thus, the impact the pressures exert will be positive (**Figure 2.26 (i) & (ii)**), but still lower relative to those on the horizontal face.
- By referring to the maximum and minimum pressures (**Figure 2.26 (ii) & (iii)**) a great variability was revealed in the zone close to the outer edge.

Chapter 2

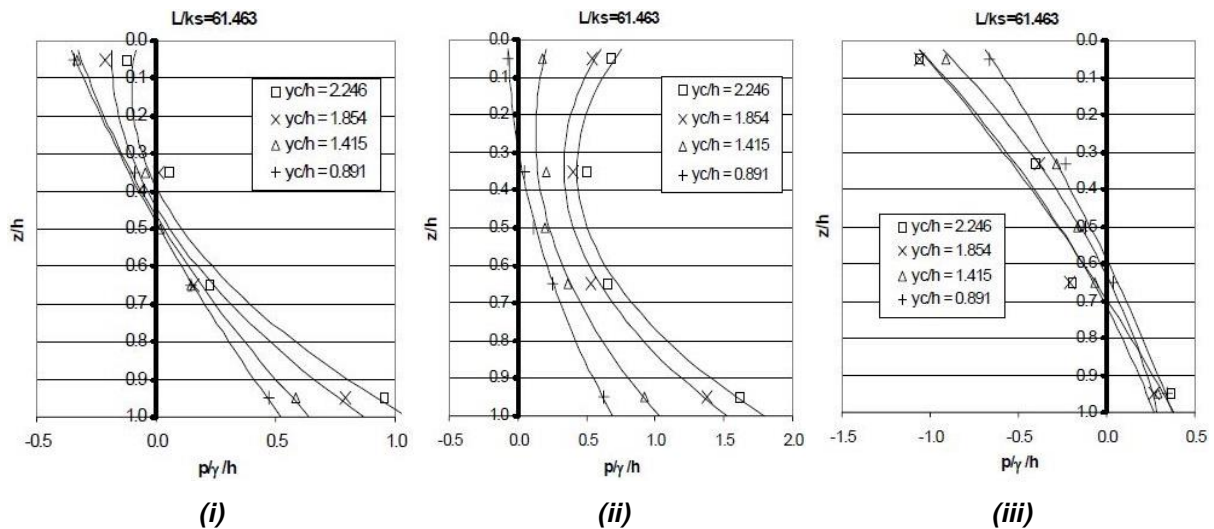


Figure 2.26: Pressure profiles on the vertical face indicating (i) Mean pressure, (ii) Maximum pressure and (iii) Minimum pressure (Sánchez-Juny, et al., 2000).

2.5.3 Summary

Since the possibility of cavitation damage is affected by both minimum pressures and the lack of aeration, measurements of both pressure and air concentration are crucial to the investigation when assessing the risk of cavitation damage. Since minimum pressure on the spillway leads to cavitation, the study focused on measuring pressure within the minimum pressure zones:

- As discussed in **Section 2.5.1**, the most severe negative pressures occur in the vicinity of the inception point, as was indicated by Sánchez-Juny *et al.* (2000) and Calitz (2015).
- Although the worst case regarding minimum pressures occur near the inception point, the possibility of cavitation still exists up to the critical point due to the lack of sufficient aeration.
- The experimental area in this study was thus from the critical point, moving upstream to the crest, where the pressure sensors were installed on the upper edge of the vertical step. This is where the most severe minimum pressures occur, as was discussed in **Subsection 2.5.2.2**.

2.6 Cavitation

Cavitation is the process of forming vapour cavities in a liquid when it is subjected to a reduced pressure, below that of the saturated water pressure, at a constant temperature. When these vapour voids are transported to regions of higher pressure, the vapour quickly condenses, the cavities implode and fill with the surrounding water. The process is noisy, disrupts the flow pattern and, most importantly, cause substantial damage if the implosion is in the vicinity of the spillway surface (Novak, *et al.*, 2007).

As identified in **Section 2.5**, low pressure regions occur at separation points where water flows alongside fixed boundaries at a particularly high flow velocity. The onset of cavitation is affected by the velocity, pressure, and duration of the flow, and the roughness and alignment of the boundary, the strength of materials and the amount of dissolved air (Kermani, *et al.*, 2013).

Chanson (1994a) identified pre-emptive measures to reduce or halt the damaging effects of cavitation by:

1. decreasing the critical cavitation number by removing surface irregularities;
2. increasing the resistance of the spillway surface to cavitation by using steel fibre concrete;
3. using a combination of the first two methods;
4. directing the cavitation bubbles away from the surface boundary;
5. introducing flow aeration.

With flow velocities of 20 to 30 m/s, the tolerances of surface finish required in order to avoid cavitation are too severe and the cost of cavitation resistant materials are prohibitive. The aeration of flow poses difficulties in terms of design, but proved to be effective by introducing air at the pseudo-bottom.

Experiments performed by Peterka (1953) and Russel and Sheehan (1974) indicated that an air concentration of 5-8% was required to protect a concrete specimen of 10-20 MPa compressive strength. Field experiments performed on prototype spillways by Deng (1988), Zhou and Wang (1988) and Zhang (1991) indicated that an air concentration of 4-8% at the spillway surface was sufficient to prevent cavitation damage for velocities up to 44 m/s.

2.6.1 Cavitation Damage

As previously mentioned, once cavitation bubbles have formed, they travel with the flow to areas of higher local pressure. There they can no longer be sustained and implode. When the cavitation bubble implodes close to or against the spillway surface an extremely high pressure is generated, which acts on an infinitesimal area for a short time period (Khatsuria, 2004). The mechanism of an individual bubble collapse was described by Falvey (1990) as consisting of different phases as the bubble diameter decreases, reaches a minimum and then grows and rebounds, as illustrated in **Figure 2.27**. The process is repeated several times until the bubble becomes microscopic in size. During the rebound phase, a shock wave forms, with a velocity equal to that of the speed of sound in water. The pressure intensity generated by the shockwave is estimated to be 200 times the ambient pressure at the collapse site. Countless such impacts erode the concrete and this is known as cavitation pitting.

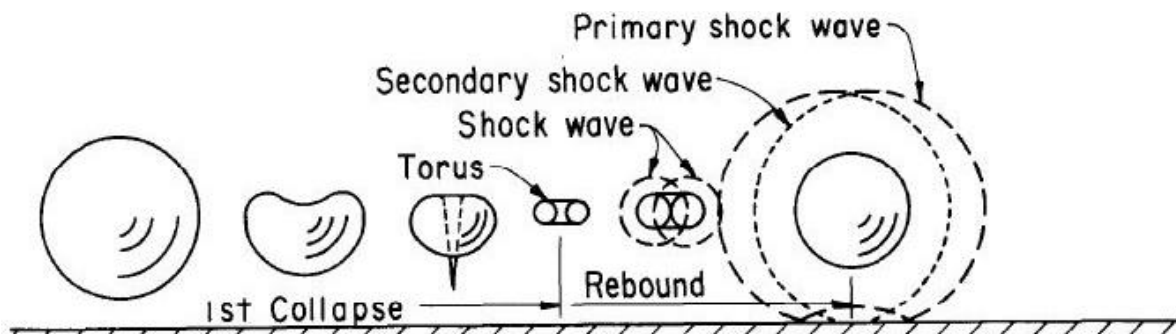


Figure 2.27: Collapse of an individual bubble near a surface boundary (Falvey, 1990).

The damaging mechanism in concrete is complicated by the presence of micro fissures among the mortar and aggregates. These fissures are filled by the compression waves in the water, which produces tensile stresses that loosen fragments of the material. As soon as cavitation damage has altered the flow regime, other mechanisms begin to act on the surface. These mechanisms consist of high velocities impacting on the irregular surface and mechanical failure, caused by the vibration of the reinforced steel (Khatsuria, 2004).

2.6.2 Cavitation Limitation Predictions

Stepped spillways were traditionally thought to be less prone to cavitation than smooth spillways; however, uncertainty in this respect has led to a conservative design approach (Frizell, *et al.*, 2012). The development of RCC has increased the popularity of stepped spillways and directed research to investigate the maximum design discharge that could safely be achieved by means of limiting the risk of cavitation. The relevant research findings are presented in the subsections that follow.

2.6.2.1 Boes and Minor (2000)

Boes and Minor (2000) examined the air concentration at the step corners for two different inclination angles according to the fundamental work of Peterka (1953), which stated that a local air concentration of 5-8% is sufficient to avoid cavitation damage. The authors considered a minimum value of 5% sufficient to avoid cavitation damage, which resulted in a maximum roughness Froude number of 38.3 for an inclination angle of 50°. From the definition of the roughness Froude number it can be concluded that the maximum unit discharge increases with an increasing step height. A maximum unit discharge of 17.3 m²/s and 138.0 m²/s was estimated for step heights of 0.3 m and 1.2 m respectively, on a stepped spillway with an inclination angle of 50°.

2.6.2.2 Boes and Hager (2003a)

The authors conducted an experimental investigation to measure the air concentration at the pseudo-bottom inception point by using a fibre-optical probe. The experimental setup was configured for different inclination angles of 30°, 40° and 50°. The authors developed a mathematical relationship between the pseudo-bottom air concentration and the non-dimensional distance from the inception point. By using this relationship, together with the fundamental findings of Peterka (1953), **Equations 2-17** and **2-18** were developed to determine the critical distance from the inception point that is essential to reach the required minimum air concentration values. The distance to the inception point was based on **Equation 2-13**, which was also developed by the authors.

$$\underline{C_b = 5\%} \quad X_{i,crit} = 5.0 \cdot (\sin \theta)^{-2.3} \quad \mathbf{2-17}$$

$$\underline{C_b = 8\%} \quad X_{i,crit} = 10 \cdot (\sin \theta)^{-3} \quad \mathbf{2-18}$$

where:

$X_{i,crit}$ = Dimensionless critical distance downstream of the inception point

$$\left(X_{i,crit} = \frac{x - L_i}{y_i} \right).$$

y_i = Inception flow depth of the mixture including air and water ($0.4 \cdot hF_b^{0.6}$)

L_{cr} = Critical distance downstream of inception point ($x - L_i$)

The authors suggest that **Equation 2-17** should be used as a design guideline based on the fact that aeration tends to be more noticeable in the prototype than in spillway models. Similar to the unaerated region upstream of the inception point, this downstream region down to the critical distance is vulnerable to cavitation damage for velocities greater than 20 m/s.

2.6.2.3 Khatsuria (2004)

Khatsuria derived an equation to estimate the incipient cavitation index considering the pressure difference of a fluid particle in close vicinity to that of a vapour bubble. **Equation 2-19** was derived by assuming that stepped spillways experience cavitation problems at high velocities.

$$\sigma_c = \frac{h_{atm} - h_v}{\frac{V^2}{2g}} \quad \mathbf{2-19}$$

where:

σ_c	=	Critical cavitation index
h_{atm}	=	Atmospheric pressure head (m)
h_v	=	Vapour pressure head (m)

2.6.2.4 Pfister, Hager and Minor (2005)

These authors developed a formula to determine the bottom cavitation index and recommended that each step edge represents a single bottom irregularity with a risk of cavitation. The principle of this approach is that downstream of the pseudo-bottom inception point, sufficient aeration is present and no cavitation damage would occur. The pseudo-bottom inception cavitation index is calculated as follows:

$$\sigma_{bi} = \frac{h_g + h_{atm} - h_v}{\frac{V_{bi}^2}{2g}} \quad \mathbf{2-20}$$

where:

σ_{bi}	=	Pseudo-bottom cavitation index
h_g	=	Gauge pressure head (m)
V_{bi}	=	Velocity at pseudo-bottom inception point (m/s)

2.6.2.5 Amador, Sánchez-Juny and Dolz (2009)

An experimental investigation consisting of pressure measurements was performed on a stepped spillway with an inclination angle of 51.3°. The authors, like many others, identified the location of minimum pressures at the upper half of the vertical step riser. By using a 0.1% probability of extreme minimum pressures, a critical mean velocity of 15 m/s was recommended at the inception point.

2.6.2.6 Frizell, Renna and Matos (2012)

The authors conducted specialised low ambient pressure experiments in a low ambient pressure chamber to investigate the potential of cavitation damage. The technical detail of this special low ambient pressure facility is described in Frizell (2016). The experimental results were captured by using high-speed videography and this revealed the flow features that drive the formation of cavitation. As previously indicated by Amador, *et al.* (2009), the high intensity shear force present just above the step edges is likely to be the location for cavitation to form; however, it is argued that cavitation inception will first appear on the vertical riser where the minimum pressures occur. From the authors' results it was found that, although the minimum pressures occurred on the step riser, the minimum peak pressure occurred within the vortical structures, above the pseudo-bottom. This was the most likely location for cavitation inception, as indicated in **Figure 2.28**. At a constant inclination angle, the authors found that the larger step heights are slightly more prone to cavitation than smaller step heights.

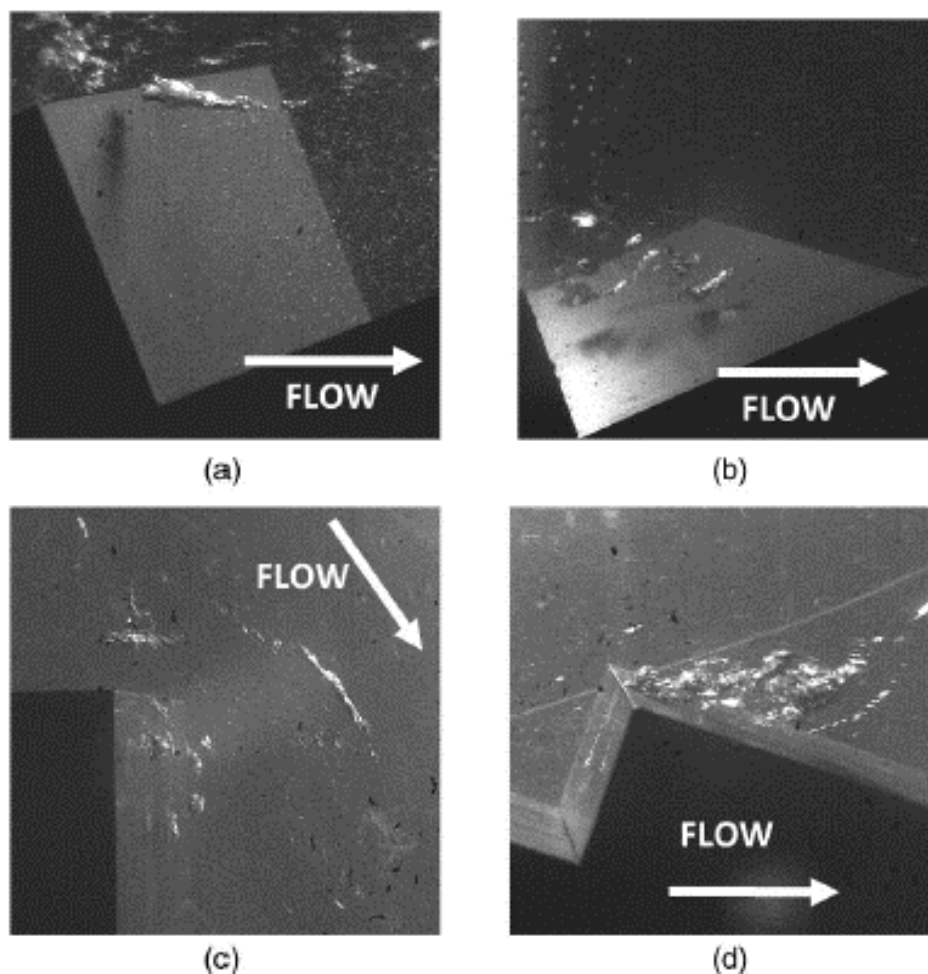


Figure 2.28: High speed video frames taken at critical cavitation indices showing the formation of cavitation voids (Frizell, *et al.*, 2012).

The study concluded with a design guideline to estimate cavitation inception. The designer specifies basic spillway characteristics, such as the spillway slope and step height from which a spillway friction factor can be calculated. By using this friction factor, the authors provided a relationship from which to estimate the critical cavitation index as follows:

$$\sigma_c = 4 \cdot f \quad \text{2-21}$$

where:

$$f = \text{Darcy-Weisbach friction factor}$$

2.6.2.7 Kermani, Barani and Ghaeini-Hessaroeeyeh (2013)

The authors developed an equation to predict the occurrence of cavitation damage on a stepped spillway by using the cavitation index. The cavitation index is a dimensionless number, used to characterise the susceptibility of a spillway to cavitate. To prevent the cavitation damage on the stepped spillway, the spillway cavitation index (σ) should always be greater than the critical cavitation index (σ_{cr}) throughout the structure.

$$\sigma = \frac{h_{atm} - h_v + h \cdot \cos \theta}{\frac{V^2}{2g}} \quad \text{2-22}$$

where:

$$\sigma = \text{Cavitation index}$$

Together with this, the authors established that the flow velocity has a remarkable effect on the cavitation damage and they broke it down into four regions as indicated in **Table 2.1**.

Table 2.1: Prediction of cavitation damage with respect to spillway velocities.

Flow Velocity	Cavitation Description
$v < 5 \text{ m/s}$	No cavitation damage
$5 \text{ m/s} < v < 16 \text{ m/s}$	Cavitation damage might or might not occur
$16 \text{ m/s} < v < 18 \text{ m/s}$	Cavitation damage occurs
$v > 40 - 45 \text{ m/s}$	Major cavitation damage occurs

2.6.2.8 Summary

Khatsuria (2004) and Frizell *et al.* (2012) developed prediction equations to estimate the incipient cavitation number, also known as the critical cavitation index, as indicated in **Equations 2-19** and **2-21**, respectively. Frizell *et al.* stated that any relevant stepped spillway friction formula may be used to determine the critical cavitation index. The following relevant frictional formulas were used and evaluated as indicated in **Figure 2.29**:

- The bottom friction factor (f_{bi}) at the inception point according to the method defined by Boes and Hager (2003b);
- The mean bottom friction factor (f_i) as defined by Tozzi (1994, cited in Khatsuria, 2004).

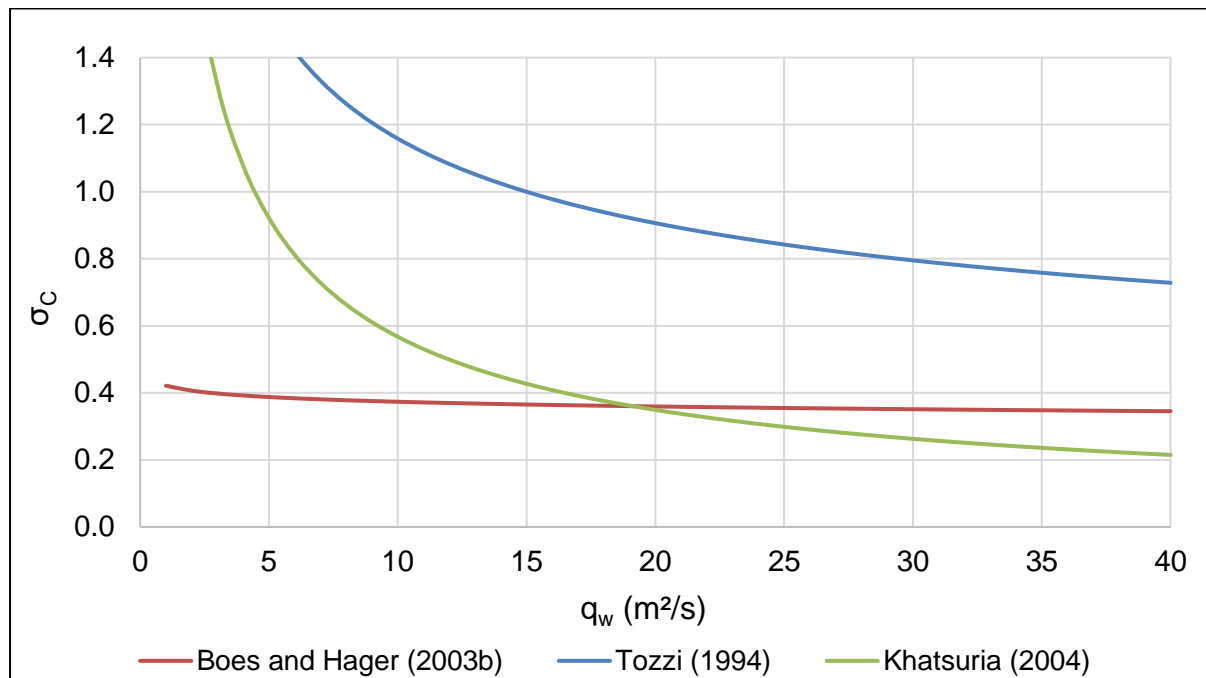


Figure 2.29: Incipient cavitation number for various unit discharges corresponding to a stepped spillway with inclination angle of 51.3° and a step height of 1.5 m.

Cavitation will commence if a stepped spillway is operated at a cavitation index below that of the incipient cavitation number. **Figure 2.29** indicates that the predictions of both Boes and Hager (2003b) and Khatsuria (2004) closely resemble each other for a unit discharge greater than $15 m^2/s$. Tozzi (1994, cited in Khatsuria, 2004), appears to predict the onset of cavitation more conservatively. The method prescribed by Frizell, *et al.* (2012) in conjunction with the friction factor determined by Boes and Hager (2003b), is the recommended approach. Frizell's method was applied in the evaluation of cavitation damage since it was based on real, observed cavitation in a custom low ambient pressure chamber.

2.7 Spillway Crest Pier

Colgate and Elder (1961) provided the concept of the prevention of cavitation damage by artificially introducing air into the flow by means of aerators. The first installation of aerators was at the Yellowtail dam (USA) in 1967. Although piers located on a spillway crest primarily add structural stability to support spillway gates or bridges, Calitz (2015) demonstrated that these piers also acted as aerators. With the addition of crest piers, the effective width of the spillway is decreased, which would inevitably increase the design head. The damming effect of the pier is minimised by placing the pier downstream of the supercritical depth on the spillway crest.

2.7.1 Flow Characteristics

Once the flow reaches the upstream surface of the crest pier the velocity abruptly decreases and the flow is deflected outwards as indicated in **Figure 2.30**. As the streamlines converge, the flow accelerates and a boundary layer grows gradually. When the fluid passes the Y-Y axis, it starts to decelerate within the boundary layer. Due to this deceleration, the fluid within the boundary layer is traveling at a lower speed than that of the fluid in the free stream. A point is reached where negative velocities arise at the inner part of the boundary layer. The dashed line in **Figure 2.30** indicates the separation layer that divides the positive and negative velocities. The negative velocity, together with the adverse pressure gradient, reduces the energy and forward momentum of the fluid by ultimately increasing the boundary layer width. Fluid from outside the boundary layer is drawn into the low-pressure zone, with the effect of generating powerful eddies. These eddies are drawn downstream and form the wake zone (Chadwick, *et al.*, 2013).

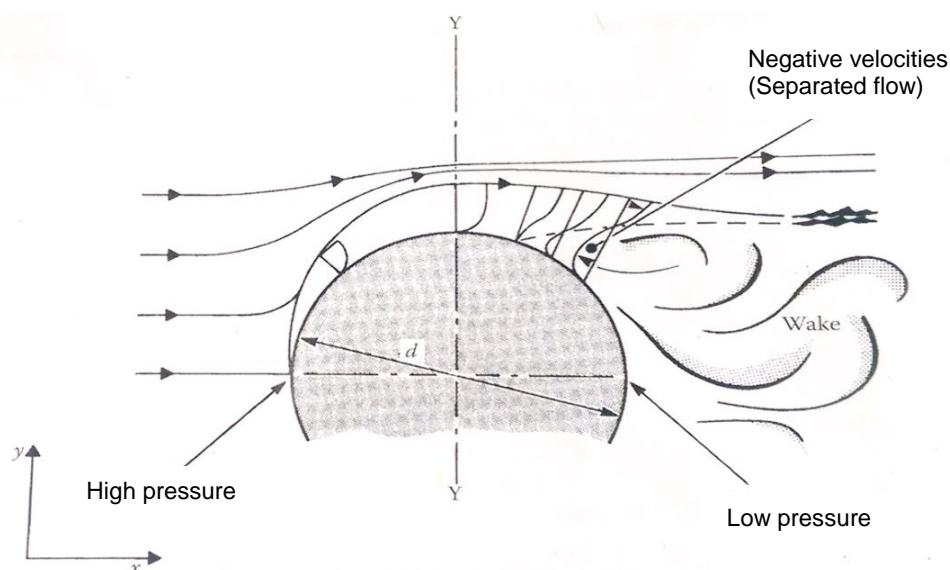


Figure 2.30: Flow separation around a cylindrical pier (Chadwick *et al.*, 2013).

The vorticity in the lee-wake vortex system is generated by the rolling up of unstable shear layers generated at the pier surface. These layers are then detached from either side of the pier at the separation line indicated in **Figure 2.30**. At low Reynolds numbers (Re), in the range between 5 and 50, these vortices form a stable and standing system close to the pier. However, for Reynolds numbers of practical interest ($Re > 1000$), the system is unstable and vortices are shed from the pier, oscillating between the two pier sides, which are carried downstream by the flow, as indicated in **Figure 2.31** (Breusers, *et al.*, 1977).

The strength of the vortices in the lee-wake system is dependent on the pier geometry and fluid velocity. A streamlined pier (for example, a sharp-nosed pier) generates a relatively weak wake compared to a blunt nosed pier, which creates a very strong one.

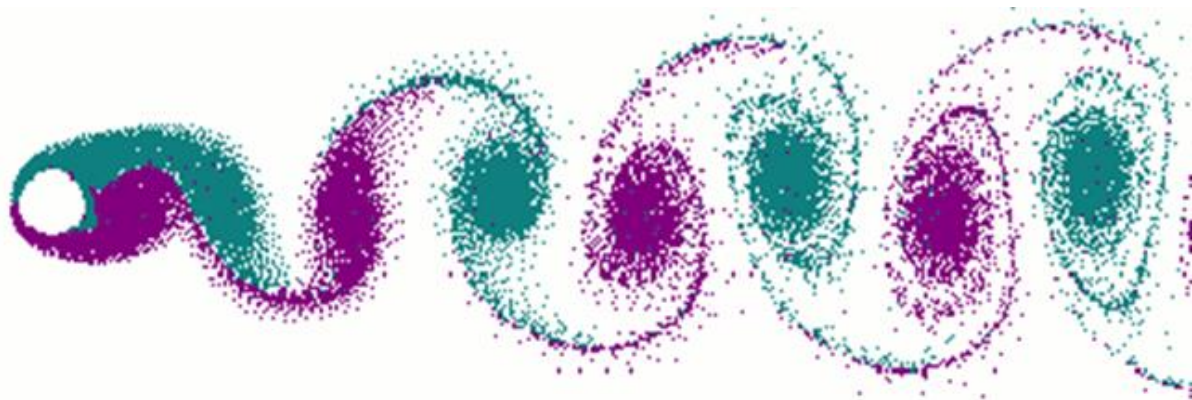


Figure 2.31: Vortex shedding from alternative sides (Siqueira, 2005).

2.7.2 Flaring Gate Pier (FGP)

The pioneering design of flaring gate piers (FGP) was first introduced by Zhenying Gong in 1974, China. This innovation arose from simply reversing the conventional trend of gate pier design. Instead of square butt ends or tapering of the pier tail, the ends were substantially flared (Lin, *et al.*, 1987). The design principle is to rapidly contract the flow and force it into a narrow, high velocity jet. There are various FGP designs, such as the X-shape, Y-shape, V-shape and T-shape.

2.7.2.1 Prototype Implementations of the Flaring Gate Pier

The prototype implementation of the FGP design has been used on high head/velocity spillways in China. A few of these implementations were tabulated in **Table 2.2**. The implementation of the FGP design exponentially increases the unit discharge capacity of stepped spillways, when compared to a standard stepped spillway. Both the Dachaoshan Dam (**Figure 2.32**) and the Shuidong Dam have experienced large floods close to the design unit discharge. The Dachaoshan Dam experienced a 93 m²/s flood, whereas the Shuidong Dam experienced a 90 m²/s unit discharge. Both stepped spillways were inspected, which led to the conclusion that no significant damages had occurred. (Shen, 2003).

Table 2.2: Prototype implementations of the FGP design (Guo, 2012, Matos & Meireles, 2014).

Dam	Type	Dam height (m)	Chute slope (°)	Step height (m)	q_{design} (m ² /s)	q_{Check} (m ² /s)	Type of FGP
Ankang	Gravity dam	128	51.3			254	Y-Shape FGP
Dachaoshan	RCC	111	55	1	165	250	Y-Shape FGP with flip bucket
Shuidong	RCC	62	60	0.9	100.2	138.7	Y-Shape FGP
Suofengying	RCC	116	49.6	1.2	179	245	X-Shape FGP



Figure 2.32: Dachaoshan Dam, China (Hongta Group, 2017).

2.7.2.2 Y-Shape Flaring Gate Pier

The most widely used flare design on Chinese dam spillways is the Y-shape FGP, which is located approximately a third of the way downstream from the spillway crest. This specific flare design is suited for use on a spillway characterised by frequent low or medium discharge floods. Due to the relatively low flows with a small discharge head, corresponding low velocities exist over the spillway crest. The piers constrict the flows, which result in narrow, supercritical flows past the FGP. The Y-shape FGP is deemed ineffective when combined with a stepped spillway since the narrow flow uses only a small area of the spillway for energy dissipation, thus deeming it less effective in the use of the available stepped spillway surface area. For the Dachaoshan Dam, the unused stepped spillway surface amounts to about 70%. This is because water wings form behind the flare and impact on the steps and stilling basin downstream (Ting, *et al.*, 2011). **Figure 2.33** illustrates the schematic design and prototype of the conventional Y-shape FGP.

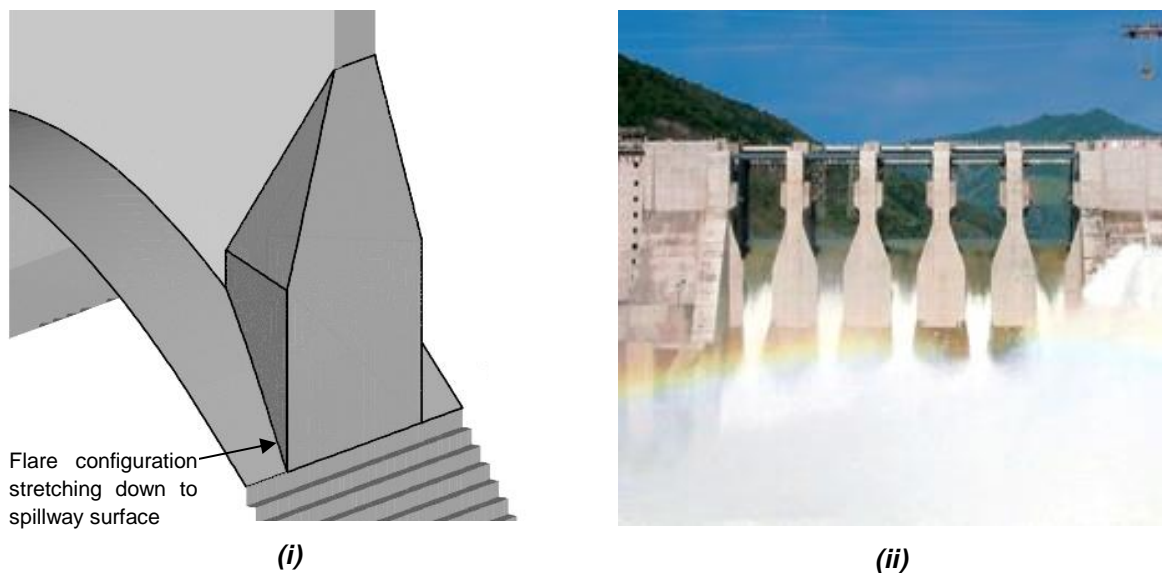


Figure 2.33: (i) Schematic illustration of the Y-Shape FGP (Ting, *et al.*, 2011). (ii) Y-Shape FGP at Dachaoshan Dam, China (Cheng, 2005).

2.7.2.3 X-Shape Flaring Gate Pier

The X-shaped FGP was designed to use more of the available stepped spillway surface area relative than the Y-shape FGP, and has the following characteristics (Bo, *et al.*, 2007):

- The bottom outlet width of the X-shape FGP is wider than that of the Y-shape FGP. In the case of a low discharge, the flow is not contracted and the utilisation of the available stepped spillway surface area for aeration and energy dissipation is possible.
- Since the flow passes mainly from the bottom outlet, at a low rate of discharge, a thin nappe develops.
- In the case of the first step being higher than others, an aerated cavity forms at the downstream face.
- A prototype observation of the Suofengying Dam, which implements an X-Shape FGP, reported an aerated flow with no cavitation.

The typical flow pattern of the X-shaped FGP was divided into two parts, the underflow and the ski-jump. The plunge pool, located downstream of the spillway, thus consisted of an underflow- and a ski-jump inflow. The underflow is defined as the flow along the spillway surface while the ski-jump is defined as the deflected flow which impacts in the plunge pool, after which it shears and rolls. This typical flow pattern is illustrated in **Figure 2.34 (ii)**.

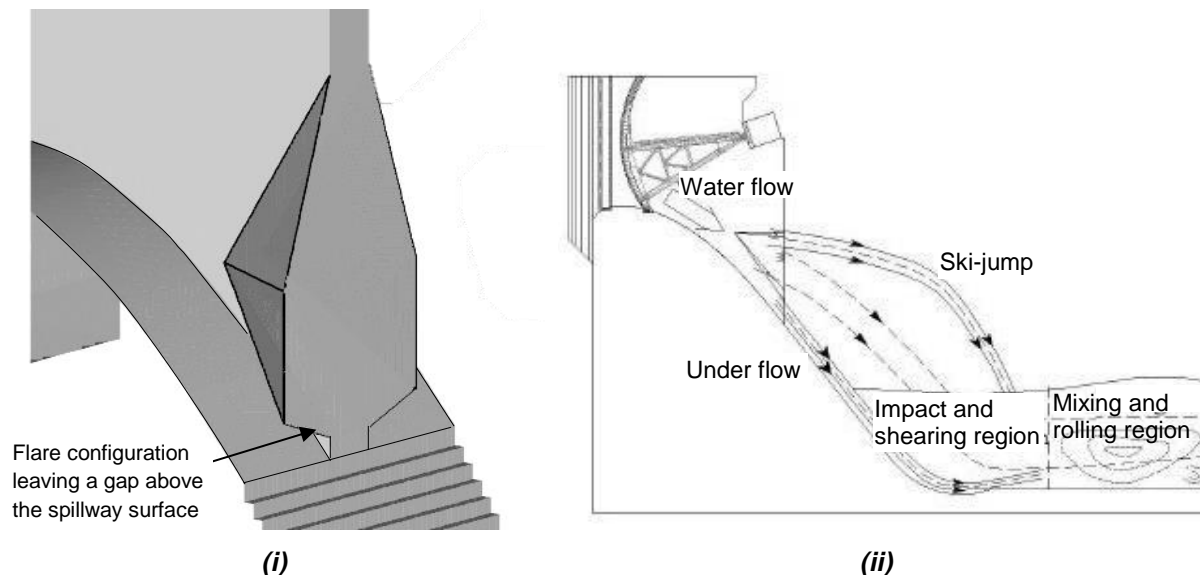


Figure 2.34: (i) Schematic illustration of an X-shape FGP (Ting, *et al.*, 2011) and (ii) the typical flow pattern of X-shaped FGP (Wei, 2013).

2.8 Scale Effects

Models form an important part of the hydraulic investigation, aiming to provide an accurate design solution. Due to the complexity of the fluid characteristics and boundary conditions, analytical and numerical methods are often defined as intractable. In these circumstances, a model investigation under controlled conditions in a laboratory would prove to be the most valuable. These models are generally constructed on a smaller scale than the corresponding prototype and typically identical in shape (Webber, 1965).

The laws of similarity govern the relationship between model and prototype performance. Realisation of the impossibility of compliance with all the scale laws, some discrepancy is usually present when extrapolating to prototype results. This is known as the scale effect.

2.8.1 Hydraulic Similarity

When conducting scale model experiments, it is required that the results be transferable to prototype. For this to be so, the flow systems require hydraulic similarity. This entails geometric, kinematic and dynamic similarity (Webber, 1965). These similarity criteria are discussed in the following subsections.

2.8.1.1 Geometric Similarity

Geometric similarity refers to the similarity of shape. The ratio of any two linear dimensions in the model corresponding to the same ratio in prototype, or expressed as:

$$\frac{(L_1)_m}{(L_2)_m} = \frac{(L_1)_p}{(L_2)_p} \quad \mathbf{2-23}$$

where:

L	=	Linear dimension (m)
m	=	Model
p	=	Prototype

The linear relationship between the model and prototype is known as the scale, presented as 1:x. The scalar relationship for the area and volume is presented as, 1:x² and 1:x³ respectively. To attain a high degree of geometric similarity, model boundary conditions should correspond to the prototype boundary conditions, according to the model scale. Due to the irregular nature of commercial finishes and materials, the exact reproduction of the prototype surface is not possible (Webber, 1965). Although the surface finish cannot be achieved on a stepped spillway model, a limited degree of conformity is present, since the scalar roughness is defined by the stepped profile.

2.8.1.2 Kinematic Similarity

Kinematic similarity is defined as the similarity of motion, introducing vector quantities and a time scale. This means that, at a homologous point and time, velocities and acceleration in the model and prototype have an identical ratio, with a corresponding direction of motion (Webber, 1965). This is expressed as:

$$\frac{(V_1)_m}{(V_2)_m} = \frac{(V_1)_p}{(V_2)_p} \quad \text{and} \quad \frac{(a_1)_m}{(a_2)_m} = \frac{(a_1)_p}{(a_2)_p} \quad \mathbf{2-24}$$

where:

$$\begin{aligned} V &= \text{Velocity (m/s)} \\ a &= \text{Acceleration (m/s}^2\text{)} \end{aligned}$$

A prerequisite for kinematic similarity is the conformity of geometric similarity, since the boundaries affect the flow pattern. This is due to the streamlines being distinctively determined by the boundary geometry.

2.8.1.3 Dynamic Similarity

Dynamic similarity is defined as the state where the forces at homologous points, in both the model and prototype, have the same ratio and act in an identical direction. This is presented in **Equation 2-25**. To achieve dynamic similarity, both geometric and kinematic similarity must be obtained, since the flow pattern is governed by the forces acting on it (Webber, 1965).

$$\frac{(F_1)_m}{(F_2)_m} = \frac{(F_1)_p}{(F_2)_p} \quad \mathbf{2-25}$$

where:

$$F = \text{Force (N)}$$

2.8.2 Similarity Laws

To achieve hydraulic similarity between the prototype and model, a number of similarity laws have to be satisfied. Due to the insignificant effect of fluid compressibility, this phenomenon was ignored in the discussion of the similarity laws in the following subsections.

2.8.2.1 Euler's Law

Leonard Euler, a Swiss mathematician and physicist, developed a basic relationship between pressure and velocity. This relationship is described by the dimensionless Euler number, as presented in **Equation 2-26**. For a model characterised by an enclosed fluid system, fully developed viscous forces, insignificant inertial forces and the absence of gravity- and surface tension forces, the Euler number is of particular interest. The pressure force is thus the independent variable. This contradicts most fluid phenomena, where the pressure force is a variable dependent of the fluid motion. To comply with the Euler's law, the model velocities are related to the equivalent prototype velocities by means of a scalar relationship, as given in Equation 3-27 (Webber, 1965).

$$E = \frac{V}{\sqrt{\frac{2\Delta p}{\rho}}} \quad \mathbf{2-26}$$

$$\frac{V_p}{V_m} = \frac{(\rho_p g(h_{pi})_p) \rho_m^{1/2}}{(\rho_m g(h_{pi})_m) \rho_p^{1/2}} = x^{1/2} \quad \mathbf{2-27}$$

where:

E	=	Euler number (dimensionless)
Δp	=	Change in pressure (kN/m ²)
h_{pi}	=	piezometric head (m)
x	=	scale factor

2.8.2.2 Froude's Law

Froude's law is applicable to models where the fluid motion is influenced predominantly by gravity and a free surface gradient is present. Froude's law is widely applied in the design of weirs, spillways, open channels, rivers and estuaries (Webber, 1965). The Froude law, together with the compliance of corresponding velocities, are indicated in **Equations 2-28** and **2-29** respectively.

$$F = \frac{V}{\sqrt{gL}} \quad \mathbf{2-28}$$

$$\frac{V_p}{V_m} = \frac{(gL_p)^{1/2}}{(gL_m)^{1/2}} = x^{1/2} \quad \mathbf{2-29}$$

2.8.2.3 Reynolds' Law

Water is a viscous fluid; thus, the possibility of viscous shear drag forces should be considered in the planning phase of the model investigation. An example of dominant viscous shear forces is found in a pipeline operating within the transition zone, where the energy grade line, rather than the slope, dictates the fluid motion. Due to the relatively low viscosity of water, the viscous forces are most often considered as a secondary effect. However, it has an important role in the development of boundary friction and fluid turbulence. Reynolds' law and compliance therewith in terms of velocities, is demonstrated in **Equations 2-30** and **2-31**, respectively (Webber, 1965).

$$Re = \frac{VL}{\nu} \quad 2-30$$

$$\frac{V_p}{V_m} = \frac{\nu_p L_m}{\nu_m L_p} = \frac{\nu_p}{\nu_m} \frac{1}{x} \quad 2-31$$

where:

$$\begin{aligned} Re &= \text{Reynolds number (dimensionless)} \\ \nu &= \text{Kinematic viscosity (m/s}^2\text{)} \end{aligned}$$

2.8.2.4 Weber's Law

Surface tension, together with an air-water interface and small linear dimensions, are significant characteristics of Weber's law. Model studies involving low weir heads, air entrainment and splash or spray should consider the influence of surface tension. Weber's law, together with the compliance with corresponding velocities, is demonstrated in **Equations 2-32** and **2-33** (Webber, 1965).

$$W = \frac{V}{\sqrt{\frac{\sigma_T}{L\rho}}} \quad 2-32$$

$$\frac{V_p}{V_m} = \frac{(\sigma_T)_p^{1/2} \rho_m^{1/2} L_m^{1/2}}{(\sigma_T)_m^{1/2} \rho_p^{1/2} L_p^{1/2}} = \frac{(\sigma_T)_p^{1/2} \rho_m^{1/2} 1}{(\sigma_T)_m^{1/2} \rho_p^{1/2} x^{1/2}} \quad 2-33$$

where:

$$\begin{aligned} W &= \text{Weber number (dimensionless)} \\ \sigma_T &= \text{Surface tension (N/m)} \end{aligned}$$

Equation 2-33 demonstrates that if the fluid in the model and prototype are identical, the model's velocities must be $x^{1/2}$ times those of the prototype (Webber, 1965).

2.8.3 Scale Model Criteria

A stepped spillway, unlike clear water open channel flow, is characterised by a highly turbulent two-phase flow which cannot be precisely modelled by Froude's similarity law. This is because of the viscosity and surface tension effects, which play a significant role in the flow development. True similarity of the aeration processes could be accomplished only by simultaneous fulfilment of the similarity laws of Froude, Reynolds and Weber, which is not achievable practically. Careful consideration is advised when scaling model results to prototype, due attention needs to be paid to scaling effects. These scale effects arise because of the inability of keeping each of the force ratios constant between model and prototype (Heller, 2011). Kobus (1984) demonstrated that, if only Froude scaling was applied, air bubbles in a scaled model would be proportionally too large, relative to those of the prototype, resulting in a higher detrainment rate and lower transport rate.

Various researchers conducted model experiments by constructing geometrically similar models on different scales (model families). These results are summarised in two subsections which follow.

2.8.3.1 Geometric Scale

- For the investigation of spillway aerators, Pinto (1984, cited in Boes, 2000) suggested a scale of 1:15.
- Vischer *et al.* (1982, cited in Boes, 2000) suggested a minimum scale of 1:15 for the accurate modelling of the aeration process.
- Speerli (1999, cited in Boes, 2000) suggested a limiting scale of 1:20 for two-phase flow models.
- Experimental investigations were conducted by Pegram *et al.* (1999, cited in Boes, 2000) for different scales and various step heights. From these experimental investigations, it was concluded that a scale model of 1:20 can faithfully represent the prototype behaviour of a stepped spillway, with the results converging more quickly for scales greater than 1:15.
- By conducting model family experiments, Boes (2000) identified minimum scales between 1:10 and 1:15 as suitable for negligible scale effects.
- Weber (1965) highlighted the important consideration that the high velocities of the prototype, which cause air entrainment and flow bulking, would not occur to the same extent on the model. By ignoring the similarity of surface roughness, Weber stated that full models of dam structures usually have scales between 1:20 and 1:100.

2.8.3.2 Reynolds and Weber Scale Criteria

- Kobus (1984, cited in Boes, 2000) proposed a minimum Reynolds number of 10^5 , with the flow depth as reference height to minimize viscous effects.
- Rutschmann (1988, cited in Boes, 2000) and Speerli (1999, cited in Boes, 2000) who both investigated spillway aerators and bottom outlets, concluded that a minimum Weber number of 110 is advised for a negligible influence of surface tension.
- Boes (2000) concluded that a minimum Reynolds number of 10^5 and Weber number of 100 is required for negligible scale effects. These conclusions were based on an experimental model family study.
- Recent studies involving two-phase flow on stepped spillways indicated that turbulence levels, entrained bubble sizes and interfacial areas are improperly scaled based on Froude similitude. Chanson (2009) indicated that a minimum Reynolds number, defined as $\frac{\rho_w q_w}{\mu_w}$, of 500×10^3 , is required.

2.8.4 Self-Similarity

Recent investigations by Chanson (2007, 2008), Felder (2017) and Heller (2017) observed self-similar relationships for two-phase flow conditions on stepped spillways. Heller defined the phenomenon of self-similarity as the spatial distribution of properties at various instances of time and spatial locations to be obtained from one another by a similarity transformation. In layman's terms, a self-similar object is exactly or approximately similar to a part of itself, irrespective of scale. Examples of self-similarity include a fern and river networks, where the smaller leaves and branches have the same form as the whole, as illustrated in **Figure 2.35**.



Figure 2.35: Examples of self-similarity include, (i) ferns (Smith, 2015) and (ii) river networks (Grambeau, 2017).

Carosi, Chanson and Felder (2007, 2017) conducted physical experiments to investigate scale effects in high-velocity free-surface flows, particularly stepped spillways. These experimental results indicated several self-similar relationships that remain invariant under scale changes. These relationships include void-fraction and interfacial velocity which are free of scale effects in the Froude similitude. **Figure 2.36** illustrates the similar void fraction distributions (C) for two different model scales, as indicated by the blue and green symbols.

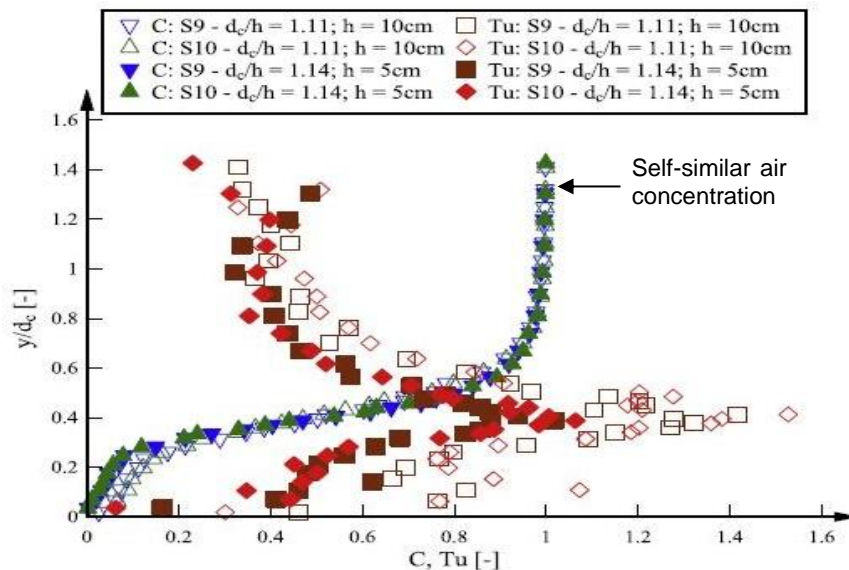


Figure 2.36: Void fractions and turbulence intensity (Felder and Chanson, 2017).

It should be noted that the process of self-similarity is based on void fractions and does not account for the significant scale effects in terms of the number of entrained bubbles and bubble sizes (Chanson, 2008). Thus, the air-water mass transfer rate cannot be accurately scaled according to the Froude similitude. Chanson and Felder (2017) stated that, despite the inaccuracies that occur when scaling the air-water mass transfer rate, void fractions can accurately be measured, without any scale limitations, for Reynolds numbers greater than 8×10^4 .

2.8.5 Avoidance of Scale Effects

2.8.5.1 Scale Model Criteria

Pinto (1984), Vischer *et al.* (1982) and Boes (2000) suggested a maximum scale of 1:15 for the accurate modelling of the aeration process. Although other studies by Pegram *et al.* (1999) suggested that a model scale of 1:20 could faithfully represent the prototype, the authors found that a scale model of 1:15 resulted in faster convergence and presented a sufficiently accurate representation of the air-water mass transfer rate. All of the listed references were cited in Boes (2000).

With the recent advances in knowledge regarding self-similarity on stepped spillways, it is possible to accurately measure air concentration on small experimental models. Despite the scale effects of increased air bubble sizes and decreased entrainment rates, experimental air concentration measurements can accurately be scaled to prototype without any scale effects for Reynolds numbers greater than 8×10^4 .

2.8.5.2 Minimum Weber and Reynolds Number Criteria

Recent studies involving two-phase flow on stepped spillways indicated that turbulence levels, entrained bubble sizes and interfacial areas are improperly scaled when based on Froude similitude (Chanson, 2009). Boes (2000) concluded that a minimum Reynolds number of 10^5 and Weber number of 100 are required for the attainment of negligible scale effects. These conditions were evaluated as indicated in **Figure 2.37** for a 1:15 scale stepped spillway model, which concluded that a minimum prototype unit discharge exceeding $5 \text{ m}^2/\text{s}$ is satisfactory.

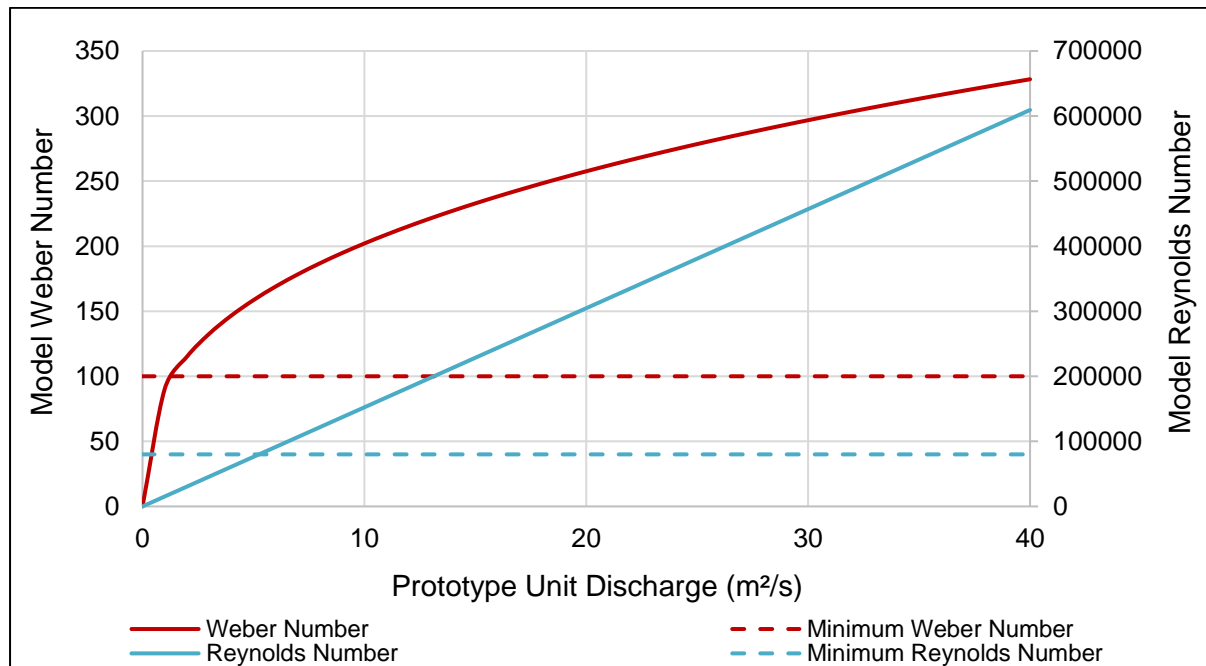


Figure 2.37: Evaluating a 1:15 model to eliminate scale effects based on minimum Weber- and Reynolds numbers.

3 Hydraulic Model Methodology

In order to achieve the objective of this study, experimental investigations were performed on two hydraulic models as mentioned in **Chapter 1**:

- The 1:15 scale Type A stepped spillway design was based on the mitigation of the hydraulic scale effects and the required spillway length to induce self-aeration for the maximum model discharge. The model scale of 1:15 was considered large enough to neglect the aeration scale effects as discussed in **Section 2.8.3**. Due to the large scale of the model and the laboratory flow limitations, a maximum unit discharge of 30 m²/s was attained.
- A 1:50 scale model Type B stepped spillway was thereafter designed to achieve high unit discharges of up to 200 m²/s, which was essential for the evaluation of the FGP design. Although the small scale of the model induced aeration scale effects, air concentration was accurately captured and scaled to prototype, with consideration that it should conform to the law of self-similarity, with the condition that the Reynolds number should be greater than 8×10^4 (**Section 2.8.4**).

The various crest pier designs, together with the X-Shape FGP were investigated on the 1:15 scale, Type A stepped spillway model for a maximum unit discharge of 30 m²/s. However, the FGPs had been designed for high head/velocity spillways and were therefore investigated on the 1:50 scale Type B stepped spillway model for unit discharges up to 200 m²/s. These hydraulic model experiments were performed at the Civil Engineering Hydraulic Laboratory at Stellenbosch University. **Table 3.1** illustrates a detailed test schedule which differentiates between the various crest pier designs and the two corresponding models on which the experiments were conducted.

A detailed description of the Type A and B stepped spillways, together with the various crest pier designs, and test results are presented in **Chapters 5** and **6** respectively.

Table 3.1: Test schedule.

Test schedule of artificial aeration methods on ogee spillway with step configurations A & B								
Configuration	Number	Model scale		1:15	1:50			
		Unit discharge		30 m ² /s	50 m ² /s	100 m ² /s	150 m ² /s	200 m ² /s
		Crest configuration						
USBR (1987) spillway with step configuration A	1	No pier <i>(Reference)</i>		Pier nose type Bullnose or Parabolic	Air & Pressure	Note: These unit discharges were not attainable on the 1:15 scale model due to laboratory restrictions.		
	2	Pier 1 (Short)			Air & Pressure			
	3				Air & Pressure			
	4	Pier 2 (Long)			Air & Pressure			
	5							Air & Pressure
	6	Pier 2 (Long) & X-Shape FGP			Air & Pressure			
	7							Air & Pressure
WES (1959) spillway with step configuration B	8	No Pier <i>(Reference)</i>			Air & Pressure	Air & Pressure	Air & Pressure	Air & Pressure
	9	Pier 3 & Y-Shape FGP			Air & Pressure	Air & Pressure	Air & Pressure	Air & Pressure
	10	Pier 3 & X-Shape FGP			Air & Pressure	Air & Pressure	Air & Pressure	Air & Pressure
	11	Pier 3, Y-Shape FGP & 43° flip bucket			Air & Pressure	Projection	Projection	Projection

4 General Laboratory Facilities and Instrumentation

This chapter provides a detailed description of the mutually applicable instruments and various analysis procedures for both the Type A and Type B stepped spillway investigations. The analysis procedure comprises a statistical and sensitivity analysis to determine the ideal sampling time and data interpretation. The chapter concludes with the transformation of the measured air concentration and pressure results which are presented as dimensionless quantities.

The instrumentation, analysis procedures and the presentation of the analysed data were implemented as described in this chapter and this description is applicable to both the Type A and Type B step configurations, unless otherwise stated.

4.1 Laboratory Flow System

The laboratory setup and flow system was on a closed cycle for both experimental investigations. Water was pumped via a 600 mm diameter pipe into a stilling basin where it was dispersed with a diffuser plate. When the water enters the basin through the inlet, the discharge momentum is absorbed by the diffuser plate before the water reaches the divider and 400 mm long flow straighteners. The purpose of the divider and flow straighteners was to create a uniform approach flow towards the spillway, with flowlines aligned normal to the axis of the spillway. Downstream of the spillway the water collected in a drainage canal, which fed the underground reservoir. The water was pumped from the reservoir, which completed the cycle as illustrated in **Figure 4.1**.

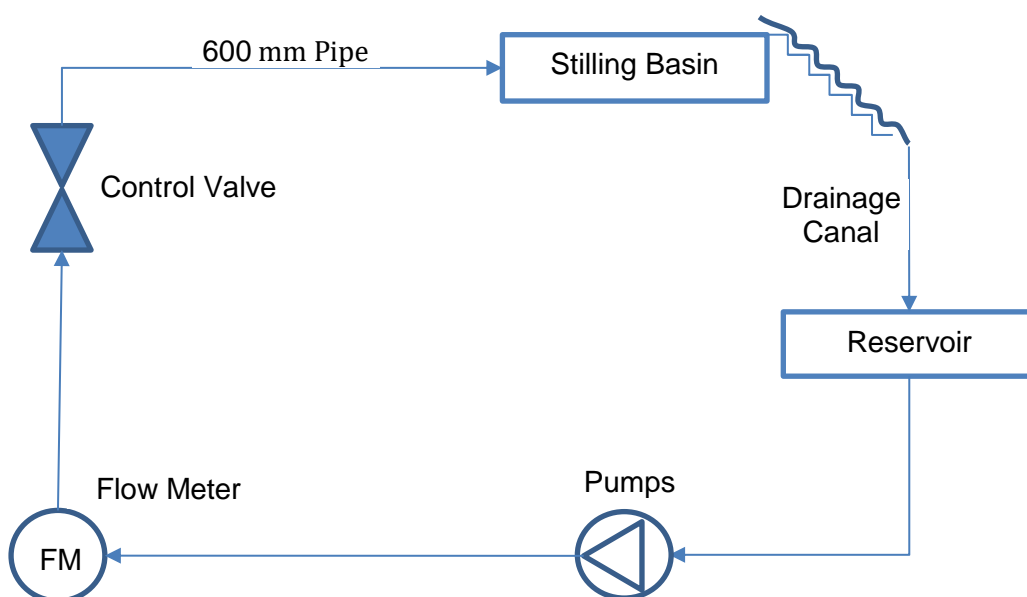


Figure 4.1: Laboratory flow cycle.

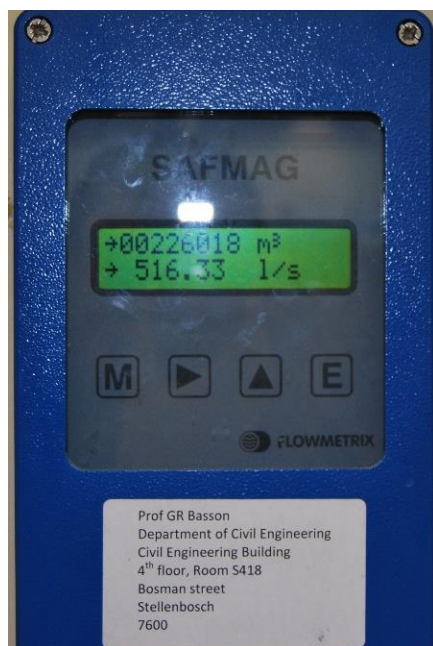
4.2 Instrumentation

The following instrumentation was essential to the accurate execution of the laboratory experiments:

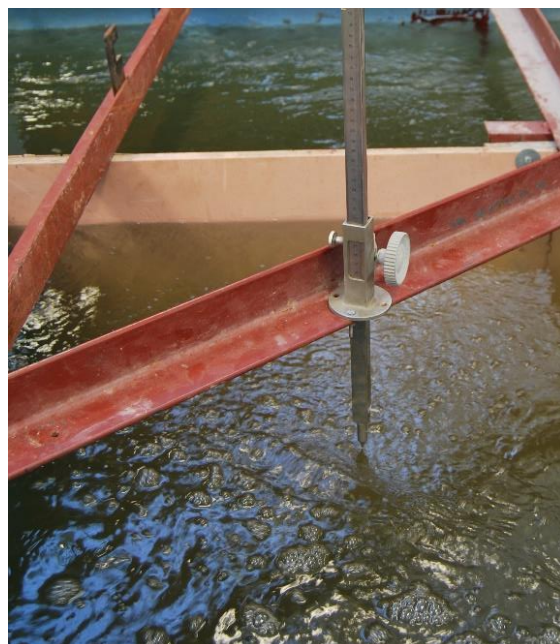
- An electromagnetic flowmeter was used to determine the spillway discharge. The discharge readings were manually documented.
- A needle gauge was installed upstream of the spillway in the stilling basin to determine the water level.
- Pressure transducers were installed in the step riser to measure the spillway pressure.
- A conductive needle probe was used to measure the spillway air concentration.

4.2.1 Discharge

The spillway discharge was measured and confirmed by using two different instrumentation devices. The first was a SAFMAG electromagnetic flowmeter, which was installed on the 600 mm inlet pipe. The flowmeter has an accuracy of $\pm 0.5\%$ with a repeatability of $\pm 0.1\%$, for velocities in the range of 0.5 m/s to 10 m/s. The electromagnetic flowmeter recorded an acceptable discharge fluctuation of $\pm 1\%$ on the displayed gauge value. The second device was a needle gauge installed upstream of the spillway in the stilling basin. The needle gauge measured the water levels with an accuracy of $\pm 5\%$. The ogee equation, together with the recorded water levels, was used to ensure the accuracy of the discharge. See **Figure 4.2** for illustrations of the SAFMAG electromagnetic flowmeter and needle gauge.



(i)



(ii)

Figure 4.2: (i) SAFMAG electromagnetic flow meter and (ii) Needle gauge.

4.2.2 Pressure

As indicated in the literature review, stepped spillways experience negative pressures that result in cavitation damage. These negative pressures were measured by using the WIKA S-10 pressure transducers. This specific type of pressure transducer has a working range of ± 1 m and an output range of 4 mA to 20 mA. The transducers were connected to pressure taps by means of 6 mm diameter tubes of approximately 100 mm in length. These taps were installed to be flush with the step riser, at a position which recorded the pressure fluctuations. Since the exact placement of the sensors differed in the two experimental models, it is specified in the descriptions of each in **Chapters 5** and **6**, respectively.

WIKA assured that the sensors provided an accuracy of $\pm 0.5\%$ and a repeatability error of $\pm 0.05\%$ of the span range. The pressure transducers were connected to a 16 channel data logger, Picolog, which recorded the output voltage at 100 Hz. The typical setup of the pressure sensors is as indicated in **Figure 4.3**.

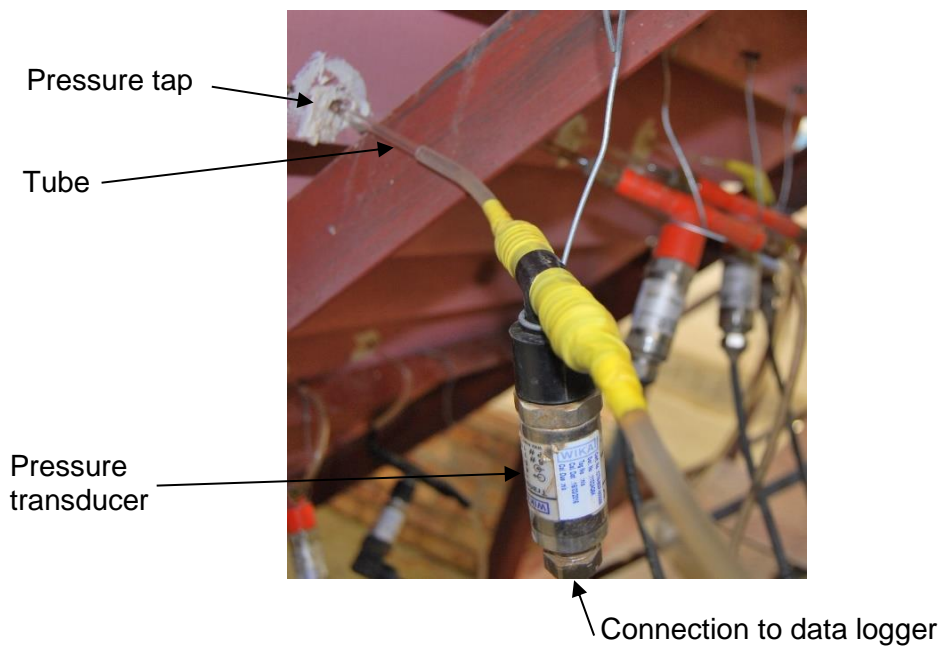


Figure 4.3: Typical setup for WIKA S-10 pressure transducers.

The pressure transducers record the pressure fluctuations in milliampere, which is converted to voltage by means of a 120 Ω resistor. The voltage is converted to hydraulic head by means of **Equation 4-1**.

$$H = \frac{(+1) - (-1)}{(20 - 4)} \times \left(\frac{1000(p)}{120} \right) - p_{cal} \quad 4-1$$

where:

H	=	Gauge pressure head (m)
p	=	Pressure reading (V)
p_{cal}	=	Calibration pressure corresponding to atmospheric pressure (V)

4.2.3 Air Concentration

The air concentration of the stepped spillway was captured with the aid of a Thermo Needle Probe system supplied by Teletronic, which was attached to a trolley moving perpendicular to the spillway. The measuring principle was based on amplitude and phase measurement of a sinusoidal stimulation fixed frequency of 10 kHz. This enables the recording of the local complex electrical impedance.

The probe tip assembly consists of a coaxial structure with three stainless steel electrodes. These electrodes are arranged in a step like order, which are isolated from each other by a non-conductive layer as illustrated in **Figure 4.4**. A bipolar voltage is applied at the central measuring electrode, which produces an electrical field in the medium. Based on the medium's conductivity, there is a current flow to the reference electrode, while the shield electrode eliminates interference from thin liquid films or a gas bubble at the probe tip. The reference electrode measures the current and sets it in proportion to the stimulation voltage. The complex impedance and relative permittivity of the medium is thus deduced and forms the raw data (Eckhard, 2016).

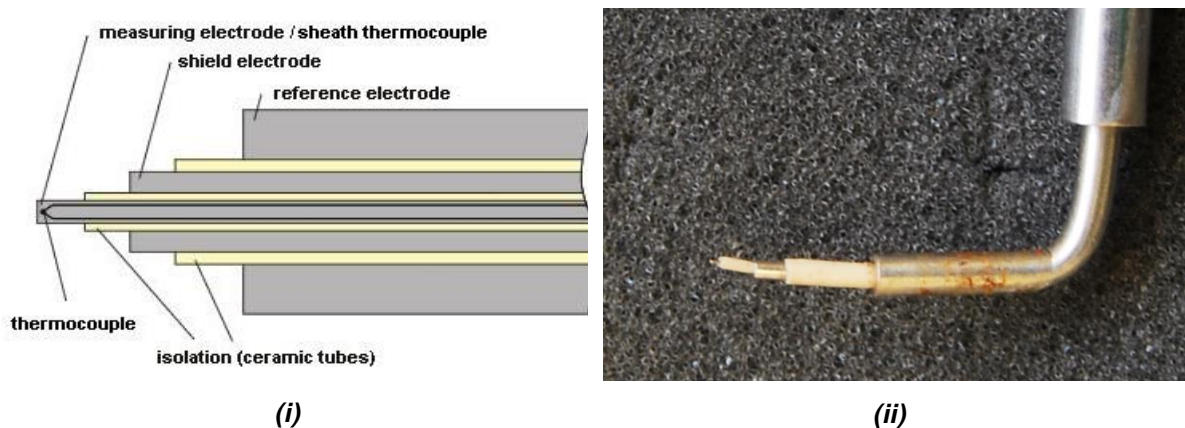


Figure 4.4: (i) Schematic illustration of the conductive probe tip (Eckhard, 2016) and (ii) laboratory conductive needle probe tip (0.1 mm).

The raw data was evaluated and visualised by using the VoidWizard software package, which was supplied by HZDR innovation. The processed data provided information such as the air concentration, the conductivity of the medium and the bubble count over a preselected time step. **Figure 4.5** illustrates the acquisition of the local conductivity in a bubble column. The probe measures a different conductivity if the medium changes between water and air, as illustrated. The upper conductivity threshold is characterised as the liquid phase, while the lower threshold is characterised as the gaseous phase. It should be noted that the probe tip measures the conductivity of only the medium with which it has contact. Also, at the sample frequency of 10 000 samples per second, the spacing of samples at, for example a 5 m/s water flow velocity, will be $5000/10000 = 0.5$ mm.

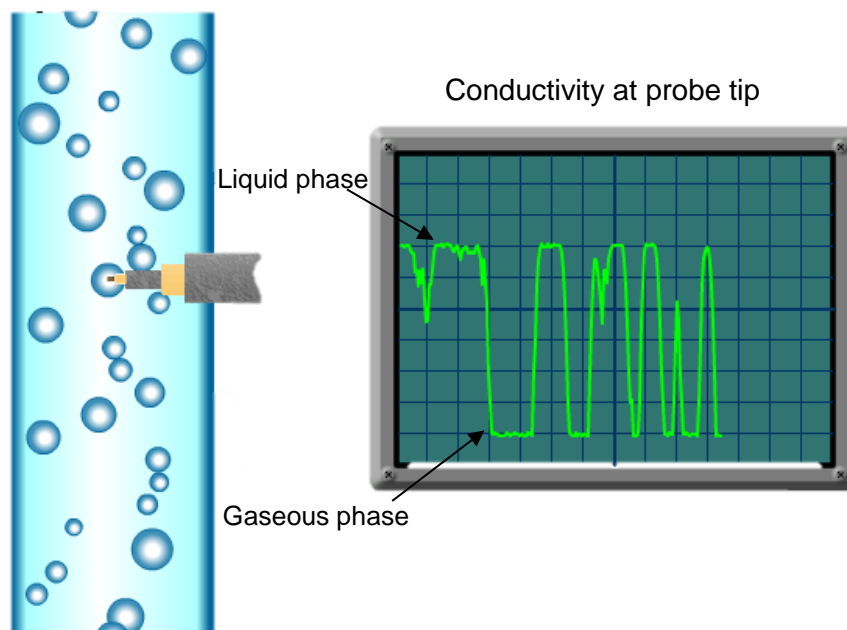


Figure 4.5: Schematic illustration of the conductivity acquisition in a bubble column (Eckhard, 2016).

4.3 Statistical Analysis

4.3.1 Air Concentration

The raw conductivity data acquired by the air probe was processed by VoidWizard software package. The processed data included the average air concentration and the number of air bubbles in contact with the probe tip. The statistical analysis was performed entirely by the software.

4.3.2 Pressure

4.3.2.1 Mean Pressure

The statistical average of the pressure data set was used to represent the mean pressure for a specific sensor and test.

4.3.2.2 Maximum and Minimum pressure

The minimum and maximum pressures were represented by a 0.15 percentile and 99.85 percentile, respectively. This was based on a normal distribution of the data set with the boundaries located three standard deviations from the mean. Fattor, *et al.* (2001) and Amador, *et al.* (2009) proposed a representative negative pressure probability of 0.1%. This is in close agreement with the probability of 0.15% which was chosen as the representative minimum pressure probability in this study. The appropriate interval was selected to accurately present the negative pressures and to eliminate outliers. The reliable representation of the negative pressures is important when assessing the possibility of cavitation damage. Other authors, such as Sánchez-Juny, *et al.* (2008), specified the 5th and the 95th percentile to represent the minimum and maximum pressures respectively. **Figure 4.6** indicates the normal distribution, with the specified confidence intervals between the standard deviations.

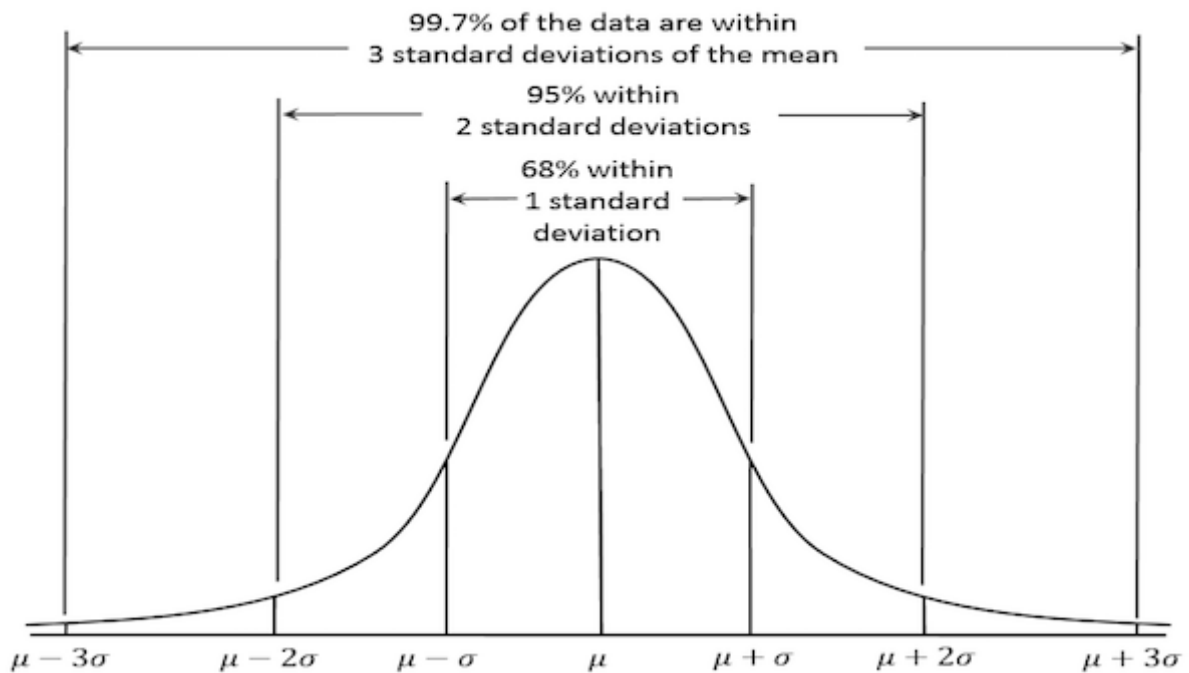


Figure 4.6: Normal distribution indicating the confidence intervals between the standard deviations (Perekupka, 2015).

Since the minimum and maximum pressures were analysed by using the central limit theorem, a prerequisite was for the data set to be normally distributed. The normality check was performed by visually comparing the data set to that of a normal distribution bell curve. The investigation was performed on two pressure sensors located in the centre of the spillway (Type A configuration) at steps 25 and 31, for a unit discharge of 30 m²/s. This specific test was conducted without a crest pier. The statistical analysis was performed on the raw voltage data, as the conversion to pressure head was not required. See **Table 4.1** for a statistical summary of the pressure data.

Table 4.1: Statistical summary of the pressure data (Type A configuration).

Sensor Location	Mean (V)	Standard Deviation (V)	Skewness	Minimum (V)	Maximum (V)	Data Samples
Step 25	1.594	0.188	0.037	0.914	2.369	60 000
Step 31	1.470	0.162	-0.034	0.766	2.121	60 000

Visual comparison to normal distribution bell curve

The graphical comparison between the normal distribution curve and the histogram, representing the pressure sensor data for step 25 and 31, are indicated in **Figure 4.7** and **Figure 4.8**, respectively.

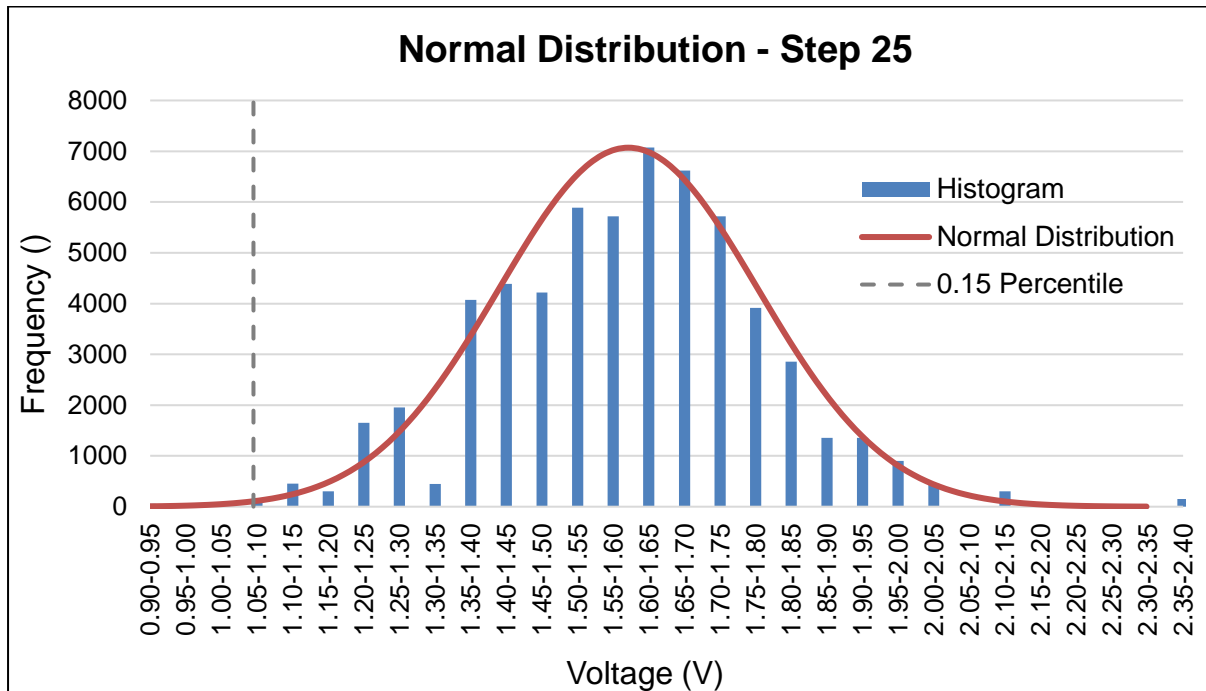


Figure 4.7: Histogram and normal distribution bell curve for step 25.

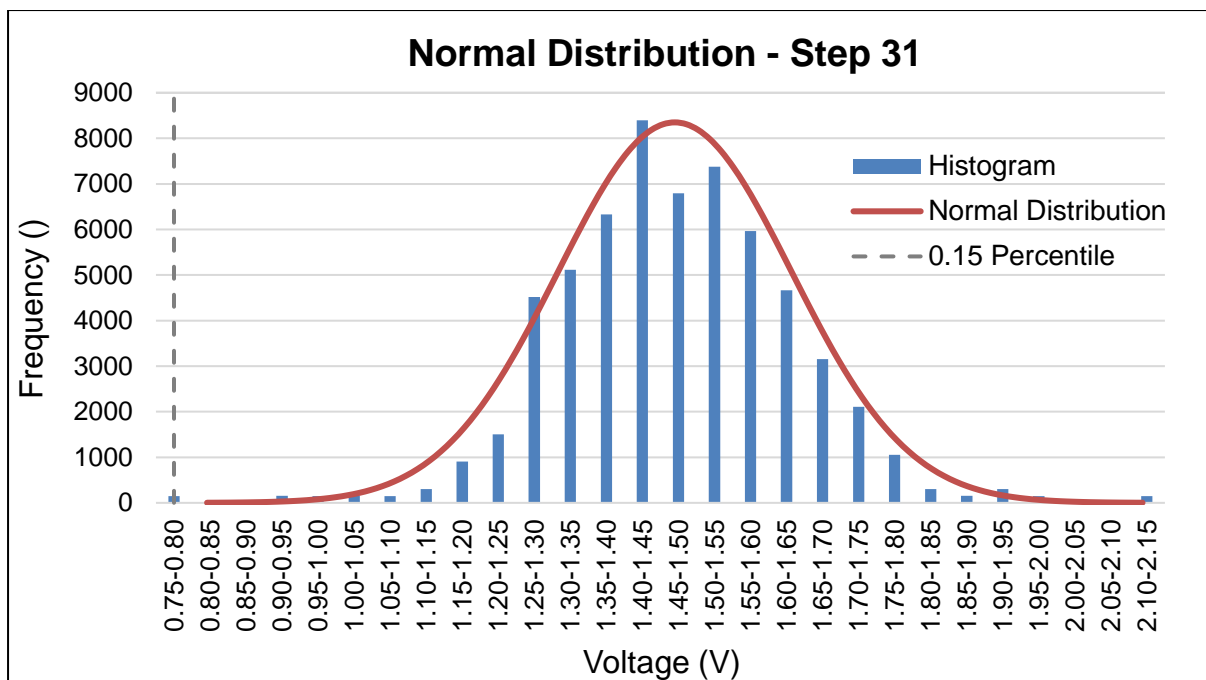


Figure 4.8: Histogram and normal distribution bell curve for step 31.

Figure 4.7 and **Figure 4.8** indicate a good relation of the histogram to the expected normal distribution curve, although slightly skewed. It can thus be concluded that the pressure sensor data follow a normal distribution, which verifies the approach taken to identify the minimum and maximum pressure values as the boundaries located three standard deviations above and below the mean.

4.4 Sensitivity Analysis of Recording Length

The aim of the sensitivity analyses was to determine the required acquisition period for the pressure and air concentration data. Experimental tests were conducted under similar conditions with varying acquisition periods to determine the ideal sampling time.

To establish the ideal acquisition period, the mean and standard deviation were calculated for each data set and compared to other sampling periods. The convergence of the results, particularly of the standard deviation, indicated the ideal acquisition period. The experimental results were independent of the acquisition period and longer periods would not have improved the accuracy.

The selected sampling periods for the pressure and air concentration differ because of the differences in the acquisition frequencies of the measuring instruments. **Table 4.2** indicates the various sampling periods for the pressure and air concentration tests, as indicated by a tick mark (✓).

Table 4.2: Various acquisition periods for the pressure and air concentration tests.

Description	Sampling Time (Minutes)							
	0.25	0.5	1	2	4	6	10	20
Pressure		✓	✓	✓	✓	✓	✓	✓
Air Concentration	✓	✓	✓	✓	✓	✓	✓	

4.4.1 Air Concentration

Experimental tests were conducted on the Type A stepped spillway to investigate the required acquisition period for independent air concentration results. The inception point was located at step 27, according to **Equation 2-13** (Boes and Hager, 2003a) and visual observation, for the tested discharge of 30 m²/s. The air concentration was measured downstream of the inception point, at step 34, to ensure that a constant number of void fractions were present. The conductivity needle probe was positioned in the centre of the 1 m wide model spillway, with the probe tip in line with the pseudo-bottom.

The average air concentration, standard deviation and bubble counts, for the various acquisition periods are shown in **Figure 4.9**. The results indicate a slight deviation for both the average air concentration and standard deviation for short acquisition periods, while the bubble count depicts a linear relationship.

It was therefore concluded that an acquisition period of 60 seconds (i.e. 6×10^5 samples) would be used for the experimental tests. This was deemed acceptable, since a 0.5% deviation in the average air concentration between the 30 and 60 second acquisition periods was negligible. Since most measurements were to be conducted within the non-aerated flow region, as indicated in **Figure 2.11**, the longer acquisition period would provide more accurate results.

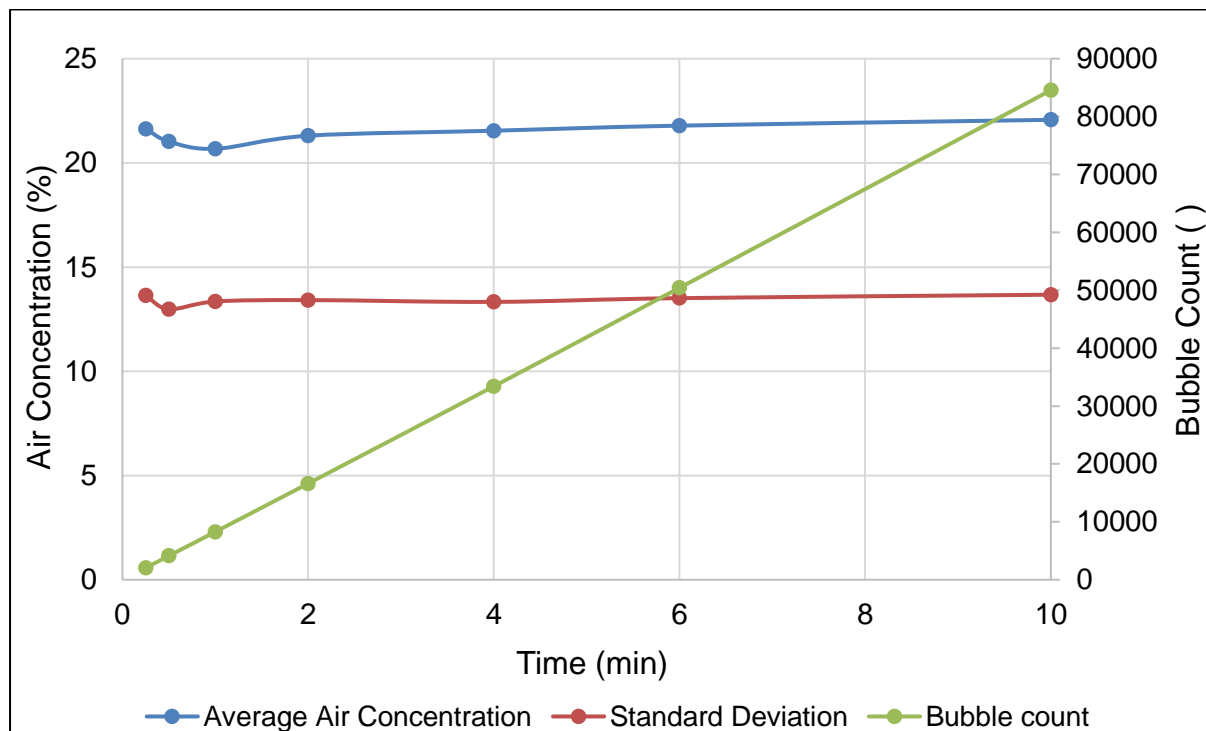


Figure 4.9: Average air concentration, standard deviation and bubble counts for various acquisition periods.

4.4.2 Pressure

Similar to the air concentration tests, experimental tests were conducted on the Type A stepped spillway to measure the chute pressures for various acquisition periods. The aim was to ensure that the results were independent of the sample period. Literature findings indicated that a negative pressure fluctuation zone occurs just upstream of the inception point. Pressure measurements were conducted within this zone to ensure that the variation of data was captured. For a discharge of $30 \text{ m}^2/\text{s}$ with no crest pier, the inception point was located at step 27. The pressure sensors were installed in the centre of the 1 m wide model spillway on the upper vertical portion of steps 21, 23, 25 and 27.

Figure 4.10 and **Figure 4.11** indicate the respective minimum pressures and standard deviations. Both the minimum pressure and standard deviation results indicate a variation at smaller acquisition periods, with convergence being reached after six minutes. It was decided that an acquisition period of 10 minutes (i.e. 6×10^5 samples) should be used to ensure that the pressure fluctuations were accurately captured.

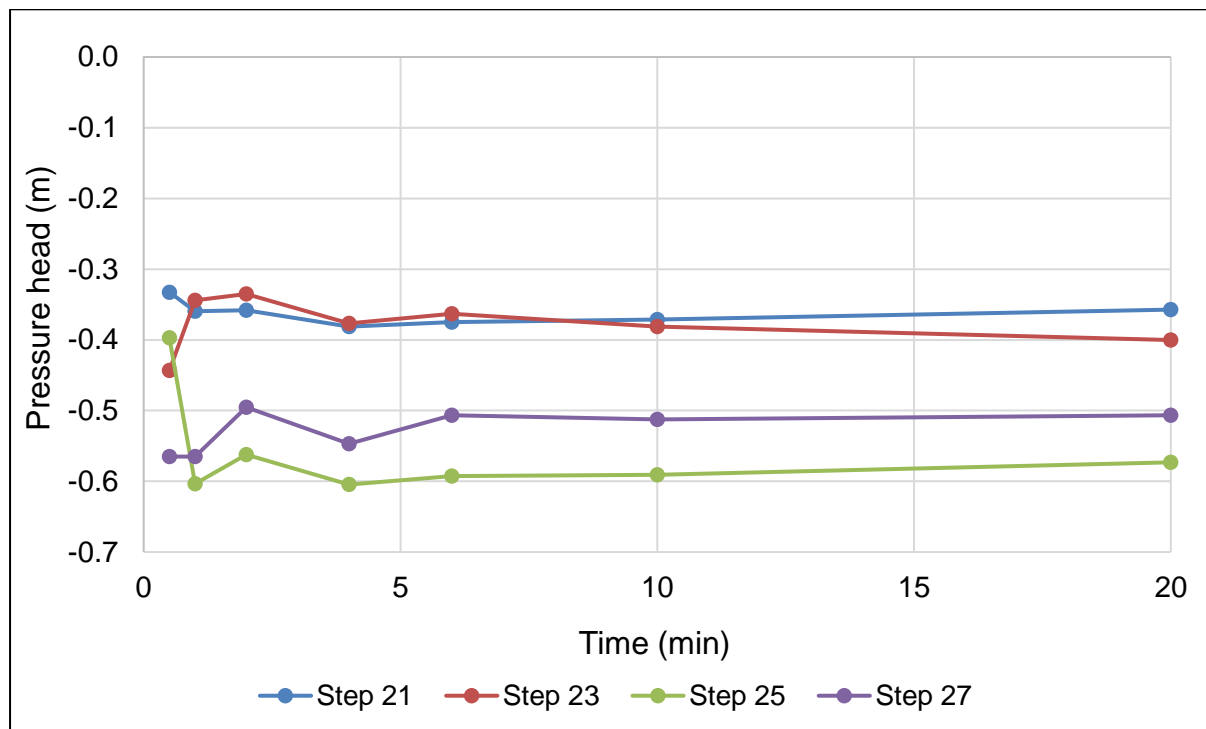


Figure 4.10: Minimum pressures for various acquisition periods and locations.

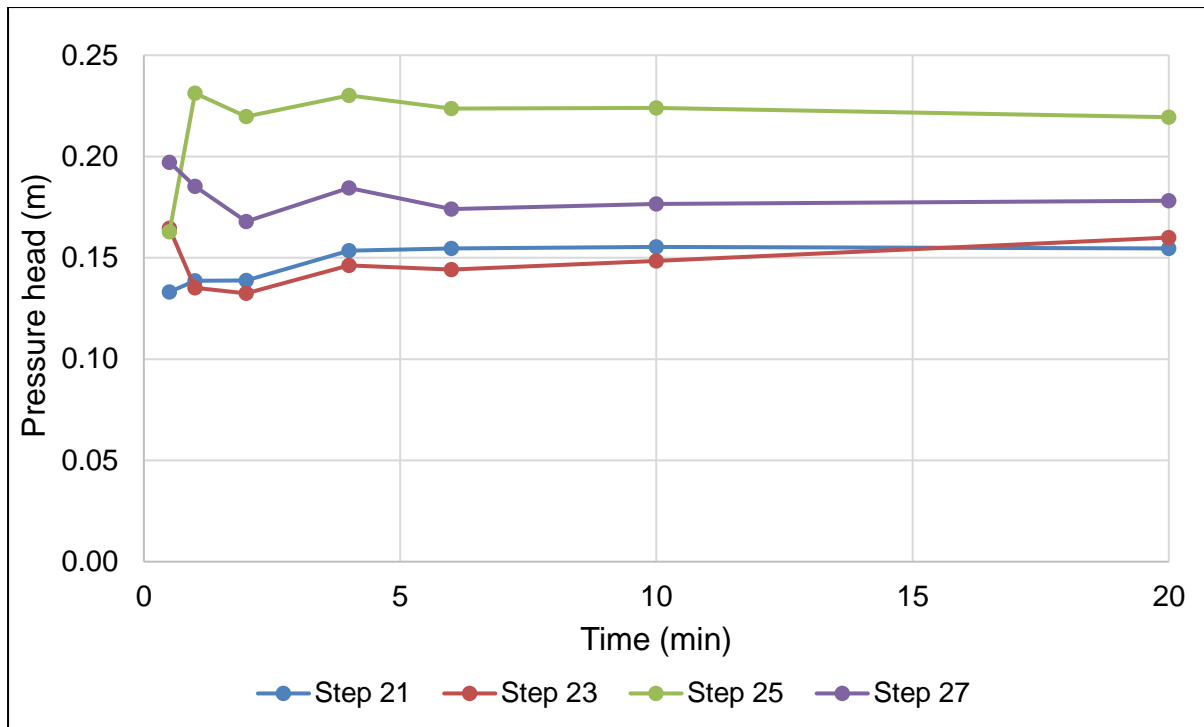


Figure 4.11: Standard deviation for various acquisition periods and locations.

4.5 Model Coordinate System

The model coordinate system, as indicated in **Figure 4.12**, was implemented for this study. Each step had a local coordinate origin as indicated on the right side of the spillway. X denoted the distance across the width of the spillway while Z indicated the vertical distance of each step riser. The streamwise distance was indicated by L, while the distance perpendicular to the pseudo-bottom was denoted by Y.

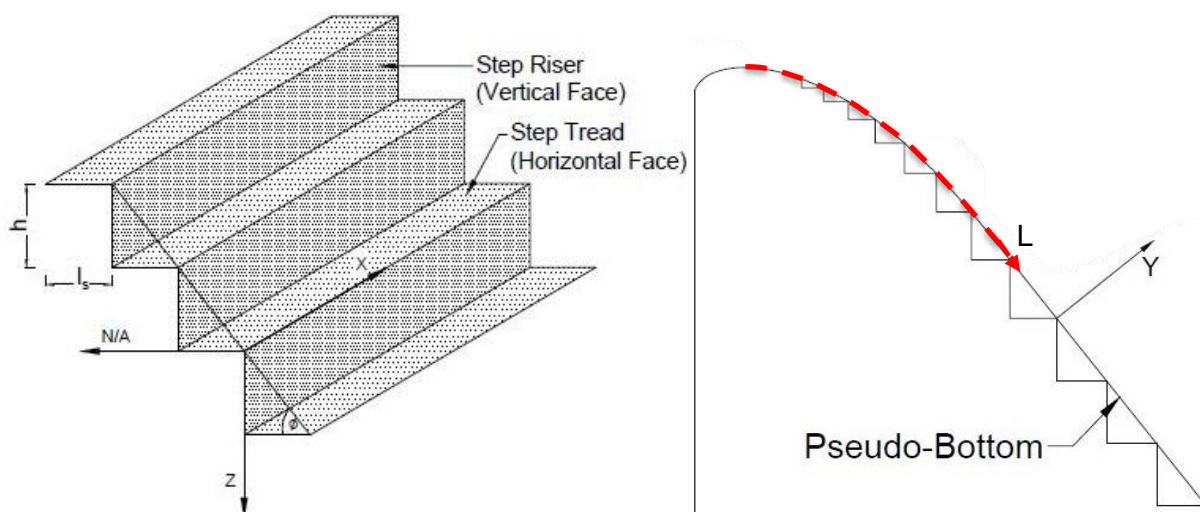


Figure 4.12: Model coordinate system (Calitz, 2015).

4.6 Presentation of Recorded Data

The air concentration and pressure results are presented as dimensionless quantities throughout this study. Dimensionless parameters simplify the efficient comparison between quantities, particularly between prototype and scaled models. The specific measuring position on a stepped spillway is presented as a prototype dimension to effortlessly validate the location of the results.

4.6.1 Air Concentration

The air concentration results were presented by considering the mean average air concentration over the specified selected period as mentioned in **Subsection 4.4.1**. All the experimental air concentration results are presented as a percentage (%).

4.6.2 Pressure

The pressure results of all the experimental tests are presented as a dimensionless parameter, as indicated in **Equation 4-2**.

$$p/\gamma/h = \frac{H}{h} \quad 4-2$$

Where:

p	=	Pressure (N/m ²)
γ	=	Specific weight of water (N/m ³)
H	=	Gauge pressure head (m)
h	=	Step height (m)

4.6.3 Position on the Stepped Spillway

The presentation of results in this thesis differs from that of literature where the spillway position is denoted by a dimensionless parameter, S_i . This method was not applicable to the Type B stepped spillway configuration, because of the high unit discharges, which made it impossible to estimate the position of the surface inception point, by either prediction equations or visual observations.

A specific position on the stepped spillway surface was thus presented as a prototype dimension. This position was defined by the streamwise distance, originating at the spillway crest and measured along the pseudo-bottom as defined in **Figure 4.12**. The spillway width is defined from the right training wall, for both the Type A and Type B spillway configurations.

5 Type A Stepped Spillway: Evaluation of Crest Piers and X-Shape FGP

This chapter discusses the design, construction and results of the 1:15 scale, Type A stepped spillway investigation. The experiments would evaluate various crest pier designs together with the addition of the X-Shape FGP. The subsections provide information regarding the hydraulic model and the crest pier design, the experimental setup and a detailed discussion of the results of the investigation. The latter comprises visual observations, air concentration and pressure measurements and a cavitation evaluation to assess the performance of the various pier designs. The chapter closes with a summary of the important conclusions regarding the performance of the crest pier and X-Shape FGP designs.

As indicated earlier, since the Type B stepped spillway (on which the X- and Y-Shape FGPs were tested) was significantly different from the Type A stepped spillway, the details and results of these experimental studies are similarly presented, but separately, in **Chapter 6**.

5.1 Type A Stepped Spillway Design

The model consisted of an uncontrolled ogee crest and stepped spillway. The ogee crest profile was designed according to the United States Bureau of Reclamation (USBR) (1987) specifications. The spillway was constructed with a constant step tread of 80 mm (1.2 m prototype) and a step height of 100 mm (1.5 m prototype), resulting in an inclination angle of 51.3°, typical for RCC dams. The stepped spillway structure is divided into three zones: the crest, the rear slope and the toe which are discussed in the following subsections. A schematic illustration of the Type A stepped spillway model is given in **Figure 5.1**.

Detailed as-built model plans are shown in **Appendix A**.

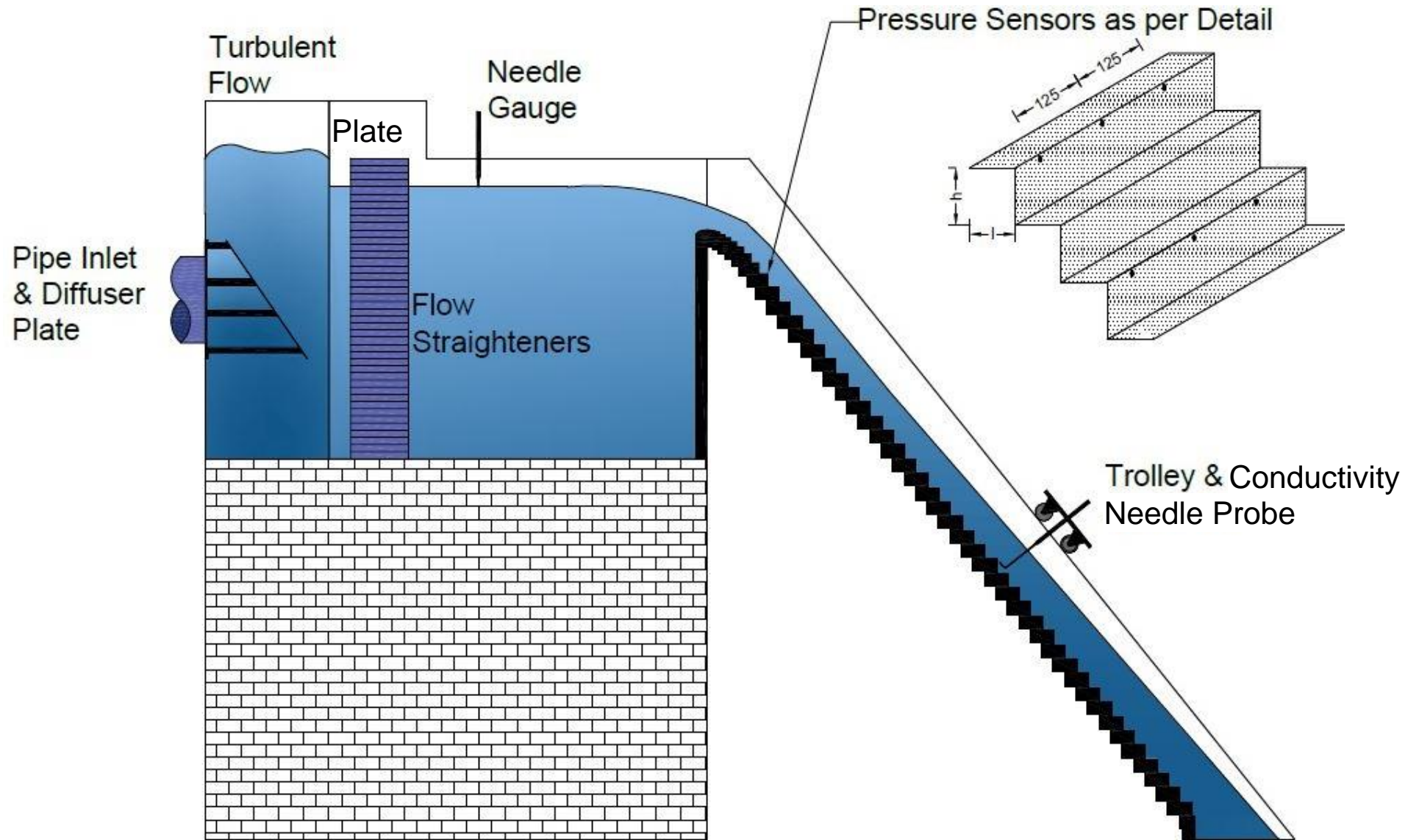


Figure 5.1: Schematic illustration of the Type A stepped spillway model (Not according to scale).

5.1.1 Crest Design

The uncontrolled ogee crest permits the water to discharge whenever the dam level exceeds the crest level. The crest design is based on an ogee profile with a vertical upstream face and no crest piers.

5.1.1.1 Discharge Characteristics

The discharge profile of an ogee crest mimics the natural nappe that forms when water flows over a sharp crested weir. The discharge over the ogee crest was derived from the characteristics of the sharp crested weir and is given by **Equation 5-1**.

$$Q = C_e L H_e^{1.5} \quad 5-1$$

where:

Q	=	Discharge
C_e	=	Variable discharge coefficient
L	=	Effective length of crest
H_e	=	Actual head on the crest, including approach velocity head

The design calculations were performed according to the guidelines stipulated by the USBR (1987), which are summarised in **Table 5.1**. As this thesis builds on prior research by Calitz (2015), which used the same model, the author's calculations were used.

Table 5.1: Design summary of ogee crest (Calitz, 2015).

Description (See Figure 5.2)	Unit	Model (1:15)	Prototype
P_d (Vertical upstream height of crest)	m	1.6	24
Design q	m ² /s	0.323	18.76
Maximum q	m ² /s	0.516	30
Effective crest length	m	1	15
H_d	m	0.280	4.2
H_e (30 m ² /s)	m	0.373	5.6
H_e/H_d	m/m	1.333	1.333
C_d		2.18	2.18
C_e		2.27	2.27
C_e/C_d		1.04	1.04
P/H_d	m/m	5.71	5.71

5.1.1.2 USBR Profile (1987)

The ogee profile was developed to approximate the profile of the undernappe of a waterjet flowing over a sharp crested weir, thereby providing the ideal form for obtaining optimum discharges. The shape of the profile is affected by the head, the inclination angle of the upstream face and the height to the crest apex. The ogee profile is as indicated in **Figure 5.2**.

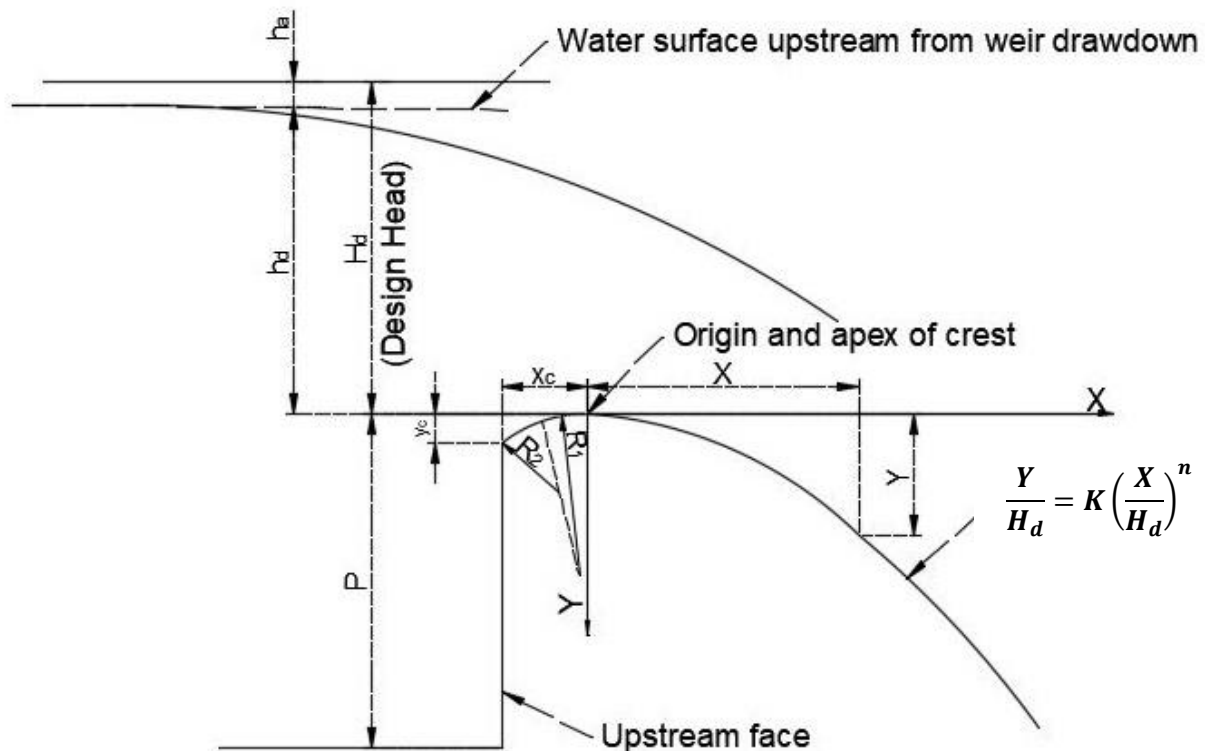


Figure 5.2: Definition sketch of an ogee crest (recreated from USBR, 1987).

The profile upstream of the crest apex is defined by a compound circular curve, while the section downstream of the crest is as described by **Equation 5-2**. With the use of **Equation 5-2** and the parameters as identified in **Table 5.2**, the ogee profile was defined.

$$\frac{Y}{H_d} = K \left(\frac{X}{H_d} \right)^n \quad 5-2$$

where:

- Y, X = Coordinates as defined in **Figure 5.2**
 K, n = Constants as defined by USBR (1987)

Table 5.2: Design of ogee profile (Calitz, 2015).

Description (See Figure 5.2)	Unit	Model (1:15)	Prototype
H_d	m	0.280	4.200
h_a/H_d	m/m	0.005	0.005
K		0.500	0.500
n		1.869	1.869
R_1 (as defined in Figure 5.2)	m	0.140	2.100
R_2 (as defined in Figure 5.2)	m	0.056	0.840
X_c (as defined in Figure 5.2)	m	0.079	1.184
Y_c (as defined in Figure 5.2)	m	0.036	0.533
Point of tangency (X-coordinate)	m	0.399	5.984
Point of tangency (Y-coordinate)	m	0.269	4.041

5.1.1.3 Transitional Steps

A stepped spillway with the ogee profile extending to the point of tangency, followed by a constant step profile, is inclined to cause flow detachments at the first step for small discharges. As the flow impacts on the first step tread, it jumps and impacts further downstream, missing the immediately subsequent steps. This jump disappears once the discharge increases to a critical value.

To achieve adequate performance of the spillway for small discharges, a transitional step profile is introduced. The CEDEX (Centro de Estudios y Experimentación de Obras Públicas) transitional step model was used in this investigation, which ensured good flow conditions for various discharges. This profile provides increasing step treads, based on the design head, until the point of tangency is reached. This design is illustrated in Figure 5.3.

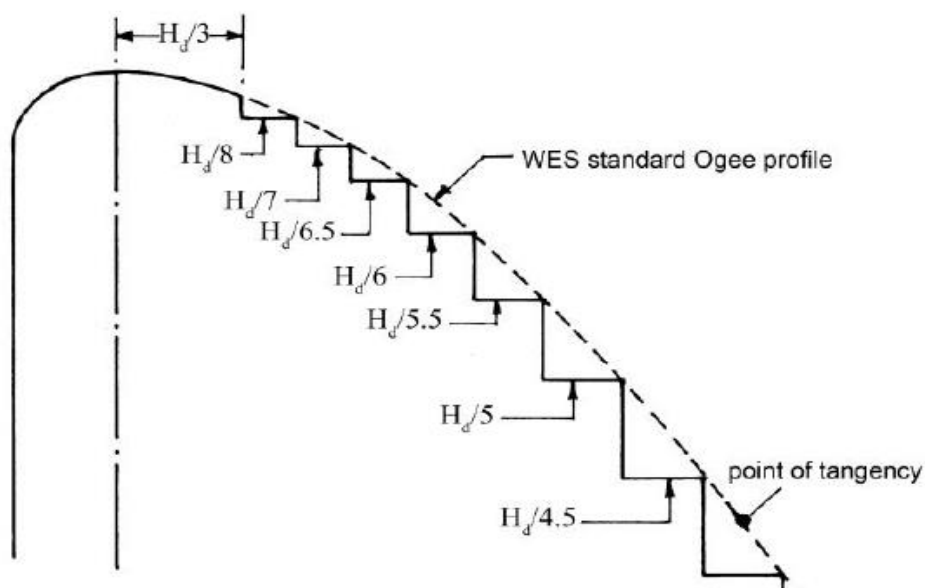


Figure 5.3: Crest and transitional step zone as proposed by CEDEX.

5.1.2 The Rear Slope

The rear slope of the spillway guides the water from the crest to the toe of the spillway. This constant slope is normally determined by the requirement of structural stability. The model was constructed with a constant slope of 51.3° . The rear slope of the model was designed as a stepped profile, which is based on prototype step dimensions of a tread length of 1.2 m and a step height of 1.5 m. This conforms to the standard RCC horizontal layer works, which are constructed in layers of 0.3 m increments. In the model, these step dimensions related to a step tread of 80 mm and a step height of 100 mm. This region of the spillway is at risk of cavitation damage and, therefore, was the focus area of the thesis.

5.1.3 The Toe

The toe is the junction between the stepped spillway and the downstream energy dissipator. The function of the toe is to guide the flow passing down the stepped spillway smoothly into the energy dissipator without the development of undesirable flow conditions. The toe of the spillway is beyond the scope of this thesis and was therefore not included in this study.

5.2 Spillway Crest Pier Design

Although crest piers are usually required to support a bridge or gates on a spillway crest, the purpose of the pier inclusion in this study was to induce artificial aeration into the flow. This thesis considered variations of the pier design, comprising two different pier nose designs, two pier lengths and the addition of flare.

5.2.1 Pier Nose Design

The pier nose shape was designed in accordance with the guidelines provided by the American Society of Civil Engineers (ASCE, 1995), as indicated in **Figure 5.4 (i)**. The pier nose shapes were designed in accordance with the requirements for a Type 2 and a Type 3 nose pier. **Figure 5.4 (ii)** and **(iii)** illustrate the bullnose and parabolic prototype pier designs, respectively.

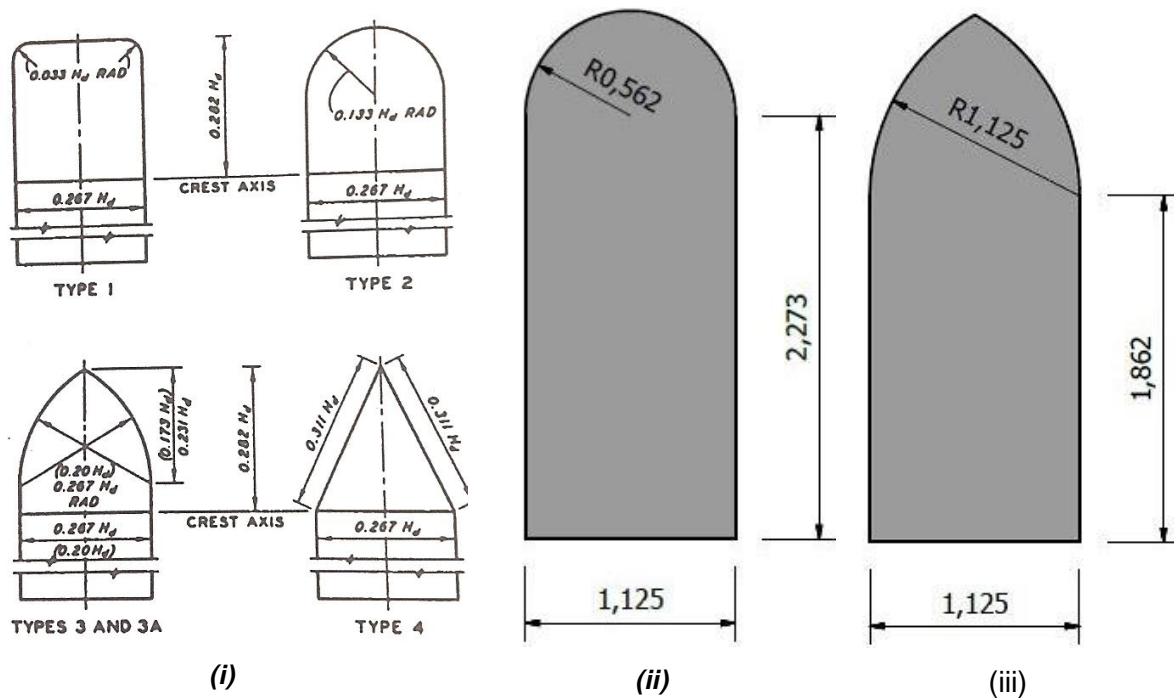


Figure 5.4: (i) Pier nose design per ASCE guidelines (1995). Prototype design of the (ii) bullnose pier shape and (iii) parabolic pier shape (dimensions in m prototype).

5.2.2 Pier Lengths

Two pier lengths were identified as suitable in order to investigate the effect thereof on the spillway aeration. The pier designs consisted of a short pier which extended 2.8 m downstream, and a long pier which extended 6.4 m downstream of the pier nose position, as indicated in **Figure 5.5**. To ensure that the piers caused minimal additional head, they were placed downstream of the ogee crest at an angle of 72° to the horizontal. This concept was based on the pier design of the Gariep Dam in South Africa, where the piers were placed downstream of the crest, within the supercritical flow region, to eliminate any additional discharge head.

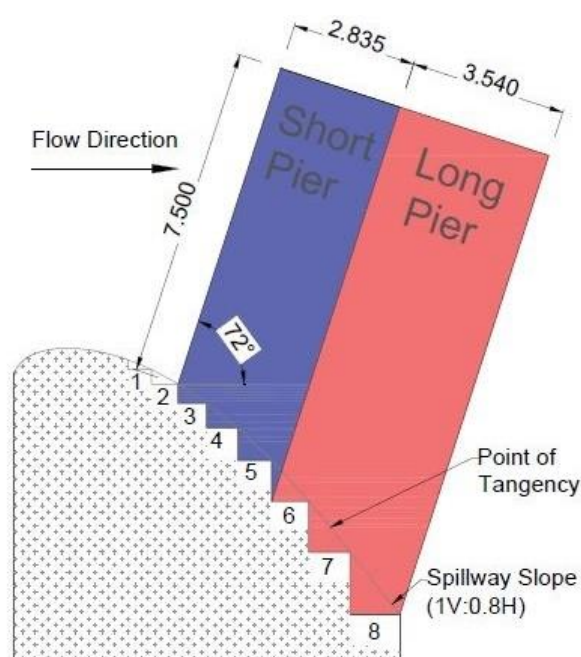


Figure 5.5: Schematic illustration of the two different pier lengths (dimensions in m prototype).

Experimental tests were conducted to determine the best pier location, as indicated in **Figure 5.5**, by comparing the additional discharge heads for each step to the discharge head of the standard stepped spillway without crest piers. Tests were conducted for two prototype unit discharges of $30 \text{ m}^2/\text{s}$ and $40 \text{ m}^2/\text{s}$. The additional head results are indicated in **Table 5.3**.

Table 5.3: Additional prototype head (m) caused by various pier positions.

Nose position (step no.)	Units	Prototype unit discharge	
		$30 \text{ m}^2/\text{s}$	$40 \text{ m}^2/\text{s}$
1	m	0.075	0.218
2	m	0.060	0.128
3	m	0.015	0.120
4	m	0.000	0.068

The first position downstream of the ogee crest which showed little to no additional head, was with the pier nose placed at step 4. Although this appeared to be an acceptable position, the turbulence and required freeboard on the pier was deemed too severe. **Figure 5.6** and **Figure 5.7** illustrate the position and freeboard of the pier, with the pier nose located at steps 1 and 4, respectively.

The pier experienced excessive freeboard and turbulence when the pier nose was situated at the 4th step and the design was deemed inappropriate. In order to minimise the additional head, the pier was thus to be placed at either step 2 or 3. Similar additional heads were experienced for both the pier locations, especially at higher discharges, as illustrated in **Table 5.3**. Supplementary tests were conducted to compare the air concentration and pressure results for each pier position. These experiments also concluded with similar results. It was therefore decided to place the pier nose at the 3rd step. This decision was based on the lower impact on the design head and a slightly better air concentration profile.

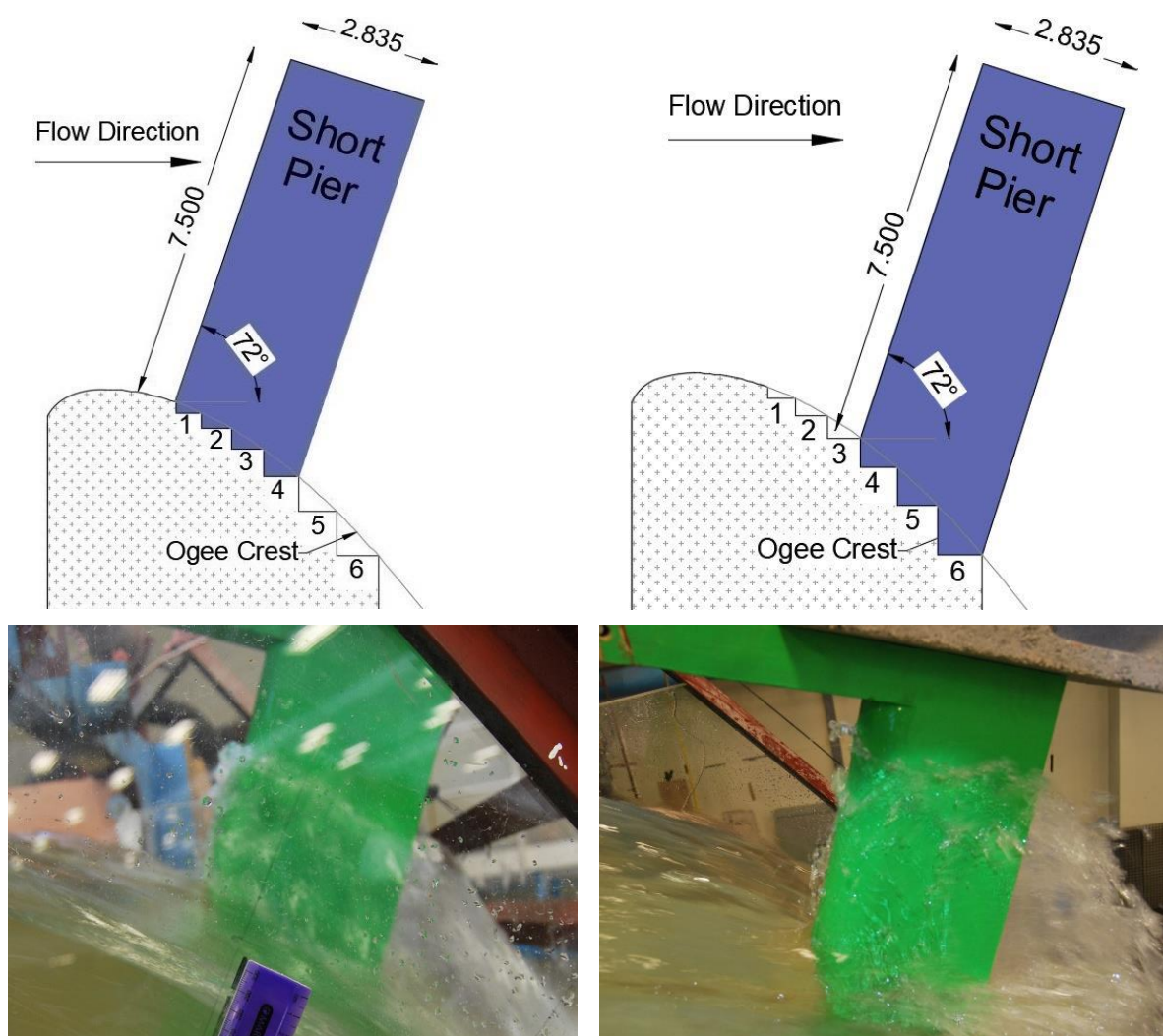


Figure 5.6: Bullnose pier located at step 1 for a prototype discharge of 40 m²/s.

Figure 5.7: Bullnose pier located at step 4 for a prototype discharge of 40 m²/s.

5.2.3 Flaring Gate Pier (FGP) Design

As stated in **Section 2.7.2**, various forms of the FGP currently exist, but the most widely used are the Y- and X-Shape FGP. However, only the X-Shape FGP was investigated on this model, since it was designed to be an improvement on the Y-shape FGP. The X-Shape was designed with a wider bottom outlet width, which would pass the low flows without any contraction or deflection. This resulted in more of the stepped profile being used for energy dissipation, typically for unit discharges less than 30 m²/s.

The design of the X-Shape FGP was based on literature findings and prototype dimensions. These dimensions were adapted, because of size limitations on the available model. Research by Chen and Zhang (2015) indicated that a contraction angle of 25° to 30° was ideal to minimise downstream pressure in a stilling basin with an optimal contraction ratio ($\beta = \frac{b}{B}$) of 0.4 to 0.6, where B is the unobstructed width between piers and b is the unobstructed width between the flare extremities. The model was designed with a contraction angle of 25° and a contraction ratio of 0.72. The contraction ratio did not conform to the advised literature guidelines; this was to avoid excessive blockage of the flow. **Figure 5.8** shows the adapted X-shape FGP design.

It should be noted that the prototype implementation of the FGP design was accompanied by piers of 40 m to 50 m in length. These pier lengths were not attainable on a 1:15 scale model, as the pier would have extended the length of the spillway. The FGP was thus evaluated together with the long pier length, as was discussed in **Section 5.2.2**.

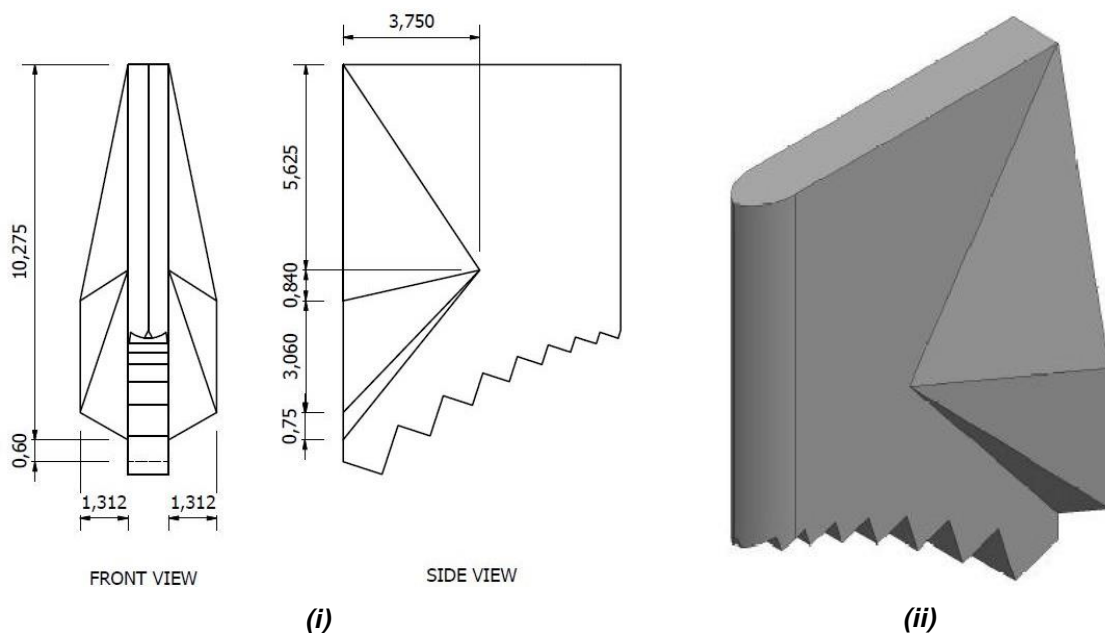


Figure 5.8: (i) Prototype design of X-shaped FGP and (ii) Isometric illustration of FGP with parabolic pier nose (dimensions in m prototype).

5.3 Experimental Setup for the Evaluation of Crest Piers

5.3.1 Model Layouts

Different model setups and pier configurations were tested on the Type A stepped spillway. All the pier configurations were located in the centre of the 1 m wide spillway ($X=500$ mm) resulting in an effective prototype pier spacing of 15 m, centre to centre. The different model layouts are shown in **Table 5.4** and include:

- A standard stepped spillway with no piers, which acted as the control test.
- A stepped spillway equipped with the different crest pier configurations.

Table 5.4: Experimental model layouts.

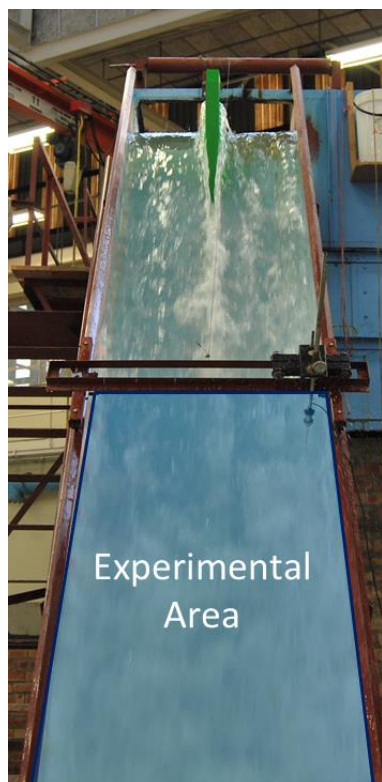
Model Layout	Pier nose	Length
1	No Pier	
2	Bullnose	Short
3	Bullnose	Long
4	Parabolic	Short
5	Parabolic	Long

5.3.2 Model Setup

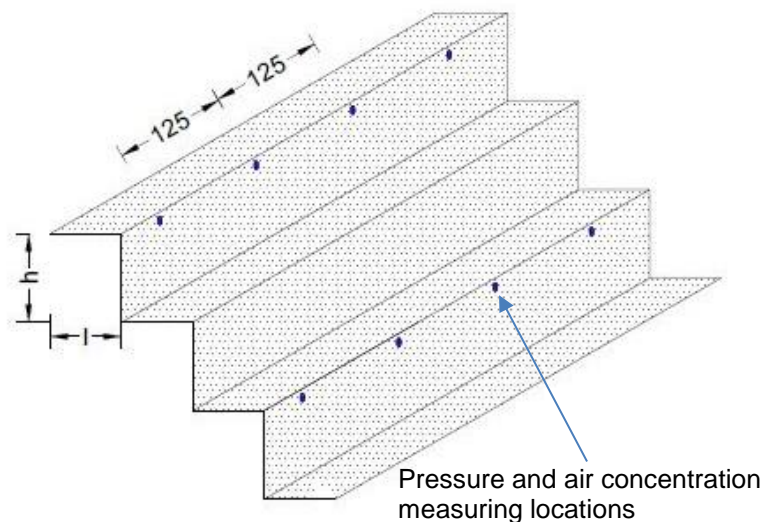
As previously mentioned in **Section 2.5.1**, the largest negative pressures occur in the vicinity of the inception point. This statement provided the basis for the experiments from which the critical experimental area was defined, which is indicated in **Figure 5.9 (i)**. The tests were conducted with a prototype unit discharge of $30 \text{ m}^2/\text{s}$. The air concentration and pressure results were measured at specific measuring positions, as illustrated in **Subsection 5.3.3** and as summarised in **Table 5.5**. Four pressure sensors were installed on each step, with the first being installed at the spillway centre. Subsequent sensors were spaced 125 mm apart (1.875 m prototype), as illustrated in **Figure 5.9 (ii)**. The air concentration data was measured at the pressure sensor location, with the probe tip positioned in line with the pseudo-bottom. The experimental tests were conducted for the five model layouts, as discussed in **Section 5.3.1**, with the pier placed in the centre of the spillway as illustrated in **Figure 5.9 (i)**.

Table 5.5: Summary of the measuring locations.

Prototype unit discharge (m^2/s)	Measuring locations for air concentration and pressure
30	Step 25, 27, 29 & 31



(i)



(ii)

Figure 5.9: (i) Illustration of the pier setup and experimental area. (ii) Schematic drawing of pressure and air concentration measuring locations (dimensions in mm model).

5.3.3 Measuring Locations

The air concentration and pressure results were measured within the experimental area to assess the performance of various model configurations. These results were measured on only half of the spillway width [$X=500$ mm (7.5 m prototype) to $X=875$ mm (13.125 m prototype)] because of the similarity that was present in the physical model. The measuring locations for both the air concentration and pressure results are given in **Table 5.6**.

The air concentration results were recorded by using the conductivity needle probe, which was positioned at the outer step edge for each measuring position. This was the closest location to the stepped profile that the conductivity needle probe could accurately measure without the risk of damaging the instrument. The air concentration results were thus captured on the pseudo-bottom.

The pressures were recorded by using pressure transducers as discussed in **Subsection 4.2.2**. These transducers were installed on the step riser, at a position 0.9 times the step height (0.9 h). This position, as indicated by the relevant literature, is the location where minimum pressures occur on a stepped spillway.











Table 5.6: Air concentration and pressure measuring locations.

Prototype Discharge (m ² /s)	Model Length, L_m (mm)	Prototype Length, L_p (m)	Step no.	X-Coordinate (mm)			
				Location A	Location B	Location C	Location D
30	2790	41.85	25	500	625	750	875
	3046	45.69	27	500	625	750	875
	3302	49.53	29	500	625	750	875
	3558	53.37	31	500	625	750	875

5.3.4 Model Test Conditions on the Type A Stepped Spillway

In order to reduce the aeration scale effects and to accurately measure the spillway air concentration, a minimum Reynolds number of 8×10^4 is required according to Chanson and Felder (2017). The model test conditions on the Type A stepped spillway are presented in **Table 5.7**. These conditions are applicable for the evaluation of both the crest piers and X-Shape FGP.

Table 5.7: Model test conditions on the Type A stepped spillway.

Model test conditions					
Model Layout	Crest configuration			Unit discharge	
				30 m ² /s	35 m ² /s
1	No pier (Reference)		Pier nose type Bullnose or Parabolic	Air & Pressure	Repeated
2	Pier 1 (Short)			Air & Pressure	
3				Air & Pressure	Repeated
4	Pier 2 (Long)			Air & Pressure	
5				Air & Pressure	
6	Pier 2 (Long) & X-Shape FGP			Air & Pressure	
7				Air & Pressure	
$R_{e\ model}$ $\left(\frac{q}{v}\right)$	Chanson and Felder (2017) recommended a minimum R_e of 8×10^4 to minimise air concentration scale effects			39.4×10^4	46.1×10^4

The Reynolds numbers complied to the recommendation of Chanson and Felder in order to minimise the scale effects. As the Reynolds numbers were significantly larger compared to the recommended minimum, no model scale effects were expected for the air concentration measurement.

5.4 Repeatability of Crest Pier Experiments

The repeatability of experiments is important to eliminate variability in measurements and ensure accurate results. A proportion of the experiments, typically 10%, was repeated to ensure that the results were reproduced. In order to validate the results, two independent tests were repeated where air concentration and pressures were measured.

5.4.1 Air Concentration

Two independent experiments were conducted at a prototype unit discharge of 35 m²/s to ensure the repeatability of the air concentration results. These tests were initially conducted at a higher discharge than the unit discharge of 30 m²/s. This was because of lab restrictions which revealed that the discharge of 35 m²/s was variable. Statistical data, as provided in **Table 5.8**, illustrate the repeatability of the results for the two independent experiments with measuring locations at Step 29B and Step 29D.

Table 5.8: Statistical air concentration data (%) for positions at Step 29B and Step 29D.

Air Concentration (%)	No Pier				Parabolic Pier			
	Step 29B		Step 29D		Step 29B		Step 29D	
	Test 1	Test 2	Test 1	Test 2	Test 1	Test 2	Test 1	Test 2
Mean	10.6	11.9	10.6	11.2	18.1	23.4	12.9	11.7
Standard deviation	14.5	12.9	14.5	13.2	17.4	21.6	15.1	14.7
Maximum	91	69	91	96	100	100	90	81
3 rd Quartile	14	17	14	14.5	25	32.8	18	17
Median	5	8	5	6	12	17	7	5
1 st Quartile	1	2	1	2	6	7	2	1
Minimum	0	0	0	0	0	0	0	0

The statistical data in **Table 5.8** indicate a good agreement for all the measuring locations with the largest discrepancy for the parabolic pier at Step 29B. To better understand the statistical data, a box and whisker plot was used to visually compare the accuracy of the independent tests. The 25th percentile, median and 75th percentile are represented by the box, while the mean is represented by the cross. The whiskers extend from the box to a minimum and maximum value, which excludes outliers. The minimum and maximum values are determined to be within the range of 1.5 times the interquartile range from the top and bottom of the box. The outliers are presented as dots. **Figure 5.10** shows the box and whisker plot for the statistical air concentration data.

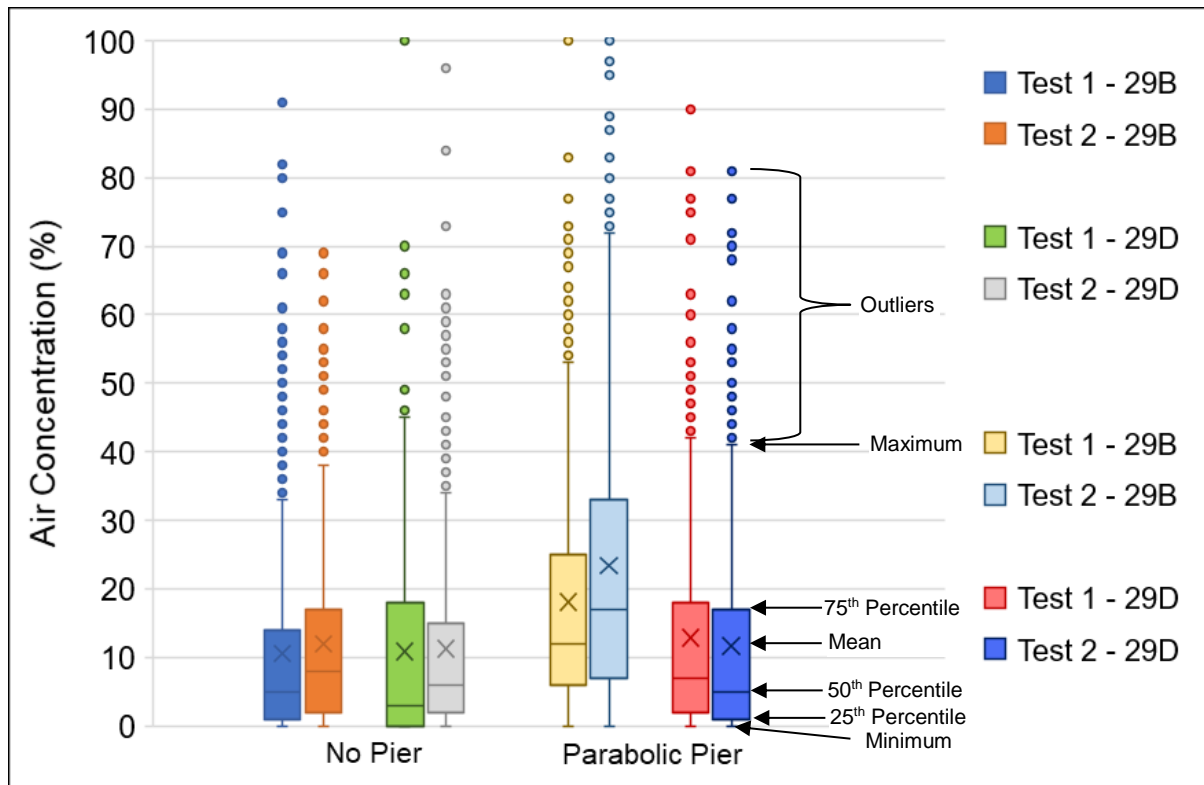


Figure 5.10: Air concentration comparisons of repeated test results at 35 m²/s.

The statistical data in **Table 5.8** and the box and whisker plot in **Figure 5.10** indicate a close resemblance between the independent experiments. The box and whisker plots indicate that the majority of the air concentration measurements were between 0% and 20% and that the outliers were measured to be above the local maximum. The largest discrepancy was located at Step 29B, for the parabolic pier experiment, as indicated in **Figure 5.10**.

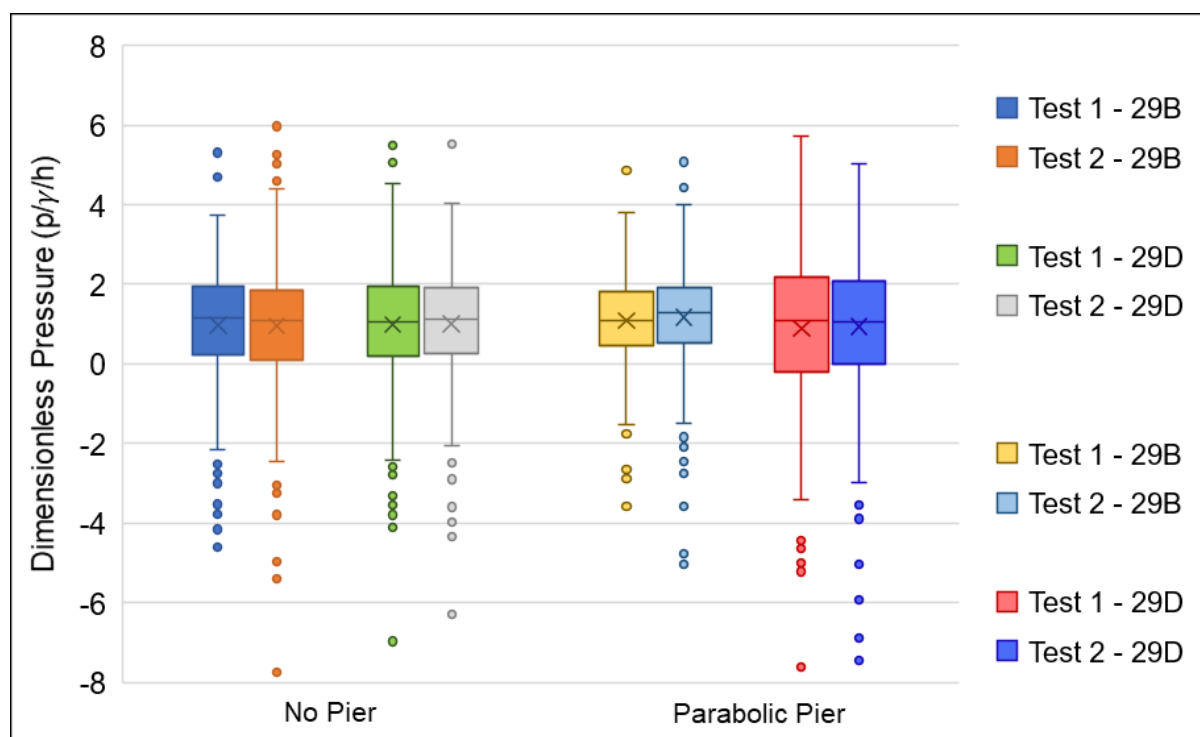
Since the mean air concentration was used in this study to present the air concentration at a specific location and the variation of the means of repeated tests are considered to be within acceptable limits, the mean of individual measurements at a location can be expected to be reliable.

5.4.2 Pressure

Similar to the air concentration repeatability evaluation, two independent experiments were conducted to investigate the repeatability of the pressure results at a prototype unit discharge of 35 m²/s. The pressure statistics are indicated in **Table 5.9**, with a box and whisker graph illustrating the pressure distribution in **Figure 5.11**.

Table 5.9: Statistical pressure data (p/y/h) for positions at Step 29B and Step 29D.

Pressure (p/y/h)	No Pier				Parabolic Pier			
	Step 29 B		Step 29D		Step 29B		Step 29D	
	Test 1	Test 2	Test 1	Test 2	Test 1	Test 2	Test 1	Test 2
Mean	0.979	0.962	0.983	1.000	1.085	1.168	0.889	0.935
Standard deviation	1.391	1.562	1.580	1.399	1.128	1.192	1.837	1.788
Maximum	5.304	5.964	5.480	5.524	4.868	5.076	5.709	5.021
3rd Quartile	1.950	1.849	1.948	1.909	1.805	1.920	2.177	2.094
Median	1.138	1.089	1.053	1.128	1.087	1.285	1.073	1.052
1st Quartile	0.221	0.078	0.188	0.253	0.451	0.524	-0.187	0.011
0.15 Percentile	-3.194	-3.723	-3.757	-3.198	-2.300	-2.410	-4.621	-4.430
Minimum	-4.591	-7.755	-6.968	-6.289	-3.580	-5.028	-7.614	-7.458

**Figure 5.11: Pressure comparisons of repeated test results at 35 m²/s.**

The statistical data in **Table 5.9**, together with the box and whisker plot in **Figure 5.11**, indicate a good relation between the two independent experiments. The box and whisker plot indicate that the majority of the pressure results were measured to be between 0 and 2.

Since the 0.15 percentile pressures were used to present the minimum pressures at a specific measuring location and the repeated test results are considered to be within acceptable limits, the 0.15 percentile pressure is expected to be reliable.

5.5 Experimental Setup for the Evaluation of the X-Shape FGP

The experimental setup for the FGP investigation was very similar to the crest pier evaluation as discussed in **Section 5.3**. The model coordinate system was kept unchanged; however, alterations were made with respect to the model layouts, model setup, measuring locations and the measuring procedure, as mentioned in the subsections that follow.

5.5.1 Model Layouts

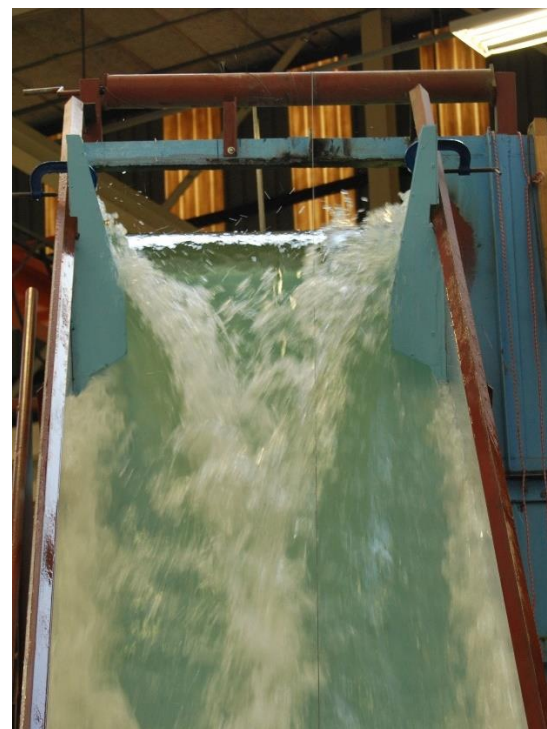
The layout for the investigation comprised two model layouts with alterations to the pier nose shape, as indicated in **Table 5.10**. Instead of placing the FGP in the centre of the spillway, as for the previous investigation, half of the FGP was placed on either side of the spillway as shown in **Figure 5.12**. This configuration is expected to mimic the damming effect in-between the flares, as was observed for a similar prototype design.

Table 5.10: Experimental model layouts for the evaluation of the X-Shape FGP.

Model Layout	Pier nose	Length	Flare
6	Bullnose	Long	X-Shape FGP
7	Parabolic	Long	X-Shape FGP



(i)



(ii)

Figure 5.12: Comparison of the (i) prototype flow pattern at the Suofengying Dam, China (Anonymous, 2012) and the (ii) model flow pattern.

5.5.2 Model Setup

Due to the uncertainty surrounding the expected performance of the FGP and how it would alter the flow pattern, as compared to the standard stepped spillway, the experimental area was defined as consisting of the entire spillway length. The experimental area ranged from downstream of the flare to a position beyond the expected pseudo-bottom inception point, as indicated in **Figure 5.13**. This enlargement made it possible to capture the air concentration and pressure data within the impact region.

The experiments were conducted at a prototype unit discharge of 30 m²/s. Pressure results were recorded in a similar manner as in the crest pier investigation. A slight alteration was made to the air concentration measuring procedure, as indicated in **Section 5.5.3**. The summarised measuring positions are tabulated in **Table 5.11**, whilst a detailed discussion is presented in **Section 5.5.4**.

Table 5.11: Summary of the measuring locations.

Prototype unit discharge (m ² /s)	Measuring locations for air concentration and pressure
30	Step 9, 13, 17, 21, 23, 25, 27, 29, 31 & 34

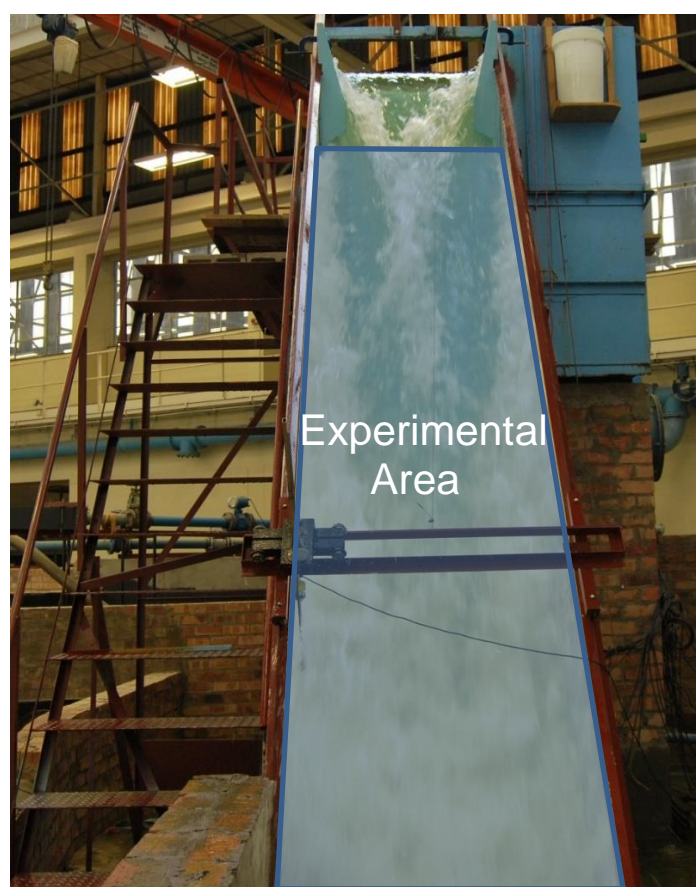


Figure 5.13: Model setup and experimental area.

5.5.3 Air Concentration Measurement

During the crest pier experiments, as described in **Section 5.3**, it was realised that the conductivity needle probe had measured the air concentration inaccurately. This was because of the high flow velocity which created an air void directly downstream of the probe. The stepped profile generated a recirculating flow regime, which transported the induced air to a position upstream of the probe tip. This compromised the air concentration results by approximately 3.5% for a unit discharge of 35 m²/s, since it measured a portion of self-induced air. At a unit discharge of 30 m²/s, the accuracy had increased due to a reduction in the proportion of self-induced air. This phenomenon is illustrated in **Figure 5.14**.

The solution to the self-induced air phenomenon was based on the design of a boat's outboard motor. The outboard motor is equipped with an anti-ventilation plate as indicated in **Figure 5.15 (i)**, which prevents surface air or exhaust gas from interacting with the propeller blades. A similar anti-ventilation plate, as illustrated in **Figure 5.15 (ii)**, was added to the conductivity needle probe, which removed the effect of the self-induced air.

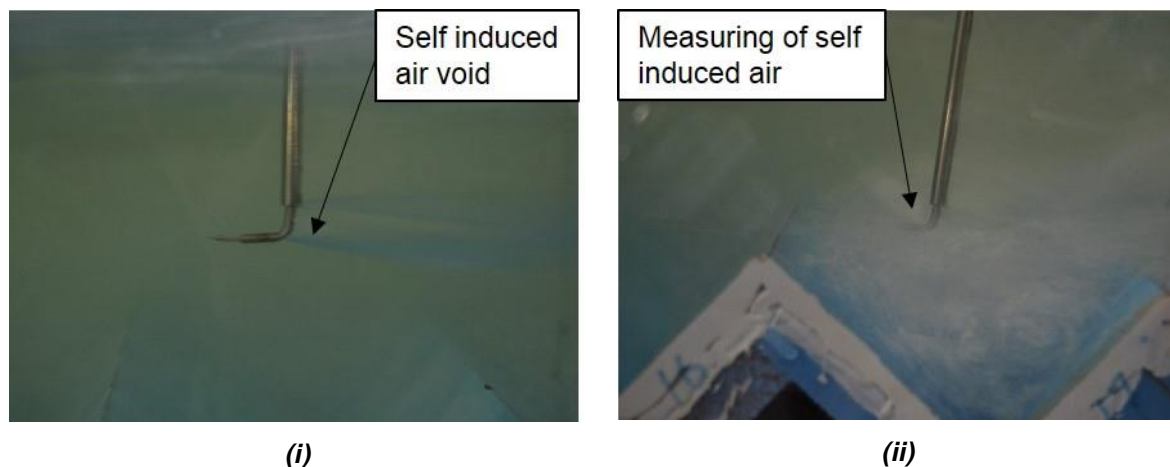


Figure 5.14: Photographs indicating (i) the air void behind the probe tip and the (ii) air mixture on the step once the probe enters the recirculating zone caused by the step profile.

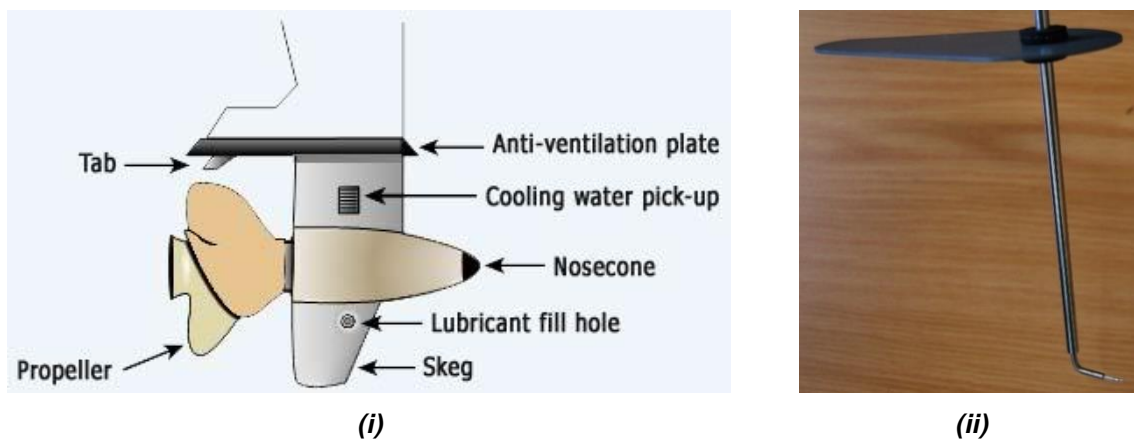


Figure 5.15: (i) Schematic presentation of an outboard motor's anti-ventilation plate (Anonymous, 2013) and (ii) the addition thereof to the conductivity needle probe.

5.5.4 Measuring Locations

Air concentration and pressure measurements were recorded within the experimental area to assess the performance of the X-Shape FGP. These results, as for the crest pier investigation, were measured on only half of the spillway width, because of the similarity of the physical model. The air concentration and pressure measuring positions are tabulated in **Table 5.12**.

The conductivity needle probe, with the addition of the anti-ventilation plate, was used to capture the air concentration data. The probe tip was positioned at the outer step edge, for each measuring position, to record the air concentration results.

The pressure data was captured by using the pressure transducers, as was explained in **Section 4.2.2**. The pressure transducers were installed at a position which was 0.9 times the step riser height (0.9 h) for each measuring location. This is the closest position that the instrumentation could be installed to the step edge without damaging the stepped profile.

Table 5.12: Air concentration and pressure measuring locations.

Prototype Discharge (m ² /s)	Model Length, L _m (mm)	Prototype Length, L _p (m)	Step no.	X-Coordinate (mm)			
				Location A	Location B	Location C	Location D
30	741	11.12	9	500	625	750	875
	1253	18.80	13	500	625	750	875
	1765	26.48	17	500	625	750	875
	2278	34.17	21	500	625	750	875
	2534	38.01	23	500	625	750	875
	2790	41.85	25	500	625	750	875
	3046	45.69	27	500	625	750	875
	3302	49.53	29	500	625	750	875
	3558	53.37	31	500	625	750	875
	3942	59.13	34	500	625	750	875

5.6 Repeatability of X-Shape FGP Experiments

As previously mentioned, the repeatability of experiments ensures accurate modelling and eliminates variable results. Two independent experiments were conducted for each model setup to validate the accuracy of both the air concentration and the pressure results.

5.6.1 Air Concentration

The independent experiments were conducted at a prototype unit discharge of 30 m²/s. The statistical data, as tabulated in **Table 5.13**, illustrate the repeatability of the air concentration results. The experiments were performed for both the bullnose and the parabolic X-Shape FGP, which specifically assessed the measuring positions located at Step 9A and Step 29A.

Table 5.13: Statistical air concentration data (%) for positions at Step 9A and Step 29A.

Air Concentration (%)	Bullnose, X-Shape FGP				Parabolic, X-Shape FGP			
	Step 9A		Step 29A		Step 9A		Step 29A	
	Test 1	Test 2	Test 1	Test 2	Test 1	Test 2	Test 1	Test 2
Mean	0.1	0.0	1.8	0.5	0.1	0.0	2.8	1.0
Standard deviation	0.3	0.0	3.2	2.4	0.3	0.3	3.9	2.7
Maximum	4	1	38	32	3	3	44	20
3 rd Quartile	0	0	2	0	0	0	3.75	0
Median	0	0	1	0	0	0	2	0
1 st Quartile	0	0	0	0	0	0	1	0
Minimum	0	0	0	0	0	0	0	0

The statistical data indicated that the biggest discrepancy occurred at Step 29A for both model layouts. This is due to the increased velocities, and subsequently increased turbulence, at the downstream section of the spillway, which induced fluctuating results. A box and whisker plot was used to visually compare the performances of the independent experiments. See **Figure 5.16** for the box and whisker plot, while the interpretation thereof was previously described in **Section 5.4**.

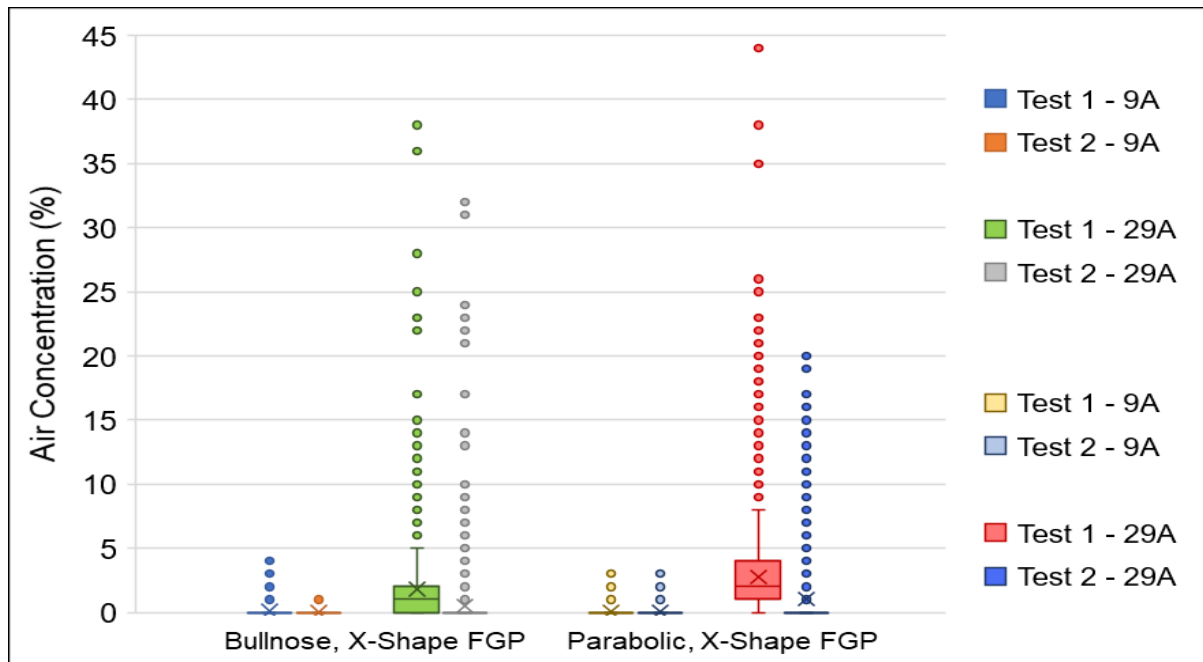


Figure 5.16: Air concentration comparisons of repeated test results at 30 m²/s.

The air concentration data indicate a good resemblance between the independent experiments as indicated in **Table 5.13** and **Figure 5.16**. The box and whisker plot indicates that the majority of air concentration results were measured as less than 5% for each of the respective measuring positions. The largest discrepancy between the independent experiments was located at Step 29A. As previously mentioned, this could be attributed to the increased velocity and turbulence at the downstream section of the spillway.

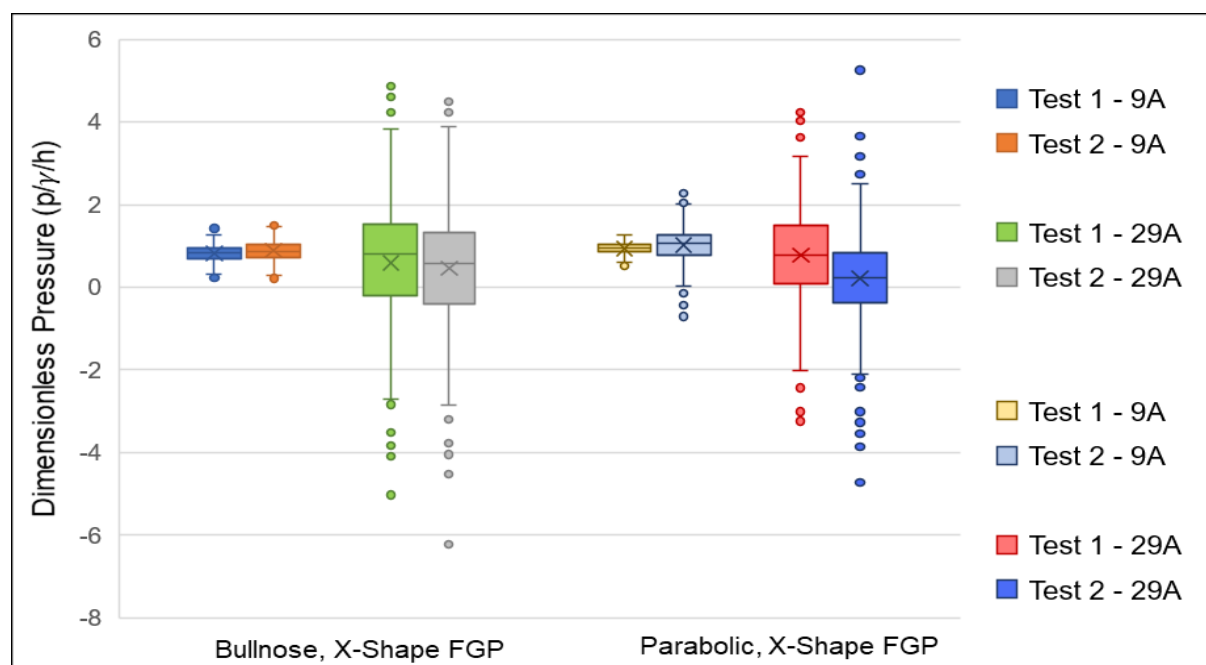
The air concentration results were interpreted based on the average air concentration of a one minute measuring period. Although the results indicated a difference exceeding 1% at the downstream section of the spillway, this was deemed acceptable, since the measurements were recorded within a highly variable region.

5.6.2 Pressure

A similar evaluation was conducted to assess the repeatability of the pressure results. Two independent experiments were conducted at a prototype unit discharge of 30 m²/s to investigate the accuracy and variability. The statistical data of the independent experiments are tabulated in **Table 5.14** with a box and whisker plot illustrating the pressure distribution in **Figure 5.17**.

Table 5.14: Statistical pressure data (p/y/h) for positions at Step 9A and Step 29A.

Pressure (p/y/h)	Bullnose, X-Shape FGP				Parabolic, X-Shape FGP			
	Step 9A		Step 29A		Step 9A		Step 29A	
	Test 1	Test 2	Test 1	Test 2	Test 1	Test 2	Test 1	Test 2
Mean	0.824	0.886	0.582	0.454	0.941	1.022	0.775	0.212
Standard deviation	0.195	0.242	1.517	1.506	0.126	0.455	1.144	1.146
Maximum	1.424	1.487	4.857	4.482	1.257	2.279	4.228	5.257
3 rd Quartile	0.956	1.029	1.513	1.325	1.028	1.279	1.488	0.840
Median	0.831	0.862	0.794	0.565	0.955	1.071	0.790	0.236
1 st Quartile	0.685	0.727	-0.216	-0.404	0.851	0.779	0.082	-0.368
0.15 Percentile	0.238	0.159	-3.968	-4.064	0.562	-0.343	-2.658	-3.227
Minimum	0.237	0.216	-8.664	-6.216	0.507	-0.710	-3.241	-4.733

**Figure 5.17: Pressure comparison of repeated test results at 30 m²/s.**

The statistical data in **Table 5.14**, together with the box and whisker plot, indicate an excellent level of accuracy for the pressures measured at Step 9A. Similar to the air concentration data, a larger variation in the data is measured at Step 29A as a result of the increased turbulence and velocity, which induce pressure fluctuations.

Since cavitation occurs at severe negative pressures, the accuracy of the minimum pressures results is extremely important. The results present a good level of agreement based on the minimum values and as the 0.15 percentile is used to denote the minimum pressures, the repeated tests are within an acceptable range, which are thereby deemed reliable.

5.7 Results

This section provides the air concentration and pressure results to establish the performance of the various aerator structures on the Type A spillway, as previously described in **Sections 5.3** and **5.5**. Along with the results, a few important visual observations were documented to enable a better understanding of the crest pier performance.

5.7.1 Visual Observations

5.7.1.1 Short Crest Piers

For the bullnose short pier, a dynamic occurrence was observed where the water flowing past the pier did not adhere to the pier sides. This was due to the impact of water on the blunt pier nose, which caused a sharp redirection of flow. The redirected flow formed a larger air void behind the pier, which allowed for a significant amount of air to be entrained. It should be noted that this was an unstable condition which only occurred after some time for the discharge of $30 \text{ m}^2/\text{s}$. **Figure 5.18** depicts the flow redirection and subsequent aeration at the bullnose short pier.

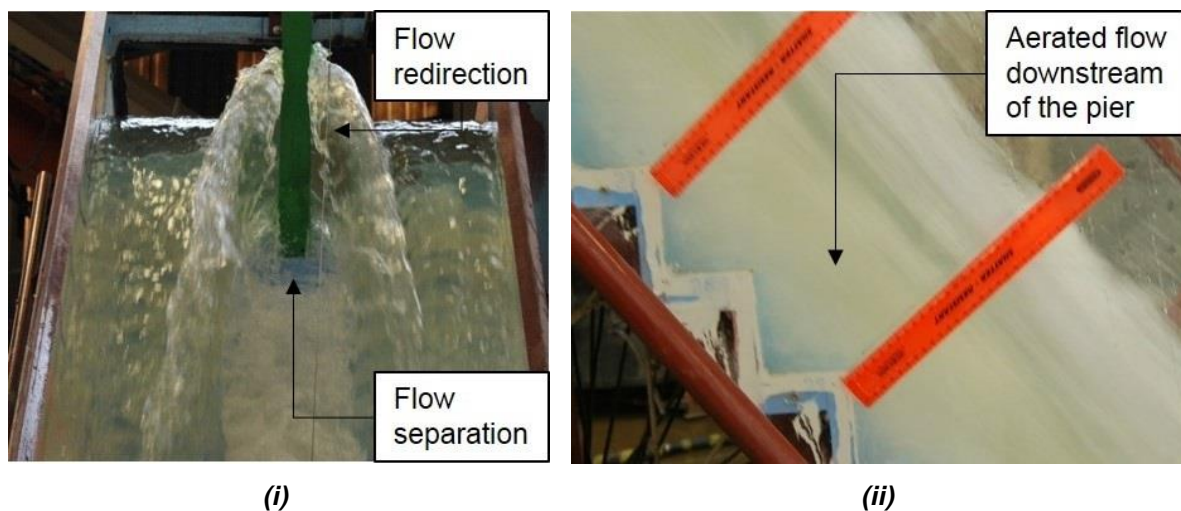


Figure 5.18: Photographs indicating (i) the redirection of flow and (ii) a significant amount of entrained air downstream of the bullnose pier.

The parabolic short pier illustrated a variation in performance where the water flowing past the pier adhered to the pier sides. This was caused by the sharper nose of the pier which gradually redirected the flow past the pier as indicated in **Figure 5.19 (i)**. The gradual redirection of flow resulted in a high flow velocity leading to jet flow, which created air pockets in the step niches (**Figure 5.19 (ii)**). A smaller, more distinct flow separation zone is present behind the parabolic short pier, as indicated in **Figure 5.19 (iii)**.

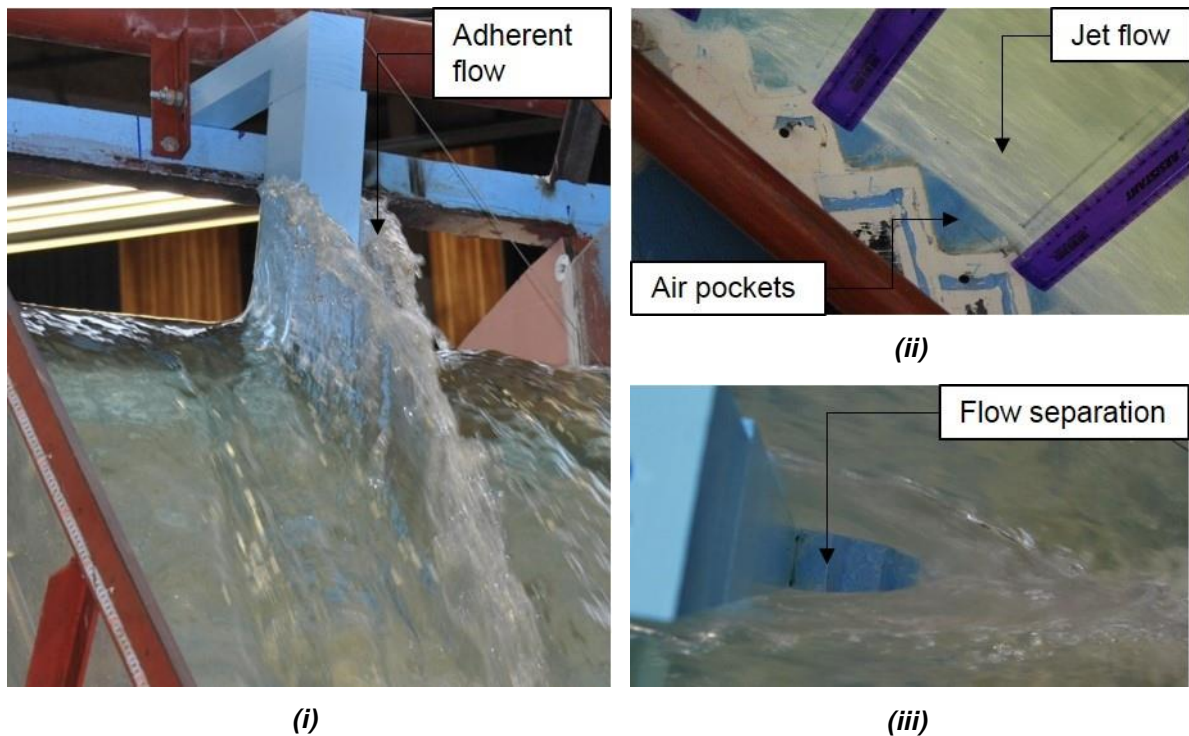


Figure 5.19: Photographs indicating (i) the adherent flow behaviour, (ii) the jet flow and air pockets and the (iii) flow separation behind the parabolic short pier.

5.7.1.2 Long Crest Piers

Adherent flow was observed for both the bullnose- and parabolic long piers. The bullnose long pier experienced an adherent flow compared to the sharp flow redirection which was experienced for the short pier length. The additional pier length thus removed the aeration on the pier side and subsequently an unaerated flow regime was experienced downstream of the crest pier, as indicated in **Figure 5.20**.

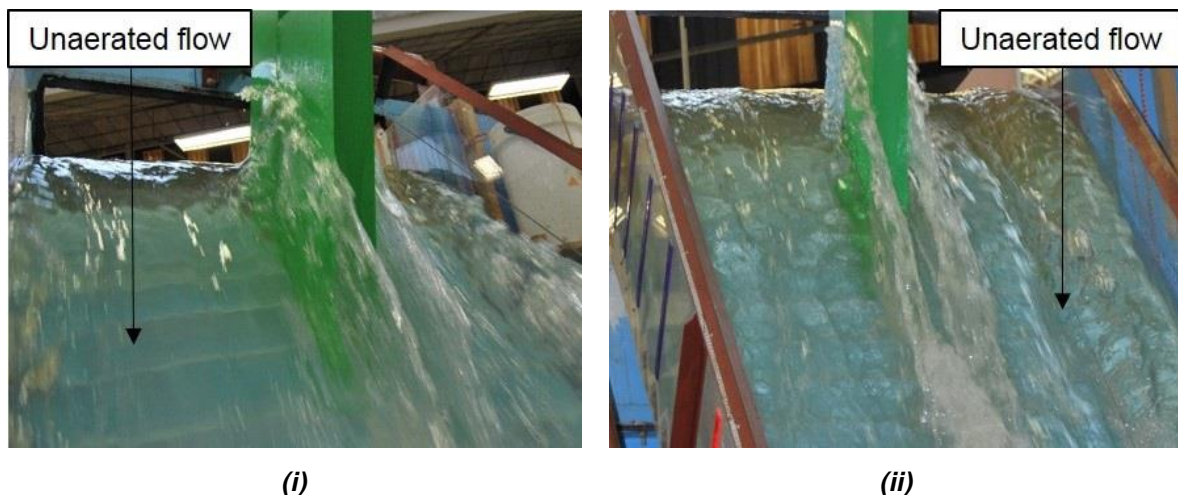


Figure 5.20: Photographs indicating the adherent flow to the pier sides for the (i) bullnose long pier and the (ii) parabolic long pier.

5.7.1.3 X-Shape FGP

The X-Shape FGP blocked and redirected a large portion of the flow, as illustrated in **Figure 5.21 (i)**. An important visual observation was made with respect to the flow pattern of the X-Shape FGP, which illustrated the ski-jump flow, generating an impact zone on the stepped spillway. See **Figure 5.21 (ii)** for a visual illustration of the impact zone. It is important to note that the impact region coincided with the cavitation regions as illustrated in **Section 5.8.3**. The aeration process commenced downstream of the FGP (**Figure 5.21 (iii)**) and gradually spread across the width of the spillway.

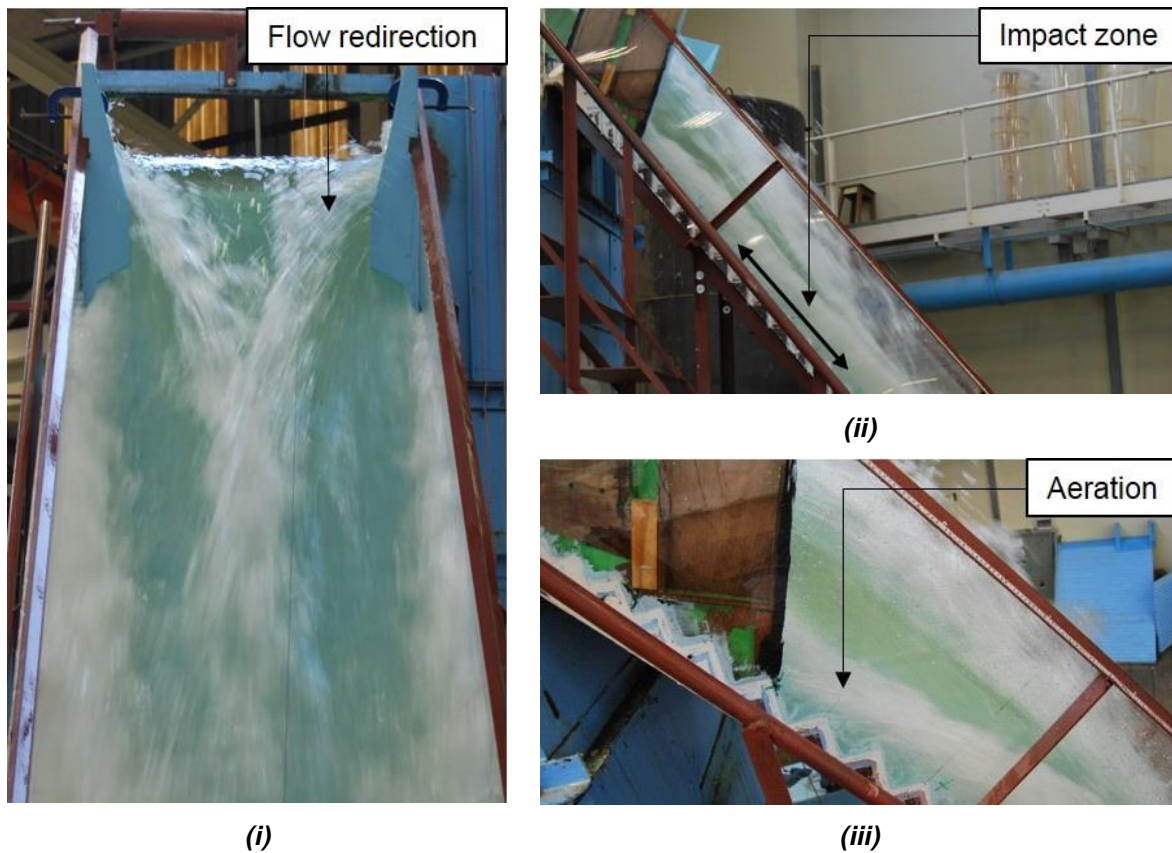


Figure 5.21: Photographs illustrating the (i) flow redirection, (ii) impact zone and (ii) aeration performance for the X-Shape FGP.

5.7.2 Air Concentration Results

The objective was to measure the air concentration at the pseudo-bottom along the length of the spillway and across the width of the spillway within the experimental area. Average air concentrations were used to represent the model's performance at each specific measuring location. The measuring locations were previously indicated in **Subsections 5.3.3** and **5.5.4**. It should be noted that the actual measuring locations represented only half of the spillway width. The results, however, were presented over the entire spillway width, based on the assumption that the air concentration was symmetrically distributed about the spillway centre line, because of the symmetry of the model setup.

Peterka (1953) stated that a local air concentration of 5 to 8% is sufficient to avoid cavitation damage. A conservative approach was followed in this study, by which the critical air concentration was determined to be 8%. Regions of insufficient aeration are indicated in red text in **Table 5.15** and **Table 5.16**.

5.7.2.1 Crest Piers

The air concentration results for the various crest pier models are tabulated in **Table 5.15**. The distance, L_p , indicates the streamwise position along the pseudo-bottom, while the X-axis represents the position along the width of the spillway (prototype scale in m). The position of the control experiment's inception point is located at the streamwise position where L_p is equal to 45.69 m. Experiments were conducted at a prototype unit discharge of 30 m²/s. The standard stepped spillway without a crest pier (model setup 1) acted as the control experiment.

Table 5.15: Air concentration results for the crest pier models at a unit discharge of 30 m²/s.

Air Concentration (%)							
L_p (m)	Model Setup 1 - No Pier						
	X = 1.88	X = 3.75	X = 5.63	X = 7.50	X = 9.38	X = 11.25	X = 13.13
41.85	10.21	10.04	7.26	7.42	7.26	10.04	10.21
45.69	18.74	31.66	34.78	28.96	34.78	31.66	18.74
49.53	10.97	13.45	10.62	9.08	10.62	13.45	10.97
53.37	26.79	28.98	22.52	19.55	22.52	28.98	26.79
L_p (m)	Model Setup 2 - Bullnose, Short Pier						
	X = 1.88	X = 3.75	X = 5.63	X = 7.50	X = 9.38	X = 11.25	X = 13.13
41.85	10.61	16.40	15.39	17.17	15.39	16.40	10.61
45.69	21.99	29.35	24.72	28.04	24.72	29.35	21.99
49.53	11.40	13.62	12.09	13.62	12.09	13.62	11.40
53.37	17.22	19.92	18.83	16.98	18.83	19.92	17.22
L_p (m)	Model Setup 3 - Bullnose, Long Pier						
	X = 1.88	X = 3.75	X = 5.63	X = 7.50	X = 9.38	X = 11.25	X = 13.13
41.85	8.14	11.30	8.07	7.45	8.07	11.30	8.14
45.69	21.00	38.56	32.89	31.62	32.89	38.56	21.00
49.53	13.93	21.88	20.15	11.46	20.15	21.88	13.93
53.37	18.53	20.42	17.04	17.56	17.04	20.42	18.53
L_p (m)	Model Setup 4 - Parabolic, Short Pier						
	X = 1.88	X = 3.75	X = 5.63	X = 7.50	X = 9.38	X = 11.25	X = 13.13
41.85	6.54	6.64	7.37	9.80	7.37	6.64	6.54
45.69	24.73	46.02	39.38	34.90	39.38	46.02	24.73
49.53	17.08	24.43	26.12	16.26	26.12	24.43	17.08
53.37	19.29	25.61	25.33	19.20	25.33	25.61	19.29
L_p (m)	Model Setup 5 - Parabolic, Long Pier						
	X = 1.88	X = 3.75	X = 5.63	X = 7.50	X = 9.38	X = 11.25	X = 13.13
41.85	7.18	9.53	6.80	5.53	6.80	9.53	7.18
45.69	32.96	45.89	36.99	33.65	36.99	45.89	32.96
49.53	20.53	24.77	21.31	14.49	21.31	24.77	20.53
53.37	31.06	39.01	29.30	25.16	29.30	39.01	31.06

Note: Regions of insufficient aeration is indicated with red text.

5.7.2.2 X-Shape FGP

The air concentration results for the bullnose- and parabolic X-Shape FGP are tabulated in **Table 5.16**. As mentioned in the X-Shape FGP experimental setup, the experimental area was enlarged relative to that of the crest piers in order to capture the impact zone of the deflected water. Another change was that of the air concentration measurement procedure, which included the addition of the anti-ventilation plate.

The results are displayed in a similar manner to the crest pier results where the streamwise distance is denoted by L_p and the width across the spillway by X , both in m. As previously mentioned, the control experiment's inception point is located at $L_p = 45.69$ m according to equations found in the literature.

Table 5.16: Air concentration results for the X-Shape FGP models at a unit discharge of 30 m²/s.

Air Concentration (%)							
L_p (m)	Model Setup 6 – Bullnose, X-Shape FGP						
	X = 1.88	X = 3.75	X = 5.63	X = 7.50	X = 9.38	X = 11.25	X = 13.13
11.11	0.02	0.00	0.00	0.08	0.00	0.00	0.02
18.80	0.13	0.01	0.00	0.03	0.00	0.01	0.13
26.48	0.34	0.03	0.02	0.01	0.02	0.03	0.34
34.16	2.57	0.71	0.04	0.00	0.04	0.71	2.57
38.01	2.89	0.82	0.10	0.05	0.10	0.82	2.89
41.85	5.00	4.31	0.36	0.18	0.36	4.31	5.00
45.69	7.30	7.74	1.61	0.69	1.61	7.74	7.30
49.53	7.55	9.04	3.46	1.80	3.46	9.04	7.55
53.37	8.31	11.91	6.67	4.43	6.67	11.91	8.31
59.14	10.06	15.34	14.81	14.54	14.81	15.34	10.06
L_p (m)	Model Setup 7- Parabolic, X-Shape FGP						
	X = 1.88	X = 3.75	X = 5.63	X = 7.50	X = 9.38	X = 11.25	X = 13.13
11.11	0.08	0.00	0.00	0.06	0.00	0.00	0.08
18.80	0.13	0.02	0.02	0.05	0.02	0.02	0.13
26.48	0.38	0.08	0.51	0.01	0.51	0.08	0.38
34.16	6.71	2.37	0.67	0.05	0.67	2.37	6.71
38.01	2.96	2.25	0.25	0.04	0.25	2.25	2.96
41.85	5.17	5.29	1.10	0.32	1.10	5.29	5.17
45.69	8.05	9.31	3.87	0.97	3.87	9.31	8.05
49.53	10.17	13.39	8.42	2.76	8.42	13.39	10.17
53.37	9.92	15.91	9.76	4.27	9.76	15.91	9.92
59.14	17.34	23.59	24.58	19.21	24.58	23.59	17.34

Note: Regions of insufficient aeration is indicated with red text.

5.7.3 Pressure Results

The pressure measurements were recorded to establish the cavitation regions on the stepped spillway for the various model setups. At each measuring position, pressures were recorded at a location of 0.9 times the step riser height ($0.9h$). Similar to the air concentration results, the pressure results were mirrored to obtain an impression of the pressure distribution across the entire spillway width.

The pressure boundary for which cavitation inception would occur is based on a prototype pressure head of -7 m atmospheric, as advised by Chadwick, *et al.* (2013). This cavitation boundary was transformed to a dimensionless pressure parameter of -4.67, based on the prototype step height of 1.5 m. The cavitation regions are indicated in red text in **Table 5.17** and **Table 5.18**. It should be noted that the pressure readings and results are relative to atmospheric pressure.

5.7.3.1 Crest Piers

The minimum pressure results for the various crest pier models are tabulated in **Table 5.17**. As previously, the streamwise distance, L_p , indicates the position along the length of the spillway, while the X-axis indicates the position across the width of the spillway (prototype scale in m). The experiments were conducted at a prototype unit discharge of $30 \text{ m}^2/\text{s}$.

Table 5.17: Minimum pressure results for the pier model setups at a unit discharge of 30 m²/s.

Pressure (p/y/h)							
L_p (m)	Model Setup 1 - No Pier						
	X = 1.88	X = 3.75	X = 5.63	X = 7.50	X = 9.38	X = 11.25	X = 13.13
41.85	-3.508	-2.865	-5.166	-5.189	-5.166	-2.865	-3.508
45.69	-3.764	-3.057	-4.532	-5.382	-4.532	-3.057	-3.764
49.53	-3.758	-3.920	-3.981	-4.399	-3.981	-3.920	-3.758
53.37	-3.538	-4.673	-4.187	-4.459	-4.187	-4.673	-3.538
L_p (m)	Model Setup 2 - Bullnose, Short Pier						
	X = 1.88	X = 3.75	X = 5.63	X = 7.50	X = 9.38	X = 11.25	X = 13.13
41.85	-4.466	-4.750	-2.744	-2.372	-2.744	-4.750	-4.466
45.69	-4.216	-2.920	-2.099	-2.605	-2.099	-2.920	-4.216
49.53	-4.498	-2.773	-1.229	-1.375	-1.229	-2.773	-4.498
53.37	-6.029	-3.402	-2.016	-1.994	-2.016	-3.402	-6.029
L_p (m)	Model Setup 3 - Bullnose, Long Pier						
	X = 1.88	X = 3.75	X = 5.63	X = 7.50	X = 9.38	X = 11.25	X = 13.13
41.85	-3.512	-5.010	-4.510	-4.519	-4.510	-5.010	-3.512
45.69	-3.791	-2.896	-3.344	-4.742	-3.344	-2.896	-3.791
49.53	-3.363	-4.119	-2.672	-2.886	-2.672	-4.119	-3.363
53.37	-3.416	-3.564	-3.510	-3.072	-3.510	-3.564	-3.416
L_p (m)	Model Setup 4 - Parabolic, Short Pier						
	X = 1.88	X = 3.75	X = 5.63	X = 7.50	X = 9.38	X = 11.25	X = 13.13
41.85	-4.547	-4.959	-3.373	-3.273	-3.373	-4.959	-4.547
45.69	-4.240	-2.930	-4.697	-3.140	-4.697	-2.930	-4.240
49.53	-4.329	-4.963	-2.113	-2.144	-2.113	-4.963	-4.329
53.37	-4.147	-3.413	-3.461	-2.770	-3.461	-3.413	-4.147
L_p (m)	Model Setup 5 - Parabolic, Long Pier						
	X = 1.88	X = 3.75	X = 5.63	X = 7.50	X = 9.38	X = 11.25	X = 13.13
41.85	-4.691	-5.095	-3.030	-4.325	-3.030	-5.095	-4.691
45.69	-4.343	-3.363	-4.433	-4.586	-4.433	-3.363	-4.343
49.53	-3.772	-3.846	-1.931	-2.859	-1.931	-3.846	-3.772
53.37	-4.747	-3.223	-3.162	-2.735	-3.162	-3.223	-4.747

Note: Regions of cavitation pressure is indicated with red text.

5.7.3.2 X-Shape FGP

The pressure results (**Table 5.18**) were measured in a similar manner to those in the crest pier investigation. The only alteration relative to the crest pier investigation was the enlargement of the experimental area. The pressures were measured at the measuring locations, with the sensor being installed at a position 0.9 times the step riser height (0.9 h).

Table 5.18: Minimum pressure results for the X-Shape FGP models at a unit discharge of 30 m²/s.

Pressure (p/y/h)							
L_p (m)	Model Setup 6 – Bullnose, X-Shape FGP						
	X = 1.88	X = 3.75	X = 5.63	X = 7.50	X = 9.38	X = 11.25	X = 13.13
11.11	-1.645	-0.893	-0.846	0.238	-0.846	-0.893	-1.645
18.80	-1.027	-2.180	-1.978	-3.075	-1.978	-2.180	-1.027
26.48	-2.792	-5.107	-3.816	-4.076	-3.816	-5.107	-2.792
34.16	-1.845	-3.447	-4.552	-2.977	-4.552	-3.447	-1.845
38.01	-3.586	-3.838	-3.519	-0.186	-3.519	-3.838	-3.586
41.85	-2.630	-3.412	-5.346	-3.108	-5.346	-3.412	-2.630
45.69	-2.050	-3.355	-1.070	-4.410	-1.070	-3.355	-2.050
49.53	-2.278	-1.718	-4.879	-3.968	-4.879	-1.718	-2.278
53.37	-2.773	-2.273	-5.164	-1.194	-5.164	-2.273	-2.773
59.14	-4.571	-2.023	-2.928	-4.173	-2.928	-2.023	-4.571
L_p (m)	Model Setup 7 – Parabolic, X-Shape FGP						
	X = 1.88	X = 3.75	X = 5.63	X = 7.50	X = 9.38	X = 11.25	X = 13.13
11.11	-1.401	-0.808	-0.440	0.562	-0.440	-0.808	-1.401
18.80	-1.353	-2.057	-2.139	-1.851	-2.139	-2.057	-1.353
26.48	-2.066	-4.166	-3.617	-3.641	-3.617	-4.166	-2.066
34.16	-2.426	-3.150	-5.105	-1.988	-5.105	-3.150	-2.426
38.01	-2.901	-3.259	-3.060	-3.812	-3.060	-3.259	-2.901
41.85	-2.864	-3.243	-3.487	-2.570	-3.487	-3.243	-2.864
45.69	-3.167	-2.557	-2.032	-3.199	-2.032	-2.557	-3.167
49.53	-1.949	-2.255	-3.062	-2.658	-3.062	-2.255	-1.949
53.37	-1.944	-1.959	-4.700	-1.262	-4.700	-1.959	-1.944
59.14	-3.278	-1.510	-1.642	-4.957	-1.642	-1.510	-3.278

Note: Regions of cavitation pressure is indicated with red text.

5.8 Analysis of the Test Results on the Type A Stepped Spillway

Analysis of the results presented in **Section 5.7** was conducted to evaluate the potential of cavitation damage occurring on the stepped spillway. The setups for the various models were evaluated with the aid of contour plots at a prototype unit discharge of 30 m²/s. The analysis is based on the air concentration and pressure results.

5.8.1 Cavitation Limits

The cavitation analysis comprised a visual presentation of the air concentration and pressure results for each of the different model setups. Peterka (1953) stated that a local air concentration of 5 to 8% is sufficient to avoid cavitation damage, due to the compressibility of the induced air, which absorbs the shock generated by the imploding vapour bubbles. A conservative approach was followed, by which the critical air concentration boundary was defined as 8%.

The cavitation pressure limit was defined as a -7 m atmospheric pressure head, which coincides with the water's vapour pressure at a temperature of 20 °C. The cavitation limit was transformed to a dimensionless pressure parameter ($p/\gamma/h$) to ease the interpretation of the results for either the model or prototype scale. This resulted in a dimensionless pressure limit of -4.67.

The air concentration and pressure results are presented as contour plots in the following subsections. It should be noted that these contour plots implement a distinct colour scale which highlights the critical areas. The colour scale for the air concentration and pressure contour plots are indicated by the colour legend with the boundary between yellow and green representing the following values:

- -7 m water pressure (-4.67 dimensionless pressure parameter) for the pressure contour plots;
- 8% air concentration for the air concentration contour plots.

Note that each contour plot has a distinct colour scale which illustrates the performance of the specific pier configuration.

5.8.2 Crest Pier Evaluation

5.8.2.1 Control Experiment (Model Setup 1)

A standard stepped spillway without crest piers, as described in **Subsection 5.3.1**, served as the control model with which the performances of the other pier designs were compared. As the addition of crest piers on stepped spillways were not considered a standard design, the stepped spillway without piers, represented the baseline performance. The air concentration and pressure results for the standard stepped spillway are displayed in **Figure 5.22**. The contour plots display the results on the spillway area where the streamwise distance, L_p , indicates the distance along the spillway length whilst the distance across the spillway width is indicated by the X-axis. The critical boundaries for the air concentration and pressure results are indicated with the dashed contour lines. The flow direction is indicated with the small arrow at the upstream section of the experimental area.

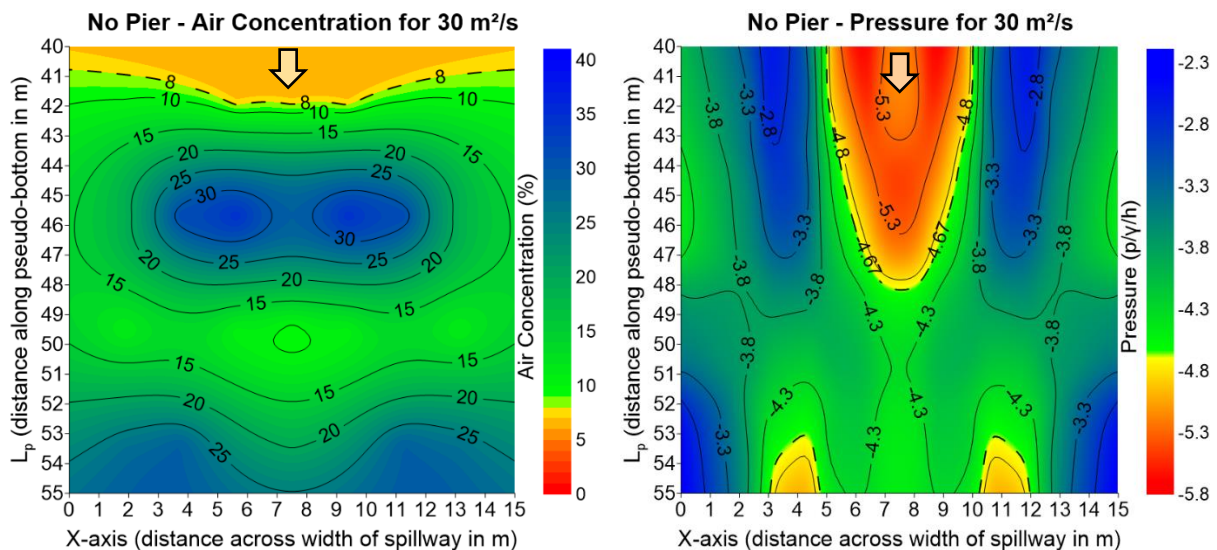


Figure 5.22: Air concentration and pressure results for the no pier model.

The air concentration results indicated a small region of insufficient aeration upstream of the inception point ($L_p = 45.7$ m). Despite this small region, the air concentration was measured as sufficient on the remainder of the experimental area. The pressure results revealed a cavitation region in the centre of the spillway which extended downstream past the inception point. Since the small region, near $L_p = 42$ m, is of insufficient aeration and cavitation pressures are coincidental, cavitation damage would occur as a result of the lack of entrained air. A standard stepped spillway, without crest piers, operating at a unit discharge of $30 \text{ m}^2/\text{s}$ has a risk of cavitation damage in a limited area upstream of the inception point.

5.8.2.2 Analysis of Pier Nose Design

This section investigated the modification of the pier nose design which consisted of a bullnose- and parabolic pier nose as illustrated in **Figure 5.4**. The performance of the two pier models are illustrated in **Figure 5.23**. The vertical dashed line in the contour plot indicate the upstream pier position with the dashed contour line indicating the cavitation boundaries.

The air concentration results indicated an earlier onset of air entrainment for the bullnose, short pier as compared to the control experiment. In contrast, the parabolic short pier illustrated a similar performance to the control experiment, with a small region of insufficient aeration upstream of the inception point. The pressure contour plots indicated cavitation pressures for both pier designs. The bullnose short pier showed small cavitation zones on the upstream and downstream sections of the experimental area. The parabolic short pier results displayed multiple cavitation regions, distributed throughout the experimental area. Individual pier comparisons indicated that the bullnose short pier induced enough aeration within the critical regions to eliminate the risk of cavitation, while the parabolic short pier was susceptible to cavitation damage at the upstream section (between $L_p = 40$ m and $L_p = 42$ m) of the experimental area. In conclusion, the bullnose short pier performed the best.

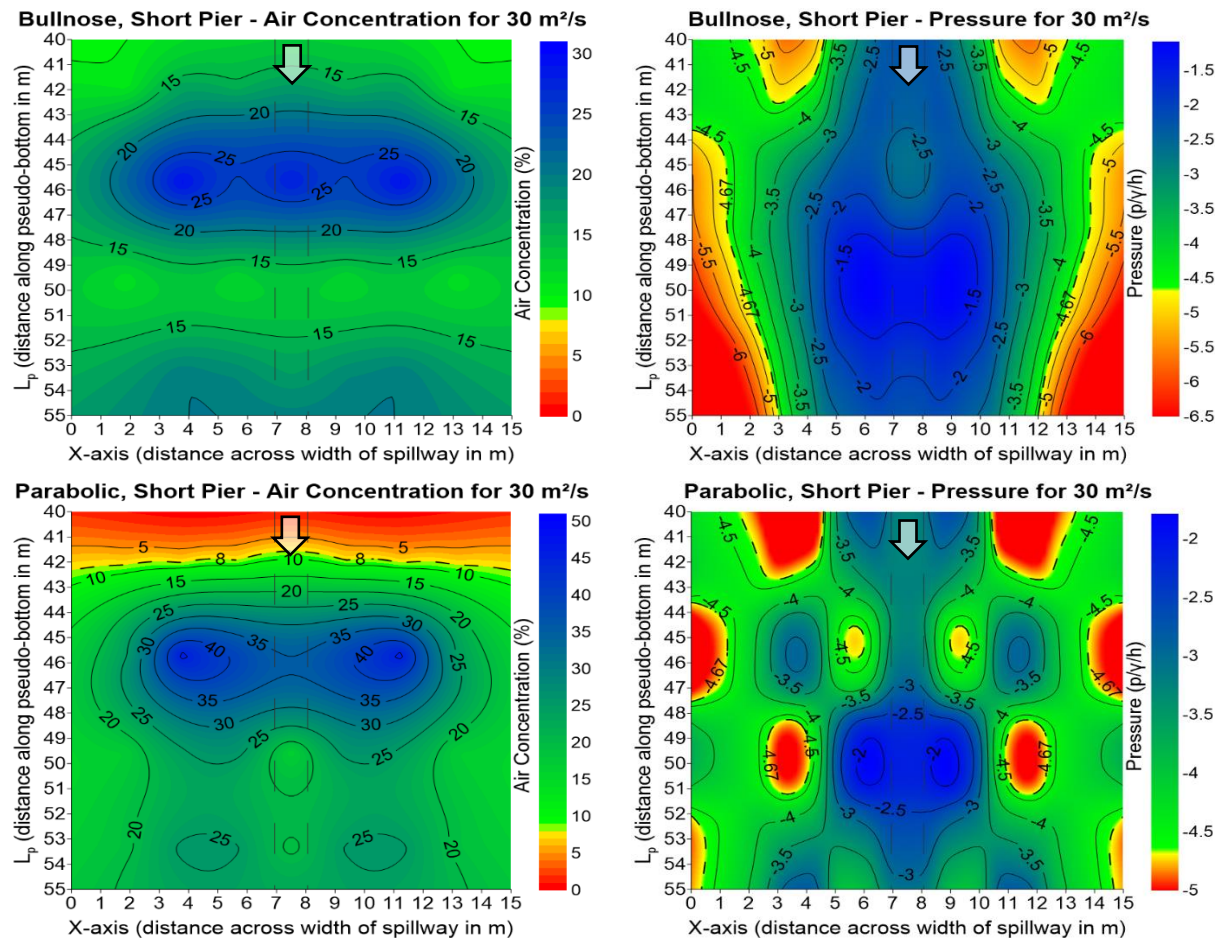


Figure 5.23: Air concentration and pressure results for the bullnose and parabolic short piers.

5.8.2.3 Analyses of Pier Length Design

The experimental pier modifications included the alteration in pier length. The investigation evaluated two pier lengths, as shown in **Figure 5.5**. The first was a short pier which corresponded to a pier length of 2.84 m. The second was a long pier, extending past the point of tangency, which corresponded to a pier length of 6.38 m. The results for both pier lengths are given in and **Figure 5.24** (the projected location of the pier is shown in these figures by two vertical dashed lines defining the width of the pier).

The air concentration results indicated a similar air concentration distribution for both pier lengths; however, a small region of insufficient aeration was present for the long pier. The air concentration distribution for the bullnose long pier was very similar to the control experiment, which confirmed that it did not improve the entrainment of air. The pressure contour plot displayed both upstream and downstream cavitation regions for the bullnose short pier. The long pier exhibited zones of cavitation upstream of the inception point. Individual comparisons indicated that the short pier would eliminate the risk of cavitation, while, the long pier would most probably experience cavitation damage on the spillway. Therefore, only the short pier provided sufficient performance to eliminate the risk of cavitation damage.

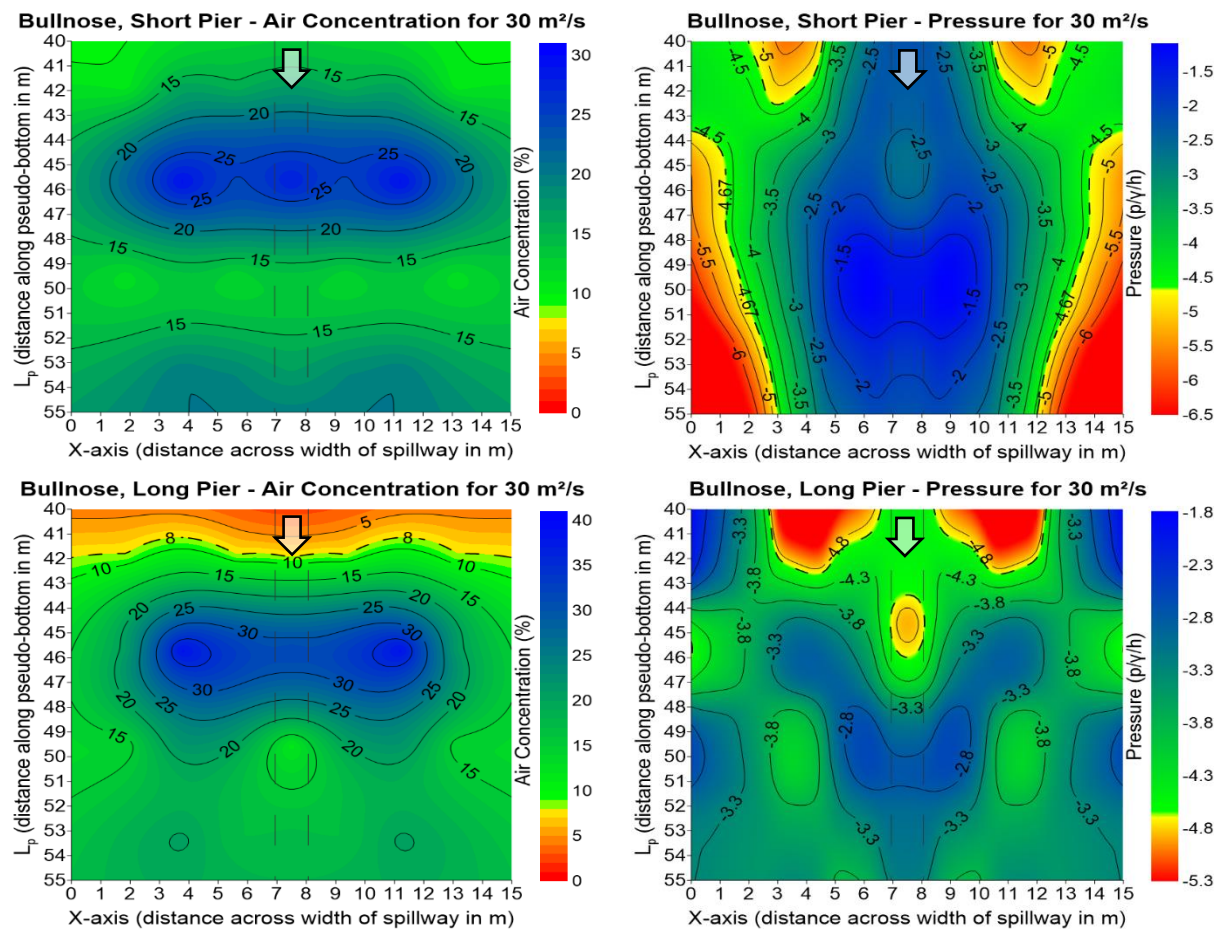


Figure 5.24: Air concentration and pressure results for the bullnose, short and long pier.

5.8.3 X-Shape FGP Evaluation

The performance of the X-Shape FGP, together with the alteration of the pier nose design, was evaluated as indicated in **Figure 5.25** and **Figure 5.26**. The experimental area consisted of the entire spillway length, and the dashed horizontal lines on the figures indicate the position of the outside edge of the flare on either side of the spillway crest. The cavitation boundaries are illustrated by the dotted contours, for both the air concentration and pressure contour plots.

The air concentration contour plots for both the bullnose- and parabolic X-Shape FGP, illustrated similar performances, with large areas of insufficient aeration. The air concentration exceeded the 8% limit only in small sections downstream of the control experiment inception point ($L_p = 46$ m). The pressure results indicated cavitation regions upstream and downstream of the inception point for both the bullnose and parabolic FGP. The downstream cavitation regions ($L_p = 48$ m and $L_p = 55$ m) for both models, occurred in areas of sufficient aeration, which prevented cavitation damage in the area. However, the upstream cavitation regions ($L_p = 24$ m and $L_p = 55$ m) coincided with the impact region of the water that was deflected from the flares. A shearing action was generated by the impact on the steps, resulting in severe negative pressures. Air was detrained within this area, as explained in **Section 2.4.4**. Neither the bullnose nor the parabolic X-Shape FGP safely passed a unit discharge of $30 \text{ m}^2/\text{s}$.

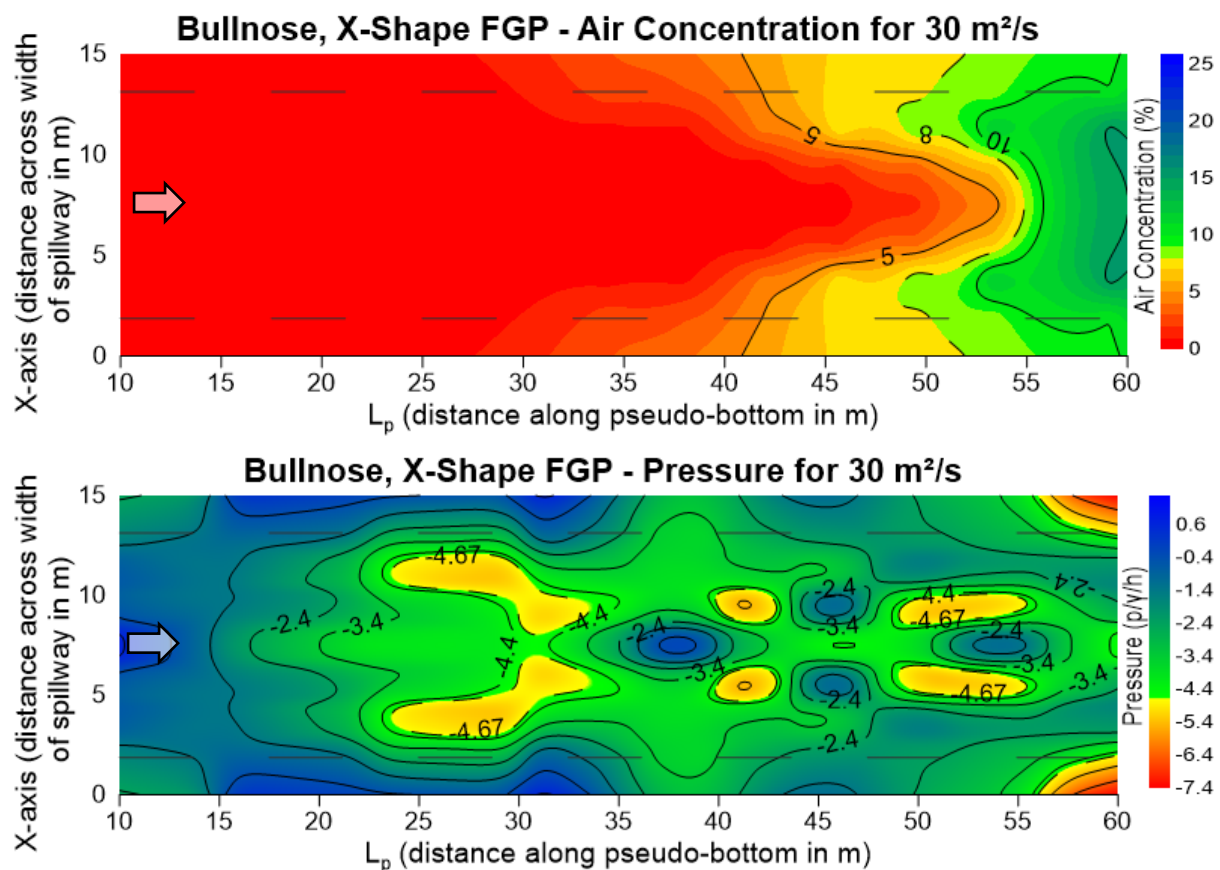


Figure 5.25: Air concentration and pressure results for the bullnose, X-Shape FGP.

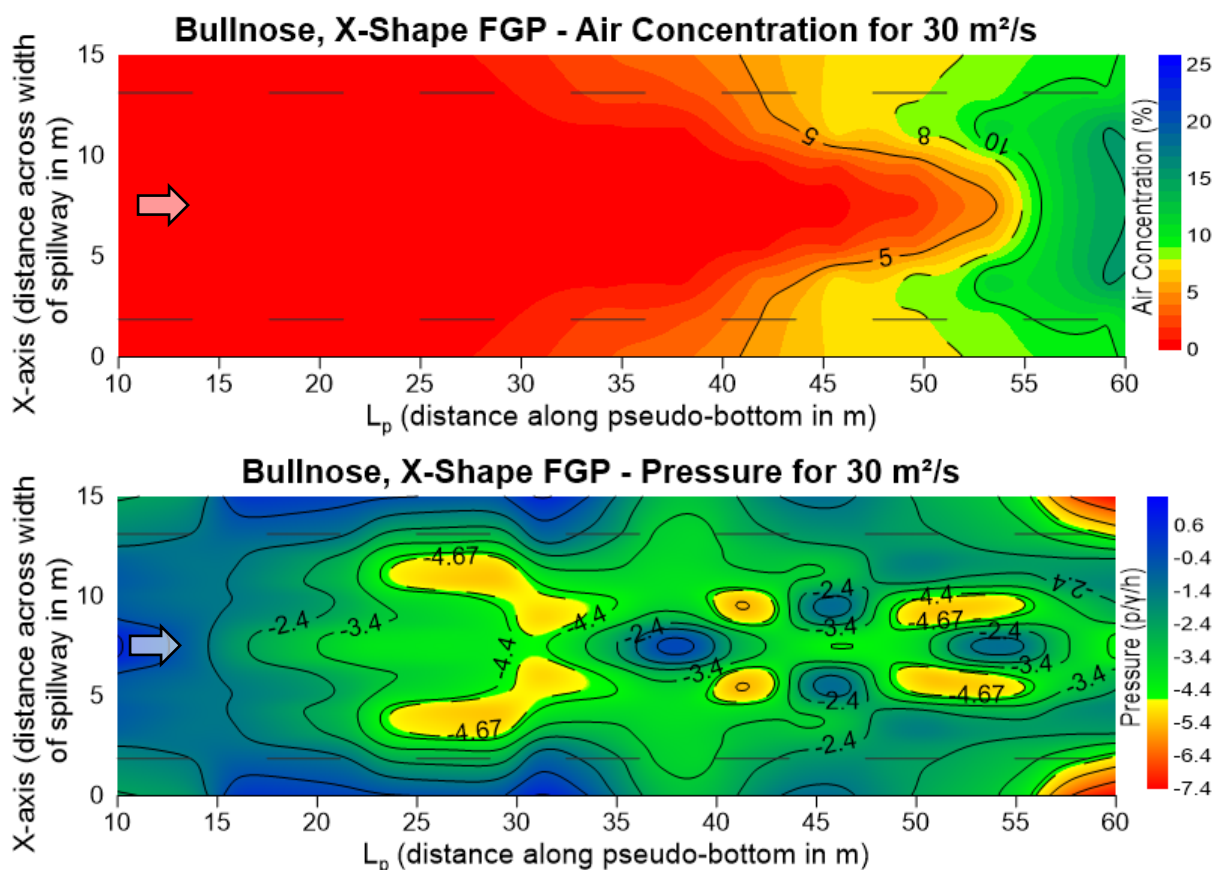


Figure 5.26: Air concentration and pressure results for the parabolic, X-Shape FGP.

5.9 Summary of the Type A Stepped Spillway Experiments

Through analysis of the experimental results, the bullnose short pier was identified as the best performing of the types of piers tested in terms of air concentration and it should be able to operate at a unit discharge of $30 \text{ m}^2/\text{s}$ without any risk of damage from cavitation. This finding supports the similar conclusion of Calitz (2015). This was the only pier model to introduce an earlier onset of entrained air than the control experiment. It should also be mentioned that the pressure results indicated that the introduction of crest piers relieved the negative pressures, relative to those experienced in the control experiment, but did not remove them.

The addition of the adapted, X-Shape FGP did not improve the performance of the stepped spillway but it enhanced the understanding of the recorded pressures and air concentrations in the region where the water (which is deflected by the flares in a “ski-jump” manner) impacts on the spillway. The measurements indicated a de-aeration and lower negative pressures in the impact zones. The performance of the FGP design is, therefore, subject to the location of the impact zone. To prevent the undesirable pressure and air concentration in the impact zone, this zone should be located in a downstream stilling basin to dissipate the impact energy.

6 Type B Stepped Spillway: Evaluation of X- and Y-Shape FGPs

This chapter describes the 1:50 scale, Type B stepped spillway model, which was constructed to investigate the FGP performance for prototype unit discharges up to 200 m²/s. Similar small-scale experiments had not previously been conducted because of the scale effects in the aeration process. Literature had mentioned significant scale effects in terms of the size and number of entrained bubbles (Chanson, 2008). However, recent investigations by Chanson (2007, 2008), Felder (2017) and Heller (2017), as mentioned in **Section 2.8.4**, had observed a self-similar relationship when measuring air concentration. This meant that air concentration results could accurately be measured and scaled to prototype, irrespective of the model scale.

The Type B spillway model was constructed to obtain greater unit discharges than those of the Type A model which was discussed in **Chapter 5**. The statistical and sensitivity analyses were unchanged, as described in **Chapter 4**.

6.1 Type B Stepped Spillway Design

The Type B stepped spillway model was based on the Dachaoshan Dam (**Figure 6.1**) which is located in Yunnan Province, China. The Dachaoshan Dam was constructed as a RCC gravity dam with a height of 111 m. The dam became operational in 2002 and has since experienced a large flood which resulted in a maximum unit discharge of 93 m²/s. The dam discharges through five discharge bays which implement Y-Shape FGPs together with a slit-type flip bucket and three bottom outlets. See **Figure 6.2** for the schematic illustration of the model; the as-built drawings can also be viewed in **Appendix B**.

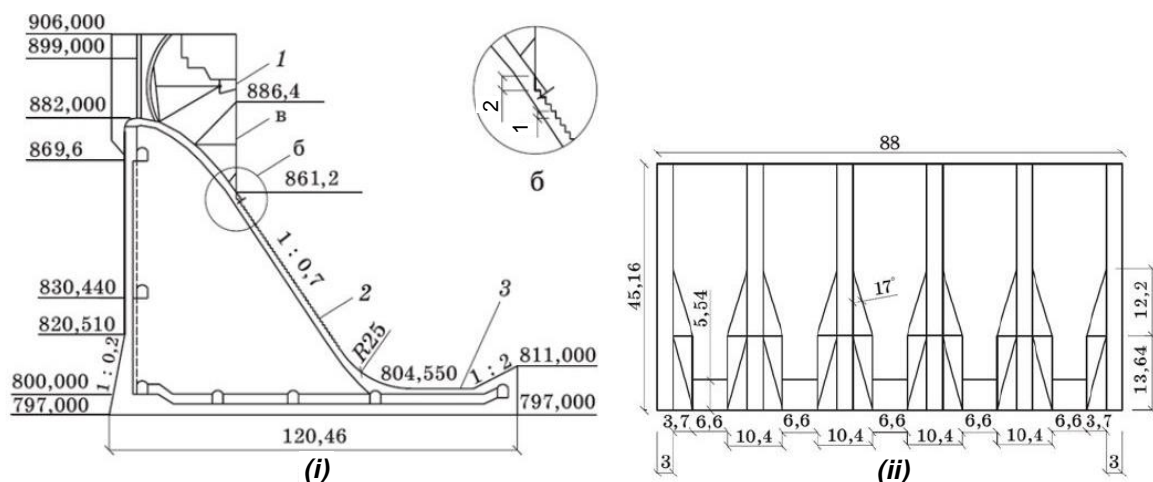


Figure 6.1: Schematic design of the Dachaoshan dam indicating a (i) typical cross-section and (ii) back view (Nan and Rumyantsev, 2014).

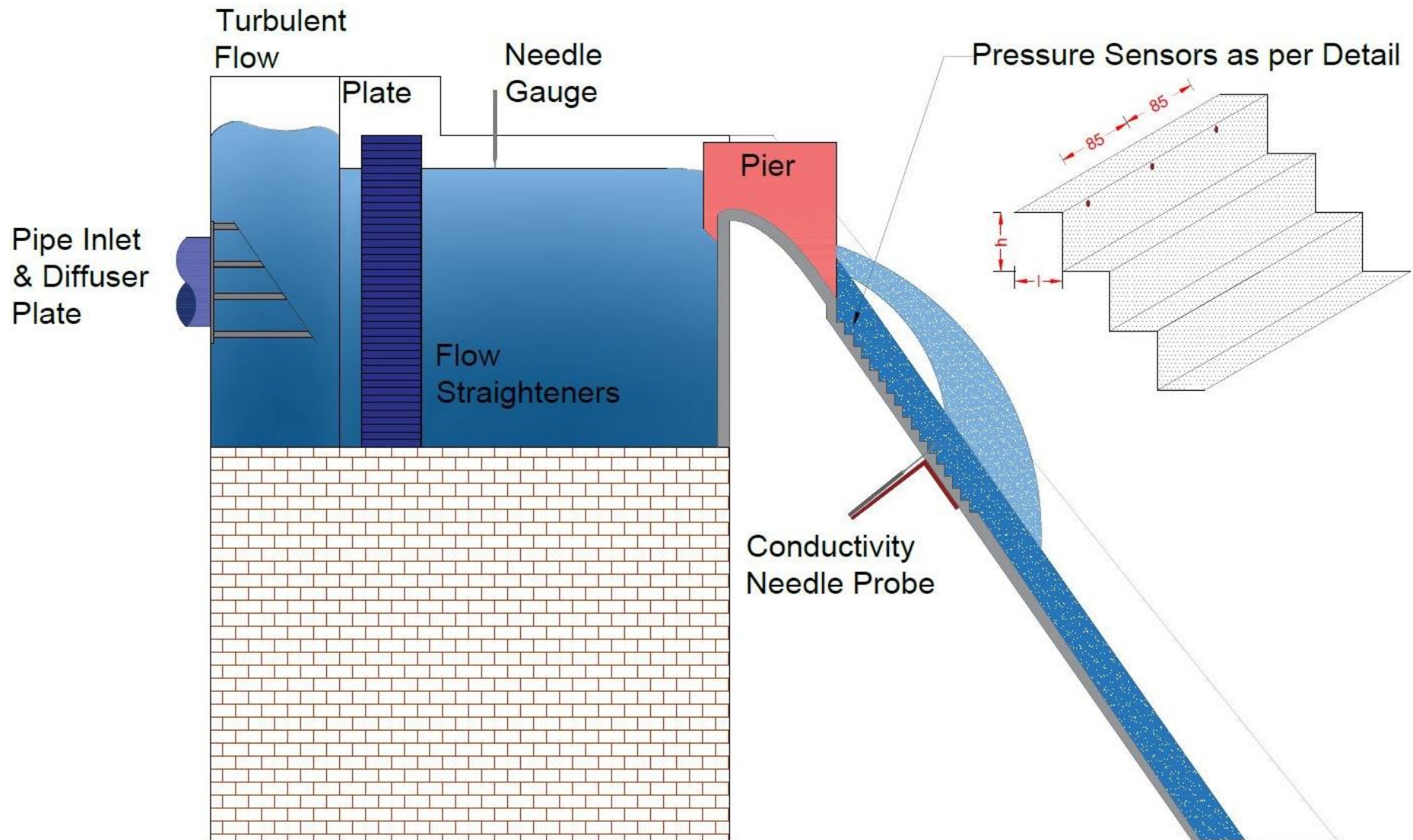


Figure 6.2: Schematic illustration of the 1:50 model setup (Not according to scale).

6.1.1 Crest Design

The Dachaoshan Dam is designed as a controlled spillway which implements five radial gates. The controlled crest was implemented here for the additional storage capacity and an increased water level, providing the required head for hydropower generation. In fact, the uncontrolled crest is considered as the design standard because of its reduced maintenance requirements and greater ability to pass large debris.

The hydraulic model, however, was designed as an uncontrolled crest. The crest design was based on a WES (1959) profile, with a vertical upstream face and four crest piers.

6.1.1.1 Discharge Characteristics

The overflow spillway discharge of the WES (1959) shape is identical to the discharge equation for the USBR (1987) ogee spillway, as described in **Subsection 5.1.1.1**. The discharge over the WES crest is calculated by using **Equation 6-1**. For spillways which implement a high, vertical upstream face ($\frac{P_d}{H_d} > 1.33$), such as the Dachaoshan Dam, the approach velocity has a negligible effect on the discharge and, consequently, on the nappe profile. The spillway crest design is summarised in **Table 6.1**.

$$Q = C_e L H_e^{1.5} \quad \text{6-1}$$

where:

Q	=	Discharge
C_e	=	Variable discharge coefficient
L	=	Effective length of crest
H_e	=	Actual head on the crest, including approach velocity head

Table 6.1: Design summary of the WES (1959) profile.

Description (Refer to Figure 5.2)	Unit	Model (1:50)	Prototype
P_d (Vertical upstream height of crest)	m	1.6	80
Design q	m ² /s	0.392	165
Maximum q	m ² /s	0.594	250
Effective crest length	m	0.84	42 (3 bays)
H_d	m	0.358	17.9
H_e (250 m ² /s)	m	0.462	23.1
H_e/H_d	m/m	1.333	1.333
C_d		2.175	2.175
C_e		2.253	2.253
C_e/C_d		1.036	1.036
P/H_d	m/m	4.47	4.47

6.1.1.2 WES Profile (1959)

The primary objective of the WES profile was to avoid negative pressures on the crest; other factors such as maximising the hydraulic efficiency, the practicality, stability and economy also played a part. The shape of the profile was affected by the design head and the inclination angle of the upstream face. The design guidelines of the WES profile are seen in **Figure 6.3**.

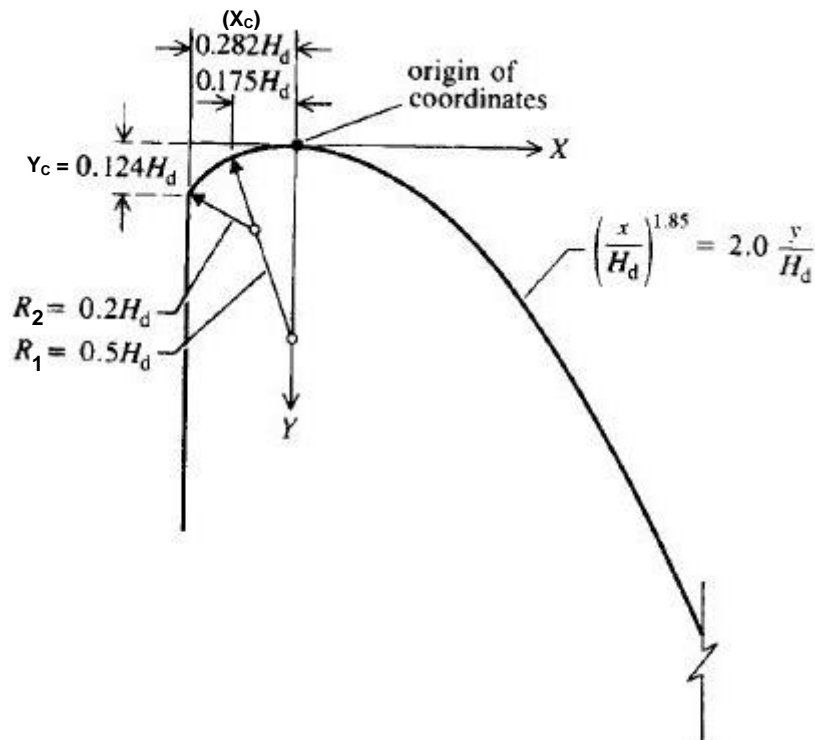


Figure 6.3: Standard WES spillway crest (US Army Waterways Experimental Station, 1959).

Similar to the USBR (1987) ogee crest profile, the WES (1959) profile defined the upstream section with a compound circular curve while the downstream section is described by **Equation 6-2**. With the use of **Equation 6-2**, together with the parameters as prescribed in **Table 6.2**, the WES ogee profile was designed.

$$X^n = K H_d^{n-1} Y \quad 6-2$$

where:

- Y, X = Coordinates as defined in **Figure 5.2**
 K, n = Constants as defined by WES (1959)

Table 6.2: Design of WES (1959) crest profile.

Description (Refer to Figure 6.3)	Unit	Model (1:50)	Prototype
H_d	m	0.358	17.900
h_a/H_d	m/m	0.036	0.036
K		2	2
n		1.850	1.850
R_1 (as defined in Figure 6.3)	m	0.179	8.950
R_2 (as defined in Figure 6.3)	m	0.072	3.600
X_c (as defined in Figure 6.3)	m	0.101	5.050
Y_c (as defined in Figure 6.3)	m	0.044	2.200
End of WES profile (X-coordinate)	m	0.699	34.950
End of WES profile (Y-coordinate)	m	0.606	30.300

6.1.2 The Rear Slope

The rear slope of the Dachaoshan Dam was designed as a stepped spillway, which was constructed from RCC. The slope of the spillway is normally defined by the required structural stability. The Dachaoshan Dam was constructed with a constant slope of 55° , resulting in a constant step height of 1 m and a step tread of 0.7 m. These step dimensions do not conform to the standard RCC horizontal layer works, which are constructed in layers of 0.3 m increments. In the model, the step dimensions related to a step height of 20 mm and a step tread of 14 mm.

The Dachaoshan Dam implemented a special measure in the design where the first step is twice as high as the constant steps, as shown in **Figure 6.1**. The higher first step was included so that the flow would project over several steps, thus forming a large air cavity underneath the jet. The higher step led to increased air being entrained at the pseudo-bottom. A prototype analysis indicated pulsating pressures as high as 10 KPa and air concentrations exceeding 30%, which is considerably higher than those on a standard stepped spillway. The analysis thus concluded that the high step is an important design criterion for the mitigation of cavitation on stepped spillways (Guo, 2012). The first step has a step height of 2 m and a step tread of 0.78 m, which is represented by a 40 mm step height and 16 mm step tread in the model.

6.1.3 The Toe

The toe of the Dachaoshan Dam was designed with a roll bucket downstream of the spillway. This roll bucket typically functions under submerged conditions with the purpose of energy dissipation. The toe design of the spillway is beyond the scope of this thesis and was therefore not included in this study.

6.2 Crest Pier and Flaring Gate Pier Designs

6.2.1 Crest Pier Design

The crest piers on the Dachaoshan Dam have two main functions, the first is to support the radial gates, since the dam is designed with a controlled crest. The second function is to support the FGPs, which are constructed downstream of the crest apex, just upstream of the stepped spillway. This dam consists of six crest piers, each 45 m in length, which form five discharge bays over the crest. The pier design and spacing was based on the hydraulic design guidelines of the US Army WES (1959). The recommendations of these guidelines advise the use of a bullnose pier for high head dams. The dam was thus designed with Type 2B piers which extend 10 m upstream of the crest apex. The upstream extension would decrease the pier contraction coefficient which resulted in a smooth transition, with increased efficiency.

The guidelines, as indicated in **Figure 6.4 (i)**, advise a recommended pier spacing of $1.078H_d$ and a recommended pier thickness of $0.205H_d$. In prototype, the piers were designed with a pier spacing of 17 m centre to centre, and a pier thickness of 3 m, which is less than the recommended values. The model was constructed to consist of 3 bays as indicated in **Figure 6.4 (ii)**.

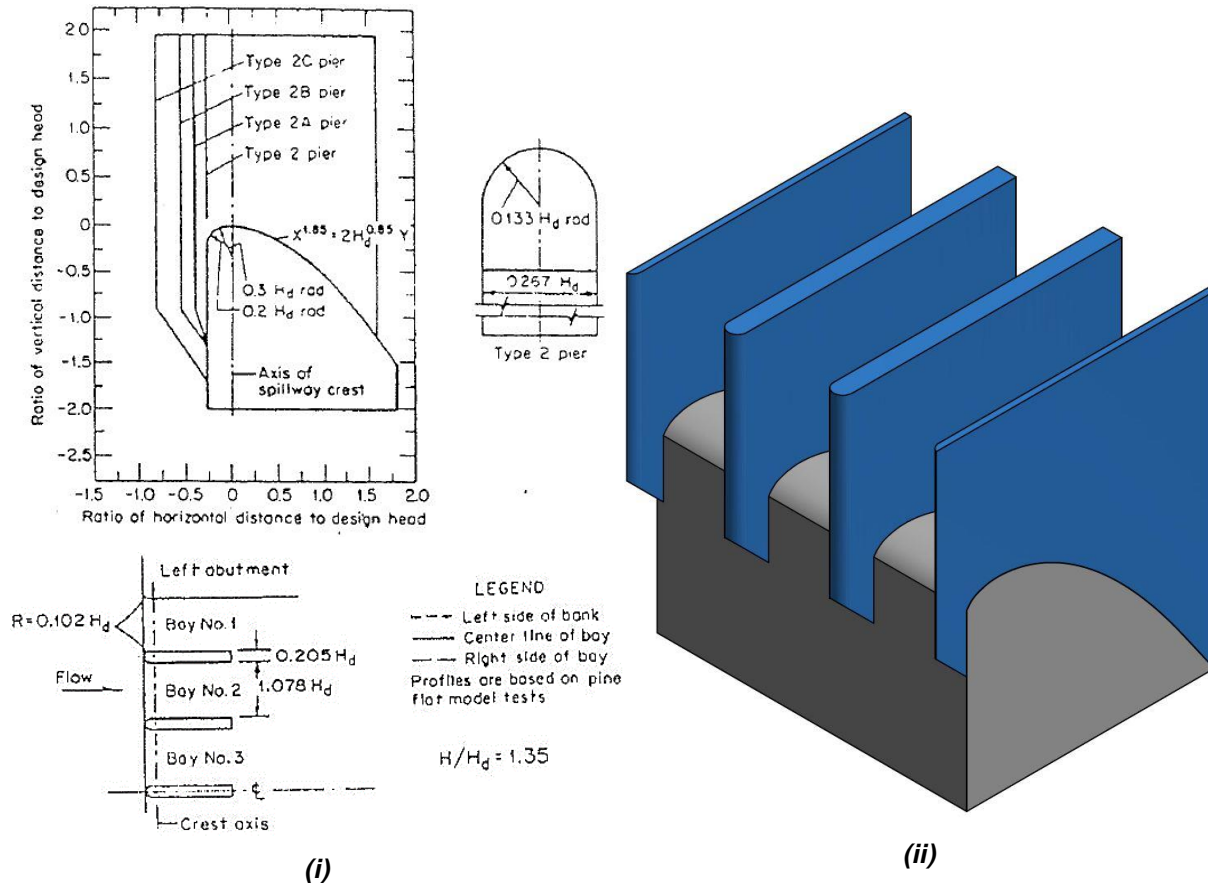


Figure 6.4: (i) Pier design guidelines of the US Army WES (1959) and (ii) model pier design.

6.2.2 Flaring Gate Pier Design

6.2.2.1 Y-Shape Flaring Gate Pier

The Y-Shape FGP is the standard flare implementation on the Dachaoshan Dam. Unfortunately, no design guidelines have been disclosed and the model design was based on the available prototype dimensions.

The Y-Shape FGP was designed with a contraction angle of 20° , a total height of 25.8 m and a width of 3.7 m. This design resulted in a contraction ratio $\left(\beta = \frac{b}{B}\right)$ of 0.47, where B is the unobstructed width between the piers and b is the unobstructed width between the flare extremities. According to the research of Chen and Zhang (2015) the contraction angle of 20° was not optimal, but the contraction ratio of 0.47 was ideal. The purpose of the flare was to contract the flow, resulting in a narrow, high velocity jet, which created several air-water surfaces where air could be entrained. The flares also add structural stability to the piers, which was probably what made it possible to decrease the pier width to 3 m, as mentioned in the previous section. **Figure 6.5** illustrates the prototype and model Y-Shape FGP design.

Detailed as-built model drawings are presented in **Appendix C**.

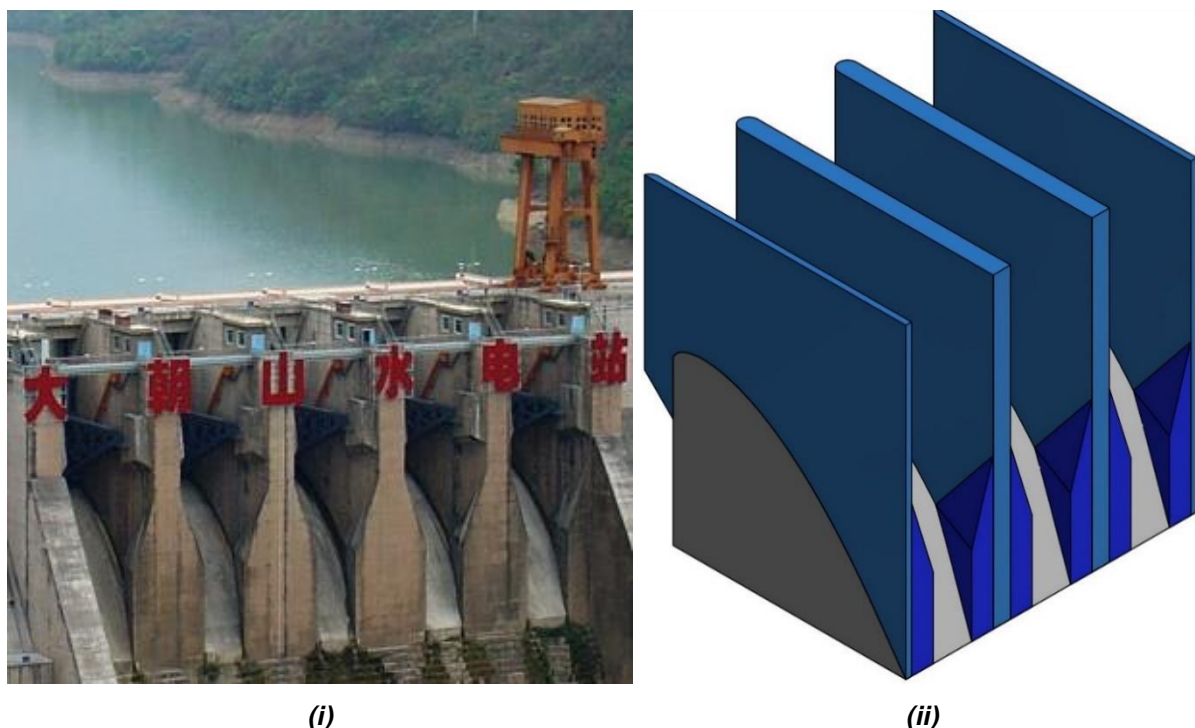


Figure 6.5: Illustration of the (i) prototype Y-Shape FGP design (Hongta Group, 2017) and the (ii) model Y-Shape FGP design.

6.2.2.2 X-Shape Flaring Gate Pier

The design of the X-Shape FGP was based on the prototype design of the Suofengying Dam which is situated in Guizhou Province, China. Similarly to the Y-Shape FGP, no design guidelines had been disclosed and the design for this model was based on the prototype dimensions. The X-Shape FGP design of the Suofengying Dam was adapted to be implemented on the Dachaoshan Dam, retaining a similar contraction angle and contraction coefficient as for the Y-Shape FGP model.

The X-Shape FGP was designed with a contraction angle of 18.3° , a total height of 31.4 m and a width of 3.5 m. This design resulted in a contraction ratio of 0.5. The X-Shape implemented a wider bottom outlet width than the Y-Shape FGP. The wide outlet was designed to safely pass a unit discharge of $30 \text{ m}^2/\text{s}$ without the use of the flares. At increased unit discharges the flare would contract and deflect the water. **Figure 6.6** illustrates the prototype and model design of the X-Shape FGP.

Detailed as-built model drawings are presented in **Appendix C**.

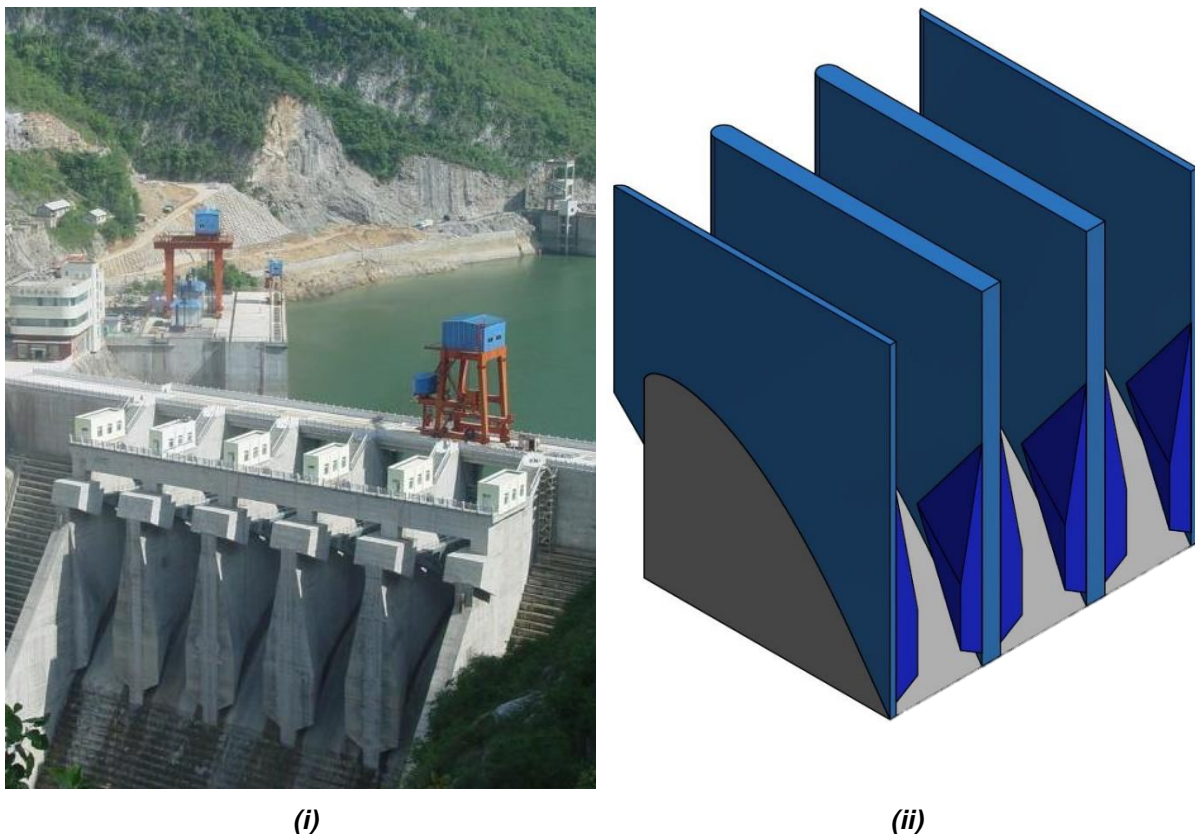


Figure 6.6: Illustration of the (i) prototype X-Shape FGP design (Large Dam Safety Supervision Centre, 2015) and the (ii) model X-Shape FGP design.

6.2.2.3 Y-Shape Flaring Gate Pier with a Slit-type Flip Bucket

Another special design consideration of the Dachaoshan Dam is the implementation of a slit-type flip bucket, located at the downstream section of the Y-Shape FGP. This design is characterised by converging side walls which then form a narrow exit. The slit-type flip bucket design, forces the departing jet to disperse in a vertical plane resulting in a long, narrow impact area. Scour in the downstream bed is greatly reduced and model studies for the Dongjiang Dam which is in the Hunan province, China, reported a reduction of up to 80% (Lin, *et al.*, 1987).

The slit-type flip bucket was designed with an inclination of 1:1.07 or a 43° angle, with a height of 3.6 m. The purpose of this flip bucket was to deflect the water away from the stepped spillway, thereby generating a large cavity. See **Figure 6.7** for an illustration of the schematic design and corresponding laboratory model.

Detailed as-built model drawings are presented in **Appendix C**.

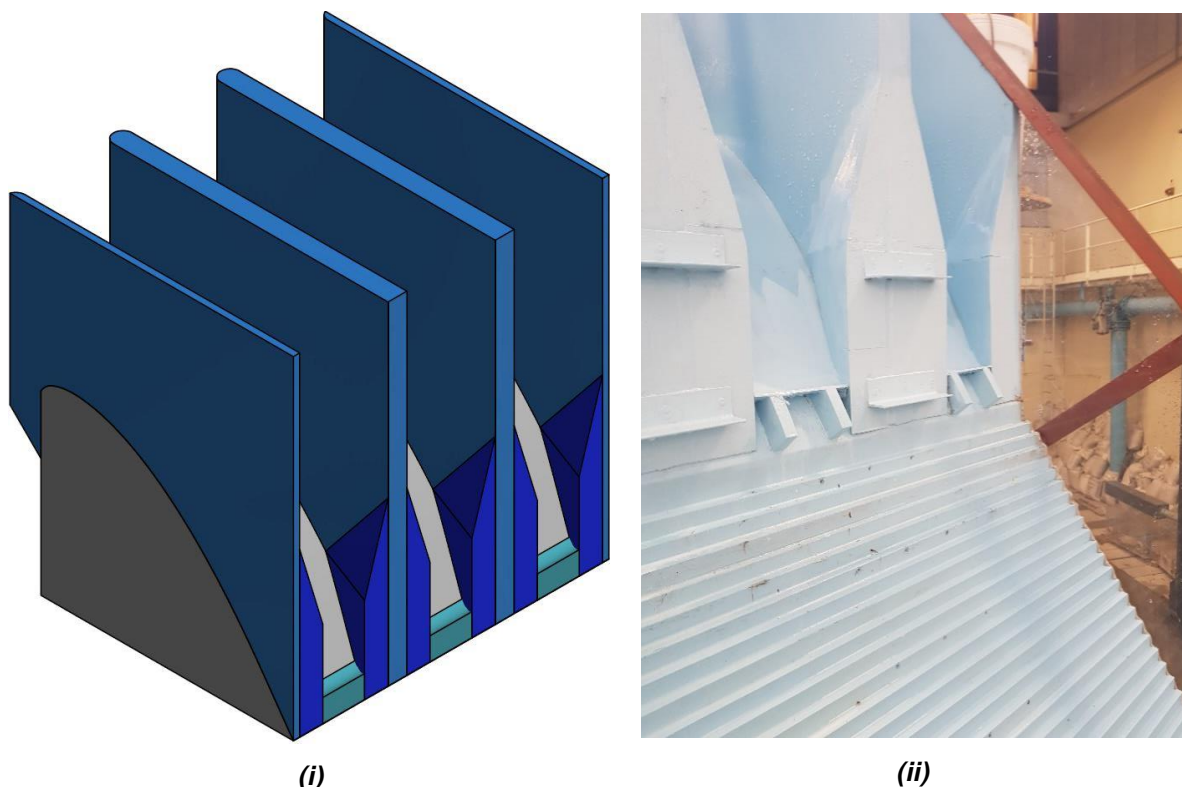


Figure 6.7: (i) Schematic illustration of the Y-shape FGP together with the slit-type flip bucket and corresponding (ii) laboratory model.

6.3 Experimental Setup

A few alterations were made to the previous experimental setups in order to conduct a comprehensive investigation for the various FGP models. The model coordinate system was kept constant for all the experimental setups and can be viewed in **Section 4.5**. The changes to the experimental setup are discussed in the following sections.

6.3.1 Model Layouts

The investigation required four model layouts with alterations to the FGP design and the inclusion of a flip bucket. The crest consisted of two piers and two half piers, which were equally spaced in order to form three discharge bays. The crest was designed with a centre to centre pier spacing of 17 m, which was constant for the various FGP investigations. The different layouts are shown in **Table 6.3** and include:

- A stepped spillway without crest piers, which acted as the control test.
- A stepped spillway with various different FGP designs and the addition of a slit-type flip bucket.

The addition of piers, especially those that protruded upstream of the crest, reduced the effective crest length, which caused an increased head. This meant that the control test would operate at reduced heads compared to Models 9, 10 and 11, at a similar discharge. In order to achieve a comparable performance, it was decided that the energy head at the spillway crest was the constant variable for all model layouts. The discharge head was thus unaltered for all the model setups, which was achieved by adjusting the model flow.

Table 6.3: Different model layouts.

Model Layout	Pier	Flare	Flip bucket
8	No Pier		
9	Bullnose crest pier	Y-Shape FGP	No flip bucket
10	Bullnose crest pier	X-Shape FGP	No flip bucket
11	Bullnose crest pier	Y-Shape FGP	43° slit-type flip bucket

6.3.2 Model Setup

Due to the high variability in the flow patterns which is induced by the various FGP designs, the experimental area consisted of the entire spillway length, in order to accurately capture the results and the impact regions. As indicated in **Figure 6.8 (i)**, the model consisted of three discharge bays, with the central bay used for pressure and air concentration measurements. Three pressure sensors were located on each measuring step within the central bay, with the first sensor being installed in the middle of the bay and the subsequent sensors spaced by 85 mm (4.25 m prototype) as illustrated in **Figure 6.8 (ii)**. The air concentration was measured only in the middle of the central bay at specific cavitation regions, because of the time-consuming recording procedure. The experimental investigation was conducted with four prototype unit discharges as indicated in **Table 6.4**.

Table 6.4: Summary of measuring locations.

Prototype unit discharge (m ² /s)	Measuring locations
50	Steps 2, 7, 12, 17, 22, 27,32, 37, 43, 47, 52, 57, 62, 67 & 71
100	
150	
200	

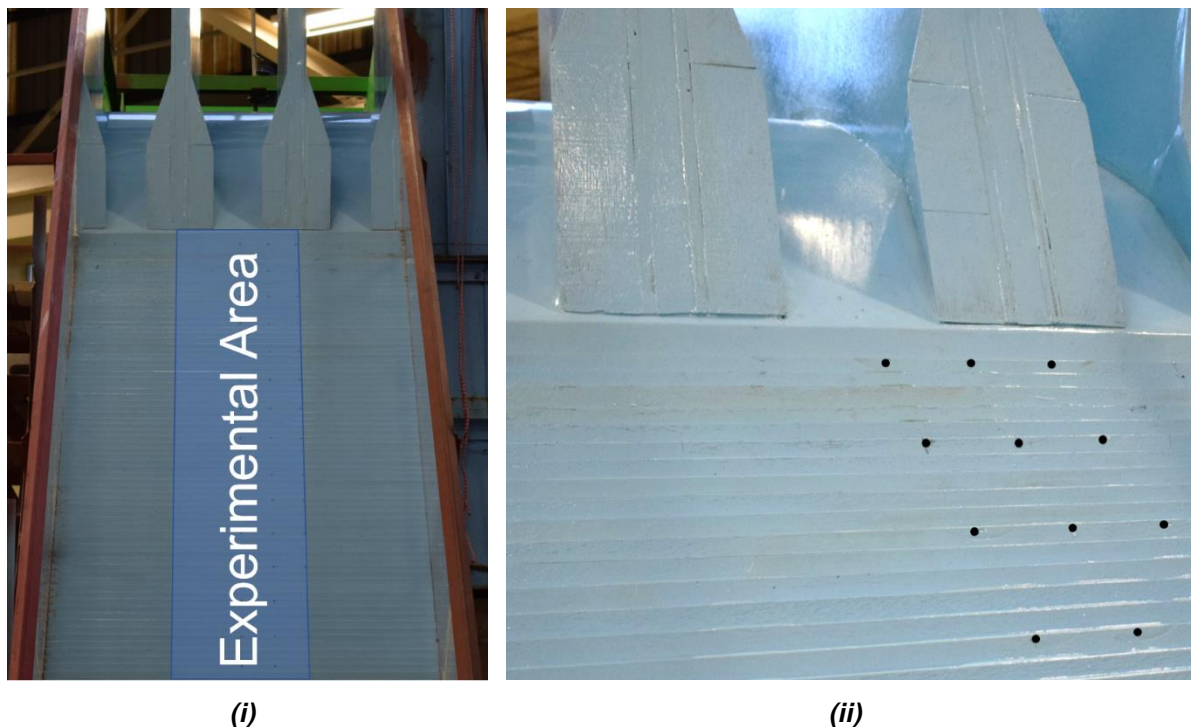


Figure 6.8: (i) Illustration of the pier setup and experimental area. (ii) Position of the pressure measuring locations.

6.3.3 Measuring Procedures

The discharge and pressure measuring procedures were unchanged, from those illustrated in **Section 4.2**. The air concentration measuring procedure was again adapted, to account for the large amount of deflected water, and the measuring of ski-jump lengths were recorded for the Y-shape FGP together with the slit-type flip bucket.

6.3.3.1 Air Concentration

The increased discharges, together with the various FGP designs, generated a substantial amount of water which was deflected to downstream regions of the spillway. This deflection made it difficult and impractical to measure the air concentration by using the same procedure as previously, where the conductivity needle was attached to a trolley, supported above the spillway.

The measuring procedure was thus adapted so that the conductivity needle probe was attached beneath the spillway, with the probe tip positioned in line with the pseudo-bottom as indicated in **Figure 6.9**. The conductivity needle probe setup required a hole to be drilled in the spillway for each measuring location, which was filled with epoxy after successful measurement. The setup and repositioning of the instrument was time consuming, which led to a few measuring positions within the cavitation regions only, instead of over the entire spillway area.

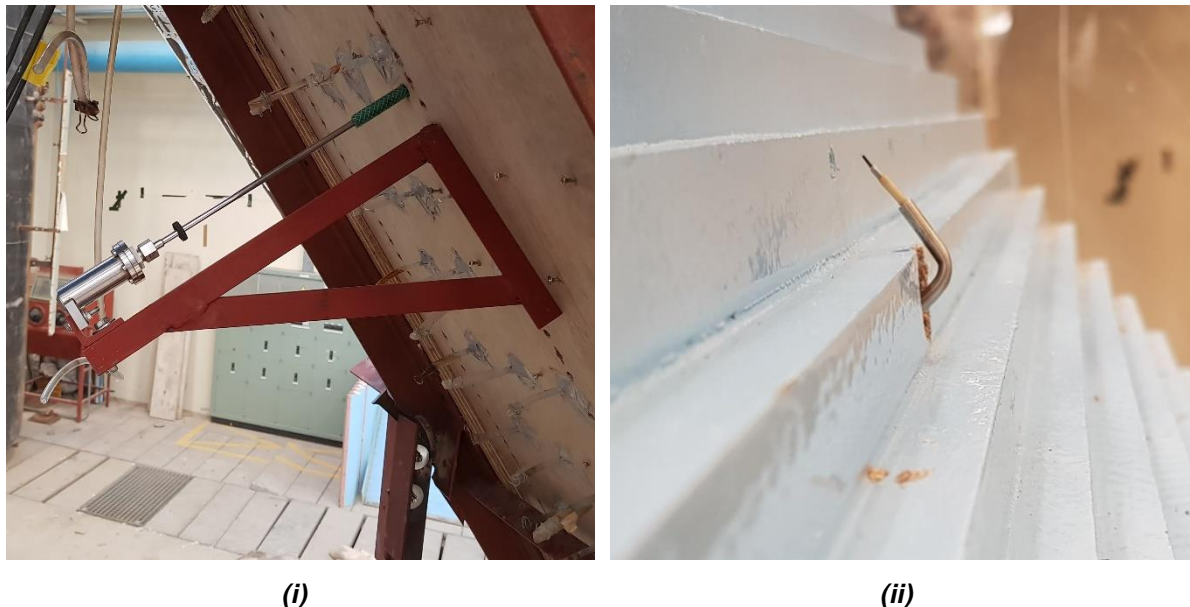


Figure 6.9: Conductivity needle probe setup for air concentration measurement.

6.3.3.2 Measuring Ski-jump Length

As described in **Subsection 6.2.2.3**, a Y-Shape FGP equipped with a 43° slit-type flip bucket was one of the FGP designs which were investigated. The addition of the flip bucket significantly altered the flow pattern and projected the water over the stepped profile, as indicated in **Subsection 6.5.1.3**. This flow pattern meant that pressure and air concentration measurements were redundant, as no water was discharging via the stepped spillway. The ski-jump trajectory was determined by physical measurements, as well as by using a method of photo scaling and dimensioning. The physical measurements were recorded by using a 1 m ruler, which was also used to correctly scale the photos. With the variability in the flow patterns, the ski-jump length was recorded to the nearest 10 mm. See **Figure 6.10** for an illustration of the ruler setup.



Figure 6.10: Laboratory setup for the measurement of the ski-jump length.

6.3.4 Measuring Locations

Air concentration and pressures were measured within the experimental area to assess the performance of the various FGP models. The results were measured on only half of the central discharge bay, as the similarity that was present in the physical model allowed for the mirroring of the results. The pressure results were recorded at the measuring locations as indicated in **Table 6.5**.

The pressures were recorded by using pressure transducers, which were installed at the measuring locations. These transducers were installed at a height of approximately 0.75 times the height of the step riser. The placement in this position was a consequence of the small model steps and relatively large size of the pressure taps, as illustrated in **Section 4.2.2**. The installed positions of the pressure transducers are within an acceptable region on the step to capture the negative pressures on the step corners.

Due to the ski-jump flow pattern which is generated by the FGPs, air concentration results were captured with some inconvenience as mentioned in **Subsection 6.3.3.1**. The time-consuming measuring procedure made it impossible to measure air concentration at all of the pressure locations and it was thus decided to measure air concentration only in the middle of the central bay (Location A). The air concentration measuring locations are tabulated in **Table 6.6**.

Table 6.5: Pressure measuring locations.

Prototype Discharge (m ² /s)	Model Length, L _m (mm)	Prototype Length, L _p (mm)	Step no.	X-Coordinate (mm)		
				Location A	Location B	Location C
50 100 150 200	1015	50.75	2	500	585	670
	1139	56.95	7	500	585	670
	1261	63.05	12	500	585	670
	1382	69.1	17	500	585	670
	1505	75.25	22	500	585	670
	1627	81.35	27	500	585	670
	1749	87.45	32	500	585	670
	1871	93.55	37	500	585	670
	1993	99.65	42	500	585	670
	2115	105.75	47	500	585	670
	2237	111.85	52	500	585	670
	2360	118.00	57	500	585	670
	2482	124.10	62	500	585	670
	2604	130.20	67	500	585	670
2701	135.05	71	500	585	670	

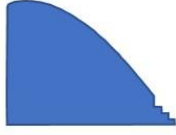
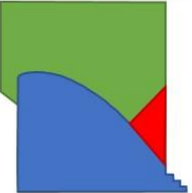
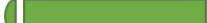
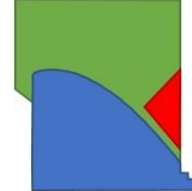

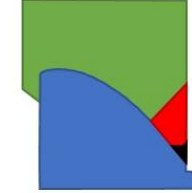

Table 6.6: Air concentration measuring locations.

Prototype Discharge (m ² /s)	Model Length, L _m (mm)	Prototype Length, L _p (mm)	Step no.	X-Coordinate (mm)
				Location A
50 100 150 200	1261	63.05	12	500
	1627	81.35	27	500
	1871	93.55	37	500
	2237	111.85	52	500
	2482	124.10	62	500
	2701	135.05	71	500

6.3.5 Model Test Conditions on the Type B Stepped Spillway

According to the law of self-similarity (**Section 2.8.4**), a Reynolds number ($Re = q/\nu$) of 8×10^4 is required for the accurate measuring and scaling of air concentration. The model test conditions of the Type B stepped spillway are presented in **Table 6.7**. The Reynolds numbers varied between 9.1×10^4 and 36.2×10^4 for the different experimental conditions. These Reynolds numbers ensured that the law of self-similarity was applicable for the discharges under consideration, thus ensuring the accurate modelling and measurement of air concentration, irrespective of the model scale.

Table 6.7: Model test conditions on the Type B stepped spillway.

Model test conditions							
Model Layout	Crest configuration			Unit discharge			
				50 m ² /s	100 m ² /s	150 m ² /s	200 m ² /s
8	No Pier (Reference)			Air & Pressure	Air & Pressure Repeated	Air & Pressure	Air & Pressure
9	Pier 3 & Y-Shape FGP			Air & Pressure	Air & Pressure Repeated	Air & Pressure	Air & Pressure Repeated
10	Pier 3 & X-Shape FGP			Air & Pressure	Air & Pressure Repeated	Air & Pressure	Air & Pressure Repeated
11	Pier 3, Y-Shape FGP & 43° flip bucket			Projection	Projection	Projection	Projection
Re_{model} $\left(\frac{q}{\nu}\right)$	Chanson and Felder (2017) recommended a minimum Re of 8×10^4 to minimise air concentration scale effects			$9,1 \times 10^4$	$18,2 \times 10^4$	$27,2 \times 10^4$	$36,2 \times 10^4$

6.4 Repeatability of Experiments

In order to ensure that the recorded data was accurate and that variable results were eliminated, nearly 50% of the experiments were repeated. For each of the three model investigations (excluding Y-Shape FGP with the slit-type flip bucket), two of the experiments were repeated to validate the accuracy of the air concentration and pressure results.

6.4.1 Air Concentration

Two independent experiments were conducted for unit discharges of 100 m²/s and 200 m²/s. These experiments were performed for both the control test and the X- and Y-Shape FGPs. The statistical air concentration data for the unit discharge of 100 m²/s is tabulated in **Table 6.8**. The data was specifically assessed for the measuring location at Step 37A.

Table 6.8: Statistical air concentration data (%) for a unit discharge of 100 m²/s.

Air Concentration (%)	Step 37A					
	No Pier		Y-Shape FGP		X-Shape FGP	
	Test 1	Test 2	Test 1	Test 2	Test 1	Test 2
Mean	0.0	0.0	4.2	4.7	0.6	0.8
Standard deviation	0.2	0.0	3.0	3.3	1.0	1.2
Maximum	6	0	18	24	13	9
3 rd Quartile	0	0	6	6	1	1
Median	0	0	4	4	0	0
1 st Quartile	0	0	2	2	0	0
Minimum	0	0	0	0	0	0

The comparison of the statistical data revealed a good agreement between the independent experiments. A maximum error of 0.5% was observed for the average air concentration of the Y-Shape FGP. The repeatability of the independent experiments was thus ensured and the variable results were eliminated.

See **Figure 6.11** for a box and whisker plot presentation of the statistical data. The box represents the 25th percentile, median and 75th percentile, while the mean is represented by the cross. The minimum and maximum values are presented by the whiskers which extend from the box, excluding the outliers. The minimum and maximum values are defined as the boundaries, which are 1.5 times the interquartile range from the bottom and top of the box. The outliers are presented as dots.

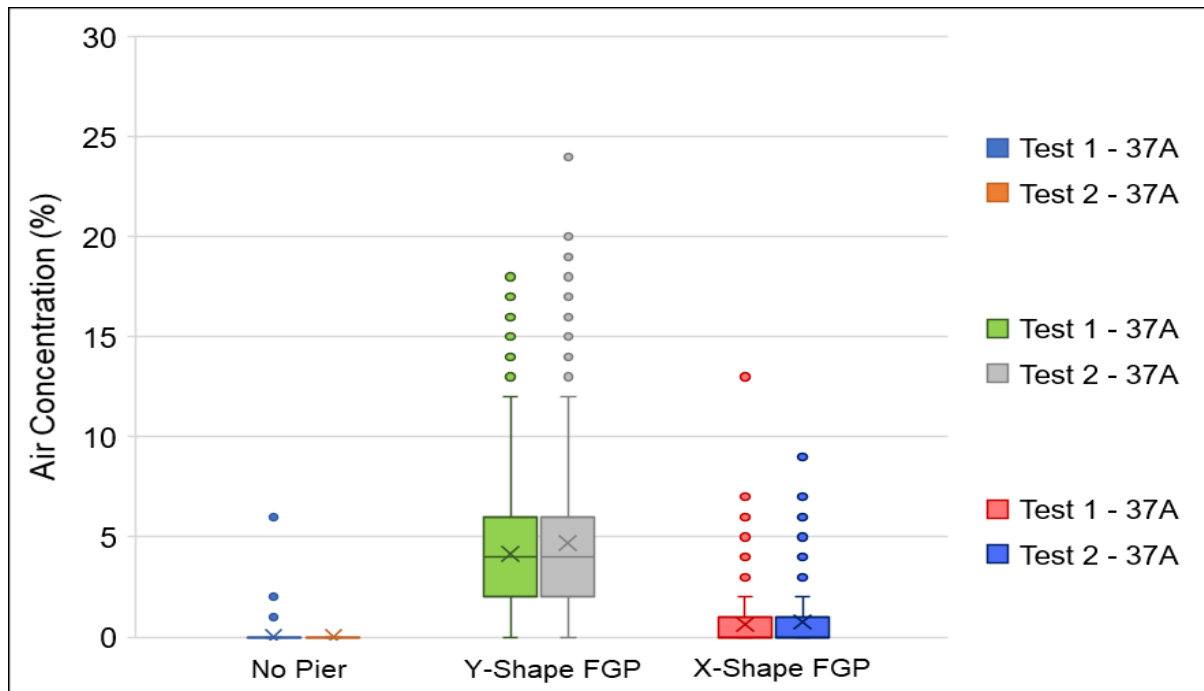


Figure 6.11: Air concentration comparison of repeated test results at 100 m²/s.

The statistical data, together with the box and whisker plot, demonstrated an excellent resemblance between the two independent experiments. The majority of the air concentration results rarely exceeded 5% and a few outliers were recorded above the local maximum. The performance for all three of the models demonstrated minimal variation.

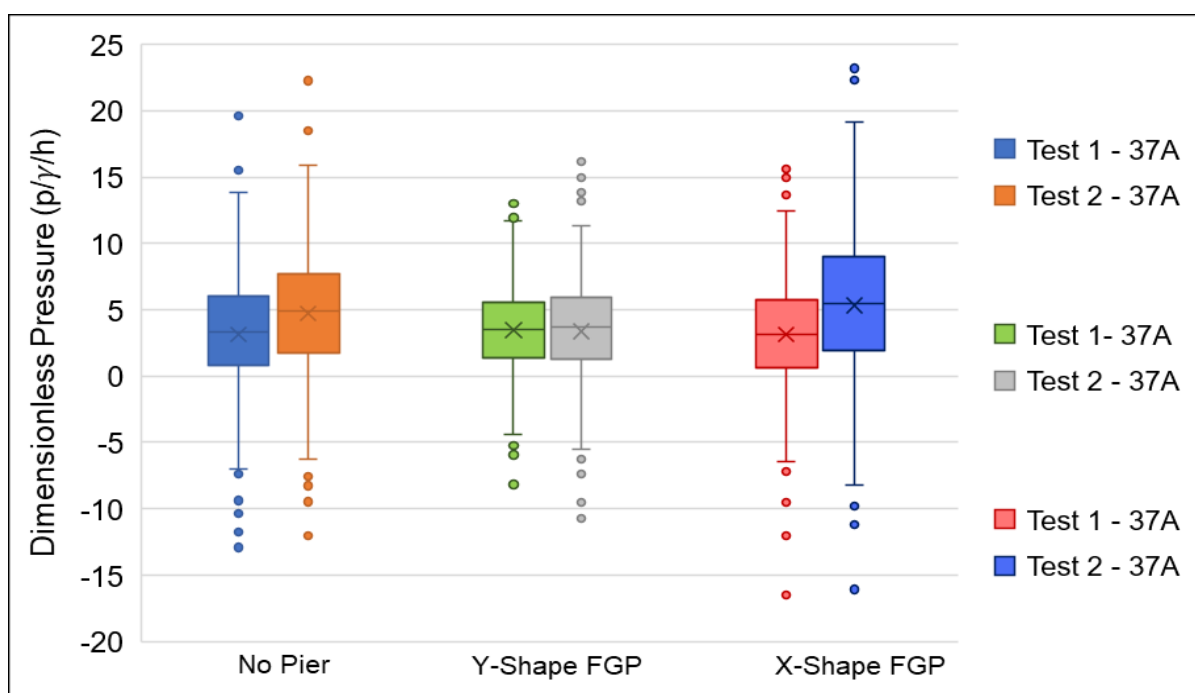
As mentioned in **Section 4.6.1**, the average air concentration is used to represent the spillway performance at specific measuring positions. The statistical data illustrated little to no variation in the mean air concentration of the independent tests and was thus considered reliable. The repeatability of the air concentration data was deemed sufficient and because of the small variance, the mean air concentration was used as an acceptable representation of the results.

6.4.2 Pressure

The pressure results were validated by the same procedure as was used for the air concentration. The repeatability of the pressure data was validated by independent experiments which were performed at unit discharges of 100 m²/s and 200 m²/s. These tests were performed for the control experiment, X- and Y-Shape FGPs. The statistical pressure data is tabulated in **Table 6.9** and is graphically compared by using a box and whisker plot (**Figure 6.15**).

Table 6.9: Statistical pressure data ($p/\gamma h$) for a unit discharge of $100 \text{ m}^2/\text{s}$.

Pressure ($p/\gamma h$)	Step 37A					
	No Pier		Y-Shape FGP		X-Shape FGP	
	Test 1	Test 2	Test 1	Test 2	Test 1	Test 2
Mean	3.131	4.718	3.473	3.385	3.142	5.342
Standard deviation	4.466	4.681	3.402	3.978	4.202	5.332
Maximum	19.589	19.589	19.589	19.589	19.589	19.589
3 rd Quartile	5.995	7.725	5.582	5.925	5.710	8.980
Median	3.287	4.913	3.550	3.685	3.158	5.439
1 st Quartile	0.787	1.736	1.363	1.290	0.606	1.897
0.15 Percentile	-10.266	-9.324	-6.733	-8.549	-9.462	-10.653
Minimum	-12.911	-12.014	-8.168	-10.742	-16.529	-16.072

**Figure 6.12: Pressure comparison of repeated test results at $100 \text{ m}^2/\text{s}$.**

The statistical pressure results in **Table 6.9**, together with the box and whisker plot comparison in **Figure 6.12**, illustrated a higher variability in the data as compared to the Type A spillway results. It should be noted that the higher variability is attributable to the smaller scale model. As the model pressure results were transformed to dimensionless pressure parameters, small variations in the model pressures were converted to represent larger discrepancies. The 0.15 percentile pressure was used to represent the minimum pressures on the spillway. The variation in the results of these pressure tests was deemed acceptable, since the distortion thereof was due to the small model scale.

6.5 Results

Within this section, the results for the various experimental setups are presented and analysed. The air concentration and pressure results were used to establish the spillway performance for each of the aerator structures. Other results included the stage-discharge relationship and the projected trajectory of the Y-Shape FGP and flip bucket. Important visual observations were documented for each of the model setups.

6.5.1 Visual Observations

6.5.1.1 Y-Shape FGP

The Y-Shape FGP's performance is characterised by large, unused spillway areas and the substantial deflection of water. These unused areas, as illustrated in **Figure 6.13 (i)**, were formed downstream of the flares, which in turn blocked a large portion of the available flow area. As mentioned in **Subsection 2.7.2.2**, the unutilised spillway area for the Dachaoshan Dam resulted to approximately 70% of the spillway area.

The flares generated a large deflection of water, especially at the higher unit discharges, as indicated in **Figure 6.13 (ii)**. These ski-jump flow regimes were combined with longitudinal impact areas, which impinged on the stepped profile. Not only to these impact regions generate severe negative pressures, but they also led to a decreased air concentration, according to Chanson (1994a). Lastly, the protrusion of the piers upstream of the spillway crest resulted in a smooth, efficient transition (**Figure 6.13 (iii)**).

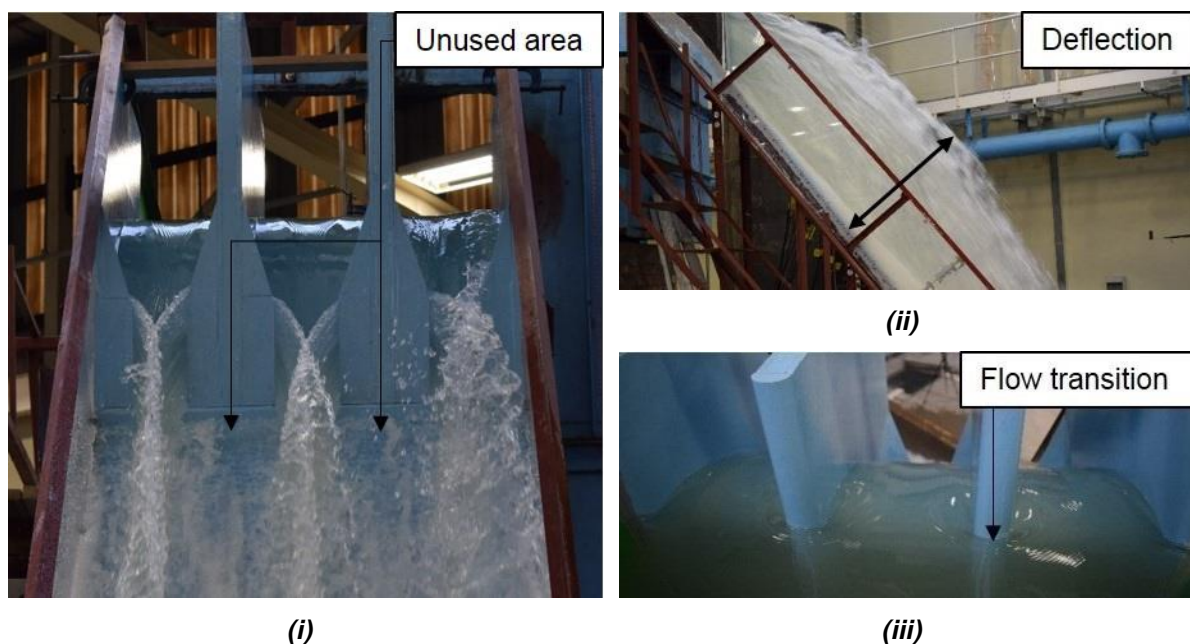


Figure 6.13: Photographs indicating the (i) unutilised spillway area, (ii) the large deflection that form the ski-jump regime and (iii) smooth flow transition which occur at the crest piers.

6.5.1.2 X-Shape FGP

The design and performance of the X-Shape FGP is very similar to that of the Y-Shape FGP. The X-Shape was designed with a wider bottom outlet to increase the use of the stepped profile for small discharges. As illustrated in **Figure 6.14 (i)**, a larger portion of the stepped spillway area was used as compared to the performance of the Y-Shape FGP. As stated in the literature, the wider bottom outlet was designed to pass a unit discharge of $30 \text{ m}^2/\text{s}$ without contraction. This design was validated for a unit discharge of $30 \text{ m}^2/\text{s}$ and, as indicated in **Figure 6.14 (ii)**, there was little to no contraction by the flares.

The X-Shape FGP was designed with a reduced flow blocking effect compared to the Y-Shape FGP. The reduced blockage led to a decreased water deflection, as indicated in **Figure 6.14 (iii)**. The reduced deflection should be beneficial since it would result in smaller, dampened impact regions. These regions where the impact had been dampened would decrease the effect of impact detrainment, resulting in a higher, entrained air concentration.

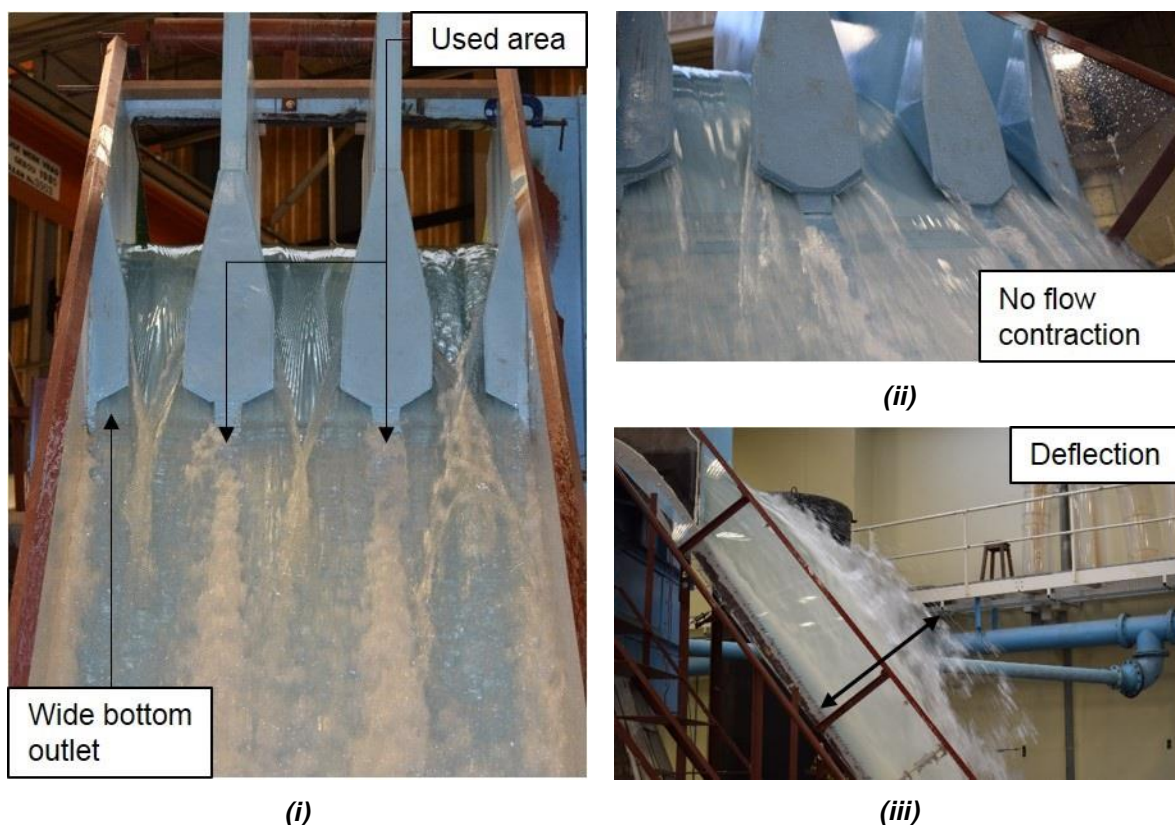


Figure 6.14: Photographs indicating the (i) wider bottom outlet of the X-Shape FGP, (ii) performance at a unit discharge of $30 \text{ m}^2/\text{s}$ and (iii) the formation of the ski-jump flow regime.

6.5.1.3 Y-Shape FGP with a Slit-type Flip Bucket

The prototype operation of the Dachaoshan Dam implemented the Y-Shape FGP design, together with a slit-type flip bucket which was positioned next to the end of the flares. The performance of this design was such that the water was not discharged by the stepped spillway. At the lowest unit discharge of $50 \text{ m}^2/\text{s}$, the water was projected over the length of the spillway. There was thus no energy dissipation by the stepped profile and the use of the steps would only be for economic benefit and the reduced construction time of RCC. **Figure 6.15** illustrates the performance of the Y-Shape FGP with the slit-type flip bucket for unit discharges of $50 \text{ m}^2/\text{s}$ and $150 \text{ m}^2/\text{s}$. Notice that in the photographs the ski-jump flow regime does not use the stepped spillway and the water impacts downstream thereof. The impact region is characterised as long and narrow, thus distributing the impact energy, which in this case would lead to a decreased amount of scour.

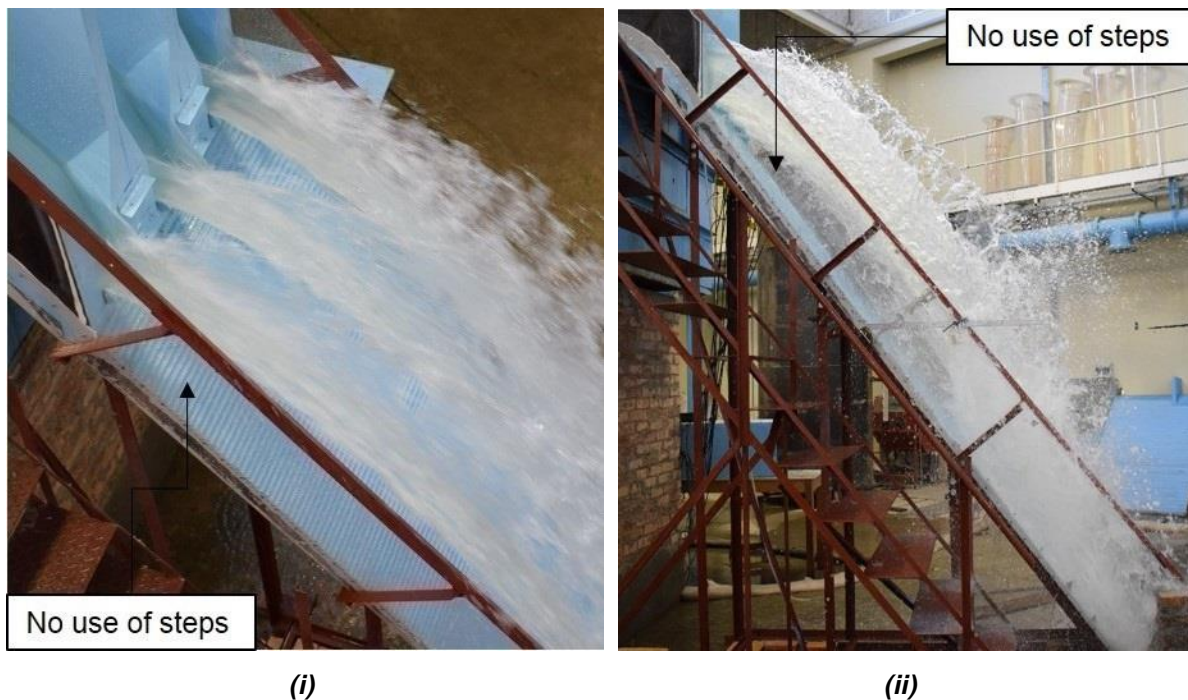


Figure 6.15: Photographs indicating the performance of the Y-Shape FGP and slit-type flip bucket for unit discharges of (i) $50 \text{ m}^2/\text{s}$ and (ii) $150 \text{ m}^2/\text{s}$.

6.5.2 Stage-Discharge Relationship

The stage-discharge relationship for the stepped spillway was determined for both the control test and the FGP experiments. See **Figure 6.16** for a graphical comparison of the stage-discharge relationship for the two different crest configurations.

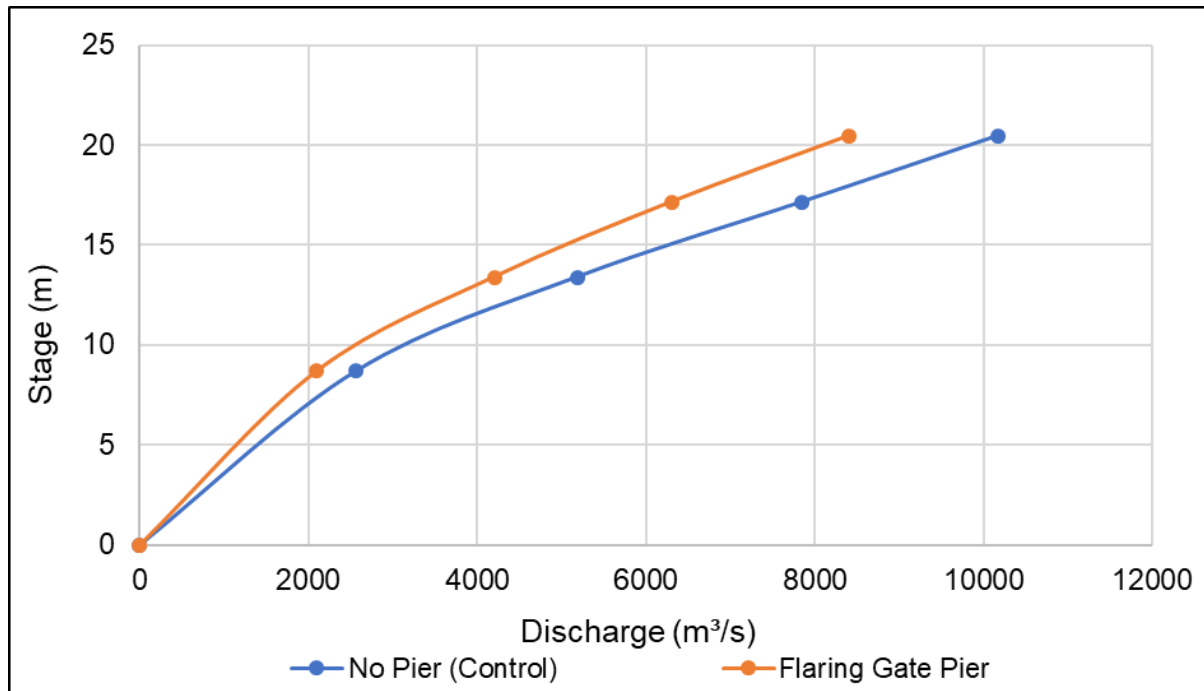


Figure 6.16: Stage-discharge relationship for the Type B stepped spillway design.

As indicated in **Figure 6.16**, the addition of FGPs on the spillway crest brought about increased heads when compared to the control experiment for the same discharge. The additional head was generated by the crest piers, which reduced the effective crest length and decreased the spillway efficiency. However, the accompanying flares and flip buckets on the downstream end of the pier did not influence the spillway head.

As previously mentioned in **Section 6.3.1**, the spillway head was used as the independent variable. By keeping the spillway head constant for specific discharges, similar spillway velocities were achieved for the respective model investigations. In order to generate the same head for the control experiment, a substantial increase in the discharge was required. By keeping the head constant, similar unit discharges were achieved for the control- and FGP experiments.

6.5.3 Air Concentration Results

Air concentration results were recorded in the middle of the central discharge bay for all of the experimental models. The locations of these measuring positions were based on the positions of the impact regions, which occurred in the centre of the discharge bay. The average air concentration was used to represent the spillway performance. As previously mentioned in **Subsections 6.3.3.1** and **6.3.4**, the measuring procedure and measuring positions were altered in order to accurately record the air concentration data despite the large deflection of water from the flares. As the performance of the control experiment was clear of any water deflections, the same measuring procedure was used as in **Section 4.2.3**. As a result of the relatively small steps in comparison to the corresponding flow depths, only insignificant recirculating vortices were formed in the step niches, which did not affect the air concentration results. This meant that the anti-ventilation plate was not required for the air concentration measurement.

As previously stated, Peterka (1953) identified that an air concentration of 5 to 8% is sufficient to eliminate the risk of cavitation damage. The critical air concentration limit for this thesis was identified as 8%. Regions of insufficient aeration are indicated with red text in **Table 6.10**.

The air concentration results for the Type B stepped spillway experiments are tabulated in **Table 6.10**. The prototype streamwise distance, L_p , indicates the position along the length of the spillway, while the X-axis indicates the distance across the width of the discharge bay. The air concentration results were recorded only in the middle of the central bay ($X = 8.5$ m) for the four unit discharges. The alteration to the measuring procedure for the control experiment made it possible to record the air concentration at more positions along the spillway length than had been done for the FGP models.

Table 6.10: Centreline air concentration results for the Type B spillway investigation.

Air Concentration (%)				
L_p (m)	Model Setup 8 - No Pier			
	50 m ² /s	100 m ² /s	150 m ² /s	200 m ² /s
	X = 8.5 m	X = 8.5 m	X = 8.5 m	X = 8.5 m
50.78	0.00	0.00	0.00	0.00
57.01	0.00	0.00	0.00	0.00
63.11	0.00	0.00	0.00	0.00
69.21	0.00	0.00	0.00	0.00
75.32	0.01	0.00	0.00	0.00
81.42	0.03	0.00	0.00	0.00
87.52	0.51	0.00	0.00	0.00
93.63	3.40	0.01	0.00	0.00
99.73	6.65	0.00	0.00	0.00
105.83	16.47	0.00	0.25	0.00
111.94	28.20	0.00	0.00	0.00
118.04	39.26	0.01	0.00	0.00
124.14	46.75	0.06	0.00	0.00
130.25	27.96	0.52	0.01	0.00
135.13	29.69	1.87	0.02	0.00
L_p (m)	Model Setup 9 - Y-Shape FGP			
	50 m ² /s	100 m ² /s	150 m ² /s	200 m ² /s
	X = 8.5 m	X = 8.5 m	X = 8.5 m	X = 8.5 m
63.11	24.70	20.21	21.89	26.42
81.42	9.85	11.14	12.41	14.27
93.63	3.17	4.15	8.09	9.60
111.94	2.03	2.02	4.18	5.54
124.14	9.72	0.32	0.57	1.57
135.13	35.74	1.01	1.60	2.67
L_p (m)	Model Setup 10 - X-Shape FGP			
	50 m ² /s	100 m ² /s	150 m ² /s	200 m ² /s
	X = 8.5 m	X = 8.5 m	X = 8.5 m	X = 8.5 m
63.11	30.00	11.32	10.95	12.40
81.42	11.36	3.30	2.65	2.92
93.63	10.96	0.64	0.48	0.56
111.94	37.85	0.72	0.09	0.09
124.14	29.81	1.93	0.04	0.10
135.13	37.97	24.94	0.46	0.09

Note: Regions of insufficient aeration is indicated with red text.

6.5.4 Pressure Results

The pressure results were recorded within the central discharge bay in order to establish the cavitation and impact regions on the spillway. The pressure sensors were installed at approximately 0.75 times the step riser height (0.75 h). Pressures were measured on only half of the width of the discharge bay, due to the symmetry of the model. The results, however, were presented as if for entire discharge bay, where the centreline acted as the symmetry axis.

The cavitation boundary, as previously mentioned for the Type A spillway investigation, was defined as a pressure head of -7 m atmospheric, as was recommended by Chadwick, *et al.* (2013). The boundary was transformed to the dimensionless pressure parameter and for a constant prototype step height of 1 m, a dimensionless pressure parameter of -7 represented the point of cavitation inception. It should be noted that all of the pressures are presented in terms of an atmospheric pressure datum.

The centreline pressure results for the Type B spillway investigation is tabulated in **Table 6.11**. The red text in the table indicates the cavitation pressures. The complete set of pressure results is contained within **Appendix D**.

Table 6.11: Centreline pressure results for the Type B spillway investigation.

Pressure (p/y/h)				
L_p (m)	Model Setup 8 - No Pier			
	50 m ² /s	100 m ² /s	150 m ² /s	200 m ² /s
	X = 8.5 m	X = 8.5 m	X = 8.5 m	X = 8.5 m
50.78	6.647	6.717	11.152	12.215
57.01	4.730	9.632	11.848	7.925
63.11	-5.628	-5.354	-2.295	-5.342
69.21	-2.561	-0.494	-2.437	-3.836
75.32	-3.729	3.275	1.806	0.202
81.42	-5.757	-6.124	-3.523	-3.277
87.52	7.087	6.389	4.605	3.997
93.63	-13.418	-10.266	-7.928	-17.619
99.73	-2.156	-4.256	-5.366	-8.651
105.83	5.030	-3.816	-5.168	-8.466
111.94	-2.298	-7.990	-4.041	-10.860
118.04	6.817	4.758	5.181	5.542
124.14	-5.163	-14.747	-13.867	-12.256
130.25	-0.106	-6.080	-6.313	-9.314
135.13	5.893	-0.406	-6.541	-17.181

L_p (m)	Model Setup 9 - Y-Shape FGP			
	50 m ² /s	100 m ² /s	150 m ² /s	200 m ² /s
	X = 8.5 m	X = 8.5 m	X = 8.5 m	X = 8.5 m
50.78	-5.131	1.729	1.382	6.560
57.01	3.950	8.027	4.328	7.866
63.11	-0.491	1.454	-1.245	1.097
69.21	-4.013	-3.746	-4.812	-5.665
75.32	-2.786	-5.867	-5.370	-2.775
81.42	-6.459	-4.200	-5.779	-6.023
87.52	4.841	6.080	6.446	6.346
93.63	-8.401	-6.733	-5.865	-5.876
99.73	-19.672	-16.876	-17.487	-13.657
105.83	-19.111	-16.746	-21.755	-12.851
111.94	-11.090	-10.413	-12.574	-11.231
118.04	5.598	5.541	5.786	5.831
124.14	-8.665	-19.024	-15.844	-13.641
130.25	-5.635	-22.130	-21.223	-21.925
135.13	-2.833	-16.626	-16.714	-18.016
L_p (m)	Model Setup 10 - X-Shape FGP			
	50 m ² /s	100 m ² /s	150 m ² /s	200 m ² /s
	X = 8.5 m	X = 8.5 m	X = 8.5 m	X = 8.5 m
50.78	6.161	7.147	7.220	10.055
57.01	1.976	2.777	2.630	3.370
63.11	2.969	0.264	1.764	0.977
69.21	-1.027	-6.488	-5.715	-6.710
75.32	0.750	-5.637	-2.676	-2.491
81.42	-4.757	-9.438	-6.455	-7.219
87.52	1.852	5.098	0.900	1.150
93.63	-4.434	-9.462	-9.793	-10.573
99.73	-4.379	-10.420	-13.190	-11.913
105.83	-3.798	-16.009	-13.938	-17.303
111.94	-1.821	-13.072	-14.643	-14.185
118.04	3.378	0.304	-1.654	-1.833
124.14	-1.610	-16.731	-22.148	-21.842
130.25	-1.349	-6.529	-15.146	-16.906
135.13	-2.292	-11.453	-58.557	-58.301

Note: Regions of cavitation pressure is indicated with red text.

6.5.5 Ski-jump Trajectory Results

As previously stated in **Subsection 6.5.1.3**, the implementation of the Y-Shape FGP together with the slit-type flip bucket projected the flow over the stepped spillway. Air concentration and pressure measurements were therefore deemed redundant and the upper and lower trajectory of the ski-jump was recorded.

The geometric projection of the upper and lower ski-jump trajectories were recorded at four measuring positions. These positions do not represent distinctive locations on the trajectory and were used merely to determine the flow trajectory. The geometric results for the upper and lower trajectory are tabulated in **Table 6.12**. The flip-bucket lip was defined as the point of origin. The horizontal distance was indicated on the X-axis and the vertical distance was indicated on the Y-axis. It should be noted that the positive direction of the Y-axis is defined to increase as the elevation decreases.

Table 6.12: Trajectory results (m) for the Y-Shape FGP and slit-type flip bucket.

Measuring Positions	Lower Trajectory							
	50 m ² /s		100 m ² /s		150 m ² /s		200 m ² /s	
	X (m)	Y (m)	X (m)	Y (m)	X (m)	Y (m)	X (m)	Y (m)
Position 1	0.00	0.00	0.00	0.00	0.00	0.00	0.00	0.00
Position 2	27.84	28.70	27.84	27.88	27.84	21.38	27.84	11.08
Position 3	49.97	54.08	49.97	53.33	49.97	44.93	49.97	33.03
Position 4	63.47	75.00	67.47	75.00	70.47	75.00	71.97	75.00
Measuring Positions	Upper Trajectory							
	50 m ² /s		100 m ² /s		150 m ² /s		200 m ² /s	
	X (m)	Y (m)	X (m)	Y (m)	X (m)	Y (m)	X (m)	Y (m)
Position 1	0.00	-5.92	0.00	-10.22	0.00	-11.37	0.00	-45.00
Position 2	27.84	-1.02	27.84	3.18	27.84	-0.82	27.84	-32.47
Position 3	49.97	10.68	49.97	17.33	49.97	12.78	49.97	-13.47
Position 4	99.98	75.00	88.97	75.00	92.72	75.00	97.82	75.00

6.6 Analysis of the Test Results on the Type B Stepped Spillway

The data, as presented in **Section 6.5**, was analysed in order to establish the spillway performance for the different aeration structures. The spillway performance was assessed by either a cavitation evaluation or by geometric analysis, depending on the model.

The cavitation evaluation was performed to determine whether cavitation damage would occur on the stepped spillway and to what extent the safe unit discharge capacity could be increased. The analysis was based on the centreline air concentration and pressure results. The geometric analysis was used to establish the performance of the ski-jump trajectory for the Y-Shape FGP with the slit-type flip bucket.

6.6.1 Cavitation Evaluation

6.6.1.1 Cavitation Limits

The evaluation and interpretation of the cavitation analysis was based on the visual presentation of the air concentration and pressure results. Until now, contour plots had been used to illustrate the air concentration and pressure results, provided that the data was recorded over the length and width of the spillway. As the air concentration was measured only in the centre of the discharge bay, this method was not applicable. The cavitation evaluation was thus based on the centreline comparison of the air concentration and pressure results along the length of spillway. As the spillway pressures were recorded along the length and across the width of the spillway, pressure contour plots were used to illustrate the spillway performance. The contour plots implemented a distinct colour scale, where the boundary between yellow and green represented the -7 m water pressure (dashed contour). Detailed results are presented in **Appendix E** and **F**.

As previously mentioned, the critical air concentration and pressure boundaries were defined as 8% and -7 m, respectively. Peterka (1953) stated that a local air concentration of 8% is sufficient to absorb the shock of imploding vapour bubbles, thus eliminating the risk of cavitation damage. The cavitation pressure limit was defined as -7 m atmospheric pressure head, which was transformed to represent a dimensionless pressure parameter of -7 for a constant prototype step height of 1 m.

Please note that each contour plot implements a distinct colour scale which corresponds to the specific model setup and discharge.

6.6.1.2 Control Experiment (Model Setup 8)

Apart from those in China, the majority of prototype stepped spillways do not commonly implement aeration structures to increase the safe unit discharge capacity. A study by Calitz (2015) identified the safe unit discharge capacity of a standard stepped spillway with a 51.3° inclination angle and 1.5 m step height to be $25 \text{ m}^2/\text{s}$. The baseline performance for the FGP investigation was thus set by a typical stepped spillway design consisting of an ogee crest without piers. By considering the safe unit discharge capacity of the previous investigation, cavitation damage is expected for the current spillway, at even the low unit discharge of $50 \text{ m}^2/\text{s}$. The corresponding cavitation evaluation which illustrates the centreline air concentration and pressure results, together with the pressure contour plots for the control experiment, is displayed in **Figure 6.17**.

The air concentration results indicated air entrainment only for the unit discharge of $50 \text{ m}^2/\text{s}$. For this specific discharge, the pseudo-bottom inception point was located at $L_p = 88.6 \text{ m}$ and the critical air concentration boundary was reached at $L_p = 100.6 \text{ m}$. Very little to no aeration was measured for the unit discharges of $100 \text{ m}^2/\text{s}$, $150 \text{ m}^2/\text{s}$ and $200 \text{ m}^2/\text{s}$. The lack of air entrainment was attributed to the relatively small steps, compared to the flow depth. These steps had a negligible effect on the development of the boundary layer and corresponding surface roughness. The lack of air entrainment meant that the boundary layer never protruded through the water surface to initiate the self-aeration process of the spillway. The recirculating step vortices were small and weak in comparison with the strong skimming flow regime which was observed on the spillway.

The centreline pressure results can be described as a wavy pattern, which illustrated that a portion of the flow was slightly redirected by the steps. A similar, smaller pattern was observed for the pressure results of Calitz (2015). The contour plots indicated multiple regions of cavitation pressure for each of the discharges. The first of these regions were observed at a position approximately 80 m (L_p) downstream of the spillway crest. Similar to the contour plot, the cavitation analysis, as illustrated in **Figure 6.17**, also displayed multiple cavitation regions in the centre of the discharge bay. These regions coincided with areas of insufficient air concentration, ultimately leading to a likelihood of cavitation damage for all of the unit discharges under consideration.

Chapter 6

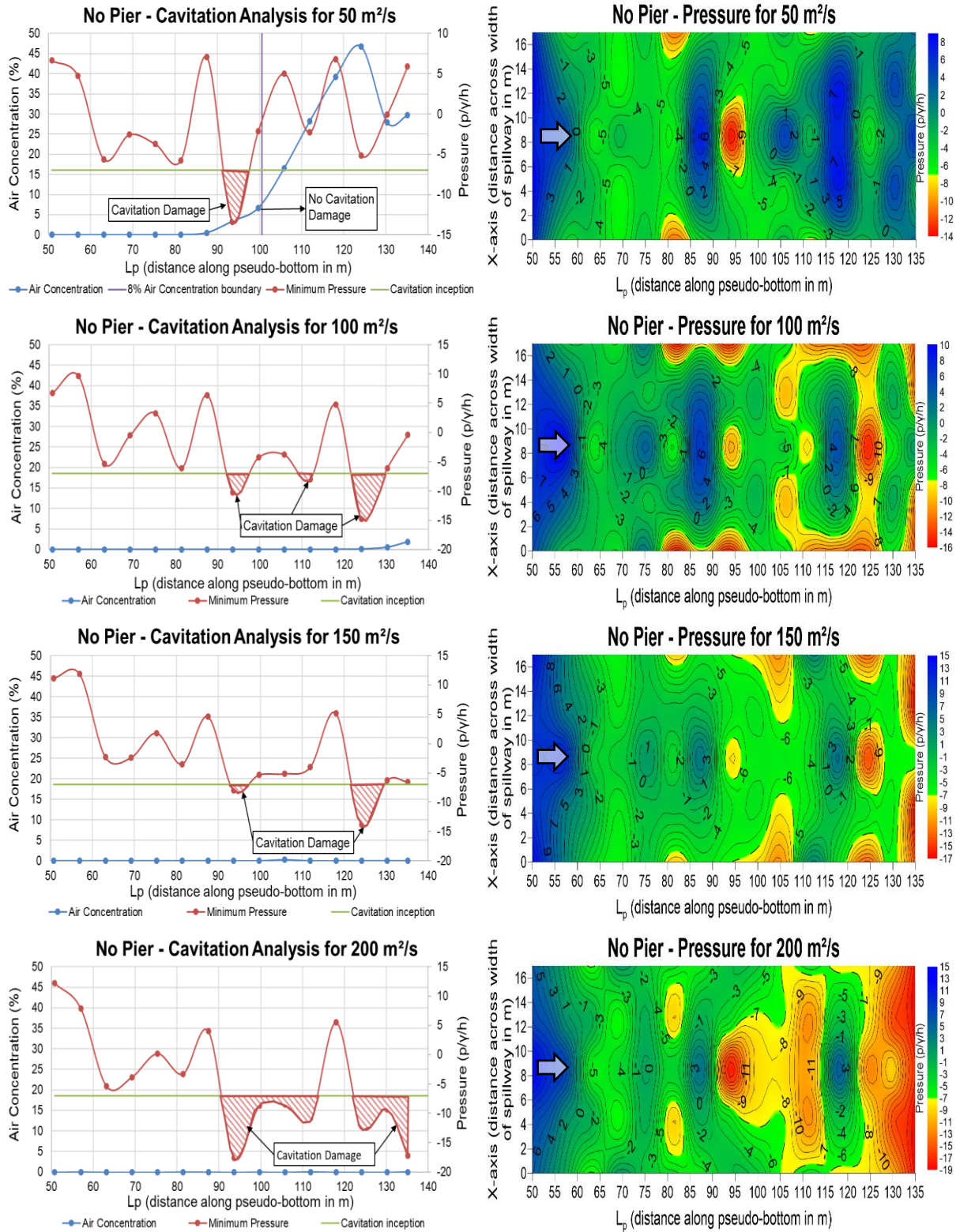


Figure 6.17: Cavitation analysis based on the air concentration and pressure measurements for the control experiment.

6.6.1.3 Y-Shape FGP Evaluation

The performance assessment of the Y-Shape FGP was based on the air concentration and pressure results as illustrated in **Figure 6.18**. The graphs demonstrate the centreline air concentration and minimum pressure results along the length of the spillway, while the contour plots display the pressure results on the spillway area. The dashed, horizontal lines on the contour plot define the flare extremities on either side of the central discharge bay.

At the upstream section of the spillway, $L_p = 63.1$ m, the air concentration was measured as exceeding 20% for all the unit discharges. It is believed that the increased air concentration is attributable to the combined implementation of the larger first step, together with the Y-Shape FGP. An air cavity is formed on the first step niche, from which air is entrained at the pseudo-bottom. Air is fed to this cavity from the downstream end of the flare. A decreasing trend in the air concentration results was observed along the length of the spillway. As previously mentioned in **Section 2.4.4**, the decreasing air concentration was due to the detrainment of air within the impact regions. For the unit discharge of $50 \text{ m}^2/\text{s}$, increasing air concentration results were observed downstream of the impact region. Overall, the Y-Shape FGP entrained more air as compared to the control experiment; however, air was detrained within the impact regions.

The pressure contour plots displayed several cavitation regions which occurred predominantly in the centre of the discharge bay, between the flare extremities. Two distinct cavitation regions were observed for each discharge. The first was located between 93 m and 112 m, while the second extended from 124 m to 135 m along the length of the spillway (L_p). The centreline pressure results identified the same cavitation regions, which formed a similar wavy pattern as had been observed in the control experiment. However, these patterns were more distinct and profound. The cavitation evaluation identified several areas vulnerable to cavitation damage for each of the tested discharges. The overall performance of the spillway was not improved with the addition of the FGP, since the safe unit discharge capacity would be less than $50 \text{ m}^2/\text{s}$. However, this could be increased to $200 \text{ m}^2/\text{s}$ if the spillway length were limited to 90 m or the operation of the spillway were to be accompanied by a substantial rise in the tail water levels.

Chapter 6

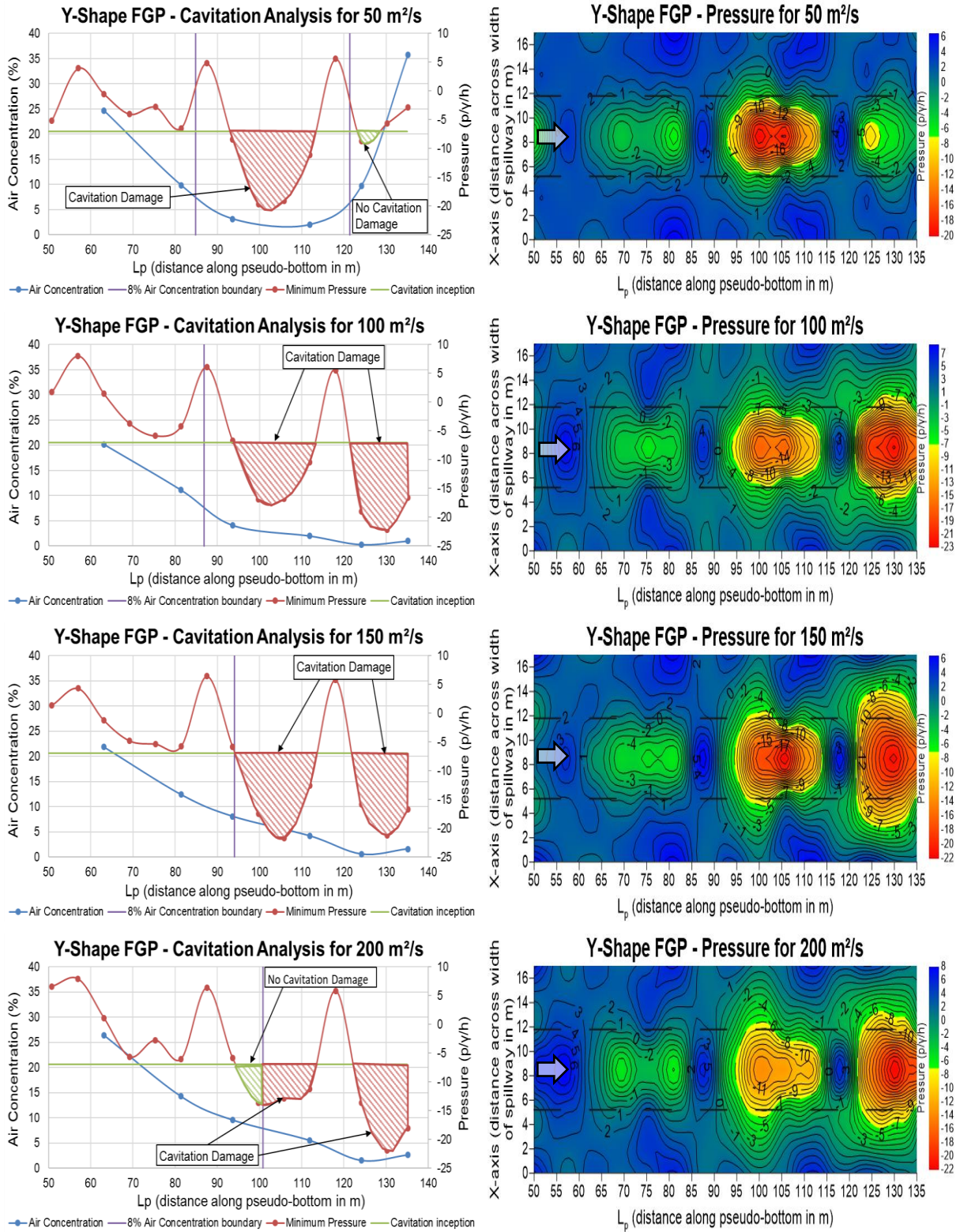


Figure 6.18: Cavitation analysis based on the air concentration and pressure measurements for the Y-Shape FGP experiment.

6.6.1.4 X-Shape FGP Evaluation

The cavitation analysis for the X-Shape FGP was performed in a similar manner as for the control experiment and Y-Shape FGP. The evaluation was based on the centreline air concentration and pressure results, as well as a pressure contour plot for each of the unit discharges. As previously stated, the dashed, horizontal lines on the contour plot illustrate the flare extremities on either side of the central discharge bay. See **Figure 6.19** for a visual comparison of the X-Shape FGP performance.

A remarkable improvement in the spillway performance was noticed for the unit discharge of 50 m²/s. Sufficient amounts of air were entrained along the entire spillway length, whilst a minimum air concentration of 11% was recorded at $L_p = 93.63$ m (minimum value on the graph is an interpolation). However, this improvement was brief, since the remainder of the unit discharges recorded reduced air concentrations at the upstream section of the spillway compared to the performance of the Y-Shape FGP. It is believed that this was due to the wider bottom outlet design, which made it difficult to efficiently feed air to the middle of the discharge bay via the large first step. A similar decreasing air concentration trend was witnessed along the length of the spillway, which is attributed to the detrainment of air within the impact regions. An increased aeration was measured downstream of the impact region for the unit discharge of 100 m²/s ($L_p = 124$ m to $L_p = 135$ m).

Similar to the air concentration performance for the X-Shape FGP, a remarkable improvement in terms of the spillway pressures was noticed for the unit discharge of 50 m²/s. No cavitation pressures were recorded along the length or across the width of the discharge bay. For the unit discharges of 100 m²/s, 150 m²/s and 200 m²/s, cavitation pressures were measured within the middle and downstream sections of the spillway. Considerably larger cavitation regions were recorded for the unit discharges of both 150 m²/s and 200 m²/s, which stretched across the entire width of the discharge bay. Not only were the cavitation regions increased in size, compared to the Y-Shape FGP, but a minimum dimensionless pressure of -58 was measured at the downstream section of the spillway. This is a decrease of 325% compared to the corresponding pressure for the Y-Shape FGP. The centreline pressure results displayed two distinct cavitation regions along the length of the spillway. As illustrated in **Figure 6.19**, cavitation damage would have occurred for all of the unit discharges, except for the unit discharge of 50 m²/s.

The implementation of the X-Shape FGP thus increased the safe unit discharge capacity of the stepped spillway to 50 m²/s. At higher discharges, severe negative pressures were measured in the downstream region of the spillway, which are highly unfavourable.

Chapter 6

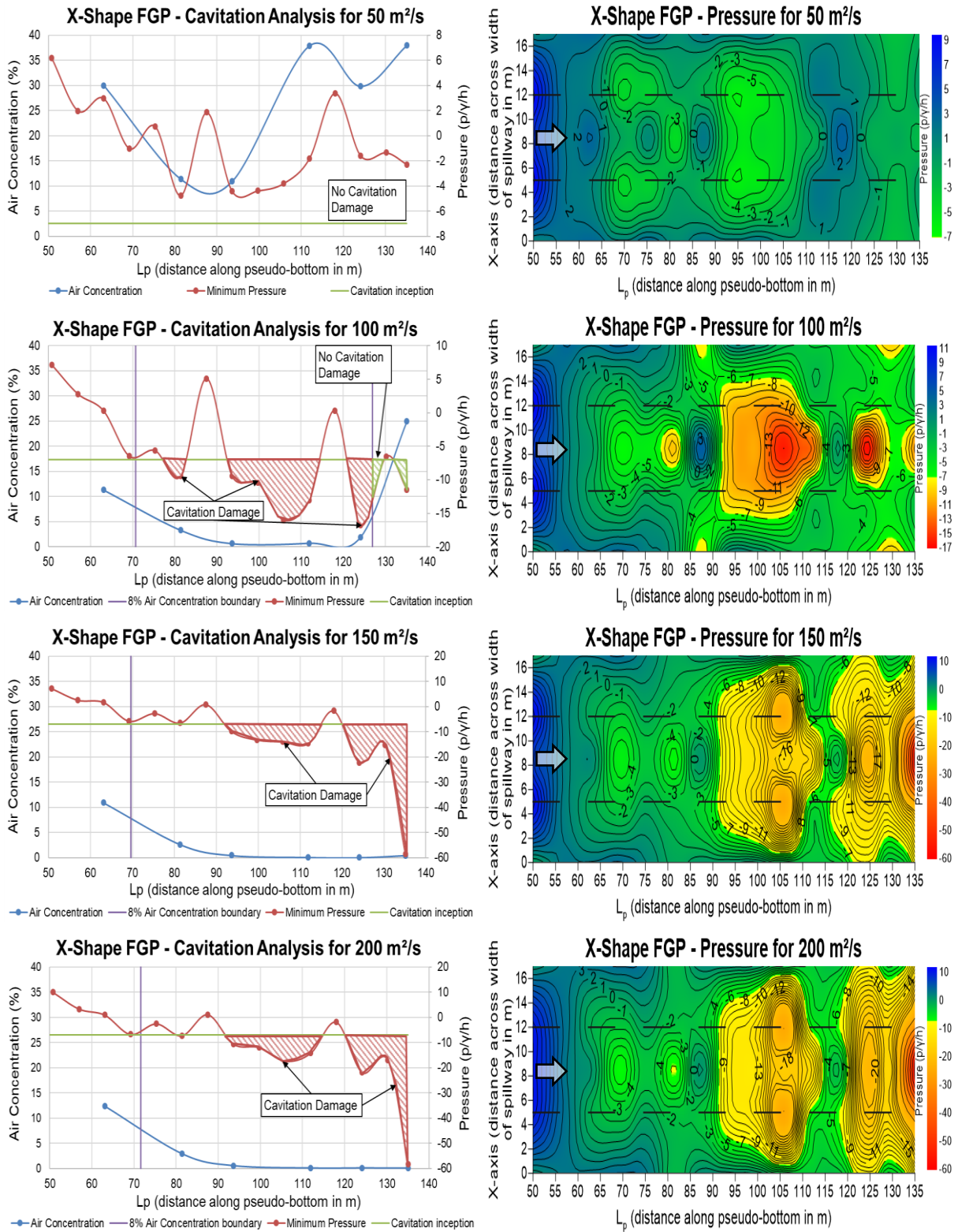


Figure 6.19: Cavitation analysis based on the air concentration and pressure measurements for the X-Shape FGP experiment.

6.6.2 Y-Shape FGP and Slit-type Flip Bucket Evaluation

The implementation of the slit-type flip bucket together with the Y-Shape FGP significantly altered the flow pattern and projected the water over the entire length of the spillway. Instead of recording the spillway air concentration and pressures, which would have been redundant, the trajectory of the ski-jump was measured for each of the flow conditions. The lower and upper trajectory of the ski-jump is indicated in **Figure 6.21** and **Figure 6.22**, respectively.

As stated in **Section 2.4.4** and as described for both the Y- and X-Shape FGP evaluation, impact regions on stepped spillways are extremely undesirable. Not only is air detrained within the impact regions, but severe negative pressures are caused by the shearing action on the step corners. It was thus crucial that the impact of the ski-jump regime was located downstream of the spillway. The lower trajectory profiles, as displayed in **Figure 6.21**, indicated that the impact region would occur downstream of the spillway, irrespective of the unit discharge under consideration. A directly proportional relationship was noticed between the horizontal throw distance and the unit discharge. As the unit discharge increased, so too did the horizontal throw distance at the downstream section of the spillway.

A different relationship between the discharge rate and trajectory was observed for the upper trajectory as illustrated in **Figure 6.22**. The horizontal throw distance of the 50 m²/s unit discharge exceeded that of the 100 m²/s, 150 m²/s and 200 m²/s unit discharges. The upper trajectory of the 50 m²/s unit discharge was very dispersed as compared to the other, which formed distinctive jets. It was considered that this was caused by the weak lateral contraction from the flares, compared to the strong deflection from the flip bucket. Instead of generating a stable collision in the air, the deflection from the flip bucket overpowered the collision point and the water deflection was higher compared to that of the other discharges.



Figure 6.20: Photographs comparing the projected trajectory for the unit discharges of (i) 50 m²/s and (ii) 100 m²/s.

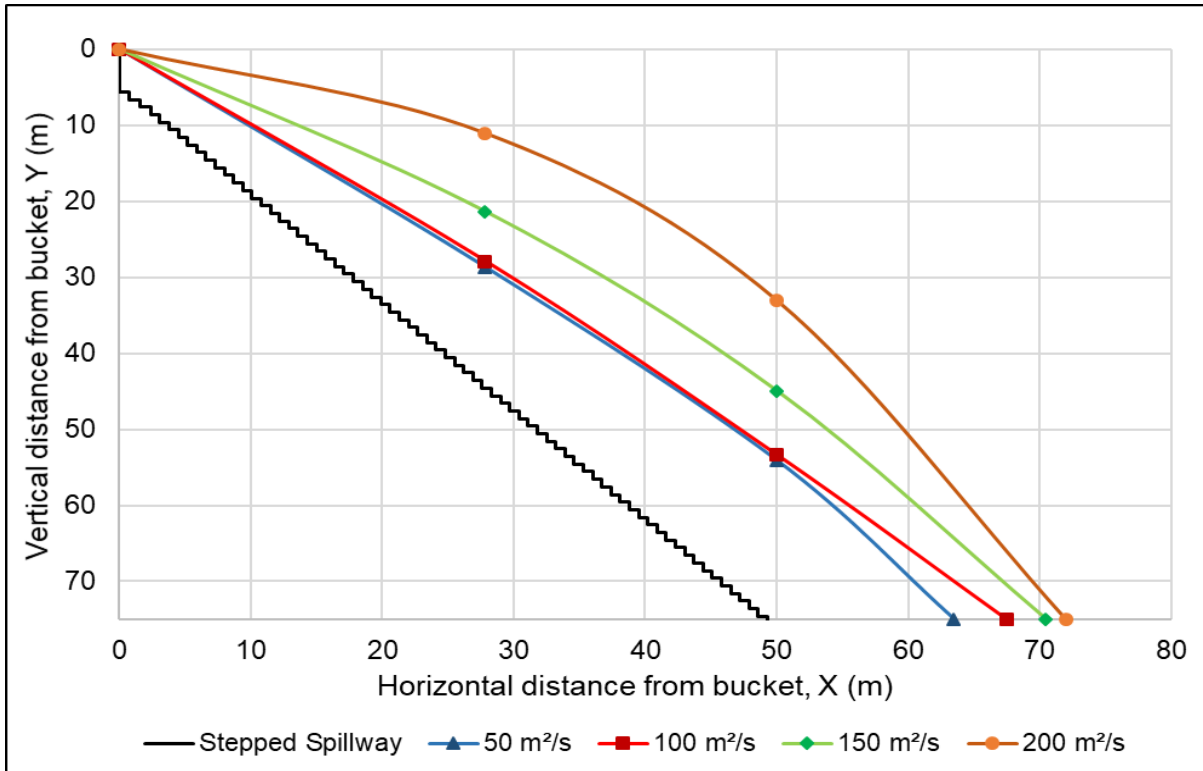


Figure 6.21: Graphical comparison of the lower trajectory for the Y-Shape FGP and flip bucket.

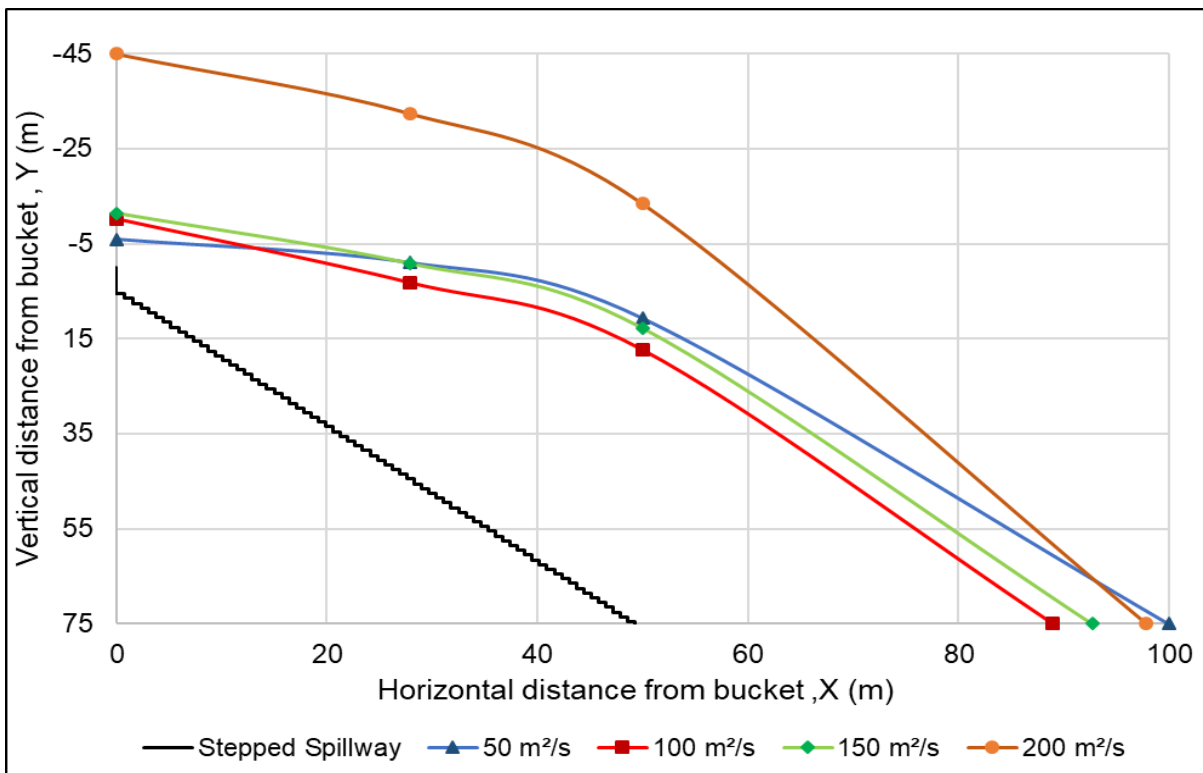


Figure 6.22: Graphical comparison of the upper trajectory for the Y-Shape FGP and flip bucket.

6.7 Summary of the Type B Stepped Spillway Experiments

The results and analysis of the Type B stepped spillway investigation are summarised in brief conclusions. The most notable of these are the improvement of the safe unit discharge to 50 m²/s with the X-Shape FGP. Although the X-Shape FGP increased the safe discharge capacity of the spillway, its performance at higher unit discharges generated severe negative pressures in the downstream region of the spillway. The performance of the Y-Shape FGP was remarkably constant, irrespective of the unit discharge under consideration. Not only were the air concentration and pressure results similar but, at the higher discharges, the Y-Shape FGP performed better than the X-Shape FGP.

The Dachaoshan Dam's stepped spillway design consisted of 44 steps, which corresponds to a spillway length of 102 m. On the other hand, the physical model design of the stepped spillway implemented 71 steps which related to a spillway length of 135 m. The additional steps were added to ensure that the required data could be captured accurately, regardless of the prototype design. The spillway length from the crest apex to the position upstream of the first cavitation pressure, is herein after deemed the 'safe spillway length' (L_s). This length was determined for each of the model layouts, as tabulated in **Table 6.13**. These results illustrate the constant performance of the Y-Shape FGP for the various unit discharges compared to that of the control experiment and the X-Shape FGP. In a specific assessment of the prototype spillway design (102 m), together with the implementation of the Y-Shape FGP, a maximum spillway length of 10.5 m is exposed to cavitation damage at the downstream section. This meant that a tail water level of 9 m above the last step could be sufficient to eliminate the risk of cavitation damage for all the tested discharges. Since most of the dams in China are constructed within narrow valleys, high tail water levels are effortlessly achieved and the possibility of safe, high unit discharges are probable.

Table 6.13: Safe spillway length for the different model setups (dimensions in m prototype).

Model Setup	Safe Spillway Length, L_s (m)			
	50 m ² /s	100 m ² /s	150 m ² /s	200 m ² /s
No FGP (Model Layout 8: Control)	78.3	78.4	79.8	62.9
Y-Shape FGP (Model Layout 9)	92.2	93.2	91.5	92.2
X-Shape FGP (Model Layout 10)	> 135	77.5	81.1	81.1
Y-Shape FGP & Flip Bucket (Model Layout 11)	> 135	> 135	> 135	> 135

7 Conclusions

The central purpose of the study was to improve the safe unit discharge capacity of stepped spillways by studying the air concentration and pressure on the pseudo-bottom of the spillway chute for the different aeration structures. Two physical model experiments were conducted to assess the performance of each of these structures. A 1:15 scale, Type A stepped spillway model was used to evaluate the effect of different pier nose designs, lengths and the addition of an X-Shape FGP. The second model, a 1:50 scale, Type B stepped spillway model was used to evaluate the design of the X- and Y-Shape FGP together with a slit-type flip bucket for high unit discharges of up to 200 m²/s. The performance of the aeration structures, for both spillway configurations, were compared to a control experiment which consisted of a stepped spillway and no crest piers.

7.1 Literature Conclusions

Several conclusions from the literature investigation were important for the experimental results and the analysis thereof. These conclusions are:

- Experimental investigations by several authors indicated that an entrained air concentration of 5 to 8% at the spillway surface is sufficient to protect a concrete specimen of 10 to 20 MPa compressive strength against cavitation damage.
- Research by Chanson (1994a) and Pfister *et al.* (2006) described the process of de-aeration within impact regions, specifically on stepped spillways. Chanson found that up to 80% of the entrained air was detrained within these impact regions. This knowledge regarding impact detrainment proved to be extremely important in the interpretation and analysis of the FGP performance.
- Based on the literature, it is generally accepted that the physical model scale should be larger than 1:20 to minimise the aeration scale effects to within acceptable limits. However, recent investigations by Chanson (2007, 2008), Felder (2017) and Heller (2017) observed a self-similar relationship pertaining to the measurement of air concentration. These authors proved that the self-similarity of air concentration (not air bubble size) implies that it can accurately be recorded, independent of model scale, provided that the Reynolds number of the model is greater than 8×10^4 .
- Accessible literature on the design and performance of the FGP aeration structures, as used on several existing Chinese dams, is limited. However, the available information mentioned that a few of the existing dams have been designed for unit discharges exceeding 200 m²/s.

7.2 Hydraulic Model Conclusions

7.2.1 Type A Stepped Spillway Investigation

A few important conclusions came from the Type A stepped spillway investigation, which are summarised as follows:

- The maximum, safe unit discharge capacity of a stepped spillway without crest piers was previously determined to be 25 m²/s (Calitz, 2015). The implementation of the short, bullnose pier at the spillway crest increased the safe unit discharge capacity to 30 m²/s, by eliminating the risk of cavitation damage. This was the only crest pier design that increased the discharge capacity.
- The full-length spillway investigation concerning the bullnose and parabolic X-Shape FGP, did not improve the spillway performance, compared to that of the control experiment without piers. Nonetheless, the results were of value as they enhanced the understanding of the FGP performance and design. The impact regions should ideally be located downstream of the spillway toe, to avoid the de-aeration of the flow and the accompanying cavitation pressures. Implementation of the FGP design ought to be accompanied by a smooth ogee crest, thus making it possible to achieve high velocities, which would maximise the deflection.

7.2.2 Type B Stepped Spillway Investigation

The Type B stepped spillway was investigated to determine how the existing, high unit discharge, stepped spillways in China performed with respect to aeration and pressure on the pseudo-bottom for each of the aeration structures. The conclusions are summarised as:

- The most notable improvement was the increase of the safe unit discharge capacity to 50 m²/s in the case of the X-Shape FGP. Air concentrations above the 8% limit were recorded along the length of the spillway, whilst the entire spillway area ($L_p = 50$ m and $L_p = 135$ m) was free of cavitation pressures. This design is not advised for higher unit discharges, since it generated severe negative pressures at $L_p = 135$ m.
- The spillway performance of the Y-Shape FGP was the most consistent, irrespective of the unit discharge. Not only were the air concentration and pressure results similar, but at higher unit discharges, the Y-Shape FGP outperformed the X-Shape FGP. However, cavitation regions were observed in a small section on the downstream end of the spillway ($L_p = 91$ m to 135 m). Future research is required to determine the tail water level in a downstream stilling basin, which would prevent cavitation damage in the downstream region.

- The Y-Shape FGP, together with the slit-type flip bucket, projected the flow over the entire length of the stepped spillway for all the tested unit discharges (50 m²/s to 200 m²/s). As none of the water was discharged via the stepped spillway, it was free of exposure to cavitation damage. As the impact region was located downstream of the modelled spillway, the impact pressure and possible scour formation downstream of the dam wall was not investigated.

8 Recommendations

Based on the findings of this thesis, the following recommendations are advised for further investigation of the Type B stepped spillway to better understand the performance of the FGP:

- As cavitation pressures were observed in the downstream section of the spillway for both the X- and Y-Shape FGP, it is considered that these cavitation regions could be eliminated by high tail water levels downstream of the spillway. Further research is thus advised to determine the spillway performance with different tail water levels for the implementation of the various FGP designs.
- Since high velocities are present at the flare position, there is a possibility of cavitation pressures on the flare surface. A CFD investigation by Ting, *et al.* (2011) observed no negative pressures for the Y-Shape FGP, but a negative pressure of approximately -2 m was observed at the bottom outlet for the X-Shape FGP. This meant that there was some form of flow separation from the flare surface. This should be investigated by using a physical model study for a range of different unit discharges.
- As indicated by the results of the Y-Shape FGP and slit-type flip bucket, the flow was projected over the stepped spillway, where it impacted downstream of the modelled dam wall. Future research is required to determine the stilling basin water depth or plunge pool scour depth that will efficiently absorb the energy of the projected flow.
- As these FGP structures are very large, and therefore costly, a proposed alternative would be to only use the flare part of the structure without the piers, i.e. an uncontrolled crest design, as shown in Figure 8.1. This would lead to a reduced cost as only the flaring structure/flip bucket would be required. This alternative would not, however, be possible for the X-Shape FGP, as the base is too thin.

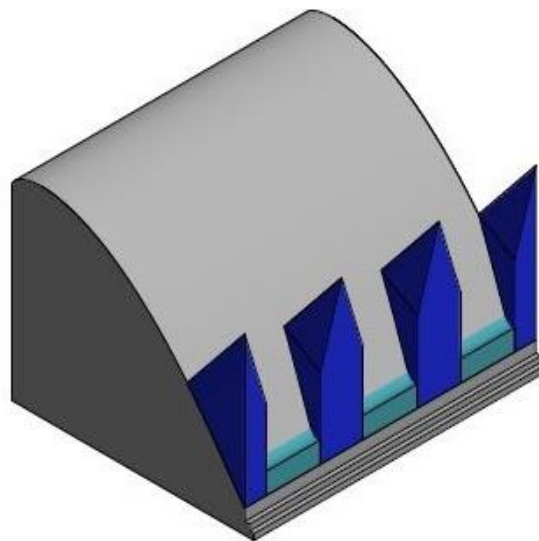


Figure 8.1: Possible implementation of the Y-Shape FGP and slit-type flip bucket.

References

- Amador, A., Sánchez-Tembleque, F., Sánchez-Juny, M., Puertas, J. and Dolz, J., 2004a. *Velocity and pressure field in skimming flow in stepped spillways*. Taylor & Francis, London.
- Amador, A., Van der Graaf, G., Sánchez-Juny, M., Dolz, J., Sánchez-Tembleque, F., Puertas, J. and Girona, C.J., 2004b. *Characterization of the flow field in a stepped spillway by PIV*, Proceedings 12th Symposium: Applications Laser to Fluid Mechanics, pp. 12-15.
- Amador, A., Sánchez-Juny, M. and Dolz, J., 2005. *Discussion of "Two-phase flow characteristics of stepped spillways" by Robert M. Boes and Willi H. Hager*. Journal of Hydraulic Engineering, Volume 131, pp. 421-423.
- Amador, A., Sánchez-Juny, M. and Dolz, J., 2009. *Developing flow region and pressure fluctuations on steeply sloping stepped spillways*. Journal of Hydraulic Engineering, Volume 135, pp. 1092-1100.
- Anonymous, 2013, *Acquainted to outboard motors* [Homepage of Boatfix.blogspot.co.za], [Online]. Available: <http://boatfix.blogspot.co.za/2011/05/acquainted-to-outboard-motors.html> [2017/03/23].
- Anonymous, 2012, 2012/02/15-last update, *Guizhou Wujiang Suofengying Hydropower Station* [Homepage of China Civil Engineering Society], [Online]. Available: <http://123.57.212.98/html/tm/29/38/69/content/1012.html> [2017/06/29].
- ASCE, 1995. *Hydraulic design of spillways*. American Society of Civil Engineers.
- Bakker, A., 2006. *Applied computational fluid dynamics*. Fluent Incorporated, Computational Fluid Dynamics class lecture 11.
- Bass, R.P., 1993. *Roller Compacted Concrete provides design alternative for dam construction*.
- Baylar, A., Emiroglu, M.E. and Bagatur, T., 2006. *An experimental investigation of aeration performance in stepped spillways*. Water and Environment Journal, Volume 20, pp. 35-42.
- Bo, W., Chao, W., Hu, Y. and Mo, Z., 2007. *Relationship of first step height, step slope and cavity in X-shaped flaring gate piers*. Journal of Hydrodynamics, Volume 19, pp. 349-355.
- Boes, R., 2000. *Scale effects in modelling two-phase stepped spillway flow*, International Workshop on Hydraulics of Stepped Spillways, Balkema Publications, pp. 53-60.
- Boes, R.M., 1999. *Physical model study on two-phase cascade flow*, Proceedings 28th IAHR Congress.
- Boes, R.M. and Hager, W.H., 2003a. *Two-phase flow characteristics of stepped spillways*. Journal of Hydraulic Engineering, Volume 129, pp. 661-670.

References

- Boes, R.M. and Minor, H., 2000. *Guidelines for the hydraulic design of stepped spillways*, Proceedings, International Workshop on Hydraulics of Stepped Spillways, Balkema, Rotterdam, The Netherlands, pp. 163-170.
- Boes, R. and Hager, W., 2003b. *Hydraulic design of stepped spillways*. Journal of Hydraulic Engineering, Volume 129, pp. 671-679.
- Breusers, H., Nicollet, G. and Shen, H., 1977. *Local scour around cylindrical piers*. Journal of Hydraulic Research, Volume 15, pp. 211-252.
- Calitz, J., 2015. *Investigation of air concentration and pressures of a stepped spillway equipped with a crest pier*, Stellenbosch University.
- Carosi, G. and Chanson, H., 2008. *Turbulence characteristics in skimming flows on stepped spillways*. Canadian Journal of Civil Engineering, Volume 35, pp. 865-880.
- Çengel, Y.A., Cimbala, V. and John, M., 2006. *Fluid mechanics fundamentals and applications. Mecánica de fluidos: fundamentos y aplicaciones*.
- Chadwick, A., Morfett, J. and Borthwick, M., 2013. *Hydraulics in civil and environmental engineering*. 5th edition CRC Press.
- Chamani, M., 2000. *Air inception in skimming flow regime over stepped spillways*, Proceedings, International Workshop on Hydraulics of Stepped Spillways, Balkema, Rotterdam, The Netherlands, pp. 61-67.
- Chamani, M. and Rajaratnam, N., 1999. *Onset of skimming flow on stepped spillways*. Journal of Hydraulic Engineering, Volume 125, pp. 969-971.
- Chanson, H., 2009. *Turbulent air–water flows in hydraulic structures: dynamic similarity and scale effects*. Environmental Fluid Mechanics, Volume 9, pp. 125-142.
- Chanson, H. and Toombes, L., 2002. *Experimental investigations of air entrainment in transition and skimming flows down a stepped chute*. Canadian Journal of Civil Engineering, Volume 29, pp. 145-156.
- Chanson, H., 2008. *Physical modelling, scale effects, and self-similarity of stepped spillway flows*, World Environmental and Water Resources Congress, pp. 1-10.
- Chanson, H., 2004. *Historical development of stepped cascades for the dissipation of hydraulic energy*, Volume 72, pp. 295-318.
- Chanson, H., 2000. *Hydraulics of stepped spillways: Current status*. Journal of Hydraulic Engineering, Volume 126, pp. 636-637.
- Chanson, H., 1996. *Prediction of the transition nappe/skimming flow on a stepped channel*. Journal of Hydraulic Research, Volume 34, pp. 421-429.
- Chanson, H., 1994a. *Aeration and deaeration at bottom aeration devices on spillways*. Canadian Journal of Civil Engineering, Volume 21, pp. 404-409.
- Chanson, H., 1994b. *Hydraulic design of stepped cascades, channels, weirs and spillways*.
-

References

- Chanson, H. and Carosi, G., 2007. *Turbulent time and length scale measurements in high-velocity open channel flows*. Experiments in Fluids, Volume 42, pp. 385-401.
- Chen, C. and Zhang, F., 2015. *Research on effect of contraction angle and ratio of flaring piers on pressure in stilling basin*.
- Cheng, Y., 2005, *Construction of the dam*. Available: <http://www.sdic.com.cn/exhibit2005/sheying/tuji1.htm> [09/09].
- CHINCOLD, 2004. *A brief introduction to Dachoashan Hydropower project*.
- Colgate, D. and Elder, R., 1961. *Design considerations regarding cavitation in hydraulic structures*, Proceedings of 10th Hydraulic Division Conference of American Society of Civil Engineers.
- Deng, Z., 1988. *Problems of flood relief/energy dissipation and high-velocity flow at Wujiangdu Hydropower Station*, International Symposium on Hydraulics for High Dams, pp. 230-238.
- Ditchey, E. and Campbell, D., 2000. *Roller compacted concrete and stepped spillways*, International Workshop on Hydraulics of Stepped Spillways, Balkema, pp. 171-178.
- Eckhard, S., 2016, 06/01/2016-last update, *Conductivity and temperature needle probes* [Homepage of HZDR], [Online]. Available: <https://www.hzdr.de/db/Cms?pOid=11943&pNid=0> [2016/11/17].
- Evans, I., 2017, 14 June 2017 *Oroville dam incident explained: what happened, why and what's next*. News Deeply.
- Falvey, H.T., 1990. *Cavitation in chutes and spillways*. US Department of the Interior, Bureau of Reclamation.
- Fattor, C.A., Lopardo, M.C., Casado, J.M. and Lopardo, R.A., 2001. *Cavitation by macroturbulent pressure fluctuations in hydraulic jump stilling basins*, Proceedings, International Association for Hydraulic Research, pp. 415-420.
- Felder, S. and Chanson, H., 2017. *Scale effects in microscopic air-water flow properties in high-velocity free-surface flows*. Experimental Thermal and Fluid Science, Volume 83, pp. 19-36.
- Frizell, K.W., Renna, F.M. and Matos, J., 2012. *Cavitation potential of flow on stepped spillways*. Journal of Hydraulic Engineering, Volume 139, pp. 630-636.
- Frizell, K.W., 2016. *Theory of use and operation of reclamation's low ambient pressure chamber (LAPC)*.
- Frizell, K.W. and Renna, F., 2009. *Cavitation potential of the Folsom Auxiliary Stepped Spillway*.
- Grambeau, T., 2017, *Amazing images of nature*. Available: <http://tiin.vn/chuyen-muc/24/nhung-buc-anh-dang-kinh-ngac-ve-tu-nhien.html> [2017/06/15].
- Guo, J., 2012. *Recent achievements in hydraulic research in China*.
-

References

- Hager, W.H., 1991. *Uniform aerated chute flow*. Journal of Hydraulic Engineering, Volume 117, pp. 528-533.
- Hay, D., 1988. *Model-prototype correlation: Hydraulic structures*, ASCE, pp. 1-24.
- Heller, V., 2017. *Self-similarity and Reynolds number invariance in Froude modelling*. Journal of Hydraulic Research, Volume 55, pp. 293-309.
- Heller, V., 2011. *Scale effects in physical hydraulic engineering models*. Journal of Hydraulic Research, Volume 49, pp. 293-306.
- Hongta Group, 2017, 2017/01/01-last update, *Dachaoshan Dam*. Available: http://www.hongta.com/language/en/aboutus/htcy/201110/t20111012_148018.htm [2017/06/25].
- James, C., Comminos, M. and Palmer, M., 1999. *Effects of slope and step size on the hydraulics of stepped chutes*. Journal of the South African Institution of Civil Engineering, Volume 41.
- Kermani, E.F., Barani, G. and Ghaeini-Hessaroeiyeh, M., 2013. *Investigation of cavitation damage levels on spillways*. World Applied Sciences Journal, Volume 21, pp. 73-78.
- Khatsuria, R.M., 2004. *Hydraulics of spillways and energy dissipators*. CRC Press.
- Kobus, H., 1984. *Local air entrainment and detrainment*.
- Kolke, D., 2017. *Oroville dam spillway damage, February 27, 2017*. California Department of Water Resources.
- Large Dam Safety Supervision Centre, 2015, *Suofengying Hydropower Station*. Available: <http://www.dam.com.cn/damView/view.jsp?id=1301> [2017/07/09].
- Lin, B., Li, G. and Chen, H., 1987. *Hydraulic Research in China*. Journal of Hydraulic Engineering, Volume 113, pp. 47-60.
- Ljubomir, T., 2005. *Dams and appurtenant hydraulic structures*.
- Matos, J., 2000. *Hydraulic design of stepped spillways over RCC dams*, International Workshop on Hydraulics of Stepped Spillways, Balkema Publications, pp. 187-194.
- Matos, J. and Meireles, I., 2014. *Hydraulics of stepped weirs and dam spillways: Engineering challenges, labyrinths of research*, 11th National Conference on Hydraulics in Civil Engineering & 5th International Symposium on Hydraulic Structures: Hydraulic Structures and Society-Engineering Challenges and Extremes, Engineers Australia, pp. 330.
- Matos, J., Quintela, A., Sánchez-Juny, M. and Dolz, J., 2000. *Air entrainment and safety against cavitation damage in stepped spillways over RCC dams*, Proceedings, International Workshop on Hydraulics of Stepped Spillways.
- Nan, F. and Romyantsev, I., 2014. *Modeling of flood routing through stepped spillway of water reservoir dam*.
-

References

- Nortjé, J., 2002. *Dam safety legislation and programme in the Republic of South Africa*, Design and Rehabilitation of Dams.
- Novak, P., Moffat, A., Nalluri, C. and Narayanan, R., 2007. *Hydraulic structures*. CRC Press.
- Ohtsu, I. and Yasuda, Y., 1997. *Characteristics of flow conditions on stepped channels*, Energy and Water: Sustainable Development, ASCE, pp. 583-588.
- Perekupka, M., 2015, *Standard Normal Distribution: Definition & Example* [Homepage of study.com], [Online]. Available: <http://study.com/academy/lesson/standard-normal-distribution-definition-example.html> [11/24].
- Peterka, A.J., 1953. *The effect of entrained air on cavitation pitting*, Proceedings: Minnesota International Hydraulic Convention, ASCE, pp. 507-518.
- Pfister, M. and Hager, W.H., 2011. *Self-entrainment of air on stepped spillways*. International Journal of Multiphase Flow, Volume 37, pp. 99-107.
- Pfister, M., Hager, W.H. and Minor, H., 2006. *Bottom aeration of stepped spillways*. Journal of Hydraulic Engineering, Volume 132, pp. 850-853.
- Pfister, M., Hager, W.H. and Minor, H., 2005. *Stepped chutes: Pre-aeration and spray reduction*. International Journal of Multiphase Flow, Volume 32, pp. 269-284.
- Russell, S. and Sheehan, G., 1974. *Effect of entrained air on cavitation damage*. Canadian Journal of Civil Engineering, Volume 1, pp. 97-107.
- Sánchez-Juny, M., Pomares, J. and Dolz, J., 2000. *Pressure field in skimming flow over a stepped spillway*, Proceedings of the International Workshop on Hydraulics of Stepped Spillways, Zurich. Edited by HE Minor and WH Hager. Balkema, Rotterdam, pp. 137-146.
- Sánchez-Juny, M., Bladé, E. and Dolz, J., 2008. *Analysis of pressures on a stepped spillway*. Journal of Hydraulic Research, Volume 46, pp. 410-414.
- Shen, C., 2003. *RCC dams in China*, Proceedings of 4th International Symposium on Roller Compacted Concrete.
- Simões, A.L.A., Schulz, H.E., Lobosco, R.J. and de Melo Porto, R., 2012. *Stepped spillways: theoretical, experimental and numerical studies*. Hydrodynamics-Natural Water Bodies.
- Siqueira, C., 2005. *Vortex-Street Animation*.
- Smith, R., 2015. *Snowflakes on my mind*.
- Ting, Z., Chao, W. and Qi, Z., 2011. *Comparison on somatotype of X-and Y-Shape Flaring Gate Pier connected with stepped spillway*, Advanced Materials Research, Trans Tech Publications, pp. 3661-3665.
- US Army Waterways Experimental Station, 1959. *Hydraulic Design Criteria*.
- USBR, 1987. *Design of small dams*. Water Resources Technical Publication.
- Webber, N.B., 1965. *Fluid mechanics for civil engineers*.
-

References

Wei, W.R., 2013. *Experimental Study on Hydraulic Characteristics of X-Shape Flaring Gate Pier and Deflecting Stilling Basin United Energy Dissipator*, Applied Mechanics and Materials, pp. 279-283.

Wood, I.R., Ackers, P. and Loveless, J., 1983. *General method for critical point on spillways*. Journal of Hydraulic Engineering, Volume 109, pp. 308-312.

Zhang, S., 1991. *Latest developments in hydraulic design of outlet works in China*. Hydraulic Engineering Royal Institute of Technology.

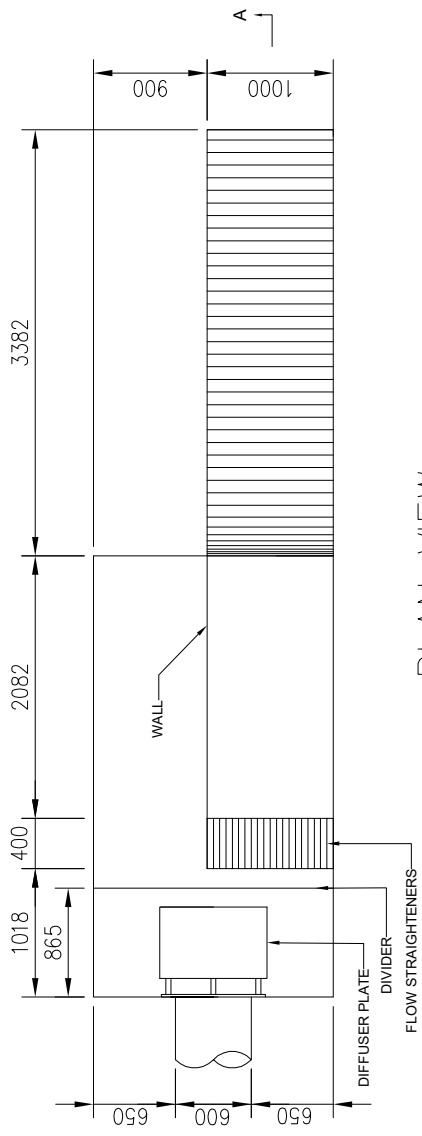
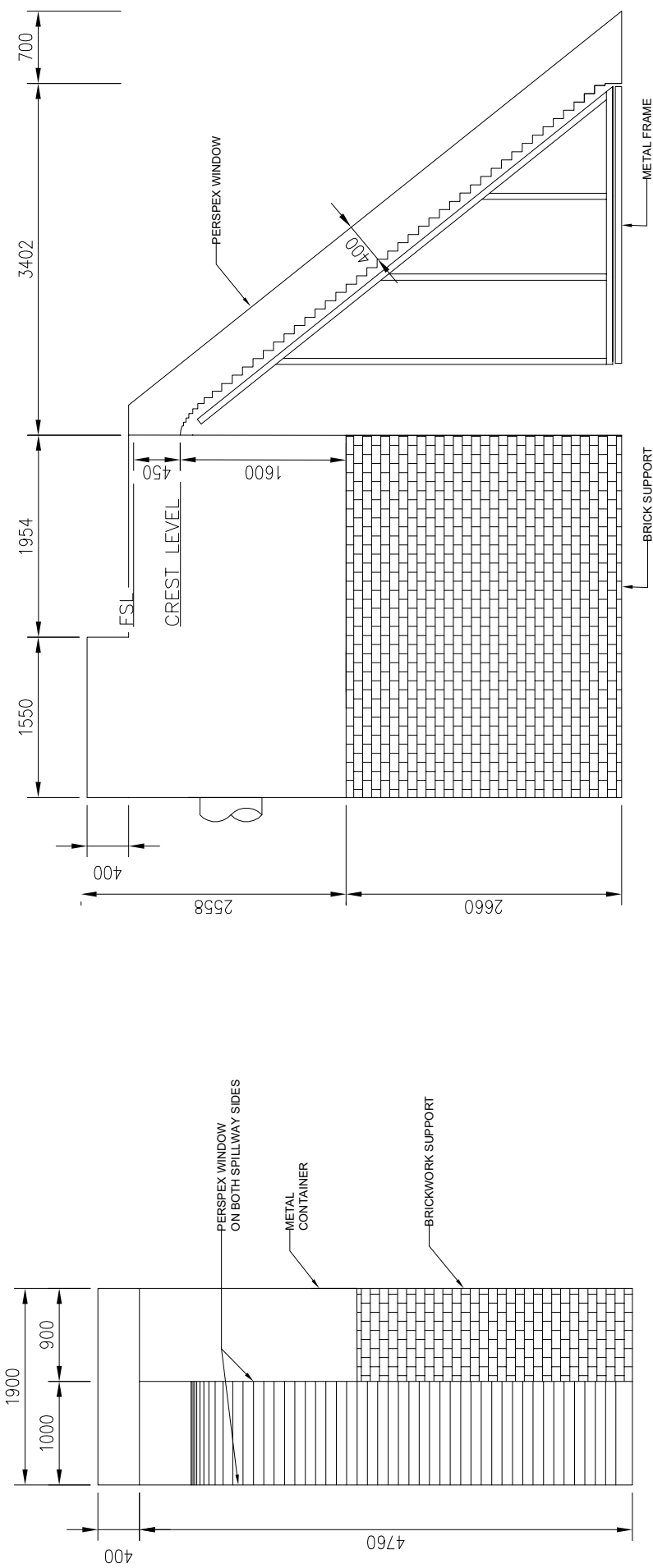
Zhou, L. and Wang, J., 1988. *Erosion damage at Fengman Spillway Dam and investigation on measures of preventing cavitation*, International Symposium on Hydraulics for High Dams, pp. 703-709.

Appendices

Appendix A

As-built drawings of the 1:15 scale Type A stepped spillway model

16	Signature/Checked
15	Date
14	Revision note
13	
12	
11	
10	
9	
8	
7	
6	
5	
4	
3	
2	
1	



Item no.	Quantity	Title/Name, designation, material, dimension etc	Article No./Reference
1	1	Spillway	3006/2016
2	1	Flow straighteners	3006/2016
3	1	Flow straighteners	3006/2016
4	1	Flow straighteners	3006/2016
5	1	Flow straighteners	3006/2016
6	1	Flow straighteners	3006/2016
7	1	Flow straighteners	3006/2016
8	1	Flow straighteners	3006/2016
9	1	Flow straighteners	3006/2016
10	1	Flow straighteners	3006/2016
11	1	Flow straighteners	3006/2016
12	1	Flow straighteners	3006/2016
13	1	Flow straighteners	3006/2016
14	1	Flow straighteners	3006/2016
15	1	Flow straighteners	3006/2016
16	1	Flow straighteners	3006/2016

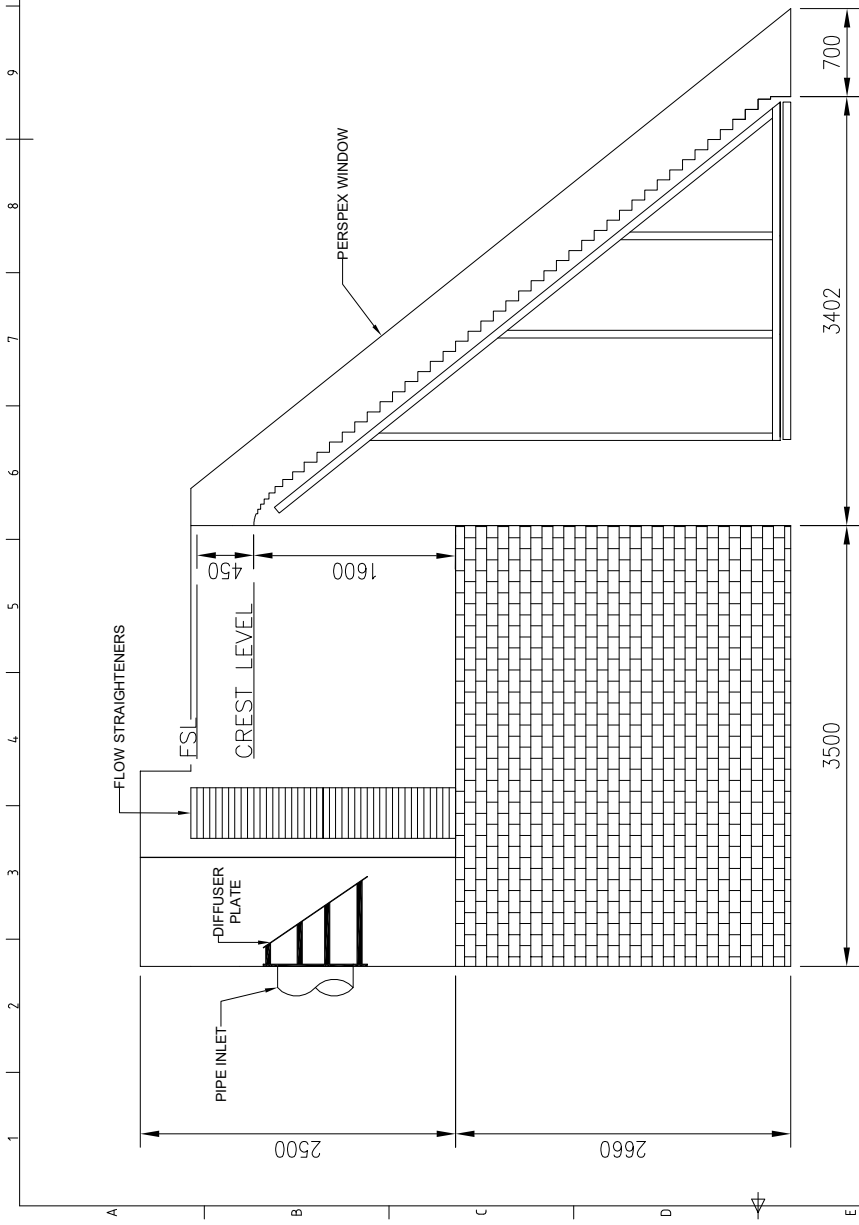
1:15 STEPPED SPILLWAY MODEL
 STELLENBOSCH
 3-15-01
 Edition 1
 Sheet 1/2

Rev	Revision note	Date	Signature/Checked
16			

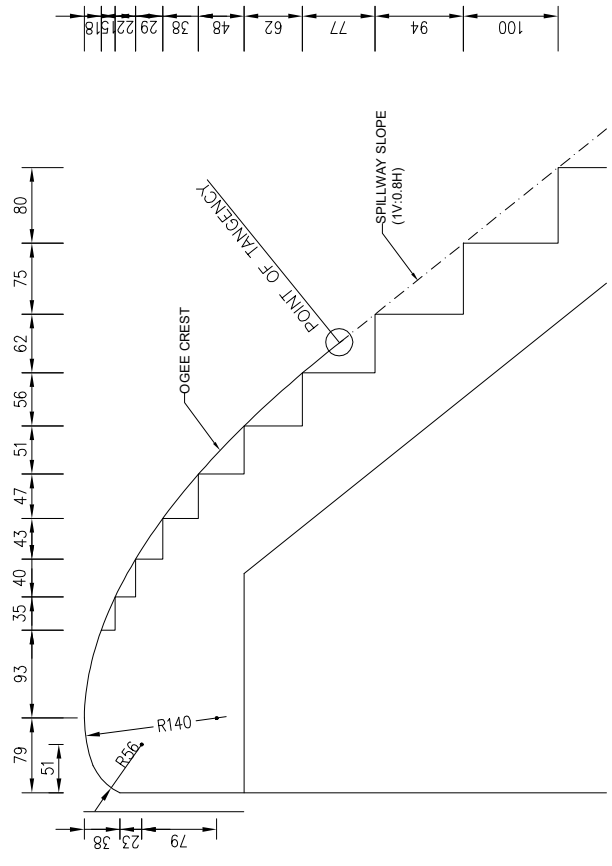
Item	Quantity	Title/Name, designation, material, dimension etc	Article No./Reference
1		CREST	JAS 510/06
2		DESIGNED BY	JAS 510/06
3		DESIGNED BY	JAS 510/06
4		DESIGNED BY	JAS 510/06
5		DESIGNED BY	JAS 510/06
6		DESIGNED BY	JAS 510/06
7		DESIGNED BY	JAS 510/06
8		DESIGNED BY	JAS 510/06
9		DESIGNED BY	JAS 510/06
10		DESIGNED BY	JAS 510/06
11		DESIGNED BY	JAS 510/06
12		DESIGNED BY	JAS 510/06
13		DESIGNED BY	JAS 510/06
14		DESIGNED BY	JAS 510/06
15		DESIGNED BY	JAS 510/06
16		DESIGNED BY	JAS 510/06

Item	Quantity	Title/Name, designation, material, dimension etc	Article No./Reference
1		CREST	JAS 510/06
2		DESIGNED BY	JAS 510/06
3		DESIGNED BY	JAS 510/06
4		DESIGNED BY	JAS 510/06
5		DESIGNED BY	JAS 510/06
6		DESIGNED BY	JAS 510/06
7		DESIGNED BY	JAS 510/06
8		DESIGNED BY	JAS 510/06
9		DESIGNED BY	JAS 510/06
10		DESIGNED BY	JAS 510/06
11		DESIGNED BY	JAS 510/06
12		DESIGNED BY	JAS 510/06
13		DESIGNED BY	JAS 510/06
14		DESIGNED BY	JAS 510/06
15		DESIGNED BY	JAS 510/06
16		DESIGNED BY	JAS 510/06

Item	Quantity	Title/Name, designation, material, dimension etc	Article No./Reference
1		CREST	JAS 510/06
2		DESIGNED BY	JAS 510/06
3		DESIGNED BY	JAS 510/06
4		DESIGNED BY	JAS 510/06
5		DESIGNED BY	JAS 510/06
6		DESIGNED BY	JAS 510/06
7		DESIGNED BY	JAS 510/06
8		DESIGNED BY	JAS 510/06
9		DESIGNED BY	JAS 510/06
10		DESIGNED BY	JAS 510/06
11		DESIGNED BY	JAS 510/06
12		DESIGNED BY	JAS 510/06
13		DESIGNED BY	JAS 510/06
14		DESIGNED BY	JAS 510/06
15		DESIGNED BY	JAS 510/06
16		DESIGNED BY	JAS 510/06



SECTION A-A
SCALE 1:60



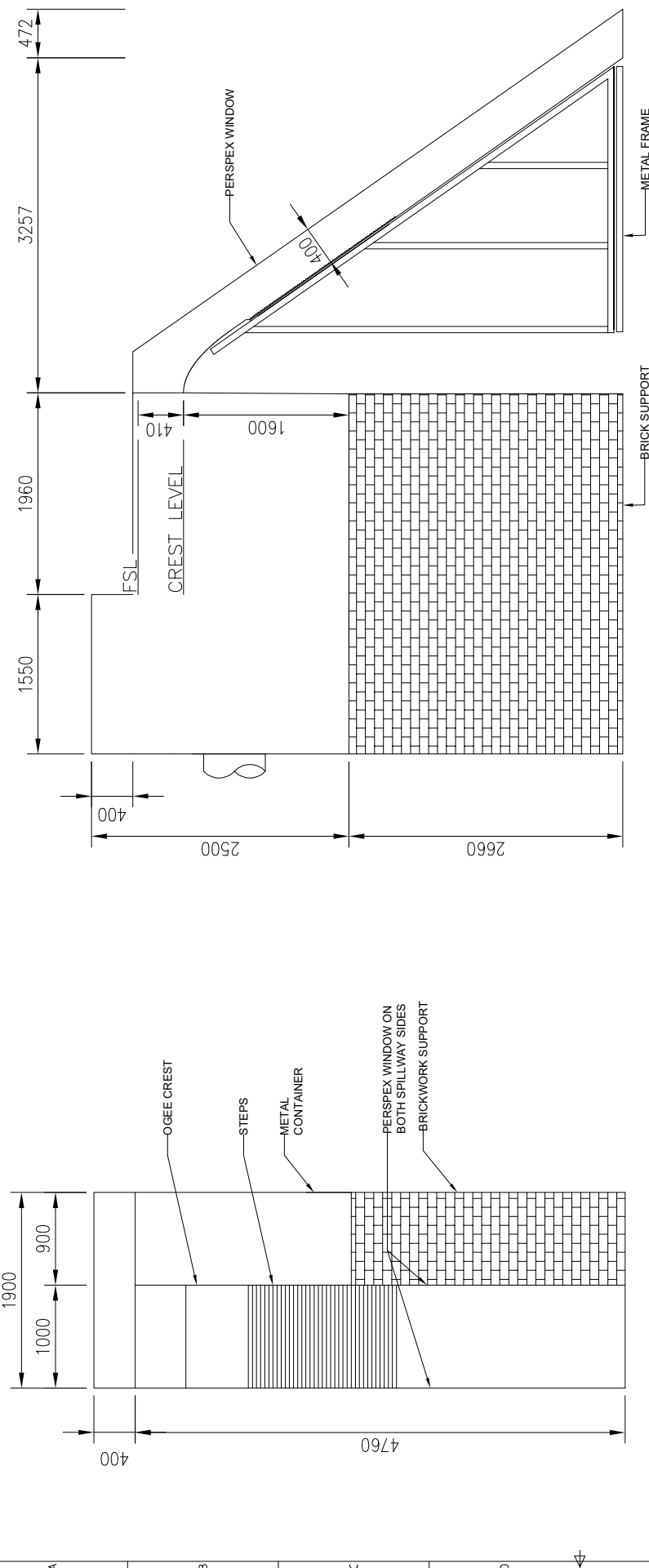
CREST DETAIL & STEP DIMENSIONS
SCALE 1:8

Appendix B

As-built drawings of the 1:50 scale Type B stepped spillway model

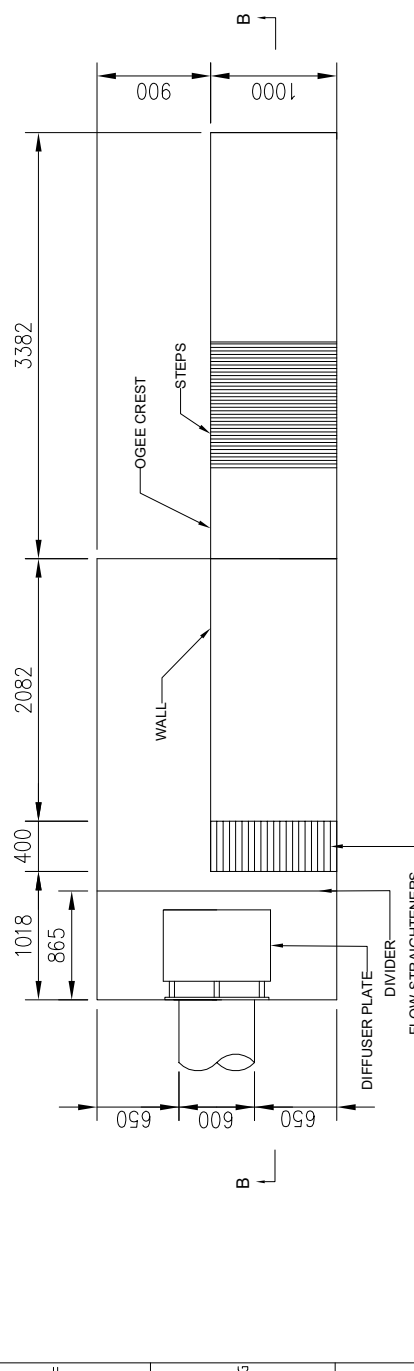
16	Signature/Checked
15	Date
14	Revision note

13	12	11	10	9	8	7	6	5	4	3	2	1
----	----	----	----	---	---	---	---	---	---	---	---	---



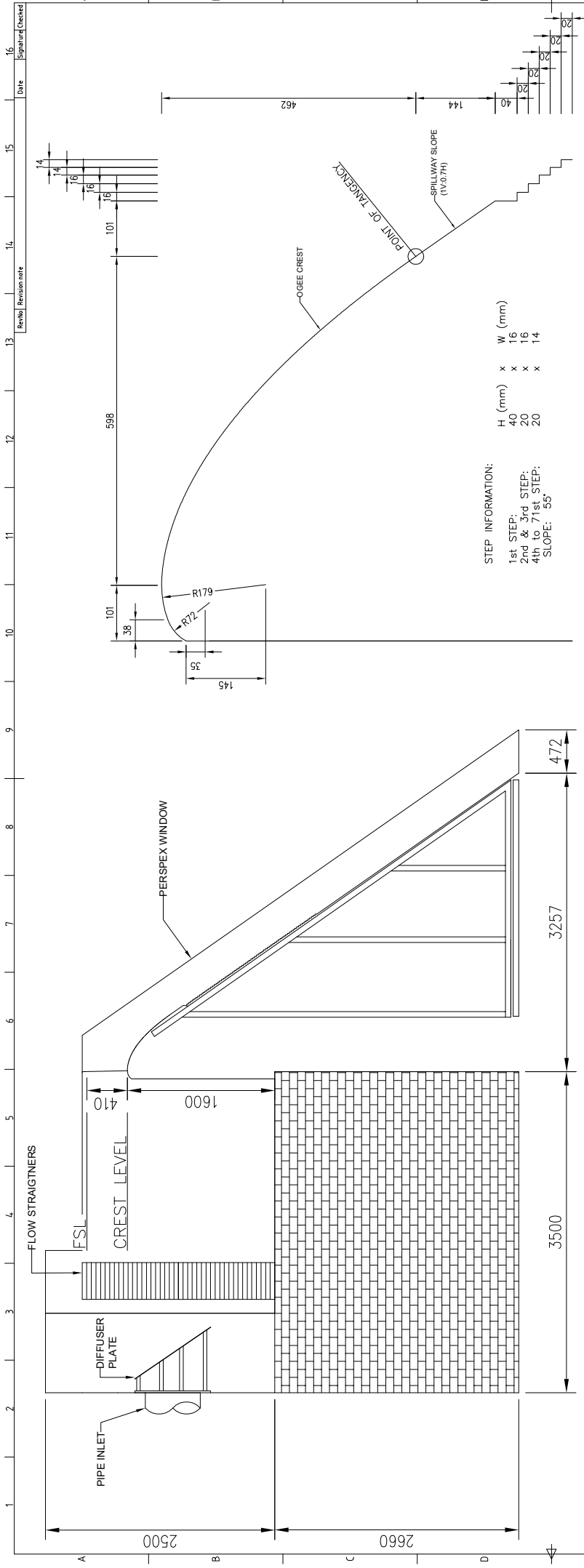
SIDE VIEW

FRONT VIEW



PLAN VIEW

Item#	Quantity	Title/Name, designation, material, dimension etc	Checked by	Article No./Reference
1	1	1:50 STEPPED SPILLWAY MODEL	J. KOBEN	3-50-01
STELLENBOSCH			Approved by	Page
			N/A	146
			N/A	01/06/2017
			Filename	Sheet
			N/A-3103/2017	1/2
			3-50-01	Edition
			1	16

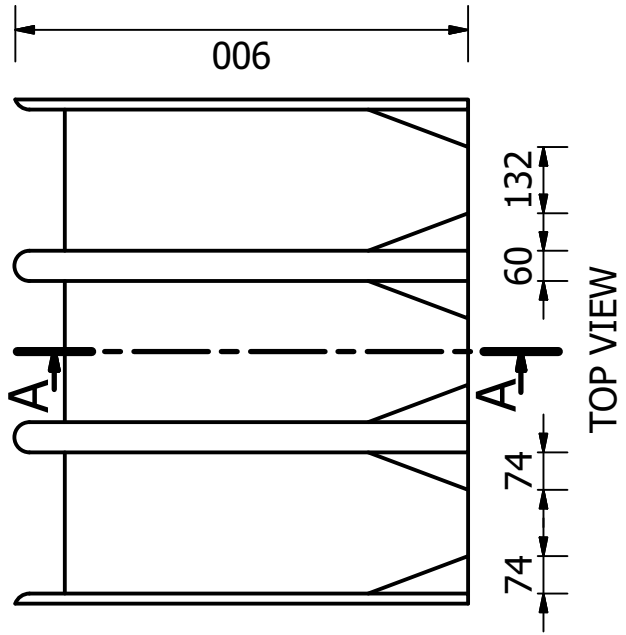
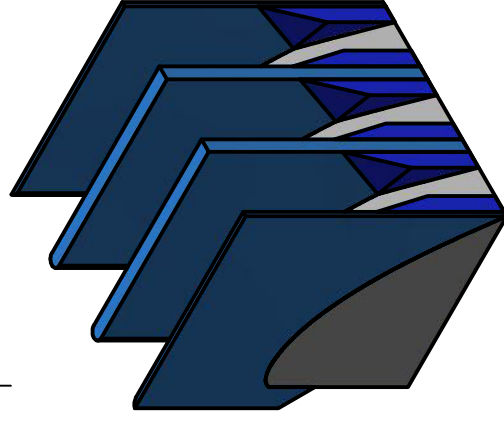
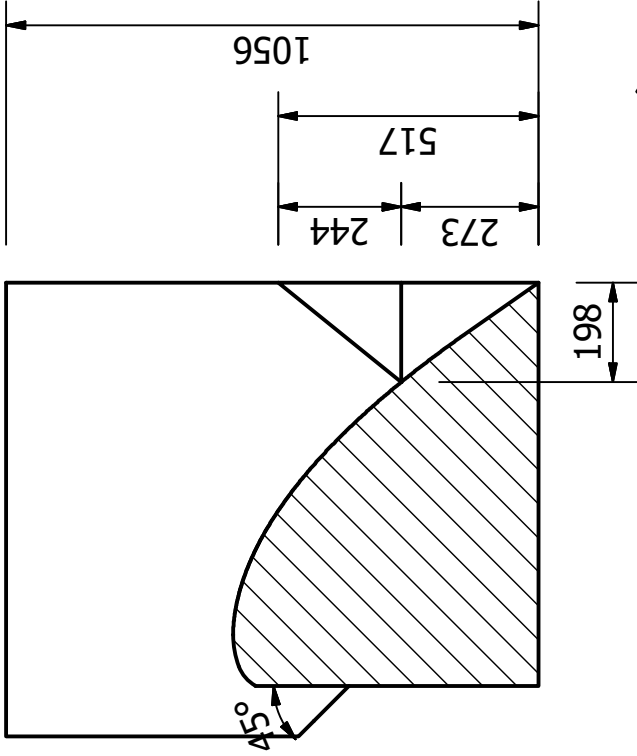
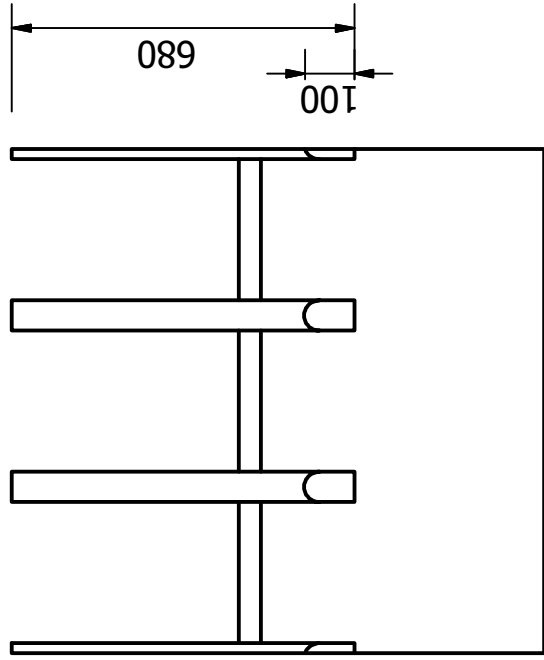


Item#	Quantity	Title/Name, designation, material, dimension etc	Article No./Reference
1	1	Model	3-50-02
2	1	Flow straighteners	3-50-02
3	1	Diffuser plate	3-50-02
4	1	Pipe inlet	3-50-02
5	1	Flow straighteners	3-50-02
6	1	Flow straighteners	3-50-02
7	1	Flow straighteners	3-50-02
8	1	Flow straighteners	3-50-02
9	1	Flow straighteners	3-50-02
10	1	Flow straighteners	3-50-02
11	1	Flow straighteners	3-50-02
12	1	Flow straighteners	3-50-02
13	1	Flow straighteners	3-50-02
14	1	Flow straighteners	3-50-02
15	1	Flow straighteners	3-50-02
16	1	Flow straighteners	3-50-02

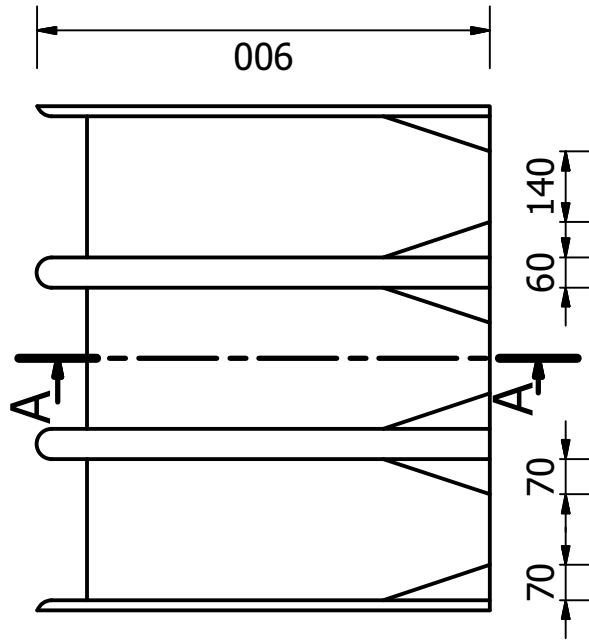
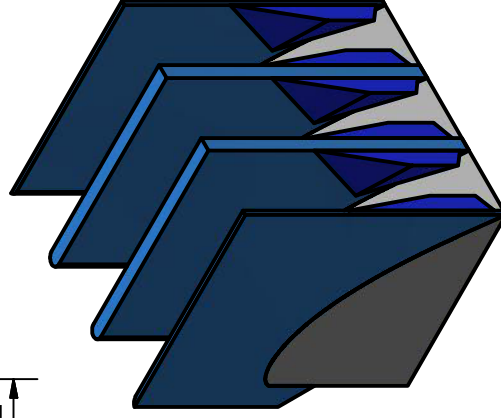
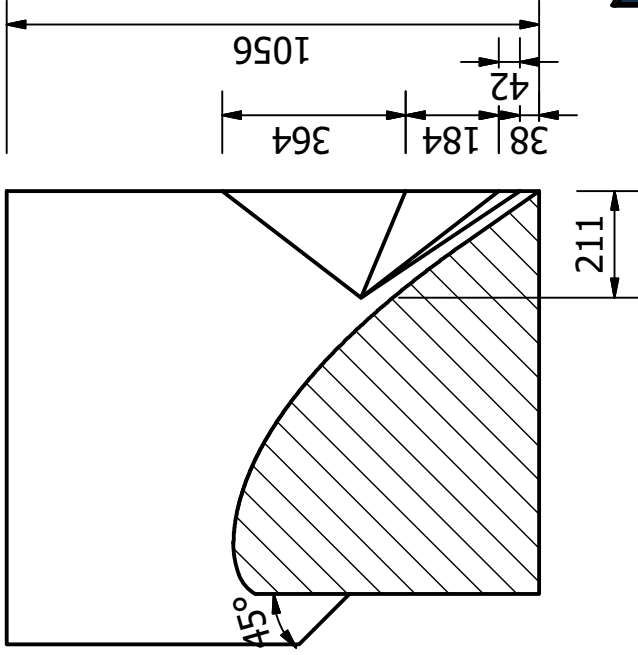
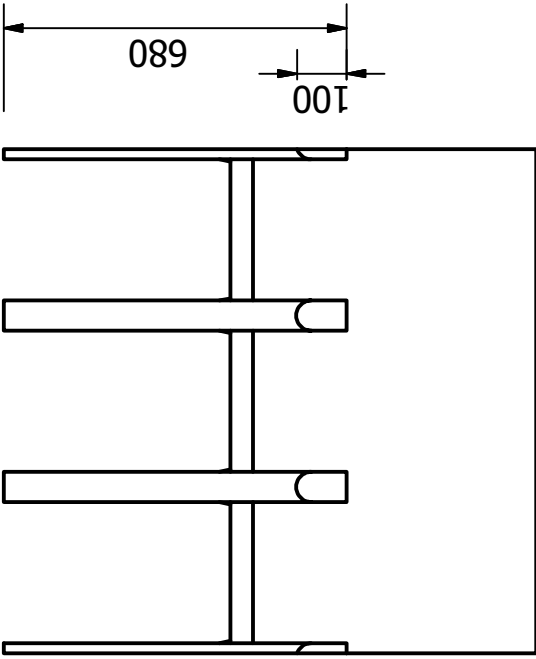
Revis	Revision note	Date	Signature/Checked
1			
2			
3			
4			
5			
6			
7			
8			
9			
10			
11			
12			
13			
14			
15			
16			

Appendix C

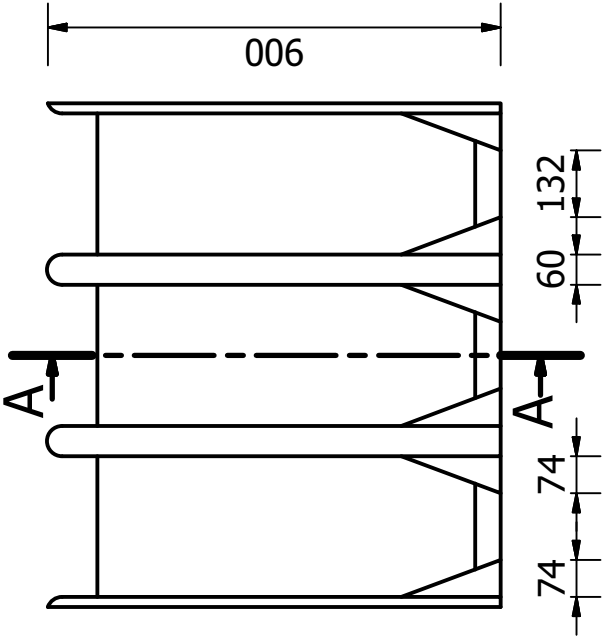
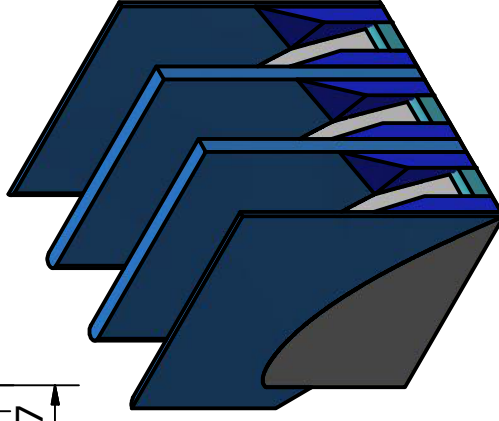
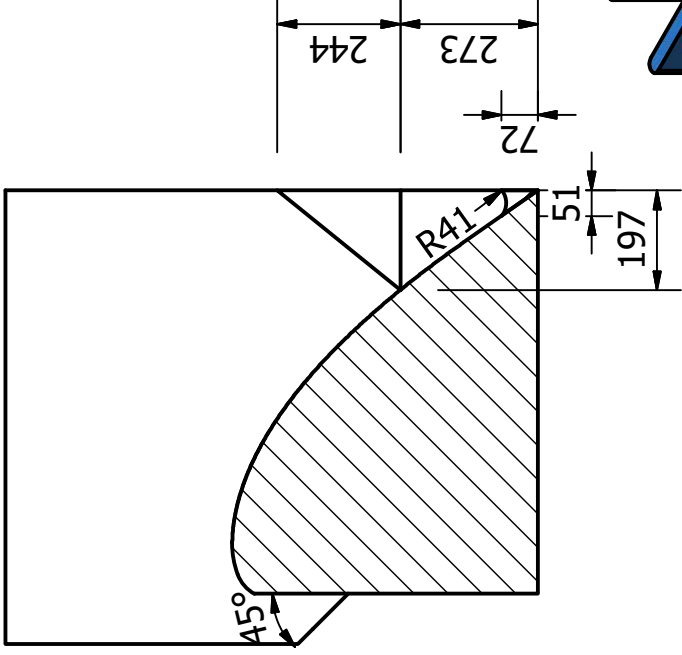
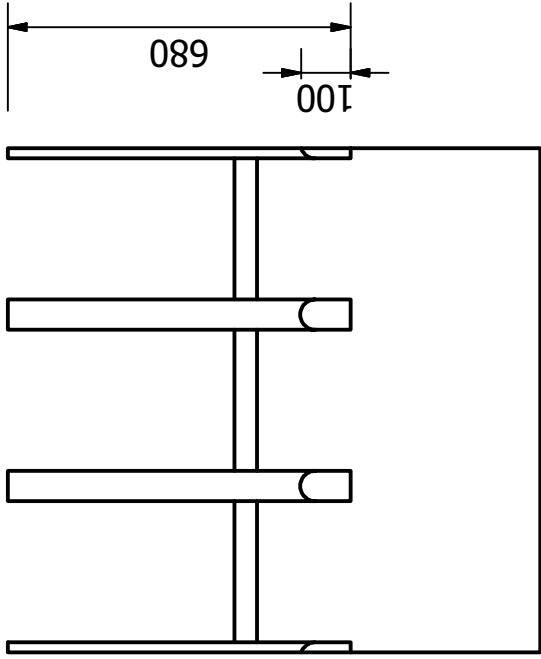
Detailed as-built model drawings of the 1:50 scale, Type B stepped spillway aeration structures



Designed by Jaco Koen	Checked by Mr. Ma	Approved by	Date	Date	Scale
			2017/07/08		1:15
50 SCALE MODEL			Y-SHAPE FGP		
			Y-Shape Assembly		



Designed by Jaco Koen	Checked by Mr. Ma	Approved by	Date	Date	Scale
			2017/07/09		1:15
50 SCALE MODEL			X-SHAPE FGP		
			X-Shape Assembly		



Designed by Jaco Koen	Checked by Mr. Ma	Approved by	Date	Date 2017/07/09	Scale 1:15
50 SCALE MODEL			Y-SHAPE, FLIP BUCKET FGP		
			Y-Shape Flipbucket		

Appendix D

Pressure results for the 1:50 scale Type B stepped spillway

Appendix D

Table D.1: Pressure results for the no pier control experiments.

Pressure (p/y/h)					
Model Setup 8 - No Pier					
L_p (m)	50 m ² /s				
	X = 0 m	X = 4.25 m	X = 8.5 m	X = 12.75 m	X = 17 m
50.78	5.305	7.832	6.647	7.832	5.305
57.01	-3.836	0.304	4.730	0.304	-3.836
63.11	-3.399	-2.606	-5.628	-2.606	-3.399
69.21	-6.195	-6.561	-2.561	-6.561	-6.195
75.32	-3.314	-4.255	-3.729	-4.255	-3.314
81.42	-10.914	-4.521	-5.757	-4.521	-10.914
87.52	-4.343	3.000	7.087	3.000	-4.343
93.63	-3.018	-4.934	-13.418	-4.934	-3.018
99.73	-5.747	-4.608	-2.156	-4.608	-5.747
105.83	-2.577	-5.186	5.030	-5.186	-2.577
111.94	-7.526	0.882	-2.298	0.882	-7.526
118.04	-2.459	7.291	6.817	7.291	-2.459
124.14	-2.190	-1.679	-5.163	-1.679	-2.190
130.25	-0.133	4.601	-0.106	4.601	-0.133
135.13	2.292	-2.748	5.893	-2.748	2.292
L_p (m)	100 m ² /s				
	X = 0 m	X = 4.25 m	X = 8.5 m	X = 12.75 m	X = 17 m
50.78	4.365	6.597	6.717	6.597	4.365
57.01	-2.515	3.586	9.632	3.586	-2.515
63.11	-2.996	-2.338	-5.354	-2.338	-2.996
69.21	-4.945	-2.244	-0.494	-2.244	-4.945
75.32	1.591	-3.413	3.275	-3.413	1.591
81.42	-15.202	-0.130	-6.124	-0.130	-15.202
87.52	-8.175	3.497	6.389	3.497	-8.175
93.63	-14.845	-2.364	-10.266	-2.364	-14.845
99.73	-5.980	-2.194	-4.256	-2.194	-5.980
105.83	-5.680	-9.750	-3.816	-9.750	-5.680
111.94	-11.236	-3.655	-7.990	-3.655	-11.236
118.04	-11.864	0.619	4.758	0.619	-11.864
124.14	-13.033	-8.261	-14.747	-8.261	-13.033
130.25	-6.181	-1.459	-6.080	-1.459	-6.181
135.13	-14.542	-12.936	-0.406	-12.936	-14.542

Appendix D

L_p (m)	150 m ² /s				
	X = 0 m	X = 4.25 m	X = 8.5 m	X = 12.75 m	X = 17 m
50.78	13.355	10.593	11.152	10.593	13.355
57.01	4.269	4.574	11.848	4.574	4.269
63.11	-3.202	0.198	-2.295	0.198	-3.202
69.21	-5.818	-5.022	-2.437	-5.022	-5.818
75.32	-1.757	-1.616	1.806	-1.616	-1.757
81.42	-8.919	-1.678	-3.523	-1.678	-8.919
87.52	-4.651	-1.279	4.605	-1.279	-4.651
93.63	-6.852	-4.702	-7.928	-4.702	-6.852
99.73	-8.158	-4.756	-5.366	-4.756	-8.158
105.83	-10.711	-7.679	-5.168	-7.679	-10.711
111.94	3.167	-4.563	-4.041	-4.563	3.167
118.04	-4.883	-1.337	5.181	-1.337	-4.883
124.14	-13.259	-4.422	-13.867	-4.422	-13.259
130.25	-6.394	-5.917	-6.313	-5.917	-6.394
135.13	-14.336	-17.443	-6.541	-17.443	-14.336
L_p (m)	200 m ² /s				
	X = 0 m	X = 4.25 m	X = 8.5 m	X = 12.75 m	X = 17 m
50.78	5.512	7.283	12.215	7.283	5.512
57.01	-0.065	1.847	7.925	1.847	-0.065
63.11	-7.234	-0.708	-5.342	-0.708	-7.234
69.21	0.634	-6.663	-3.836	-6.663	0.634
75.32	-2.669	-0.667	0.202	-0.667	-2.669
81.42	-4.607	-9.097	-3.277	-9.097	-4.607
87.52	-5.541	-0.739	3.997	-0.739	-5.541
93.63	-2.230	-4.254	-17.619	-4.254	-2.230
99.73	-2.672	-7.372	-8.651	-7.372	-2.672
105.83	-7.245	-6.872	-8.466	-6.872	-7.245
111.94	-5.292	-12.149	-10.860	-12.149	-5.292
118.04	-7.596	-2.289	5.542	-2.289	-7.596
124.14	-7.745	-7.349	-12.256	-7.349	-7.745
130.25	-11.016	-15.699	-9.314	-15.699	-11.016
135.13	-18.632	-19.026	-17.181	-19.026	-18.632

Note: Regions of cavitation pressure is indicated with red text.

Appendix D

Table D.2: Pressure results for the Y-Shape FGP experiments.

Pressure (p/y/h)					
Model Setup 9 - Y-Shape FGP					
L_p (m)	50 m ² /s				
	X = 0 m	X = 4.25 m	X = 8.5 m	X = 12.75 m	X = 17 m
50.78	1.147	2.827	-5.131	2.827	1.147
57.01	2.805	2.267	3.950	2.267	2.805
63.11	0.990	2.474	-0.491	2.474	0.990
69.21	2.618	1.925	-4.013	1.925	2.618
75.32	3.205	2.423	-2.786	2.423	3.205
81.42	6.479	2.335	-6.459	2.335	6.479
87.52	2.894	2.046	4.841	2.046	2.894
93.63	3.469	0.159	-8.401	0.159	3.469
99.73	0.576	-2.403	-19.672	-2.403	0.576
105.83	1.433	2.279	-19.111	2.279	1.433
111.94	5.116	1.503	-11.090	1.503	5.116
118.04	1.499	1.102	5.598	1.102	1.499
124.14	1.121	2.776	-8.665	2.776	1.121
130.25	3.288	-0.044	-5.635	-0.044	3.288
135.13	0.122	3.607	-2.833	3.607	0.122
L_p (m)	100 m ² /s				
	X = 0 m	X = 4.25 m	X = 8.5 m	X = 12.75 m	X = 17 m
50.78	5.749	1.612	1.729	1.612	5.749
57.01	1.268	3.590	8.027	3.590	1.268
63.11	3.977	2.290	1.454	2.290	3.977
69.21	2.481	0.836	-3.746	0.836	2.481
75.32	3.317	5.445	-5.867	5.445	3.317
81.42	6.356	0.697	-4.200	0.697	6.356
87.52	0.913	1.201	6.080	1.201	0.913
93.63	2.743	0.656	-6.733	0.656	2.743
99.73	0.570	-3.530	-16.876	-3.530	0.570
105.83	2.457	0.258	-16.746	0.258	2.457
111.94	6.774	-0.896	-10.413	-0.896	6.774
118.04	2.161	-2.736	5.541	-2.736	2.161
124.14	2.795	-3.260	-19.024	-3.260	2.795
130.25	4.529	-6.732	-22.130	-6.732	4.529
135.13	0.050	-2.144	-16.626	-2.144	0.050

Appendix D

L_p (m)	150 m ² /s				
	X = 0 m	X = 4.25 m	X = 8.5 m	X = 12.75 m	X = 17 m
50.78	5.576	-1.176	1.382	-1.176	5.576
57.01	1.747	1.631	4.328	1.631	1.747
63.11	0.471	2.303	-1.245	2.303	0.471
69.21	2.285	0.691	-4.812	0.691	2.285
75.32	3.197	2.340	-5.370	2.340	3.197
81.42	6.289	1.938	-5.779	1.938	6.289
87.52	1.399	1.808	6.446	1.808	1.399
93.63	3.349	-1.101	-5.865	-1.101	3.349
99.73	0.161	-5.964	-17.487	-5.964	0.161
105.83	1.838	1.207	-21.755	1.207	1.838
111.94	6.264	-1.444	-12.574	-1.444	6.264
118.04	2.141	-2.327	5.786	-2.327	2.141
124.14	4.521	-9.608	-15.844	-9.608	4.521
130.25	1.356	-10.114	-21.223	-10.114	1.356
135.13	0.609	-3.425	-16.714	-3.425	0.609
L_p (m)	200 m ² /s				
	X = 0 m	X = 4.25 m	X = 8.5 m	X = 12.75 m	X = 17 m
50.78	5.889	1.294	6.560	1.294	5.889
57.01	1.649	3.585	7.866	3.585	1.649
63.11	3.753	2.088	1.097	2.088	3.753
69.21	2.243	1.658	-5.665	1.658	2.243
75.32	3.344	4.467	-2.775	4.467	3.344
81.42	6.140	1.023	-6.023	1.023	6.140
87.52	1.518	1.840	6.346	1.840	1.518
93.63	2.995	-1.399	-5.876	-1.399	2.995
99.73	0.683	-6.353	-13.657	-6.353	0.683
105.83	1.850	-1.613	-12.851	-1.613	1.850
111.94	6.316	-0.762	-11.231	-0.762	6.316
118.04	2.577	-2.240	5.831	-2.240	2.577
124.14	4.065	-6.872	-13.641	-6.872	4.065
130.25	1.541	-7.099	-21.925	-7.099	1.541
135.13	0.702	-2.463	-18.016	-2.463	0.702

Note: Regions of cavitation pressure is indicated with red text.

Appendix D

Table D.3: Pressure results for the X-Shape FGP experiments.

Pressure (p/γ/h)					
Model Setup 10 - X-Shape FGP					
L_p (m)	50 m ² /s				
	X = 0 m	X = 4.25 m	X = 8.5 m	X = 12.75 m	X = 17 m
50.78	0.956	8.158	6.161	8.158	0.956
57.01	2.414	2.007	1.976	2.007	2.414
63.11	2.824	0.921	2.969	0.921	2.824
69.21	1.148	-4.209	-1.027	-4.209	1.148
75.32	2.788	-3.853	0.750	-3.853	2.788
81.42	0.475	-0.892	-4.757	-0.892	0.475
87.52	2.039	-2.023	1.852	-2.023	2.039
93.63	1.362	-5.581	-4.434	-5.581	1.362
99.73	1.907	-5.274	-4.379	-5.274	1.907
105.83	0.328	-3.061	-3.798	-3.061	0.328
111.94	0.328	1.773	-1.821	1.773	0.328
118.04	0.679	0.959	3.378	0.959	0.679
124.14	-1.344	-0.024	-1.610	-0.024	-1.344
130.25	-2.934	-2.573	-1.349	-2.573	-2.934
135.13	-1.317	-0.130	-2.292	-0.130	-1.317
L_p (m)	100 m ² /s				
	X = 0 m	X = 4.25 m	X = 8.5 m	X = 12.75 m	X = 17 m
50.78	0.395	10.219	7.147	10.219	0.395
57.01	4.049	2.510	2.777	2.510	4.049
63.11	3.088	-0.438	0.264	-0.438	3.088
69.21	4.232	-2.656	-6.488	-2.656	4.232
75.32	2.305	-0.338	-5.637	-0.338	2.305
81.42	0.230	-1.477	-9.438	-1.477	0.230
87.52	-7.533	-4.173	5.098	-4.173	-7.533
93.63	1.438	-8.684	-9.462	-8.684	1.438
99.73	0.913	-9.624	-10.420	-9.624	0.913
105.83	-1.630	-9.392	-16.009	-9.392	-1.630
111.94	-3.122	-2.593	-13.072	-2.593	-3.122
118.04	-3.361	-3.891	0.304	-3.891	-3.361
124.14	-6.030	-4.224	-16.731	-4.224	-6.030
130.25	-8.737	-5.064	-6.529	-5.064	-8.737
135.13	-4.794	-1.939	-11.453	-1.939	-4.794

Appendix D

L_p (m)	150 m ² /s				
	X = 0 m	X = 4.25 m	X = 8.5 m	X = 12.75 m	X = 17 m
50.78	0.123	10.277	7.220	10.277	0.123
57.01	3.369	2.518	2.630	2.518	3.369
63.11	3.115	-0.608	1.764	-0.608	3.115
69.21	4.147	-2.490	-5.715	-2.490	4.147
75.32	1.964	-0.132	-2.676	-0.132	1.964
81.42	-0.344	-1.805	-6.455	-1.805	-0.344
87.52	0.919	-3.726	0.900	-3.726	0.919
93.63	0.922	-9.930	-9.793	-9.930	0.922
99.73	1.226	-13.846	-13.190	-13.846	1.226
105.83	-0.932	-24.217	-13.938	-24.217	-0.932
111.94	-2.470	-3.818	-14.643	-3.818	-2.470
118.04	-3.243	-9.452	-1.654	-9.452	-3.243
124.14	-7.924	-14.160	-22.148	-14.160	-7.924
130.25	-2.434	-12.668	-15.146	-12.668	-2.434
135.13	-9.077	-20.599	-58.557	-20.599	-9.077
L_p (m)	200 m ² /s				
	X = 0 m	X = 4.25 m	X = 8.5 m	X = 12.75 m	X = 17 m
50.78	1.522	9.208	10.055	9.208	1.522
57.01	3.245	3.707	3.370	3.707	3.245
63.11	3.374	-0.951	0.977	-0.951	3.374
69.21	4.050	-1.966	-6.710	-1.966	4.050
75.32	3.125	0.234	-2.491	0.234	3.125
81.42	-1.664	-1.852	-7.219	-1.852	-1.664
87.52	1.639	-2.690	1.150	-2.690	1.639
93.63	1.360	-9.289	-10.573	-9.289	1.360
99.73	0.709	-11.901	-11.913	-11.901	0.709
105.83	-2.030	-24.156	-17.303	-24.156	-2.030
111.94	-3.082	-5.202	-14.185	-5.202	-3.082
118.04	-2.438	-6.878	-1.833	-6.878	-2.438
124.14	-8.476	-18.499	-21.842	-18.499	-8.476
130.25	-4.152	-15.439	-16.906	-15.439	-4.152
135.13	-12.721	-25.555	-58.301	-25.555	-12.721

Note: Regions of cavitation pressure is indicated with red text.

Appendix E

Pressure contour plots for the 1:50 scale Type B stepped spillway

Appendix E

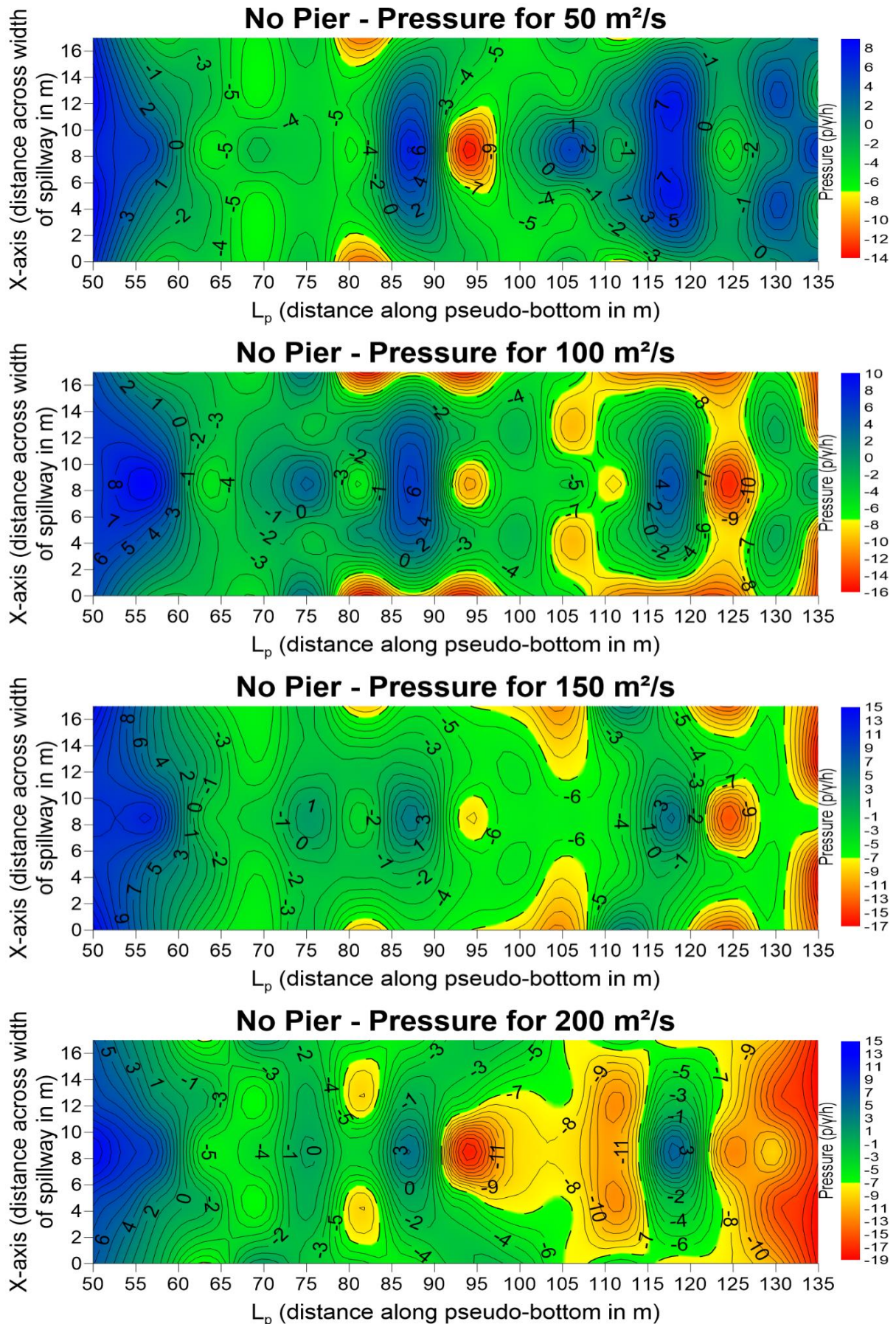


Figure E.1: Pressure contour plots for the no pier control experiments.

Appendix E

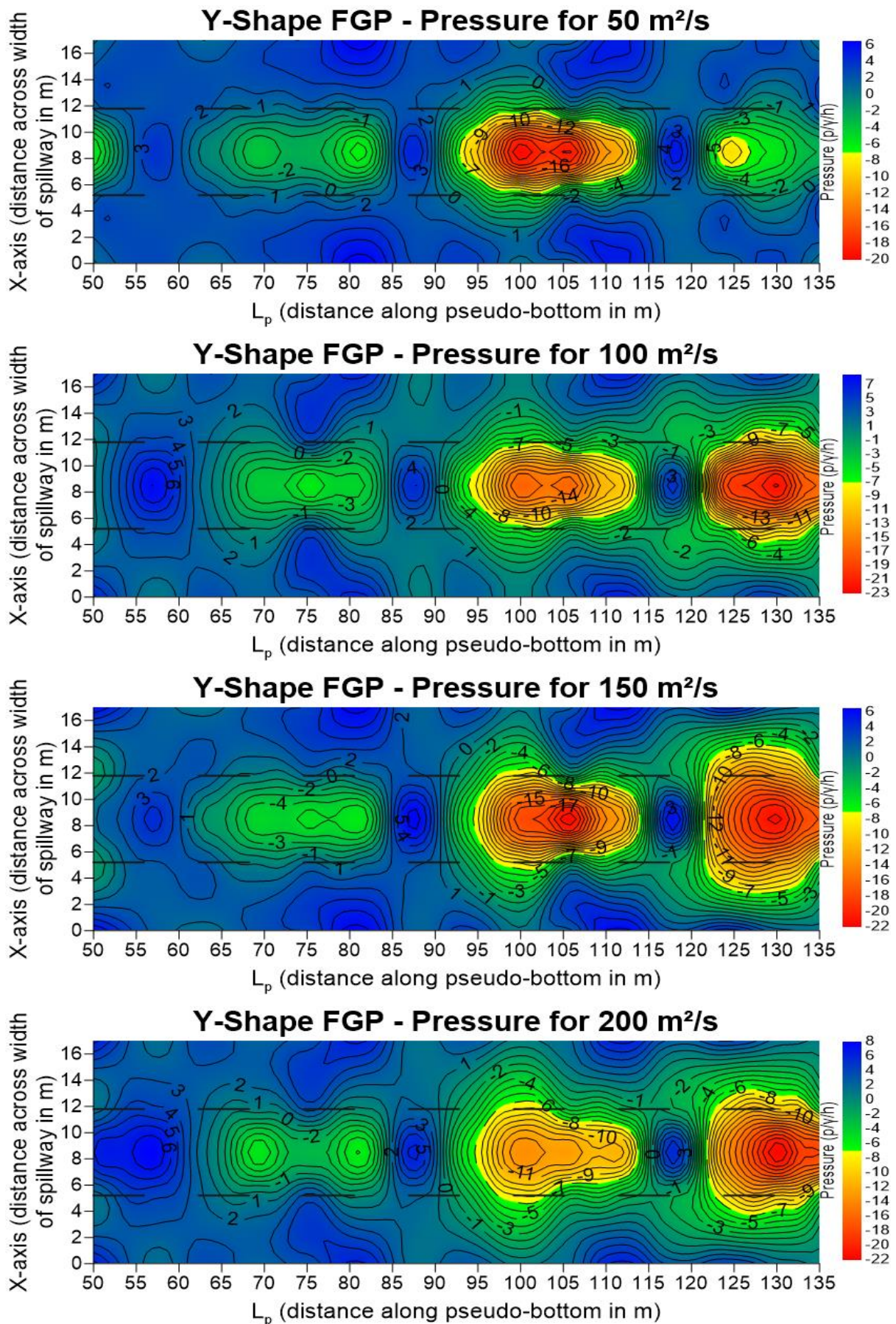


Figure E.2: Pressure contour plots for the Y-Shape FGP experiments.

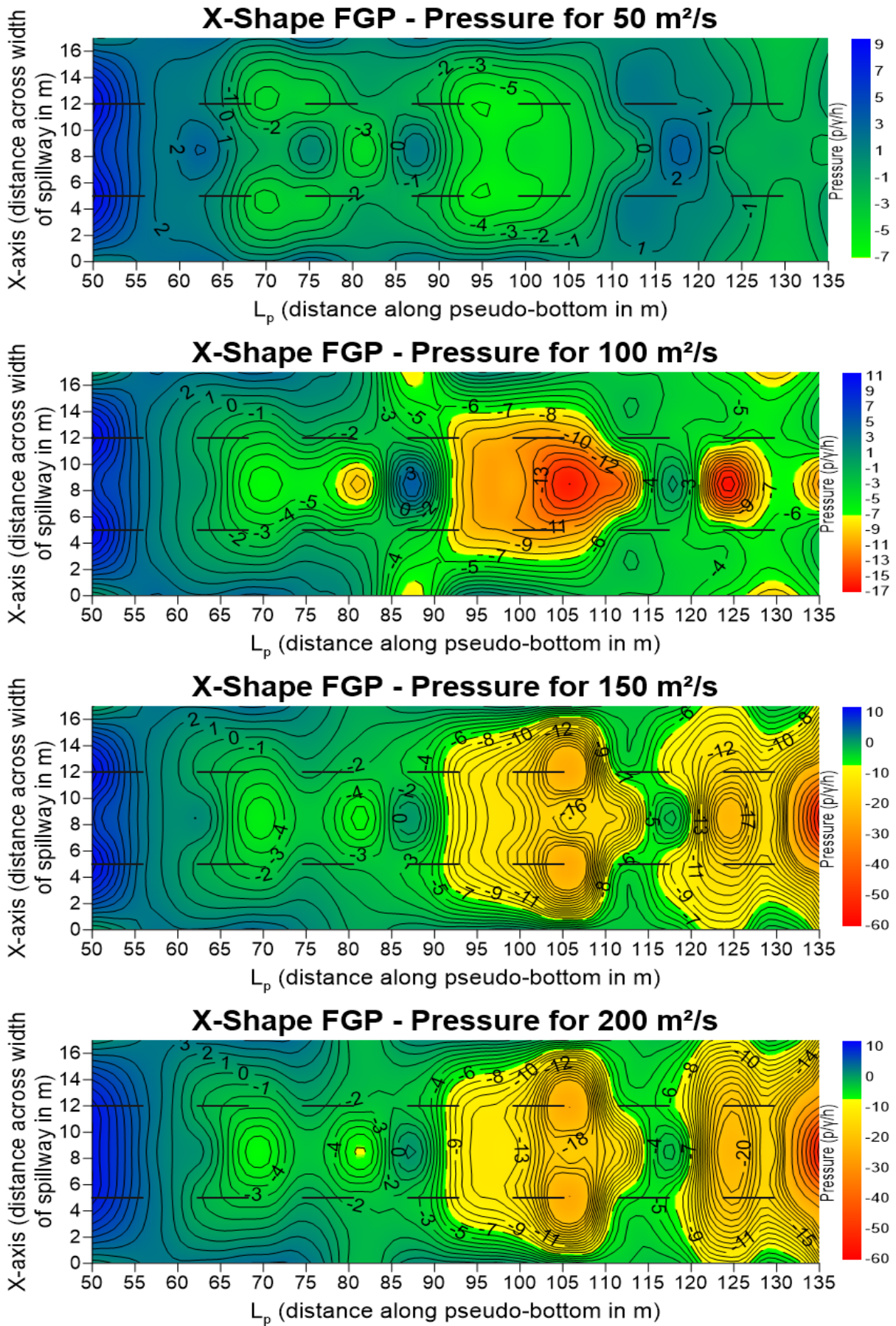


Figure E.3: Pressure contour plots for the X-Shape FGP experiments.

Appendix F

Cavitation analysis of the 1:50 Type B stepped spillway

Appendix F

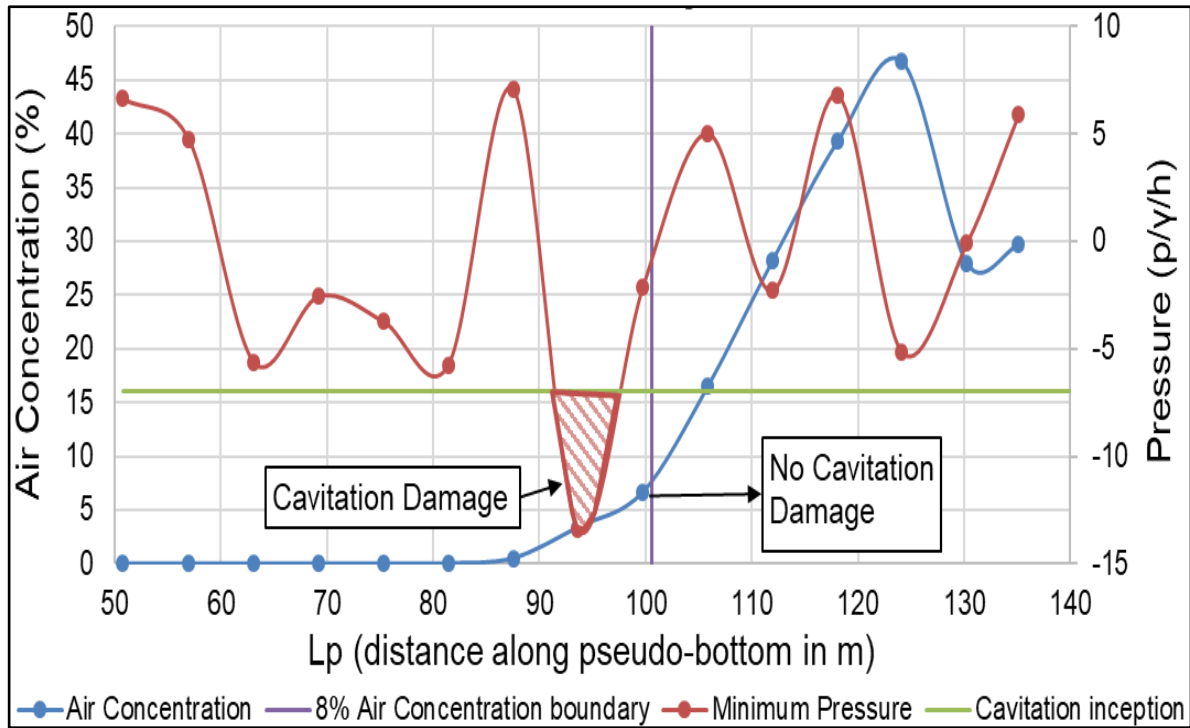


Figure F.1: Cavitation analysis for the control experiment at a unit discharge of 50 m²/s.

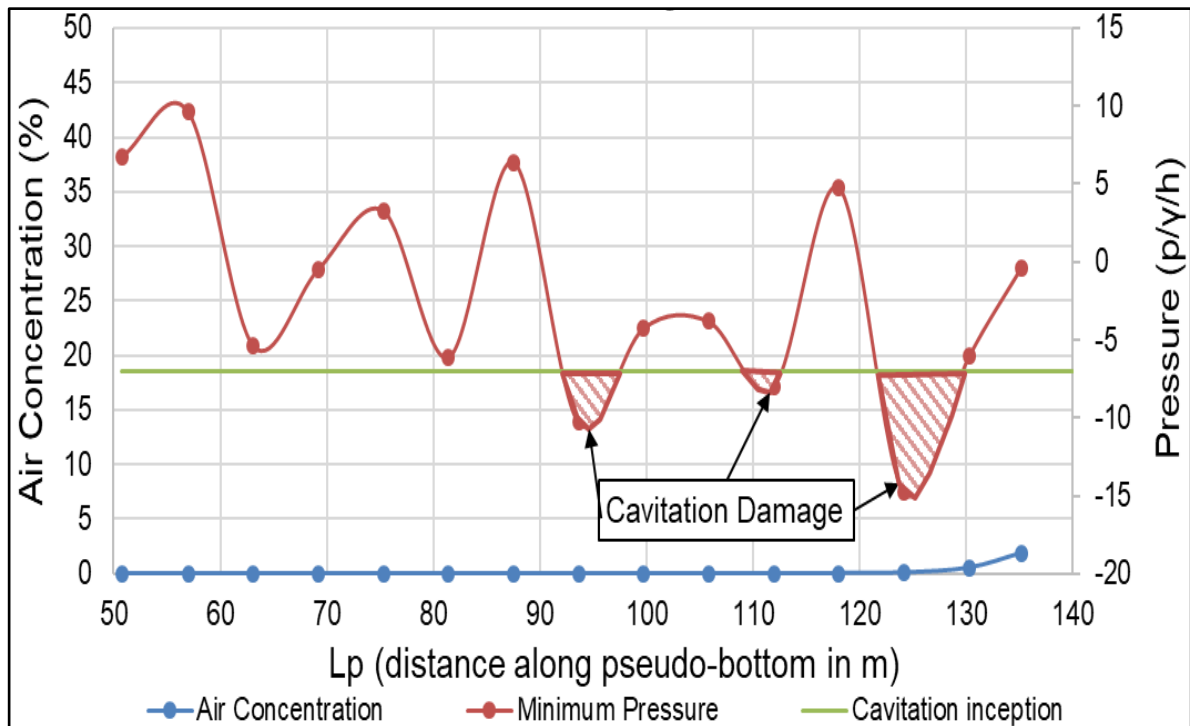


Figure F.2: Cavitation analysis for the control experiment at a unit discharge of 100 m²/s.

Appendix F

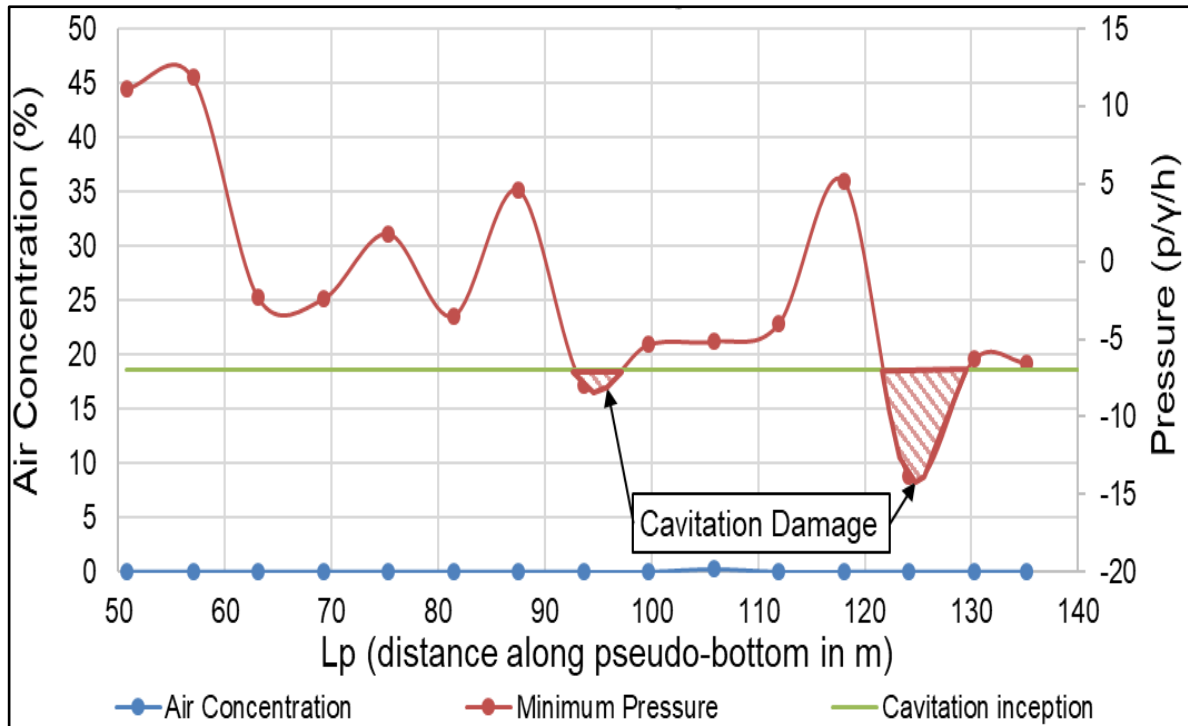


Figure F.3: Cavitation analysis for the control experiment at a unit discharge of 150 m²/s.

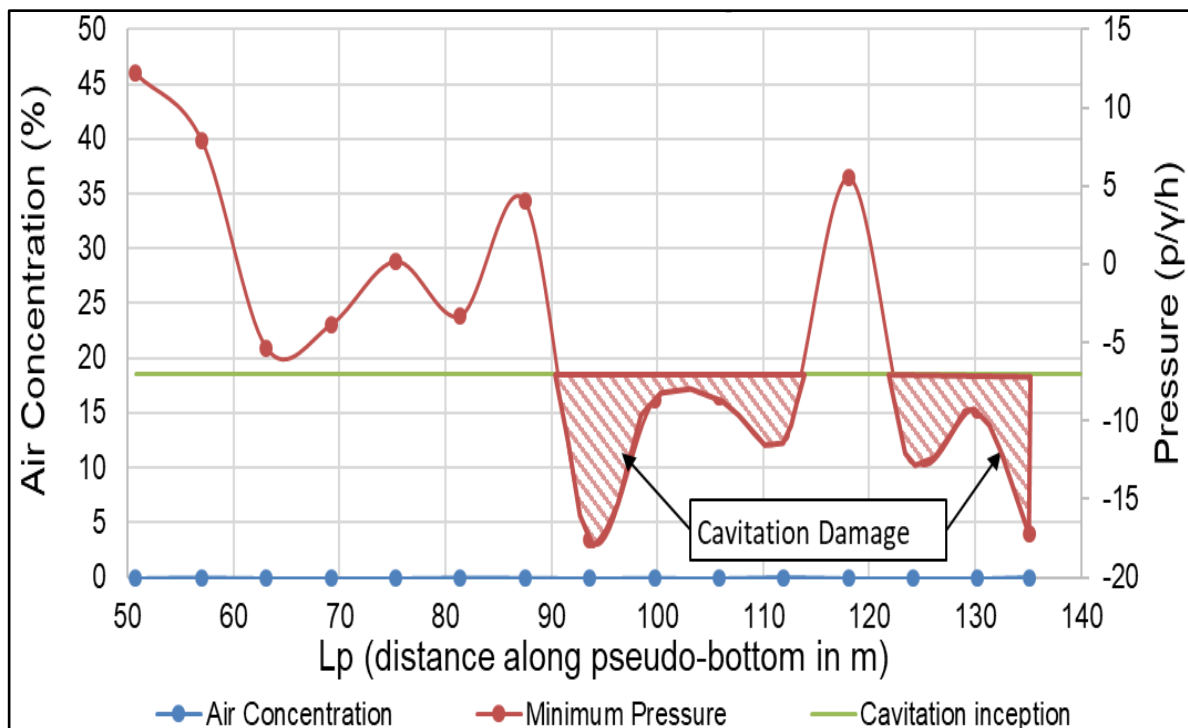


Figure F.4: Cavitation analysis for the control experiment at a unit discharge of 200 m²/s.

Appendix F

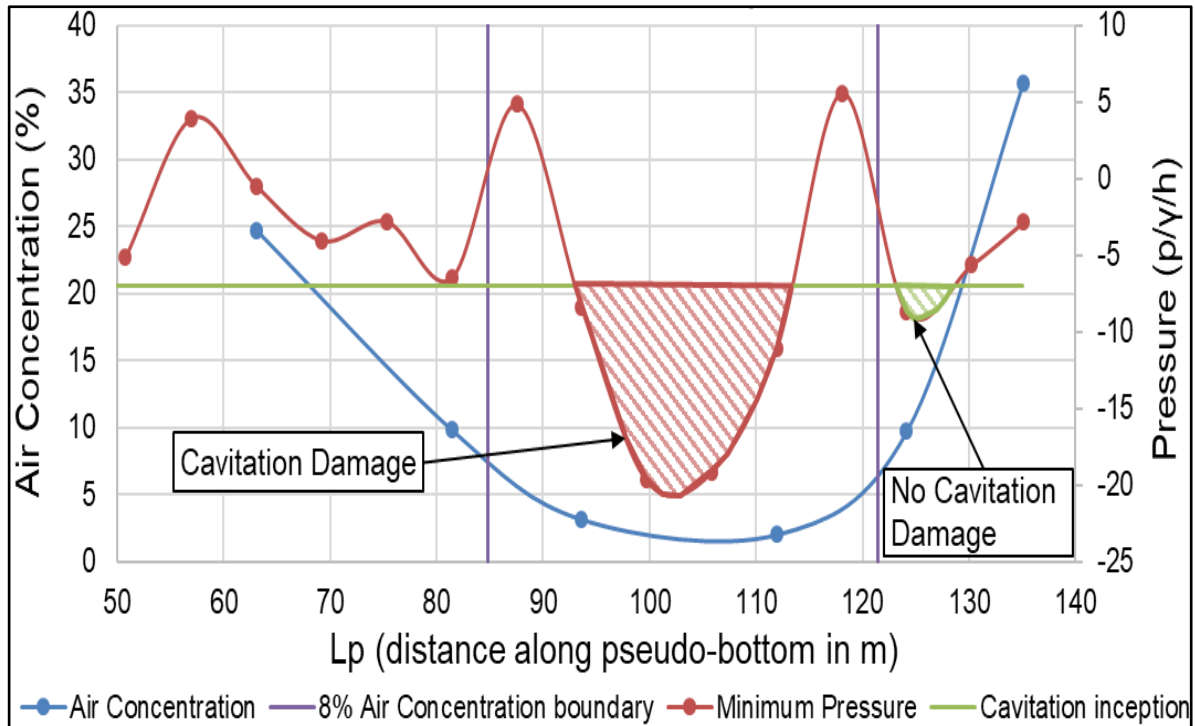


Figure F.5: Cavitation analysis for the Y-Shape FGP at a unit discharge of 50 m²/s.

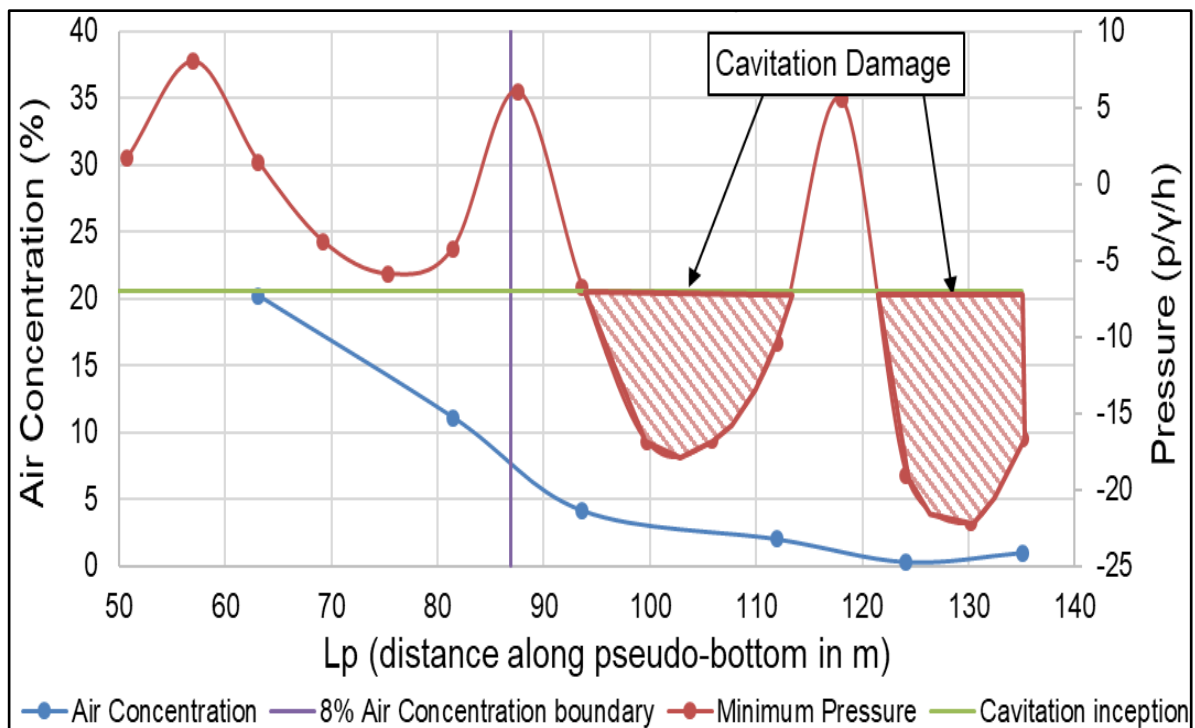


Figure F.6: Cavitation analysis for the Y-Shape FGP at a unit discharge of 100 m²/s.

Appendix F

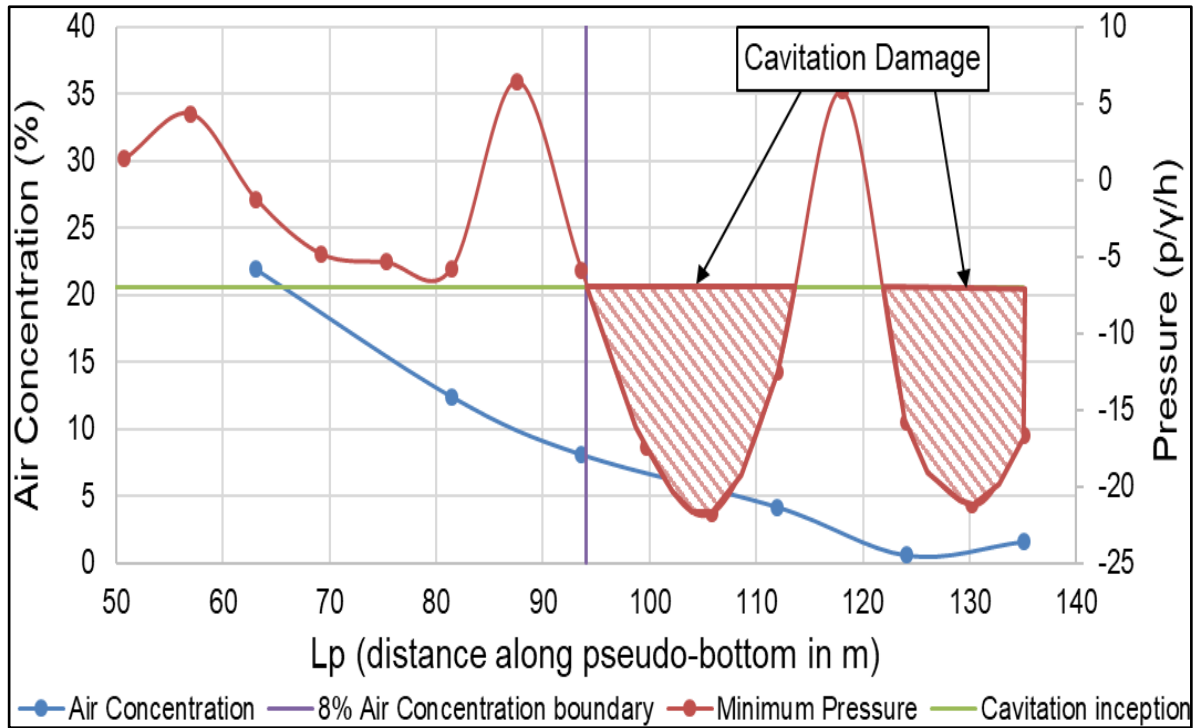


Figure F.7: Cavitation analysis for the Y-Shape FGP at a unit discharge of 150 m²/s.

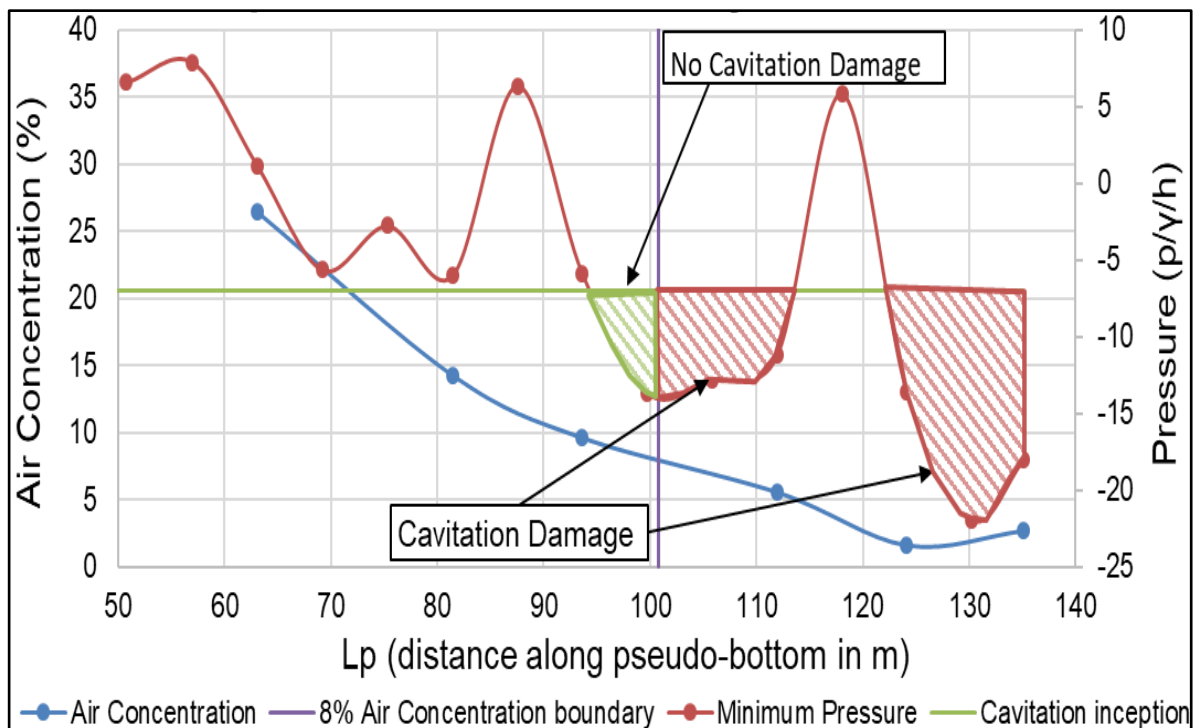


Figure F.8: Cavitation analysis for the Y-Shape FGP at a unit discharge of 200 m²/s.

Appendix F

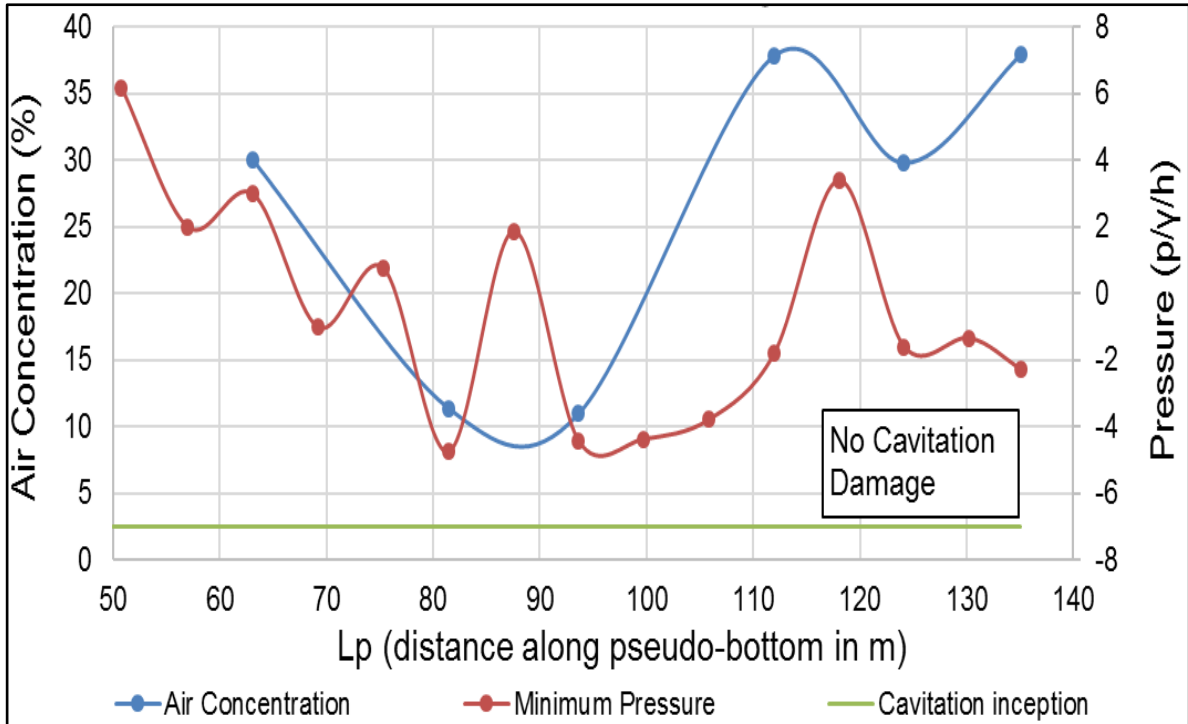


Figure F.9: Cavitation analysis for the X-Shape FGP at a unit discharge of 50 m²/s.

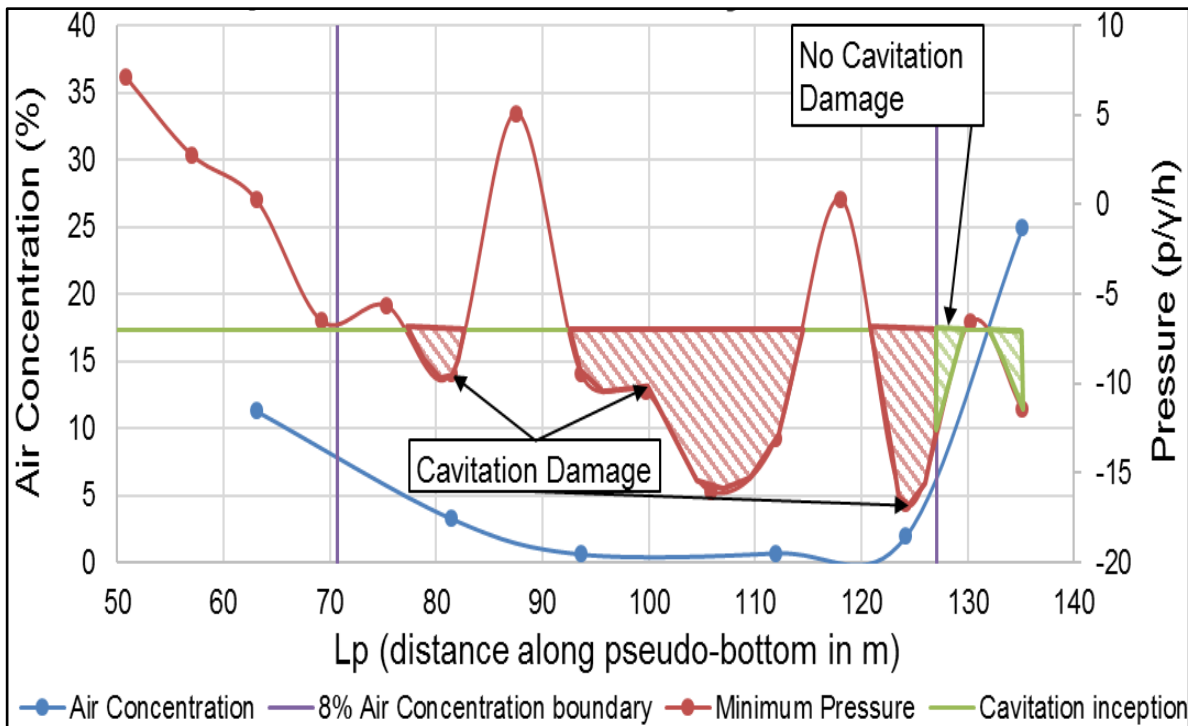


Figure F.10: Cavitation analysis for the X-Shape FGP at a unit discharge of 100 m²/s.

Appendix F

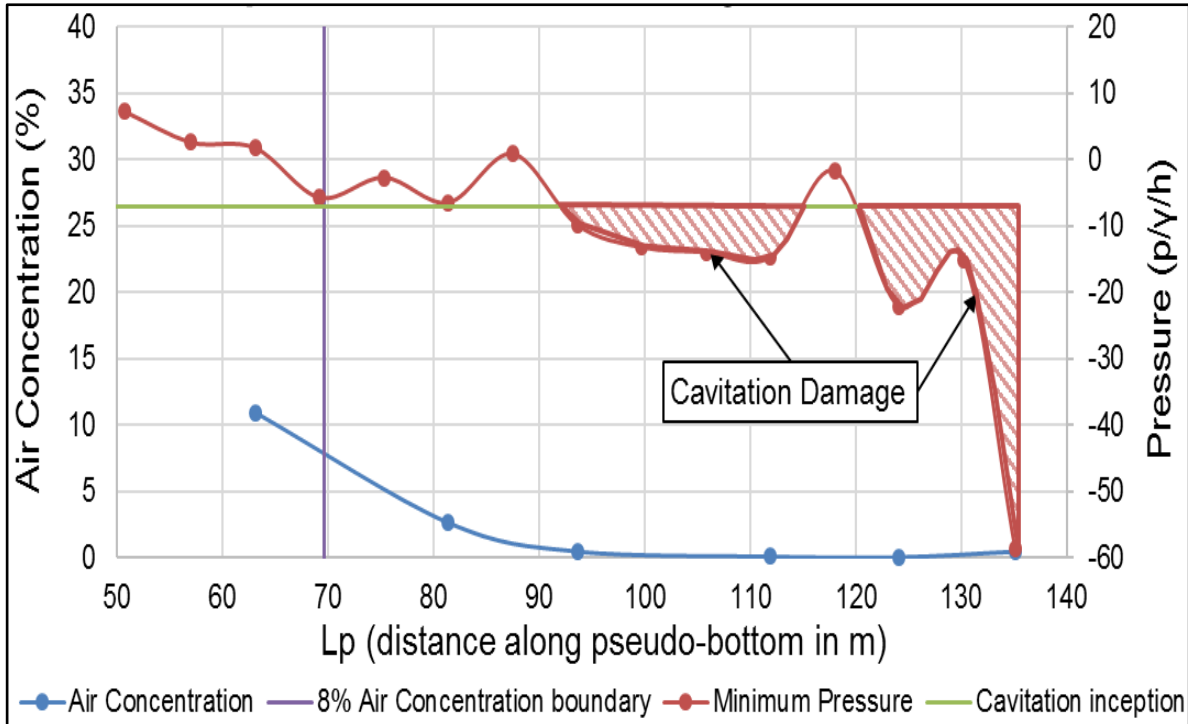


Figure F.11: Cavitation analysis for the X-Shape FGP at a unit discharge of 150 m²/s.

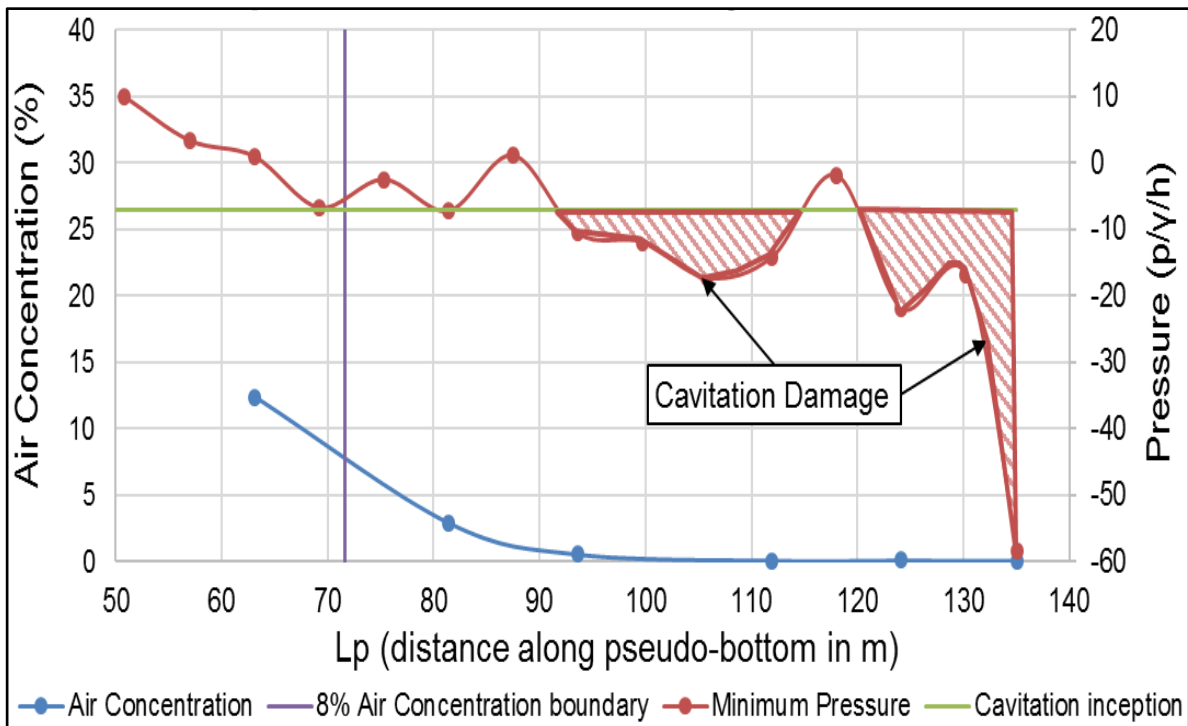


Figure F.12: Cavitation analysis for the X-Shape FGP at a unit discharge of 200 m²/s.